New Mapping Method of a Radial Turbine

Wang, Haizhu

Award date:
2023

Awarding institution:
University of Bath

New Mapping Method of a Radial Turbine

submitted by

Haizhu Wang

for the degree of Doctor of Philosophy

of the

University of Bath

Department of Mechanical Engineering

Bath, August 2023

Declaration

I declare that I have read and understood the entry in the Student Handbook for the Department of Electronic and Electrical Engineering on Cheating and Plagiarism and that all material in this thesis is my own work, except where I have indicated with appropriate references. It is being submitted for in fulfilment of the requirements of the degree of Doctor of Philosophy in Electronic and Electrical Engineering. No portion of the work in this document has been submitted before for any degree or examination at any other university.

Signature of Author. 

Date.....11th August 2023.....

Abstract

Turbocharging is one of the most essential techniques in internal combustion engine technology, and they are often modeled as look-up tables in 1D engine models by using the mapping data collected under steady-state conditions. However, turbochargers are often used with internal combustion engines where the reciprocating motion results in unsteadiness.

The thesis proposes a new mapping method for a radial turbine in numerical and experimental ways, where this method involves the usage of pulsations and different wastegate openings.

A detailed literature review of the up-to-date mapping methods for turbocharger turbines will be illustrated by highlighting research gaps:

- There is a lack of a precise and accurate experimental methodology to quantify the instantaneous behaviors of the turbine.
- How will unsteady behavior of a radial turbine differ from steady state mapping results and how to quantify it by using a robust model?
- Without unsteady data, is CFD possible to use as a model to predict mapping results with the correction of mechanical loss and heat loss?
- How to model a wastegate accurately and is it possible to map a turbine with different wastegate openings?

Conventional gas stand mapping data were collected for a specific turbocharger with a fixed geometry that comes from a production of a 1.5 L gasoline engine, extended data are captured by using a closed-loop configuration. The experimental data collected is then used as a baseline to compare with 1D model with pulsations and steady CFD models.

The author also analyzed a dual-orifice model which was validated by engine test data. The model's results give a detailed comparison of how the turbine will react under pulsating conditions in a range of different frequencies versus steady data. The model also gives the feasibility of assessing unsteady mapping by modeling different sensors.

A computational fluid dynamics (CFD) model was also built and analyzed as an alternative to the mapping experiments. This 3D CFD turbine model is built based on the geometry of the turbine. The results show good agreement with the use of a mechanical loss model that this author built, thus in this way, a CFD model coupled with a mechanical loss model can be used in turbine mapping work.

What is more, the use of a wastegate in turbine mapping is also explored. The thesis collected the mapping results of this radial turbine with different wastegate openings by using a set of two hotwire probes to measure the mass flow rate that passed through the turbine inlet volute as well as the wastegate in different wastegate positions. The results are then validated with a CFD model with the wastegate open. A wastegate flow coefficient model is then built based on the data collected, which is able to give a prediction of the turbine under different wastegate opening positions.

Dedication

This PhD thesis is dedicated to my family.

Acknowledgement

I would like to give my thanks to two lead supervisors of mine in my PhD journey. Firstly my first lead supervisor, Dr Colin Copelandr, thank you so much for offering me the opportunity of a PhD when I felt lost during my gap years. Secondly, as my second lead supervisor, Prof. Richard Burke, thank you so much for your encouragement in my academic work and daily life, your support has given me so much confidence and you are such a great role model! I would also give my thanks to Dr Aaron Costall as my second supervisor for giving me so many instructive suggestions and inspiration! Thank you so much to all of my colleagues in IAAPS, especially Dr Tomasz Duda, Dr Stefan Tuechler, Dr Misan Madamedon, Dr Adamos Adamou, Mr Simon Orchard, Mr Nick Evans, Mr Davide Di Blasio, Mr Matthew Turner, and the technician teams.

Thank you to my friends I met in Bath: Dr Yang Liu, Dr Zichen Liu, Dr Zheng Liu, Dr Luyao Li, Dr Linzhen Tan, Miss Xue Bai, and Mr Han Wang, thank you for your tolerance of my bad temper, and thank you so much for being wonderful mentors for studying, cooking, and playing Switch games! Many thanks and love to my bestie Wenjie, my baby sister Sophie, and my dear boyfriend Qibei, I love you so much!

Thank you so much to my parents for your support, I feel so lucky to have your love, and thank you so much for always being proud of me. And last but not least, many thanks to the cutest dog in the world-our Burger King, you are such a good boy!

Contents

List of Figures

Nomenclature

Abbreviations

c_p	Specific heat of air$[J/(kgK)]$
$1D$	One Dimensional
$3D$	Three Dimensional
A	Area$[m^2]$
aSt	Acoustic Strouhal Number
Cd	Discharge Coefficient
Cf	Flow Coefficient
CFD	Computational Fluid Dynamics
CTA	Constant Temperature Anemometers
f	Pulse Frequency[Hz]
FS	Full Scale
FSt	Fourier series Strouhal Number
GHG	Green House Gas
h	Oil film thickness[mm]

HWA Hot wire anemometry

ICE Internal Combustion Engine

$INST$ Instantaneous

M Mach Number

MFP Mass Flow Parameter

MFR Mass Flow Rate

N Rotational speed[mm]

P Pressure[Pa]

PDE Partial Differential Equations

PR Pressure Ratio

Q Heat Loss

r Radius[mm]

RPM Revolutions Per Minute

RSS Root Sum Square

SST Shear-Stress Transport Model

St Strouhal Number

T Temperature

t Time

U Blade speed$[m/s]$

VGT Variable Geometry turbochargers

WG Wastegate

Greek Symbols

η Efficiency

γ Ratio of specific heats

ν Kinetic Viscosity

ρ Density

τ Torque

θ Angle of Degrees

Subscripts

$Baro$ Barometric

$Calib$ Calibrated

$comp$ Compressor

$isen$ Isentropic

jb Journal Bearing

ref Reference

$t-s$ total to static

$t-t$ total to total

tb Thrust Bearing

$temp$ Temperature

$turb$ Turbine

Chapter 1

Introduction

1.1 Background

There are strong incentives for research and development in the automotive industry as the Business Enterprise Research and Development outlined in their research for the automotive research and development evaluation. On the other hand, irrecoverable climate change due to the emission of greenhouse gases (GHG) at unsustainable levels is by far the greatest global environmental challenge of the 21^{st} century. CO_2 is labeled as a harmful pollutant to human health because of climate change, EURO 6, EURO 7, and other emission regulations have set limits on the release of exhaust pollutants from vehicles (Avola (2017)). One of the reasons contributing to that is the waste of heat in a conventional internal combustion engine in the automotive industry. The government strongly supports the research and innovation for the Low Carbon Vehicles Innovation Platform as well as High-Value Manufacturing and Transport System Catapults. Engine downsizing is one of the critical issues in the interventions.

From Figure 1-1, what can be seen is that boosting technologies will remain relevant well into the 2040s, and the reason for engine boosting technique will be discussed in the following section.

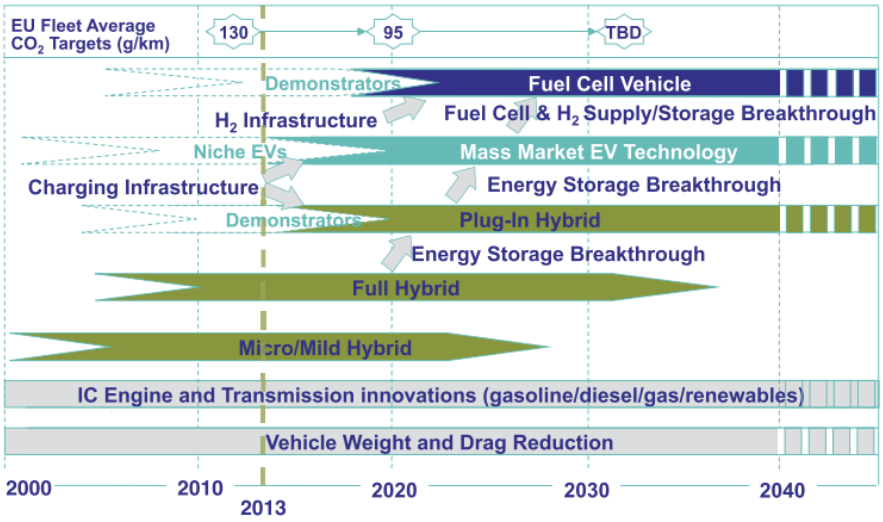

Figure 1-1: An independent report on the future of the automotive industry in the UK, New Automotive Innovation and Growth Team,(Department for Business, Energy Industrial Strategy, 2020)

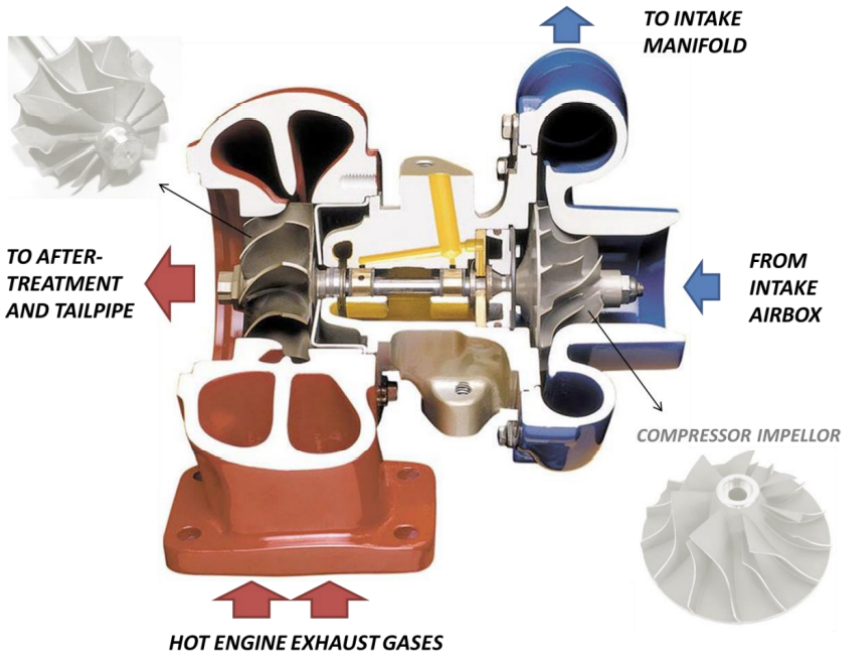

Figure 1-2: Turbocharger system layout (Liu, 2020)

1.1.1 Engine downsizing and turbocharging

Engine downsizing is to replace a large capacity natural aspirated engine (Liu and Copeland, 2018) with a boosted downsized engine of small capacity, while the same engine performance is achieved but with a reduced break specific fuel consumption and emissions (Holt, 2012). Downsizing will improve fuel efficiency because of these reasons:

- Low frictional losses will contribute to fewer and smaller cylinders
- Low heat loss thus comes from a smaller engine
- Lower weight of engines will make it easier to package a lighter and more aerodynamic vehicle

Turbocharging as shown in Figure 1-2 as a key boosting technology is widely used in the vehicle industry as its effectiveness to recover energy from the exhaust gas, it extracts energy from the hot, high-pressure exhausted gas from the engine. With all of these years of development, the turbocharger has become a mature technology where the room for product differentiation is extremely small and project profitability highly depends on the delivered quality. This is because penalty clauses imposed by customers could have a strong bad effect on the business.

As a result, turbo manufacturers are constantly being pushed to improve the product performance in different ways.

Figure 1-3 shows the main objectives both technical and commercial for manufacturers to consider, for the industry perspective, engineers need to take into consideration of turbocharger performances under different working conditions and their trade-offs, they will also need to consider the costs.

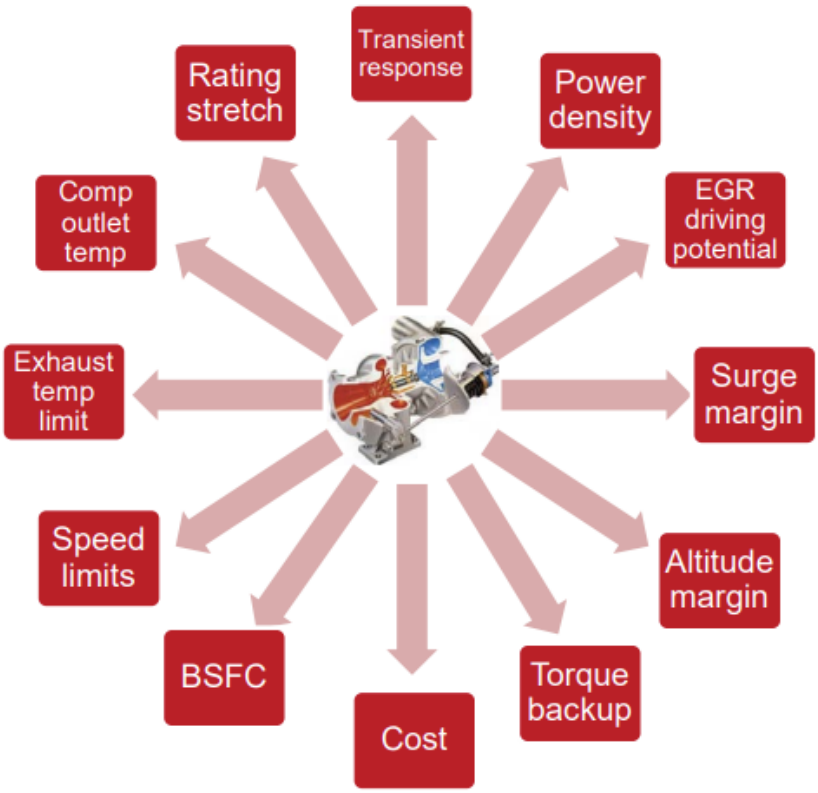

Figure 1-3: Objectives for turbocharger technology (Costall, 2015)

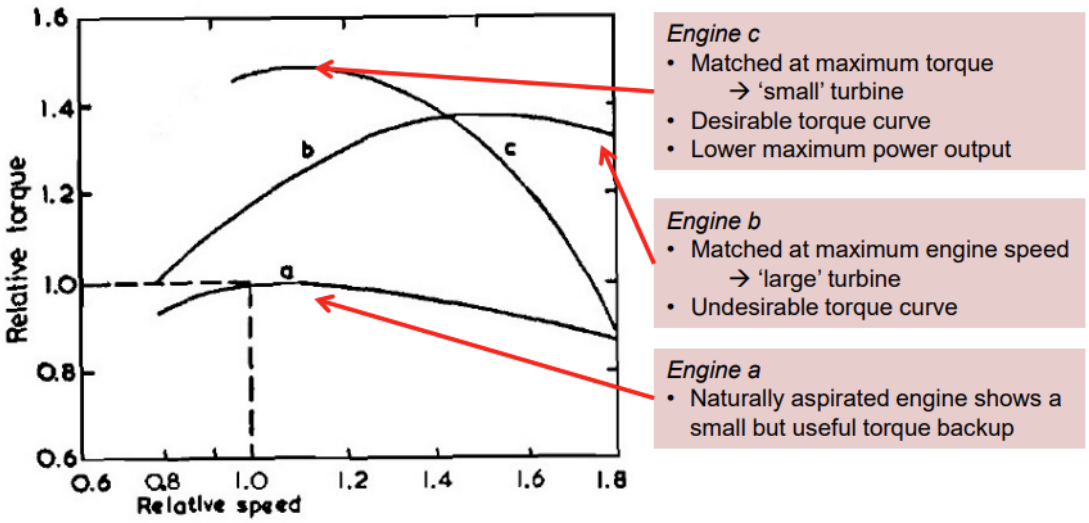

Figure 1-4: Turbine matching example (Costall, 2015), and (Watson and Janota, 1982)

1.1.2 Matching and boost control

Turbocharger matching is the process of selecting the optimal combination of compressor and turbine, with a specific engine design. In general, off-the-shelf components are used from large libraries of existing products to give the best combination of requirements for a handful of full-load engine operating points, taking into consideration of engine smoke limit, cylinder pressure limit, exhaust gas temperature, and turbo speed limit. Bad matching will result in many drawbacks including redesigning the turbine and compressor, poor efficiency, and not meeting the targets.

As for the turbine, Figure 1-4 gives an example where a represents a naturally aspirated engine as a baseline. Engine b is matched at maximum engine speed, and engine c is matched at maximum torque. Sizing of the turbine will determine the ability of the turbochargers to provide a boost at different engine speeds, when reducing turbine area in Figure 1-5, specific available energy increases at all engine speeds hence available boost energy increases. On the other hand, turbine efficiency will decrease with rising pumping work and overall brake-specific fuel consumption.

Boost control methods are widely used in order to control the power extracted from

the exhaust by the turbine at different operating points. The main practical implementations include:

- Wastegated (WG) turbochargers
- Variable geometry(VG,VGT,VTG,VNT)

Wastegated turbochargers with fixed geometry are most common and are widely used in turbocharging systems due to their effectiveness, low cost, and ability to work at high exhaust gas temperatures (Capobianco and Marelli, 2007). To achieve optimal matching of engine-turbocharger, turbine performance when the wastegate valve is partially or totally opened should be studied both in a steady state and in the typically unsteady flow conditions occurring in automotive engines.

Unfortunately, turbocharger manufacturers usually provide very little information about steady flow turbine characteristics in the opened wastegate field, even though this is a fundamental input for theoretical simulation models (Capobianco and Marelli, 2007). A wastegate, as shown in Figure 1-6 works by passing some proportion of the flow around the turbine wheel. When boost energy is high enough, the actuator will open the wastegate valve so a decreased amount of air will go through the turbine wheel.

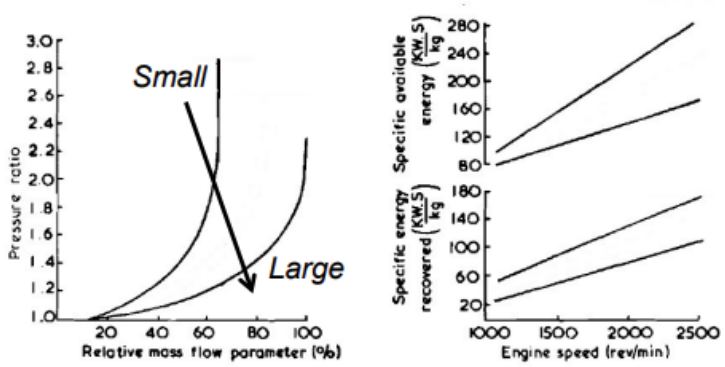

Figure 1-5: The effect of turbine area (Watson and Janota, 1982)

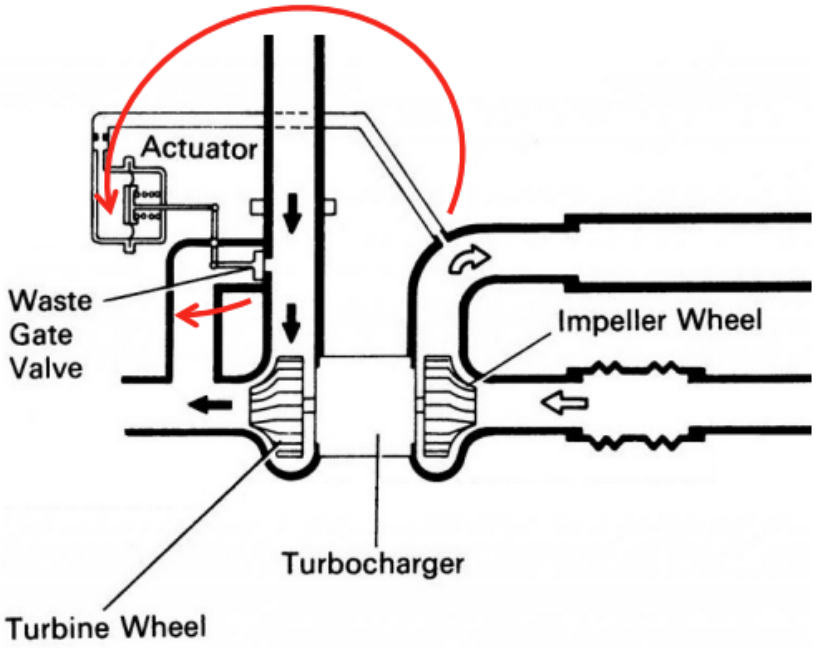

Figure 1-6: The wastegate (Costall, 2015)

1.1.3 Turbocharging mapping and pulsating flows

Unlike a turbocharger compressor, a turbocharger turbine is exposed to pulsating flow due to the opening and closing of the exhaust valves, and the reciprocating motion of pistons, thus the turbine operates a wide range of working conditions, leading to significant instantaneous variations. The conventional way of gathering a turbine performance map is to use a steady gas stand test in which the whole picture of the pulse nature of turbine characteristics cannot be entirely captured since they are limited by the surge and choke of compressors, and extrapolated by a small range of data. Errors occur because of the lack of flow physics in the extrapolation process, and a lot of research has given evidence about the departure of the turbine under pulsating inflow condition performance from steady mapping data. This thus will have a negative effect on the on-engine performance prediction, because turbocharger turbines are often modelled as a look-up table in one-dimensional engine cycle simulation tools as they are working under quasi-steady conditions, which leads to unreliability in simulation

results.

1.2 Research Question and Objectives

Based on the research gaps identified in the background information above, the aim of this thesis is to improve the accuracy of mapping a fixed geometry wastegated radial turbine. This will be used for further matching purposes for engines or fuel cell systems.

This research aims to answer the following questions:

1. What is the state-of-art mapping method for single-entry radial turbines?
2. How to collect mapping data and quantify the operating conditions for a single entry radial turbine precisely?
3. How to model a single-entry radial turbine precisely in 1D and 3D?
4. How to measure and model a turbine under unsteady conditions?
5. Can CFD models be used to map a turbine?
6. How to measure and model different wastegate openings in mapping?

To answer these research questions, the following objectives are laid down:

1. To conduct a detailed literature review on up-to-date mapping methods for turbocharger turbines.
2. To develop a precise experimental methodology where the characteristics of the turbine can be correctly captured and apply it to a specific radial turbine.
3. To build a 1D model and use it to predict turbine behavior under both steady and unsteady conditions.

4. To build a 3D CFD model which can predict turbine performance and compare it to experiments.

5. To build a mechanical loss model and couple it to a 3D CFD model and predict turbine performance with improved agreement compared to data collected experimentally.

6. To map the turbine in different wastegate conditions correctly and precisely, and model different wastegate conditions with the comparison of experimental data.

1.3 Thesis Outline

To achieve these objectives, the thesis is divided into eight chapters: Chapters 2-7 will answer the six objectives listed in section 1.2, and Chapter 8 will give the conclusion of the thesis:

CHAPTER 2 *Literature Review*

This chapter aims to answer research question 1 based on objective 1. This chapter gives a detailed literature review of the state-of-the-art work regarding turbocharger turbine mapping methods and the unsteady behavior. The research gap as well as the research objectives have been pointed out.

CHAPTER 3 *Experimental Methodology*

This chapter aims to answer the research question 2 based on objective 2. Based on the literature review, a detailed experimental methodology is described in which both averaged and instantaneous measurements of turbine characteristics are correctly captured. An uncertainty analysis is conducted for all of the parameters used.

CHAPTER 4 *Numerical Methodology*

This chapter aims to answer the research question 3 based on objective 3. This chapter

presents the model approaches used. A dual-orifice 1D model of a gas stand will be used to compare the steady and unsteady performance of a radial turbine, engine stand turbine experimental data have validated this model. This model will be further discussed in Chapter 5 *Unsteady Mapping Method*.

Additionally, two 3D CFD models, a simplified CFD model, and a CFD model with wastegate will also be used in this thesis, and both models' domain settings and mesh sensitivity will be discussed. These two CFD models will be further discussed in Chapter 6 *Can CFD be Used to Map a Turbine Accurately?* and Chapter 7 *How to Map a Wastegate Turbine?*

CHAPTER 5 *Unsteady Mapping Method*

This chapter aims to answer the research question 4 based on objective 4. To use a dual-orifice model where the characteristics of a radial turbine under pulsating flow conditions could be accurately captured. Both effects of pulse frequency and turbine geometry characteristics will be analyzed using this 1D dual-orifice model. This chapter will also demonstrate how different sensors as illustrated in Chapter 3 *Experimental Methodology* used for mapping will react in unsteady gas stand experiments.

CHAPTER 6 *Can CFD be Used to Map a Turbine Accurately?*

This chapter aims to answer the research question 5 based on the objective 5. The matching of the simplified CFD model described in Chapter 4 with the steady turbine mapping results by using the apparatus of Chapter 3 will be discussed. In order to decrease the error between CFD results and experimental data, a sensitivity study of the correlations will be illustrated and a mechanical loss model using seven parameters in regard to bearing surface finish and clearance will be built based on the analysis.

CHAPTER 7 *How to Map a Wastegate Turbine?*

This chapter aims to answer the research question 6 based on objective 6. A method-

ology using hotwire probes to measure the wastegate behavior correctly and accurately will be illustrated, and both the mass flow passing through the turbine wastegate and the inlet tongue will be captured in three wastegate opening positions. The hotwire measurement results will be validated against V-Cone flow measurement under steady conditions. A model of flow coefficient will be discussed based on a fitting method determined by experimental data.

The CFD model with wastegate discussed in Chapter 4 will be further validated by the steady mapping results collected by using the apparatus described in Chapter 3, and this model will then be used as a validation of the wastegate flow coefficient.

CHAPTER 8 *Conclusions*

This chapter gives a summary and conclusion of this research and also lists future work.

Chapter 2

Literature Review

2.1 Outline of the Chapter

This chapter aims to answer the first research question illustrated in Chapter 1, that is, what is the state-of-art mapping method for single-entry radial turbines? To answer this question, this literature review is conducted in regard to turbocharger mapping methods in pulsating flow conditions and can be divided into three parts:

- Turbine modeling

  Section 2.2 will cover the review of turbine modeling methods including zero-dimensional turbine modeling by using a mathematical model, a one-dimensional mean-line model, a 1D model with the pulsating flow, as well as 3D CFD models. These different modeling methods serve different purposes. This section will discuss their different purposes and seek to conclude each modeling type where there are gaps including the precision of the models and the lack of data in empirical models.

- Turbine experiment method for mapping

Section 2.3 will cover the experimental methods used for turbine mapping under unsteady conditions and the ways of collecting and selecting data.

- Turbine wastegate study

  Section 2.4 of this literature review is about the wastegate study, where both the wastegate mass flow rate measurement and modeling are covered.

2.2 Turbine Modelling

To understand the up-to-date mapping method for single-entry radial turbines, one needs to understand the types of turbine modeling methods used for various purposes. Thus, in this section, the author will compare different turbine modeling methods and seek the gaps.

Numerical turbine models can be classified according to their complexity (Liu and Copeland, 2018), i.e. empirical model, one-dimensional code model, as well as three-dimensional CFD model.

2.2.1 Empirical models

Turbine modeling techniques are widely used for predicting turbine swallowing capacity as well as efficiency characteristics, where empirical models use analytical functions to fit the limited range of turbine test data (Sieros, Stamatis and Mathioudakis, 1997; Fang et al., 2010; Fang and Dai, 2010; Gamma Technologies Inc., 2017). This type of model is widely used as a sub-model for engine system models used for matching work in software like GT-Power because of its fast response and reasonable computational costs. Figure 2-1 shows a typical turbine map with a look-up table and built-in extrapolation method in the 1D engine model in WAVE, and in Figure 2-1, the+ dots represent the data collected under steady conditions in a gas stand.

In 1987, Watson and Janota (1982) proposed a simple model in which an adiabatic noz-

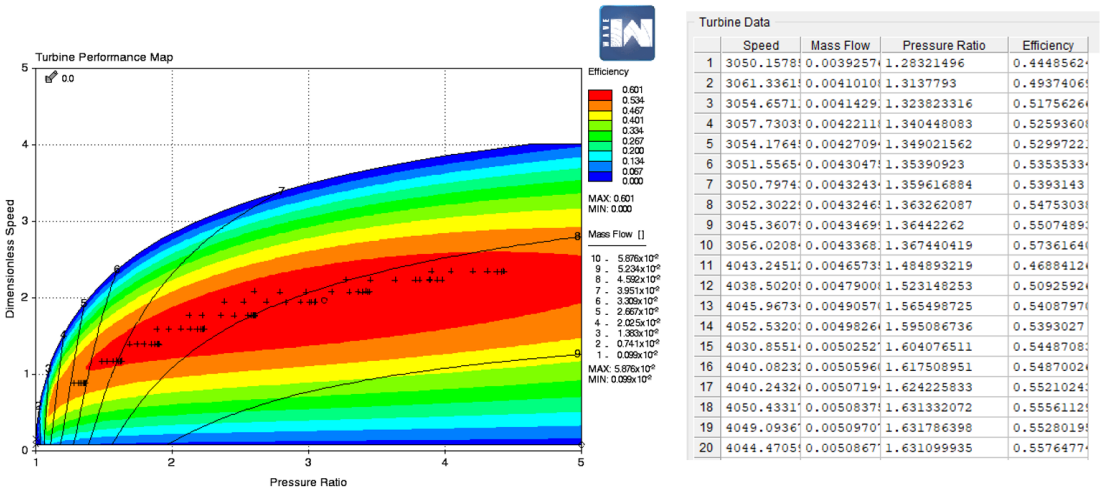

Turbine Data

	Speed	Mass Flow	Pressure Ratio	Efficiency
1	3050.1578	0.0039257	1.28321496	0.4448562
2	3061.3361	0.0041010	1.3137793	0.4937406
3	3054.6571	0.0041429	1.323823316	0.5175626
4	3057.7303	0.0042211	1.340448083	0.5259360
5	3054.1764	0.0042709	1.349021562	0.5299722
6	3051.5565	0.0043047	1.35390923	0.5353533
7	3050.7974	0.0043243	1.359616884	0.5393143
8	3052.3022	0.0043246	1.363262087	0.5475303
9	3045.3607	0.0043469	1.36442262	0.5507489
10	3056.0208	0.0043368	1.367440419	0.5736164
11	4043.2451	0.0046573	1.484893219	0.4688412
12	4038.5020	0.0047900	1.523148253	0.5092592
13	4045.9673	0.0049057	1.565498725	0.5408797
14	4052.5320	0.0049826	1.595086736	0.5393027
15	4030.8551	0.0050252	1.604076511	0.5448708
16	4040.0823	0.0050596	1.617508951	0.5487002
17	4040.2432	0.0050719	1.624225833	0.5521024
18	4050.4331	0.0050837	1.631332072	0.5556112
19	4049.0936	0.0050970	1.631786398	0.5528019
20	4044.4705	0.0050867	1.631099935	0.5576477

Figure 2-1: The turbine look-up table in a 1D engine model

zle represents the turbine with an effective area that could produce the same pressure drop in the same mass flow rate condition.

$$\frac{\dot{m}\sqrt{T_{01}}}{P_{01}} = A_{eff} \cdot \sqrt{\frac{2\gamma}{R(\gamma-1)}\left[\left(\frac{1}{PR_t}\right)^{\frac{2}{\gamma}} - \left(\frac{1}{PR_t}\right)^{\frac{\gamma+1}{\gamma}}\right]} \tag{2.1}$$

Where A_{eff} represents the effective area of the turbine which is a linear function of the expansion ratio, that is to say,

$$A_{eff} = k_1 \cdot PR_t + k_2 \tag{2.2}$$

However, one of the main drawbacks of this simple model is that a nozzle usually reaches choked flow conditions with an expansion rate of approximately 1.89 whereas a radial turbine is able to reach a total expansion ratio of 3.0 (Serrano et al., 2008). In 1991, Jensen et al. (1991) proposed an improved model by including choked flow conditions, and the equations to characterize turbine became:

$$\begin{aligned}\frac{\dot{m}\sqrt{T_{01}}}{P_{01}} &= A_{eff}\cdot\sqrt{\frac{2\gamma}{R(\gamma-1)}\left[\left(\frac{1}{PR_t}\right)^{\frac{2}{\gamma}}-\left(\frac{1}{PR_t}\right)^{\frac{\gamma+1}{\gamma}}\right]PR_t^{cirt}} \\ &= \left(\frac{2}{\gamma+1}\right)^{\frac{\gamma}{\gamma-1}}\frac{\dot{m}\sqrt{T_{01}}}{P_{01}} \\ &= A_{eff}\cdot\sqrt{\frac{2\gamma}{R(\gamma-1)}\left[\left(\frac{1}{PR_{t,Critical}^{cirt}}\right)^{\frac{2}{\gamma}}-\left(\frac{1}{PR_t^{cirt}}\right)^{\frac{\gamma+1}{\gamma}}\right]}\end{aligned} \tag{2.3}$$

In their model, when the turbine expansion ratio is higher than a critical number, the new equation is applicable, and vice versa. The critical number is defined as:

$$PR_t^{cirt} = \left(\frac{2}{\gamma+1}\right)^{\frac{\gamma}{\gamma-1}} \tag{2.4}$$

2.2.2 One-dimensional models

Zero-dimensional turbine mapping

Zero-dimensional turbine map or map-based turbine model is widely used for commercial 1D codes such as GT-Suite (Gamma Technologies Inc., 2017) and Ricardo-Wave (Ricardo-Wave, 2019), in which an SAE standard map (SAE, 1995b) (SAE, 1995a) conducted under steady flow conditions and this limited range of experimental data is then extrapolated within the software so that the turbine sub-model will work as a look-up table to predict its characteristics. If a steady map is used in 1D simulation in unsteady conditions, the turbine will follow the same steady performance data at any instantaneous time within the simulation; This is called quasi-steady method (Gamma Technologies Inc., 2017),(Ricardo-Wave, 2019). 1D simulation software usually solves the 1D form of the Naiver-Stokes equations governing the transfer of mass, momen-

tum, and energy for compressible gas flows and includes sub-models for combustion and emissions. In a one-dimensional model, turbines are modeled as a sub-model. The volute is often modeled as a duct with specified volume and length and the rotor is often modeled as a look-up table with mapping data of a mean-line model to account for the energy transferred in it (Chiong et al., 2012),(Copeland et al., 2012),(Liu and Copeland, 2018). The fluid is conducted within different shapes of ducts, i.e. straight, curved and tapered, and the frictional losses are also taken into consideration in (Copeland et al., 2012) and (Chiong et al., 2012) for curvature effects.

Payri, Benajes and Reyes (1996) improved the method of using the empirical model based on the study of (Watson and Janota, 1982). Two nozzles in series are used to represent a turbine as shown in the following Figure 2-2 and Figure 2-3.

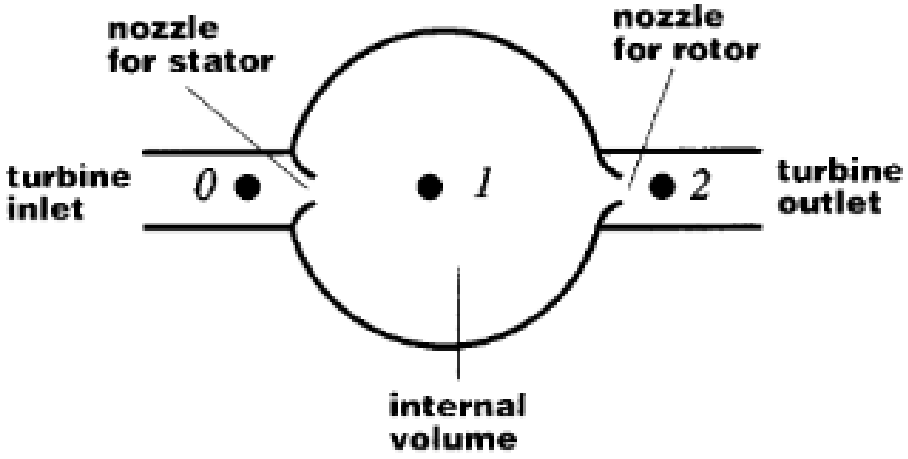

Figure 2-2: Geometric model for a single-entry turbine (Payri, Benajes and Reyes, 1996)

In their model, the first nozzle stands for the turbine stator and the second nozzle stands for the rotor passages (Payri, Benajes and Reyes, 1996). They assumed that half of the expansion took place in the stator and the other half took place in the rotor. They also extended this method for twin entry turbine by using two nozzles to represent two entry discharging into a common intermediate chamber (Payri, Benajes

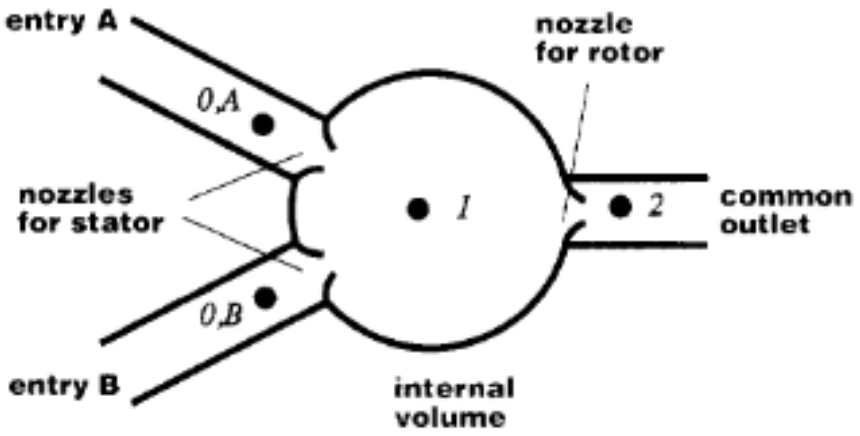

Figure 2-3: Geometric model for a double-entry turbine (Payri, Benajes and Reyes, 1996)

and Reyes, 1996).

Mean-Line turbine model

Mean-line approach models turbine performances as if there is a mean streamline of gas flowing through a turbine (Futral and Wasserbauer, 1965) (Liu and Copeland, 2018). One of the earliest research using the mean-line model approach is in 1965 (Futral and Wasserbauer, 1965). They developed a program in which radial turbines with nozzle casting off-design performance can be predicted by using mean-line equations as well as turbine geometry and dimensions. Kastner and Bhinder (1975) built a method for predicting the performance of a nozzle-less radial flow turbine with the assumption that the working fluid is treated as ideal gas inside of the turbine expanding adiabatically. In 1973, Whitfield and Wallace (1973) improved the incidence loss in radial and mixed-flow turbines by noting that the inlet blade angle is not zero and the optimal efficiency for mixed flow turbine occurs at the incidence angle range between -20^o and -40^o.

In 1980, an improved mean-line model was conducted by Meitner and Glassman (1980). In their model, the rotor loss coefficient was correlated by using a stator-to-rotor throat area ratio. The ratio was less influential on the rotor loss coefficient when it is above

0.6, while the rotor loss coefficient increased rapidly when the ratio decreased from below 0.5, thus a mean-line model for VGTs have been developed. In 1983, Meitner and Glassman (1983) further improved the mean-line model by taking rotor blade back sweep into consideration. In summary, the mean-line model calculates turbine efficiency by estimating the energy losses as air flows through different sections of the turbine, and these losses are commonly modeled by a function of velocity triangles and loss coefficient by using empirical equations, and validation against experimental data often conducted for a more accurate result. The loss models used in these early mean-line models are still commonly used by later researchers.

One-dimensional model considering pulsating flows

Chen and Winterbone (1990) are among the earliest researchers who coupled the 1D gas dynamic codes with mean-line models to predict turbine performances under unsteady flow, and they calculated the incident angle of the rotor by using free vortex equation based on the flow condition at the inlet of the volute domain. Chen, Hakeem and Martinez-Botas (1996) further improved the model by conducting numerous loss term calculations using slip factors for the velocity triangle calculation at the incidence, thus the effects of flow separation were taken into consideration. This model gives a good agreement of instantaneous power with experimental data while the swallowing capacity was underestimated compared with the experiment. Abidat et al. (1998) developed a model in which the model can be used in the steady and unsteady flow performance, and they studied the effects of pulse frequency and amplitude, concluding that the departure of both mass flow and power was close to the cycle-averaged quasi-steady assumption.

Costall and Martinez-Botas (2007) and Costall et al. (2011) analyzed the behavior of turbocharger turbines under unsteady environments for both single entry and twin entry as shown in Figure 2-4; They built up a simulation and compared the results versus experiment data. The unsteadiness used Fourier analysis and decompose the

pulse into constituent frequencies. An unsteady boundary condition was applied at the volute inlet so that the same pulsed pressure was reproduced. Their model gives a good prediction with the limiting numbers of the Fourier series Strouhal and acoustic Strouhal number $FSt \leq 0.15$ and $FaSt \leq 0.02$. In the research of Chiong et al. (2012), they improved the model of Costall et al. (2011) by using the 1D code built by Costall et al. (2011) as well as the mean-line model. In their model, a single-entry nozzle-less mixed flow turbine characteristics are simulated on a time-resolved basis. They assumed that the absolute flow angle is constant and calculated by the A/r ratio and density change across the volute. Their model showed good agreement between the predicted averaged isentropic power and experimental data but suggested that the instantaneous mass flow rate prediction should be improved.

Chiong et al. (2012) further improved their model for a single entry turbine by firstly modeling the unsteady flow propagation in turbine volute using 1-D gas dynamic code and then evaluating its instantaneous turbine power using the mean-line model. As shown in Figure 2-5, the flow is assumed to enter the rotor from three entries at different azimuth positions at 90 deg, 180 deg, and 270 deg respectively, and as a result, the prediction of turbine performance especially the instantaneous mass flow rate is improved when compared with experimental data in Figure 2-6.

Chiong et al. (2013) further improved their model for the usage of the twin-entry turbine under full admission pulsating flow conditions in 2013 and they pointed out that the tapered ducts in 1D have an impact on increasing the fluctuations of the secondary flow. They also compared the steady calibrated mean-line model results with unsteady map data, and they found that in regard to turbine output power, unsteady model prediction is quite close to quasi-steady assumption on the cycle-averaged basis while there are noticeable deviations in terms of instantaneous performance. Chiong et al. (2014) did further research by comparing the model performance for a different number of rotors and no improvement is gained. They also studied the effects of

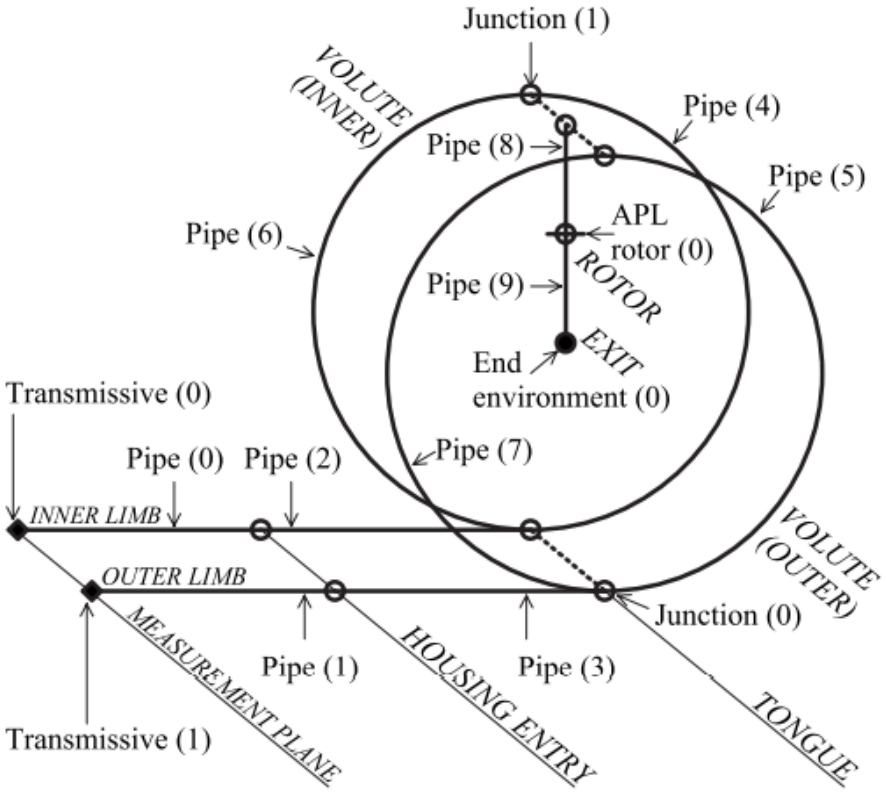

Figure 2-4: The twin entry model that (Costall et al., 2011) built-domain arrangement, nodes along broken lines are coincident

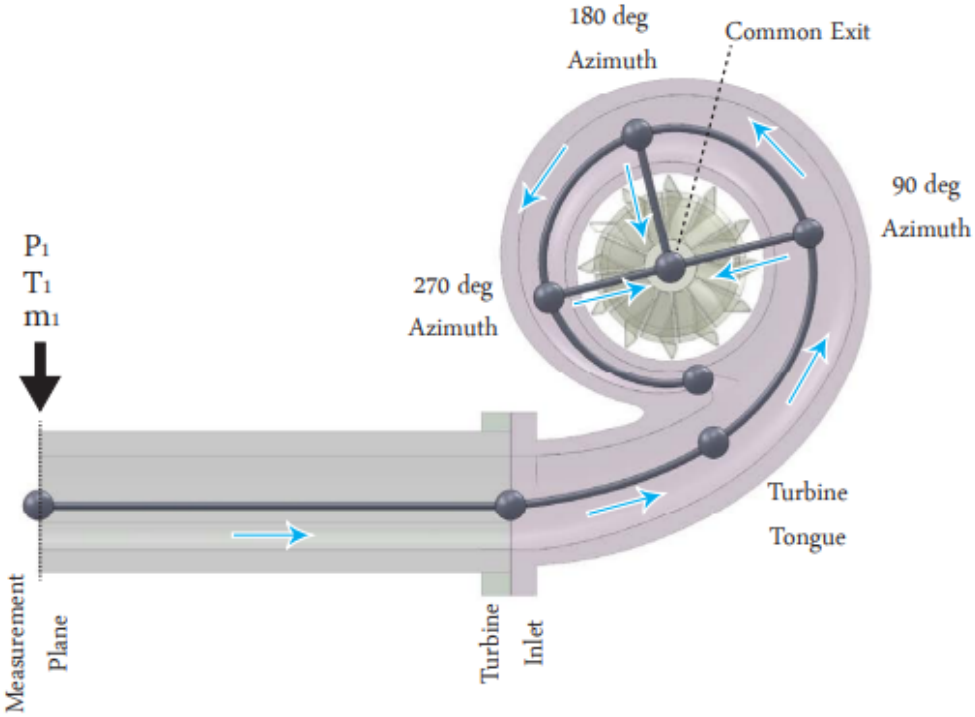

Figure 2-5: Azimuth schematic diagram of the numerical model (Chiong et al., 2012)

the discretion length/diameter ratio, concluding that the maximum L/D(discretion length/pipe diameter) ratio of 0.55 gives a good compromise between computational time and accuracy. Chiong et al. (2015) modeled a turbine by using a non-adiabatic pressure loss boundary condition, which required significantly lower geometry inputs and reduced the computational time by 38.6%.

2.2.3 Three-dimensional models

Most zero dimensional models or 1D models used quasi-steady assumption to predict the unsteady behavior of the turbine, and in order to have a more detailed view of the fluid field inside of a turbine system, three-dimensional CFD codes are widely used.

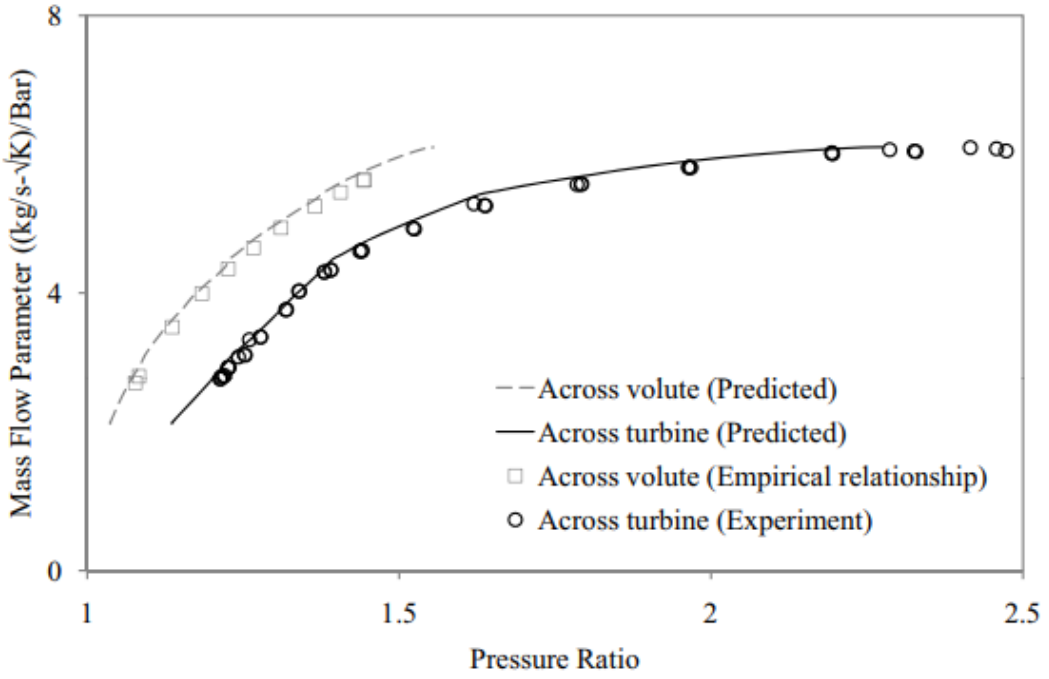

Figure 2-6: The MFP-PR across stator and turbine (Rajoo, Romagnoli and RF, 2012)

Chen, Hakeem and Martinez-Botas (1996) are among the earliest researchers towards 3D modeling methods. They used a quasi-three-dimensional design method where the two-dimensional potential flow equations are streamlined equations and are solved to calculate the geometry of spiral volutes. Their model also built a tongue loss model, which in total gives good agreement when compared with experimental data.

One of the biggest controversies in regard to 3D modeling is how to treat the interface between the stationary and rotational interface. In 2002 Lam, Roberts and McDonnell (2002) used a 3D model of a single-entry turbocharger turbine under pulsating flow conditions. The frozen rotor approach is used to model the rotor stage. This frozen rotor method, also known as multiple reference frame, is commonly used in steady conditions in which the flow at the interface between the rotational rotor and other stationary domains is assumed to be uniform. It keeps the mesh stationary and simulation uses a rotating coordinate system to simulate the motion. One of the benefits of

using a frozen rotor is that a larger time step can be used to reduce its computational cost since the time scale inside of the rotor domain is treated unresolved so that the blade passage effect and the stator-rotor interaction are neglected. They noted that in their model the pulse frequency was much lower than the rotor passing frequency.

On the other hand, the sliding mesh method (SM) is also widely used by researchers to model the interface between the rotor and stator. This method moves the rotor mesh during the calculation, and the stator and rotor mesh are coupled together at each time step thus increasing the computational cost.

In the research of Palfreyman and Martinez-Botas (2005), they found that the frozen rotor approach may give damping results of mass flow rate and efficiency while the SM method can capture the hysteresis type curve numerically. Similar results were also found by many researchers (Liu and Hill, 2000), (Hellström, 2010). Hellström also pointed out that the sliding mesh method takes into account the viscous losses at the stationary and rotational domain interface so that it is better than the frozen rotor approach in loss definition.

Galindo et al. (2013) studied a radial variable geometry turbine (VGT). They also compared these two impeller movement techniques as well as the experimental data. In Figure 2-7, corrected mass flow $\dot{m}_1^*$ vs overall pressure ratio π_{1t5s}, turbine torque tau vs overall pressure ratio π_{1t5s} and turbine efficiency η vs overall pressure ratio π_{1t5s} were compared. It showed that the difference is small when the turbine is working within or close to design points while the difference becomes obvious when working at off-design points. The differences reached up to 24% and 11% in regard to corrected mass flow and efficiency respectively. They also pointed out that the volute section is the domain where most of the time-shift in the mass flow occurs and the volute shows a significant unsteady behavior with the increase of the pulse amplitude and frequency. The flow in the nozzle domain presented a limited hysteretic behavior in regard to the pulsating flow capacity and the impeller flow behavior was less affected by wave actor

and accumulation effects.

Padzillah et al. (2014) provide a detailed and validated comparison of steady and pulsating conditions flow field behavior for the nozzled and nozzle-less turbines. They found that the frozen-rotor approach gives a similar instantaneous flow rate prediction as the sliding mesh method under steady conditions, and the main differences between these two configurations were significant in regard to flow angles. The nozzle-less volute gave more variation of flow angles at both inlet and outlet; The variation of exit flow angle was more significant close to the tongue.

2.2.4 Conclusion of turbine modeling

Based on the literature review on turbine modeling, the main findings are listed:

- Low-order models including zero-dimensional and one-dimensional models are effective ways to predict turbine characteristics with fast response and reasonable computational costs thus they are often used as sub-models in engine system models.

- Mean-line turbine models are used and improved by several researchers on the loss model, and they are able to capture the unsteady behavior of the turbine with the hypothesis of quasi-steady behaviors.

- CFD models are widely used for the study of detailed insight into turbine fluid dynamics, and the previously mentioned models are often fitted against CFD data with a need for high computational cost.

- Apart from CFD, all models discussed rely on experimental characterization of the turbocharger and therefore it is important in the next section to review the state-of-the-art in terms of experimental methods for turbines.

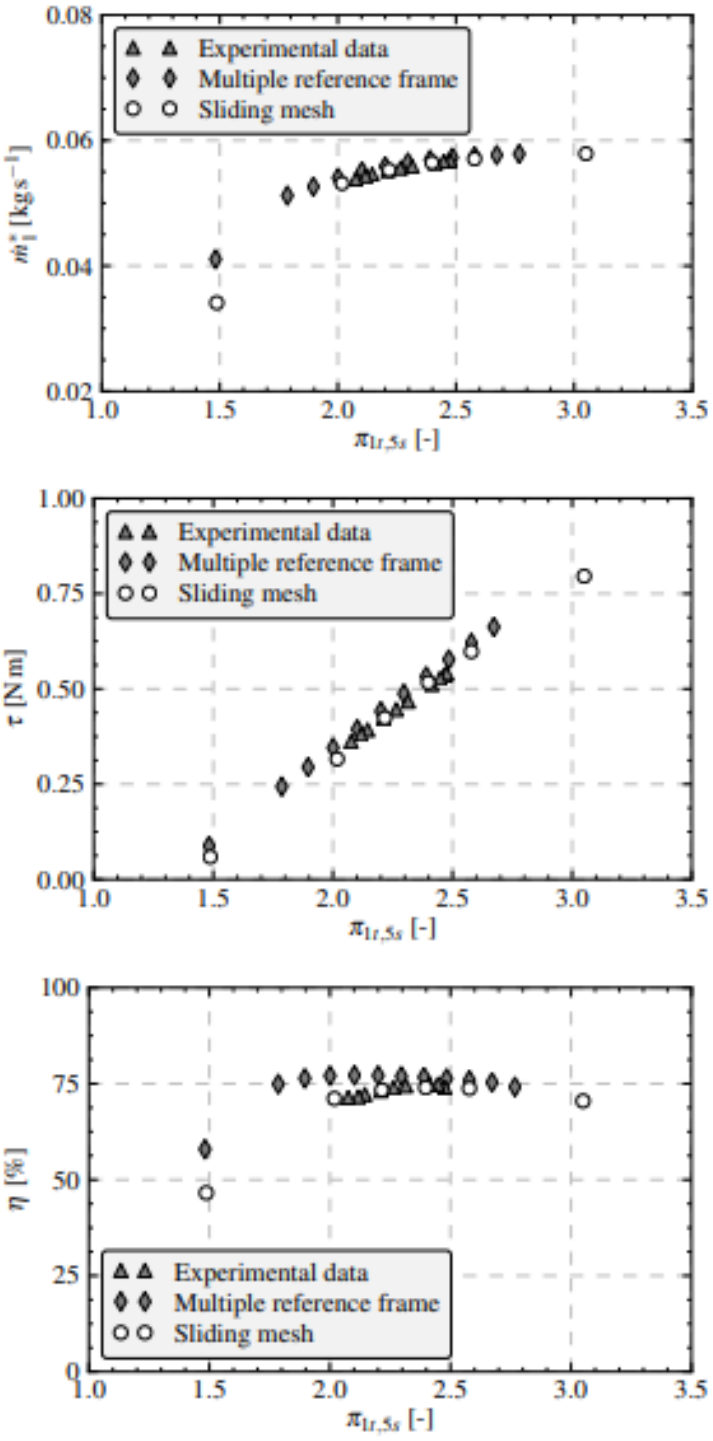

Figure 2-7: Comparison of different impeller movements technique (Galindo et al., 2013)

2.3 Experimental Work of Turbine Mapping

As aforementioned, the experimental method plays an important role in turbine mapping. In this section, the thesis will discuss the state-of-art methods of turbine mapping experiments.

Gas stands are widely used to characterize turbochargers since the 1990s. Figure 2-8 shows a schematic of an electrically heated gas stand with a dual air supply to characterize twin entry turbines (Benson and Scrimshaw, 1965).

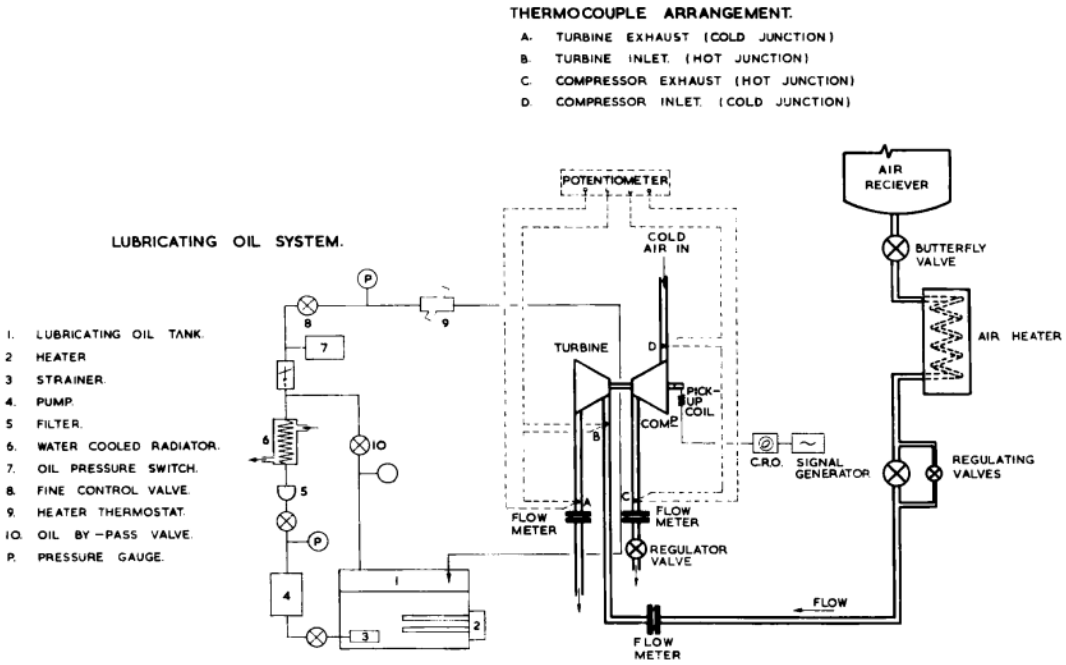

Figure 2-8: Arrangement of early steady turbocharger rig (Benson and Scrimshaw, 1965)

In the arrangement of the gas stand shown in Figure 2-8, heaters are used to heat up the compressed high-pressure air that comes from the air receiver. Turbine inlet conditions will thus be hot. Electrical heating is the standard turbine mapping method in the industry. For higher temperatures, a fuel-fired burner may be utilized rather than electrically heating (Duda, 2017). The turbine and compressor are thus mapped together in steady conditions.

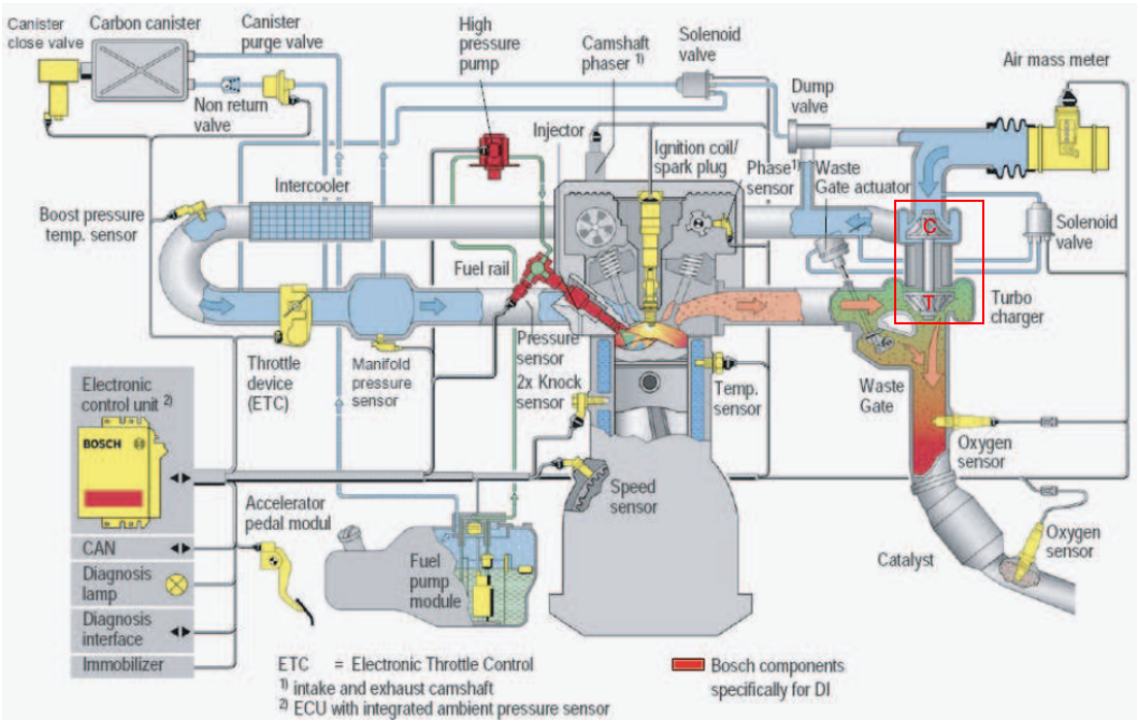

Figure 2-9: Configuration of a turbocharged gasoline direct injection engine (Lee et al., 2010)

For comparison, the configuration of a turbocharged gasoline direct injection engine equipped with variable intake and exhaust camshafts is shown in Figure 2-9. The heaters in a gas stand are used to generate the hot air of the exhaust gas at the turbine inlet. The difference between an engine stand and a gas stand is that for an engine stand, there will be exhaust gas from the engine in the turbine inlet while for a gas stand, it was heated compressed air.

In 2010, the research of Leufven and Eriksson (2010) firstly built a method to determine turbocharger performance in an engine test bench. Their research mainly focused on compressor maps but some attention was also given to turbine swallowing capacity. In their research, only a limited range of operating points were reached due to the exhaust temperature limit for turbine protection and the lack of a 'hot' mass flow measurement for the turbine inlet.

In 2016, the research of Avola et al. (2016) improved the engine gas stand to study the turbocharger performances in engine-like conditions as shown in Figure 2-10. In their apparatus, a 2.2 L diesel engine was externally pressurized by a boost rig so that the intake air was regulated for pressure, temperature, and mass flow rate. The CBP shown in the layout represents a compressor back pressure (CBP) valve, which is controlled to generate the load on the compressor. Additionally, the fuel consumption has also been measured to quantify mass flow through the turbine, and the exhaust gas re-circulation circuit was kept closed when generating turbine maps (Avola et al., 2016). The main challenge of using an engine gas stand is that it is hard to capture the fluctuations of instantaneous temperature and mass flow rate at the turbine side and in their research. The matching work of the turbine is based initially on validated 1D simulation tools which used steady turbine data as the input.

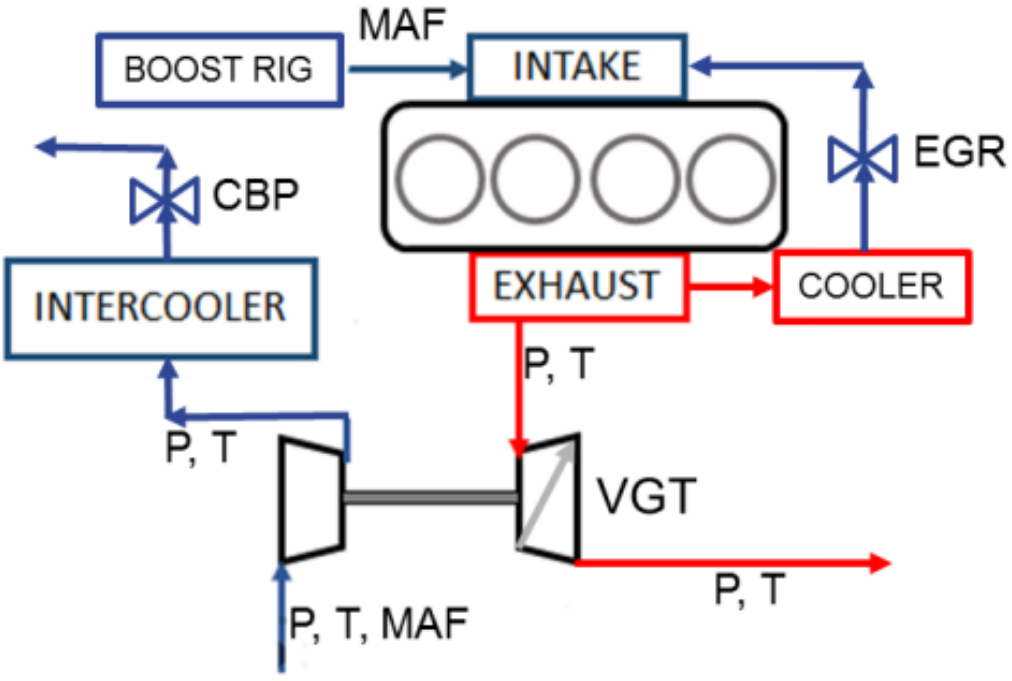

Figure 2-10: Configuration of the engine gas-stand (Avola et al., 2016)

Early research about pulsating flow nature

The steady flow characteristics of turbines have been investigated and studied by many researchers since the 1950s. However, Wallace and Blair in 1965 (Wallace and Blair, 1965) pointed out that in order to investigate turbine characteristics under pulsating conditions, new numerical and experimental methods should be used.

They first came up with a quasi-steady assumption, in other words, the flow is considered as a large number of small intervals, and during these intervals, the conditions of flow with regard to pressure and temperature are considered to be identical with those that would be obtained in steady flow conditions. By summing up the products of those intervals, total efficiencies as well as the corresponding isentropic enthalpy drops in a pulse could be thus obtained.

In their research, a high-power pulsator rig is used, and quasi-steady theory was adopted to evaluate the mass flow as well as power by using a recorded superimposition wave profile upstream of the turbocharger turbine. For every interval, the instantaneous specific total to static isentropic enthalpy drop was evaluated by the conditions of current upstream data and then subsequent flow. The results were compared with steady flow tests. Their research gave a prediction with absolute errors of up to 25 percent of turbine power output but an acceptable indication of trends.

They used steady-flow characteristics for full admission rather than partial admission in all cases, which is to say, no windage losses were applied for corrections. They drew a conclusion that the quasi-steady flow hypothesis becomes progressively less accurate with the increase in pulse frequency. Additionally, because they used full admission efficiencies when applying the quasi-steady flow to calculate power, the power was overestimated, and as for partial admission, a drastic underestimate was given. Additionally, because they used a turbo compressor as a brake, only a limited range of speed and power data were captured (Wallace and Blair, 1965).

Wallace and Miles (1970) extended their work and compared two flows treatments of unsteady and quasi-steady as shown in Figure 2-11 by combining the analyses of unsteady flow investigation on radial flow turbines and steady flow research of very high-pressure ratios and multiple admission together to give a coherent treatment of single and multiple admission.

They compared different cases involving single entry, two entry, and three entry. The unsteady flow tests showed a satisfying agreement of pressure and mass flows between modeling and experimental data, but due to the inclusion of internal losses, a less satisfactory agreement was shown for power. Their two treatments both showed good agreement in the case of a single entry, as for two entry turbine cases, mass flow gave satisfying agreement in both two treatments, but unsteady treatment underestimated the power while quasi-steady was overestimated in the same case. They only tested unsteady flow treatment in three entry cases. According to their research, acceptable results (mass flow of 1 percent error and power with 20 percent error) were obtained. They drew a conclusion that the quasi-steady assumption gives an acceptable result in terms of pulse amplitude predictions compared with the full unsteady flow treatment.

In 1974, Benson (1974) investigated the non-steady flow effect in a nozzle-less radial gas turbine. Differences between predicted performance using steady flow data and unsteady flow performance were emphasized, and they raised a new method in which a form factor I, which is related to pulse shape. Experimental data showed that turbine performances are related to the factor. Generally speaking, they found that mass flow prediction based on steady flow data is independent of this, but power predictions are related to this. However, their research assumed that pressure in the turbine exhaust stays constant, which causes some of the non-steady influences.

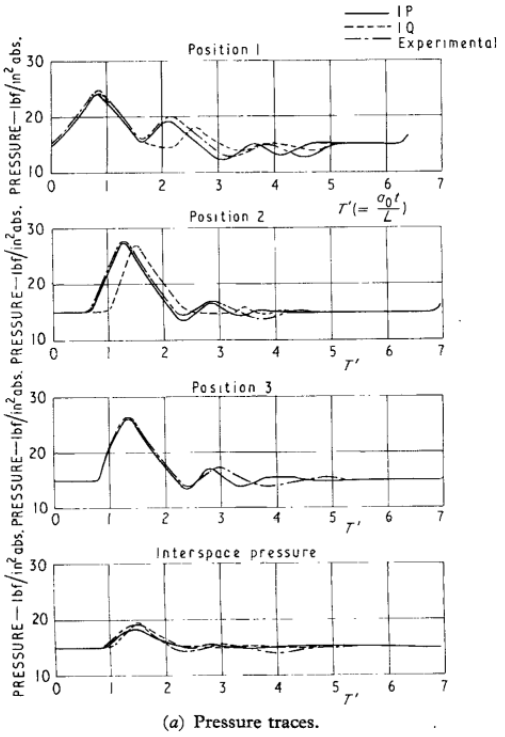

(a) Pressure traces.

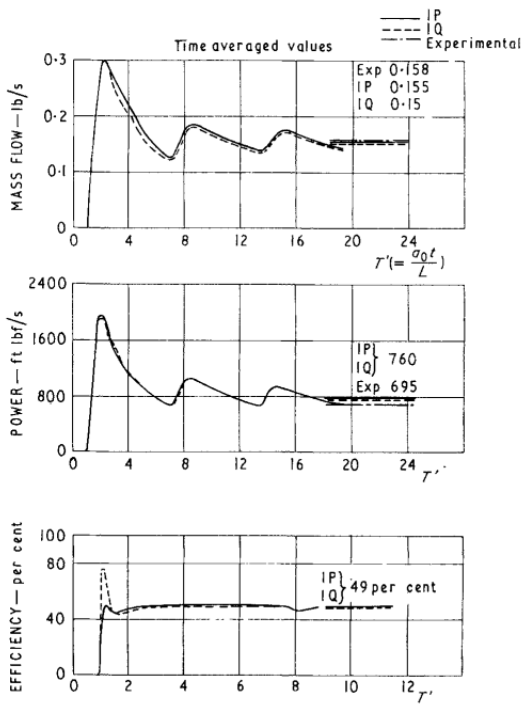

(b) Time-averaged flow, power and efficiency.

(a) Single entry casing

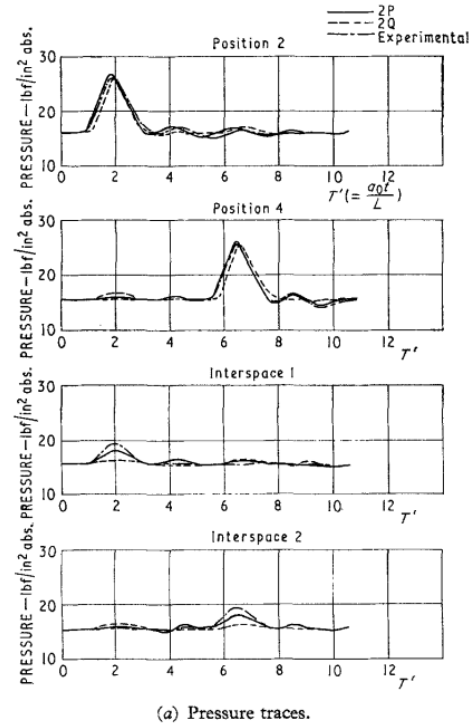

(a) Pressure traces.

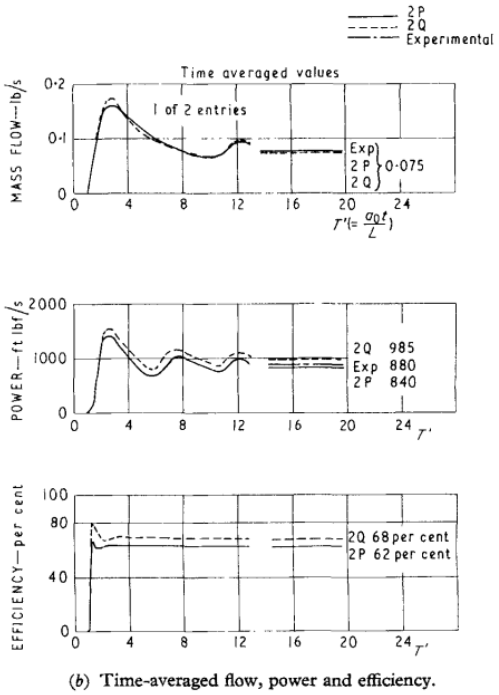

(b) Time-averaged flow, power and efficiency.

(b) Two entry casing

Figure 2-11: Two flow treatment comparison (Wallace and Miles, 1970)

Extrapolation method for pulsating flow mapping

Those standard gas stand measurements cannot always capture the pulsating flow conditions where a physical phenomenon called negative efficiency usually occurs Liu and Copeland (2018). This will lead to an error in the prediction of the compressor power.

For the compressor side, standard steady gas stand measurement data are quite straightforward because the data are adequate to cover most of the conditions operating on the engine. On the other hand, paramount is that when a turbine is mounted on an internal combustion engine, the reciprocating motion of the pistons will result in the fluctuation of upstream gas, which will lead to a wide range of different working conditions for turbines so that the blade speed ratio will vary in those cases. By using conventional steady gas stand measurements, some convincing data could be captured especially when the turbine is working as a part of a turbocharger, in other words, the range of data captured by conventional gas stand measurement might well be not sufficient to cover all of the working conditions in which the turbine might be exposed to. That is to say, for simulation work, some extrapolations should be taken into consideration in order to get enough data for the turbine apart from the limited data available. This process when the extended data need to be extrapolated is one of the key areas in which errors can occur in the prediction of turbocharger characteristics, which may have a serious influence on the entire engine Liu and Copeland (2018).

Empirical relationships are widely used by many researchers in which for turbine characteristics, polynomial or exponential relationships are used among turbine mass flow parameters, turbine efficiency, turbine blade speed ratio, as well as turbine expansion ratio, and the coefficients are often obtained with experimental data as well as regression analyses. These kinds of models are also called mean-value models (Kacker and Okapuu, 1982),(Qiu, Anderson and Baines, 2009),(Chiong et al., 2014),(Rahbar, Mahmoud and Al-Dadah, 2016),(Da Lio, Manente and Lazzaretto, 2017).

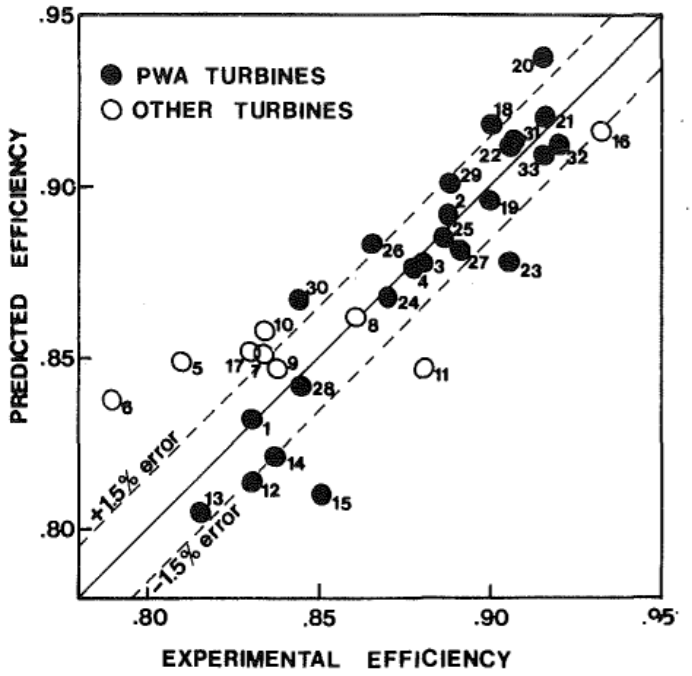

Figure 2-12: Comparsion of predicted efficiency with experimental efficiency of 33 turbines (Kacker and Okapuu, 1982)

Blade lengths and radii are determined early in the design cycle before blade shapes are known, and this is based on the assumption that the thermodynamic processes could be represented in the means of the velocity triangles at midspan. (Kacker and Okapuu, 1982) did research where a mean line loss system is described, capable of predicting the design point efficiencies of current axial turbines of gas turbine engines, and the prediction method is then validated by the data of a wide range of axial turbines with acceptable accuracy within ±1.5% for 33 sets of turbines as shown in Figure 2-12.

Payri et al. (2012) used a physical-based methodology for extrapolation of radial turbine performance maps, in the curve of mass flow characteristics and turbine efficiency. For their first method to extend the mass flow chart, they used the nozzle equation. The turbine stages were idealized as a single nozzle. They carried out a fitting by using the nozzle equation and the limited mass flow experimental data, and they obtained an estimation of mass flow to unknown values of expansion ratios. As for extrapolating the

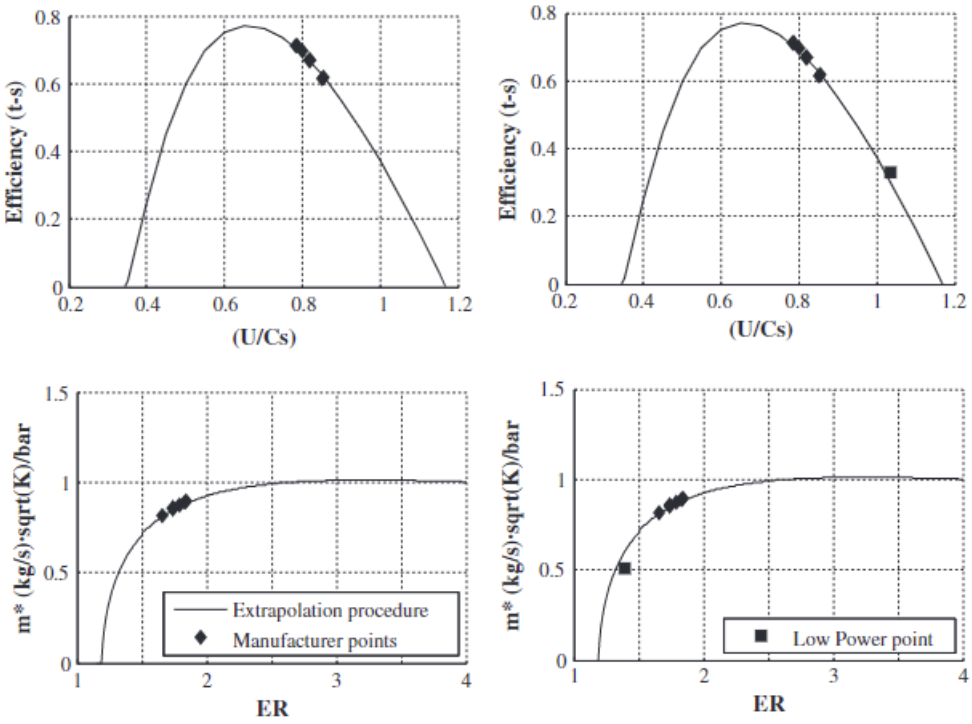

Figure 2-13: Comparison of predicted model results with experimental data (Payri et al., 2012)

efficiency curve, they used an equation developed from physical principles involving the definition of the total to static efficiency, velocity triangles as well as the thermodynamic behaviors of the flow. To conclude, in their research, a procedure for the extension of both swallowing capacity and efficiency maps for a radial turbine has been analyzed which provided a good methodology for obtaining the extended turbine maps and is able to implement 0D and 1D codes for turbochargers simulation. Additionally, in their results, the points at very low power of VGT have also been analyzed with an underestimated mass flow rate and an overestimated efficiency as shown in Figure 2-13.

Similar explorations are used by a lot of researchers (Fang et al., 2010), (Zhu, Deng and Liu, 2015), but one of the biggest weaknesses of these extrapolations suffer from the limitation of data as this method needs a range of experimental data for fitting and extrapolation. Apart from this extrapolation method, many studies were carried

out to understand the turbine unsteadiness in a better way. One of the most common ways among turbocharger unsteadiness analysis is to consider the volute as an unsteady component and rotor as a quasi-steady condition, but those methods may rely on a large library testing data or be faced with some errors in different cases, especially for off-design regions (Winterbone, Nikpour and Alexander, 1990) and it is also challenging to take mechanical efficiency of the shaft into consideration. It is shown that by using the negative efficiency in the turbine map, the simulation results showed a clear improvement in terms of turbine speed and compressor power prediction (Zhu, Deng and Liu, 2015),(Liu, 2020) in other words, by using unsteady data, many shortcomings of turbine mapping in the current industry-wide by steady mapping on the gas stand can be addressed. The core creativity of this method of mapping the turbine performance is to use the pulse itself and therefore a small range of data could be used for extrapolation. In the research of Liu and Copeland (2018), the researcher used the pulse itself to generate quasi-steady data, and this data are then fed into the extrapolation methods for turbine swallowing capacity as well as turbine efficiency, but they only did this for a single speed line due to the complexity of unsteady mapping measurement. Additionally, in their experiment, the turbine instantaneous mass flow rate relies on validated CFD data in which the heat transfer and mechanical loss effects are neglected.

Criterion for unsteadiness in turbochargers

At the beginning of 1990, the first research gave a criterion to quantify the level that unsteadiness deviated from quasi-steady. Chen and Winterbone (1990) used a dimensionless parameter, Strouhal number, S_t and they recommended in the condition when the Strouhal number is less than 1, the turbine can be considered as working in a quasi-steady manner, and when Strouhal number is more than 1, unsteady behavior will occur, and when Strouhal number is near 1, the turbine can be considered as

working in the transition region in both quasi-steady and unsteady.

$$S_t = \frac{fL}{u} \tag{2.5}$$

where f represents inlet pulse frequency, l is the length of the flow passage, and u is the time-averaged fluid velocity, and this S_t number calculation determined the unsteadiness of the flow, which shows:

- $S_t > 1$ Unsteady
- $S_t < 1$ Quasi-steady

Szymko (2006) took a factor into account of the basic Strouhal number and built the 'normalized Strouhal number'.

$$S_t.^* = \frac{fL}{\bar{U}} \frac{1}{2\phi} \tag{2.6}$$

where ϕ is the pulse period as a fraction of the cycle period and the factor $\frac{1}{2}$ represents the normalized frequency where the pulse period constitutes half of the cycle period as shown in Figure 2-14 as an example, where ϕ equals to $\frac{1}{3}$ and the pulse generator are open for 120 degree per revolution. This researcher then scaled this normalized Strouhal number by the Mach number M to get $S_t.(a)^*$

$$S_t.(a)^* = St^* M = \frac{fL}{\bar{a}} \frac{1}{2\phi} \tag{2.7}$$

and scaled by pressure wave propagation

$$S_t \cdot (p)^* = St^* \frac{M}{M+1} = \frac{fL}{\bar{U} + \bar{a}} \frac{1}{2\phi} \tag{2.8}$$

These scaled S_t numbers can give information on the onset of unsteady effects with the relationship of the acoustic travel time and pressure wave propagation, and this showed its benefits in assessing the unsteady influence in the measurement of the point-

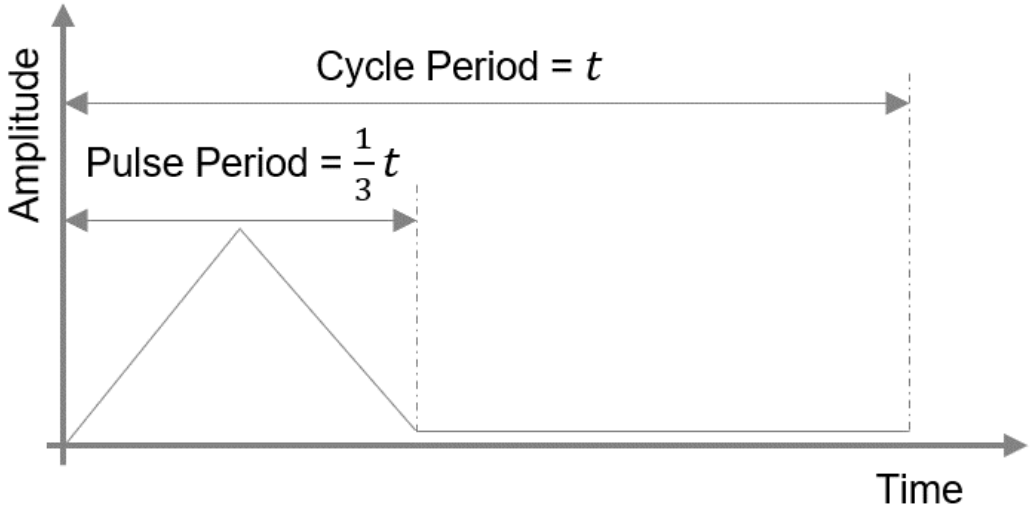

Figure 2-14: Normalized Strouhal number scale definitions (Szymko, 2006)

by-point instantaneous efficiency based on experimental results. From this research, the selection of different models is listed as:

- $S_t{\cdot}^* < 0.1$, 'Quasi-steady' model
- $S_t \cdot (p)^* < 0.1 < S_t{\cdot}^*$, 'Filling and Emptying' model
- $S_t \cdot (p)^* > 0.1$, 'Wave Action' model

Costall and Martinez-Botas (2007) proposed a Fourier series Strouhal number where FSt is defined by:

$$FSt = \sum_{k=1}^{\infty} \left(\frac{|a_k|}{\sum_{k=1}^{k} |a_k|} St_k \right) \tag{2.9}$$

and

$$St_k = \frac{f_k L}{v} \tag{2.10}$$

and k represents the k^{th} components, a_k is the real Fourier coefficient. In this coefficient, the sum of the individual levels of unsteadiness is calculated as indicated in the

definition of the Strouhal number, but calculated for each component, which means the Strouhal number is multiplied by the real Fourier coefficient a_k normalized by the sum of a_k for each component k. In this way, the data points whose frequencies have a greater proportion will, as a result, dominate because of a higher magnitude. Similarly, with the acoustic Strouhal number in Equation 2.7, the researcher further added an acoustic effect on this Fourier series Strouhal number

$$FaSt = \sum_{k=1}^{\infty}(\frac{|a_k|}{\sum_{k=1}^{k}|a_k|}aSt_k) \tag{2.11}$$

where aSt here is the acoustic Strouhal Number,a is the acoustic velocity

$$aSt_k = \frac{f_k L}{\bar{u} + \bar{a}} \tag{2.12}$$

The researcher suggested using both FSt and $FaSt$ as indicators to change the model from 'filling and emptying' to 'wave action' and use $FaSt$ as an additional coefficient to compare the unsteadiness of different waveforms in the 'wave action' model only.

- $FSt \leq 0.15$ and $FaSt \leq 0.02$, 'Filling and Emptying' model

Due to the lack of consideration for the phasing of each component, the unsteady nature was captured sufficiently, and only three-term Fourier series were examined.

Copeland et al. (2012) noted the physical interpretation of Strouhal number based on Greitzer, Tan and Graf (2007) is that 'if a fluid is flowing at a speed v_0 through a domain of a length L_0 that is also pulsating at a frequency f_0, the Strouhal number represents the ratio of time needed for a particle to travel the length of the domain $T_0 = L_0/v_0$ to the time associated with the disturbance being considered $t_0 = 1/f_0$.' which means:

$$S_t = \frac{fL}{u} = \frac{t_{fluid}}{t_{pulse}} = \frac{T_0}{t_0} \tag{2.13}$$

Thus if the travel time T_0 is short enough and comparable to a local change of pulse,

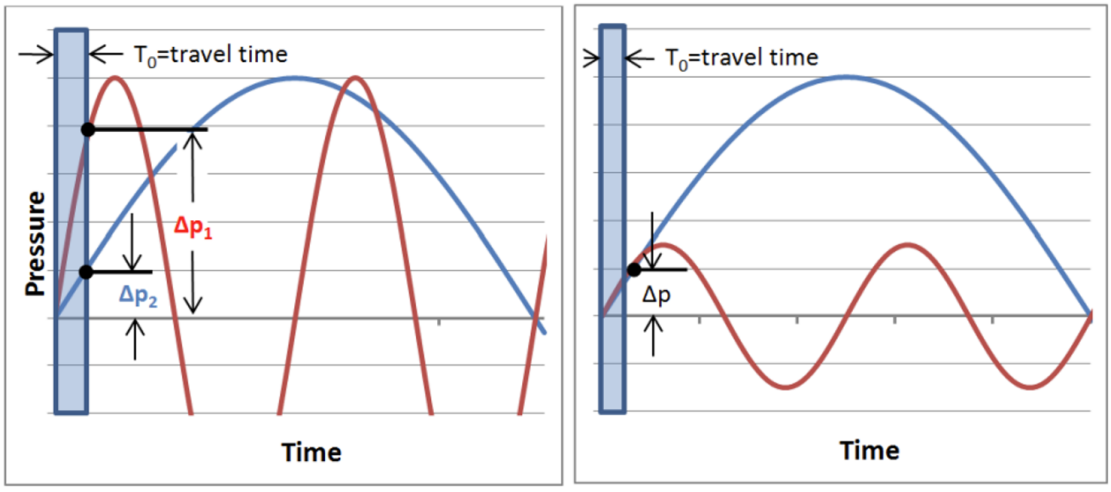

a) Similar Amplitudes

a) Different Amplitudes

Figure 2-15: Comparison of a change of flow condition(pressure) under different frequencies (Copeland et al., 2012)

the division of T_0 and t_0 will be infinite. The researchers then drew a conclusion that the unsteady time-dependent term, as well as the convective term, will influence the flow behavior, as shown in Figure 2-15, where the left Figure shows the influence of two different pulse frequencies with the same mean velocity(same travel time T_0). Due to the fact that the change of pressure δp_2 in low-frequency case is much lower than higher frequency case over the distance in this travel time, the low-frequency case should be close to quasi-steady behavior and the Strouhal number will give a higher value in the higher frequency pulse. As for the right-handed Figure, these two pulsating flows have different frequencies and amplitude, although the calculation of the Strouhal number will show a higher value at a higher frequency, the actual change of flow condition of these two flows δp in travel time T_0 are the same. In conclusion, once the Strouhal number approaches unity, the pulse flow amplitude should also be taken into consideration. In their research, a weighting factor Π is used to show the value of pressure amplitude, thus the calculation of this lambda criterion is built as:

$$\Lambda = \Pi f_r = \frac{2AfL}{\gamma \bar{P} \bar{v}} \tag{2.14}$$

where is Π multiplication of amplitude correction factor and f_r reduced frequency, and the unsteadiness of the model is based on

- $\Lambda \sim 0$ Quasi-steady
- $\Lambda > 0$ Unsteady

Λ represents the ratio of the cycle averaged mass flow through the domain to the mass flow change rate of the time, this researcher also pointed out the volute shows the most obvious unsteady behavior.

Cao et al. (2014) laid emphasis on the influence of pulse frequency, pulse amplitude as well as pulse gradient by using CFD work. Their new criterion of unsteadiness is mainly based on the temporal local reduced methods:

where

$$|\varepsilon(t)| = \frac{|\Delta p(t)|}{\bar{p}}, \quad \beta_{\text{local}}\,(t) = \frac{t_f}{\Delta t} \tag{2.15}$$

$$|\varepsilon(t)| \beta_{\text{local}}\,(t) = \frac{|\Delta P(t)|}{\bar{P}} \frac{t_f}{\Delta t} \tag{2.16}$$

the temporal local gradient of the pressure wave is

$$\left| \frac{\partial p(t)}{\partial t} \right| \tag{2.17}$$

the time mean value of pressure wave $\bar{P}$ and time-averaged for a fluid particle to travel through the domain t_f are used to normalize the pressure gradient, changing the equation to be:

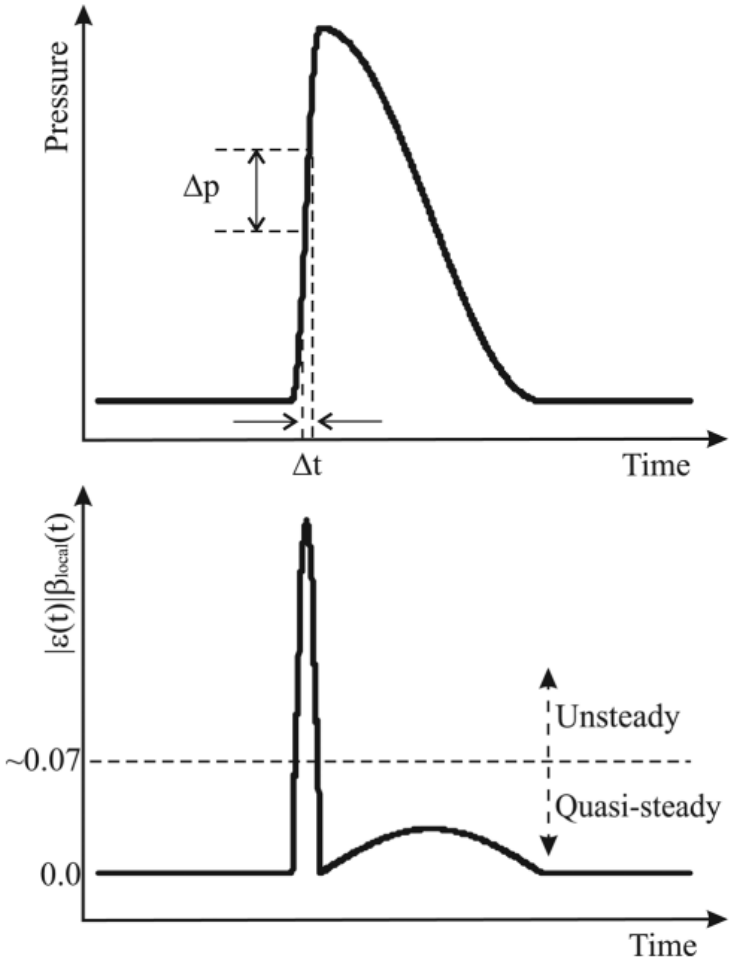

Figure 2-16: Sketch to show temporal local concept (Cao et al., 2014)

$$\left|\frac{\partial p(t)/\bar{p}}{\partial t/t_f}\right| \tag{2.18}$$

,

and the average time for a fluid particle traveling through the turbine passage t_f are used to normalize the pressure gradient, according to their research, it showed that:

- $|\varepsilon(t)|\beta_{\text{local}}\,(t) > 0.07$,Unsteady
- $|\varepsilon(t)|\beta_{\text{local}}\,(t) < 0.07$,Quasi-steady

As Figure 2-16 shows, the selection of δt is determined by the definition of the research and will be corrected by δp, the unsteadiness criterion will rise with a high-pressure gradient. This 'temporal local' concept concluded that the rotor will respond to the pulse wave locally in time by the instantaneous performance, and this concept can point out the temporal location of the unsteadiness. It coincidences with the lambda criterion when it is time averaged over a pulse and divided by the specific heat capacity γ.

$$\frac{\int_0^T |\varepsilon(t)|\beta_{\text{local}}\,(t)dt}{\gamma T} = \frac{\sum_{k=1}^{n} \frac{|\Delta p_k|}{\bar{p}} t_f}{\gamma T} = \frac{2A}{\gamma \bar{p}} \frac{t_f}{T} \Rightarrow \Pi S_t = \Lambda \tag{2.19}$$

In conclusion, the Λ criterion can be used to indicate the unsteadiness of the rotor in terms of the cycle-integrated performance. For all the cases (largest Λ is about 0.02), the rotor behaves quasi-steadily in terms of cycle-integrated performance. The existence of instantaneous unsteadiness highlights the need for having a temporal local pressure corrected reduced frequency. Thus pulse frequency and pulse amplitude must be both considered and any isolated consideration may mislead the conclusion of turbine unsteadiness under pulsating flow conditions.

In 2021, Deng et al. (2021) did research where a new non-dimensional modeling approach was used to characterize the turbocharger by two new dimensionless quantities defined with the respect to mechanical and heat loss behavior. These two quantities were then used with the Strouhal number for flow transients. Their thermal dimensionless parameter $\delta_{thermal}$ was defined by:

$$\delta_{thermal} = \frac{Q_{turb} \cdot f}{\dot{Q}_{turb}} \tag{2.20}$$

which calculates the ratio between the time to change the turbine housing temperature and the time period of system oscillation (Deng et al., 2021). The mechanical loss term

of this dimensionless method δ_{mech} was defined by:

$$\delta_{\text{mech}} = \frac{\tau_{\text{turb}} \cdot f}{I_{\text{shaft}} \cdot \omega} \tag{2.21}$$

,

where the mechanical inertia I_{shaft} of the turbocharger was included as well as the turbine torque τ_{turb} .

They used this non-dimensional parameter method to depict the different aspects of the dynamic response, as shown in Figure 2-17. According to the simulation results collected from an engine-validated model, the results of Strouhal number give a good prediction of turbine unsteadiness for different sizes of turbines under a pulse frequency of $60Hz$ when this Strouhal number is in the region of 0.07-0.5. As for the thermal parameter, the results showed that the quasi-steady assumption was valid when this dimensionless parameter is below 0.05, while the critical dynamic range is between 0.05 and 10, and this parameter may not be valid when the value is above 15. As for the mechanical parameter, the results show that the quasi-steady assumption will hold when values are below 0.01, and the critical dynamic range is for values between 0.01 and 0.2, while this parameter is not valid when values are below 0.03 according to the research of Deng et al. (2021).

Instantaneous parameters measurements in turbine mapping

The instantaneous measurement for turbine characteristics has been a challenge since the beginning of 1920s (Mottram, 1992) because of the recuperation motion nature of the engine, and the pressure differences measurement system such as V-Cone is designed for steady mass flow rate measurement and not capable for the fast variation of flow (Newton, 2014). The definition of pulsating flow is an unsteady flow where there is a regular cycled variation of flow velocity exists. The measurement of the root-mean-square of the variation U_{rms} and the time mean of the bulk-mean velocity

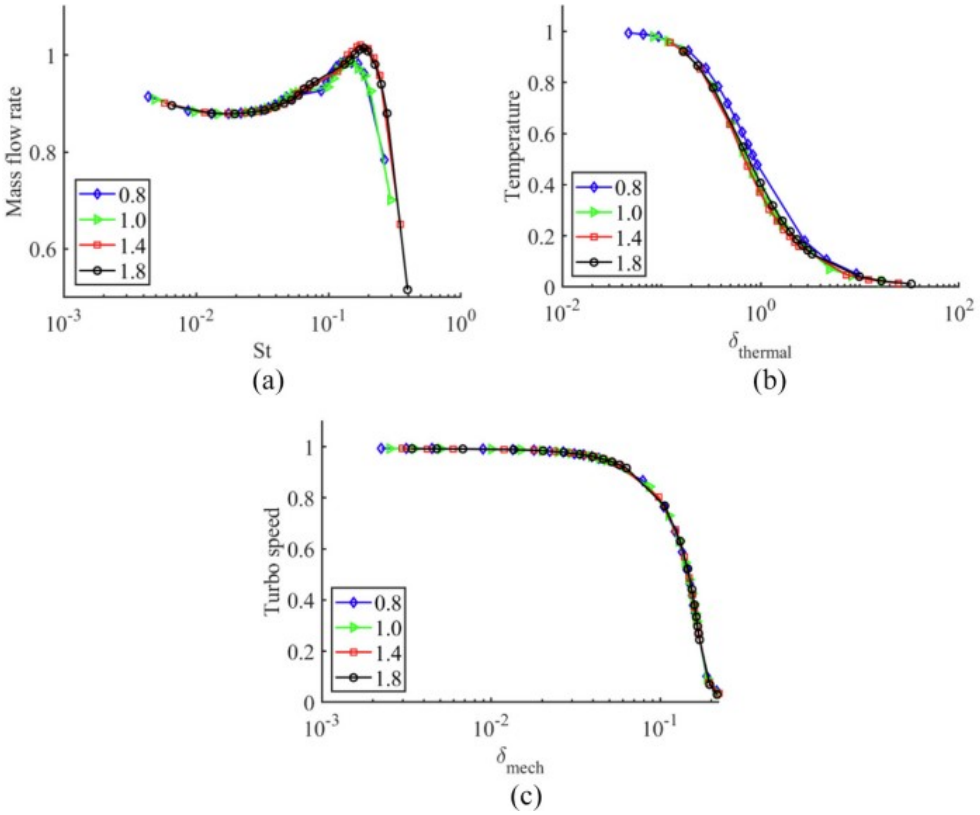

Figure 2-17: Prediction of speed and temperature responses using dimensionless parameters, with the different turbine sizes being shown in the legend: (a) normalized mass flow rate in the turbine volute, (b) turbine housing temperature response, and (c) turbocharger speed response (Deng et al., 2021)

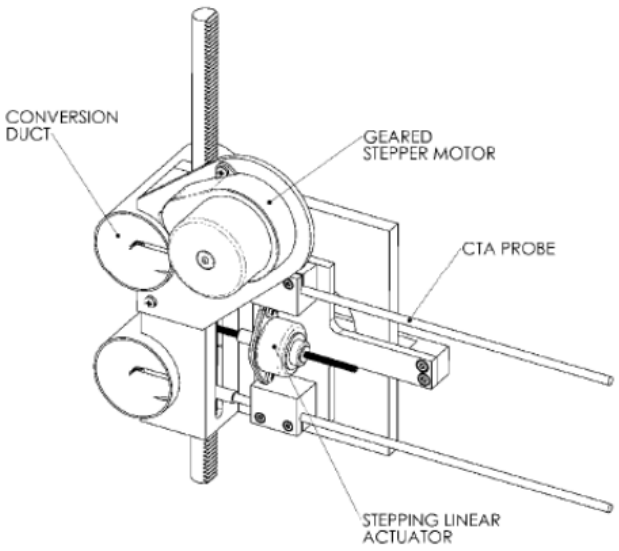

Figure 2-18: Traversing mechanism for hotwire probes (Newton, 2014) , (Szymko, 2006),and (Khairuddin and Costall, 2018)

U could be difficult. A hot-wire probe can only provide a response to local velocity (Mottram, 1992), (Bruun, 1996). The distribution of mean flow velocity, pulsating flow velocity variation, and turbulence velocity fluctuations may result in a multiplying factor, thus a single hot-wire measurement could only give an approximation of the velocity in pulsating flow conditions. Newton (2014) used a hotwire element to measure the instantaneous mass flow rate under cold conditions in Imperial College from Dantec Dynamics. They used a traversing mechanism as shown in Figure 2-18 and Figure 2-19 to control the position where the probe is mounted on the system.

According to their research in Figure 2-19, each point of 21 points were recorded for 30 pulse cycles to obtain the time-resolved mass flow rate, and they calibrated two single sensor miniature probes $55P11$, then used these for two limbs entered the turbine respectively. They used the constant temperature anemometry system (CTA), which has an advantage over the constant current anemometry that the thermal inertia effects can be ignored since the probe was operated at a fixed temperature during its measurement

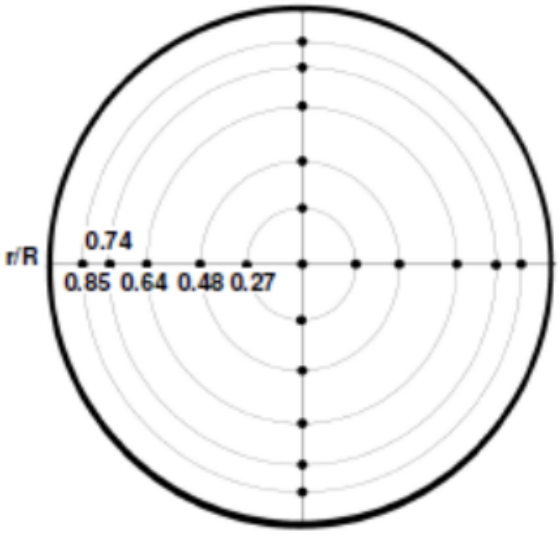

Figure 2-19: Traversing mechanism grid for hotwire probes (Newton, 2014) , (Szymko, 2006),and (Khairuddin and Costall, 2018)

process (Bruun, 1996). The probe was placed in a Wheatstone bridge. The wire was connected to one arm and heated by an electrical current. A servo amplifier keeps the bridge in balance by controlling the current to the sensor so that the resistance – and hence temperature was kept constant during measurement, independent of the cooling imposed by the fluid. The bridge voltage represents the heat transfer and is thus a direct measure of the velocity. The combination of the sensor's low thermal inertia and the high gain of the servo loop amplifier gives a very fast response to fluctuations in the flow (Dantec Dynamics, 2019).

In the research of Newton (2014), the relationship function of the flow velocity and the voltage across the hotwire was developed following the equations:

$$Nu = \boldsymbol{A} + \boldsymbol{B}Re^{1/2} \tag{2.22}$$

where Nu is the Nusselt number and represents the ratio of heat conduction along the

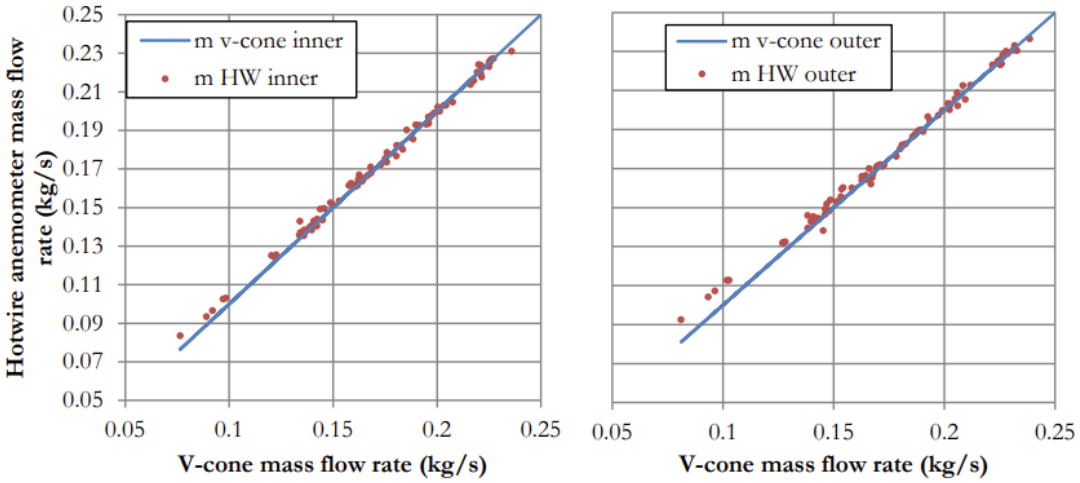

Figure 2-20: Hotwire calibration points for the inner(left) and outer(right) limbs (Newton, 2014)

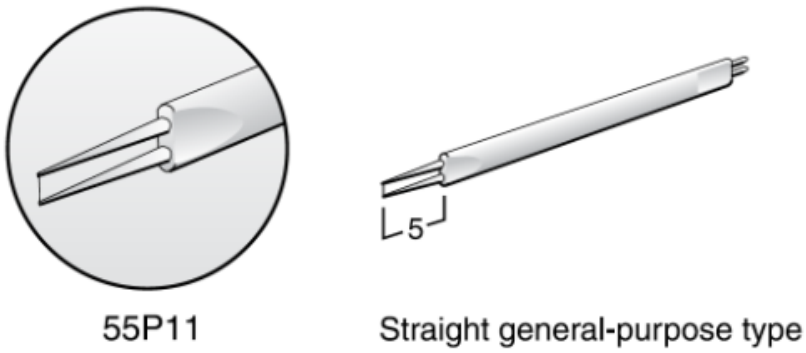

Figure 2-21: 55P11 hotwire element from Dantec Dynamics, the sensing wire is $1.25mm$ (Newton, 2014),(Dantec Dynamics, 2019)

length of the cylinder to the convection of heat from the cylinder surface (Bruun, 1996):

$$Nu = \frac{hd_w}{k} \tag{2.23}$$

The Reynolds number which is used to represent the ratio of inertial force and viscous force in a fluid domain is defined as:

$$Re = \frac{\rho U d_w}{\mu} \tag{2.24}$$

$$\left(\frac{\left(\frac{T_w - T_{ref}}{T_w - T_\infty}\right)^{1+m} \left(\frac{T_{ref}}{T_\infty}\right)^{0.83} E^2 - \boldsymbol{a}}{\boldsymbol{b}} \right)^{1/n} / \left(\frac{T_{ref}}{T_\infty}\right)^{0.73} = \rho U \tag{2.25}$$

the T_w in this equation represents the hotwire temperature and the T_{ref} is a reference temperature measured by the system temperature thermistor in this research during the calibration process. T_∞ is the free steam temperature, while a and b are determined from calibration related to the factor A and B in Equation 2.22. The definition of the temperature correction coefficient is:

$$\left(\frac{T_w - T_{\text{ref}}}{T_W - T_\infty}\right)^{1+m} \tag{2.26}$$

Where $m \approx 0.2$ is suggested from the manufacturer website (Dantec Dynamics, 2019), and 0.83 and 0.73 are derived from the research of Bruun (1996) based on the fluid properties from the reference temperature conducted in calibration. Despite the uncertainty of measurement seems to decrease by these 21×30 data sets, it added the error for hotwire calibration shown in Figure 2-20 due to the fact that they calibrated the hotwire by using the slow response system temperature measurement $90H10$ shown in Figure 2-21 of Dantec Dynamics Streamline commercial unit shown in Figure 2-22. Thus the calibration points shown in their research between V-Cone and hotwire under steady conditions in Figure 2-20 are acceptable, but the differences under the unsteady

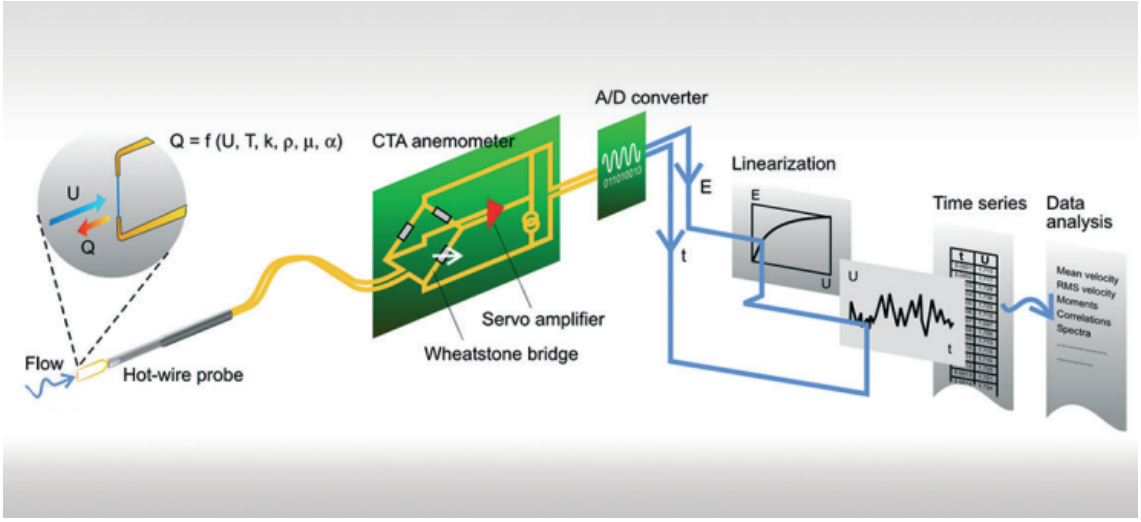

Figure 2-22: Dantec hotwire system (Dantec Dynamics, 2019)

condition of a fast variation of temperature are out of scope.

2.3.1 Conclusion of turbine experimental work

Based on the literature review conducted, several key findings are listed:

- Steady turbine mapping experiment is widely used to provide data for lower-dimensional turbine models.
- The engine environment that turbines usually work in is different from the quasi-steady assumption.
- The up-to-date techniques are able to measure instantaneous mass flow rate and temperature with considerable costs and dedicated operations.
- There are both non-dimensional and dimensional ways to show the unsteady nature of the turbine.
- Most of the experimental methods take no consideration of iterations between wastegate and turbine, and the wastegate is usually absent or welded shut for mapping.

Thus the next section of this literature review will discuss the wastegate study for turbine mapping.

2.4 Wastegate Study

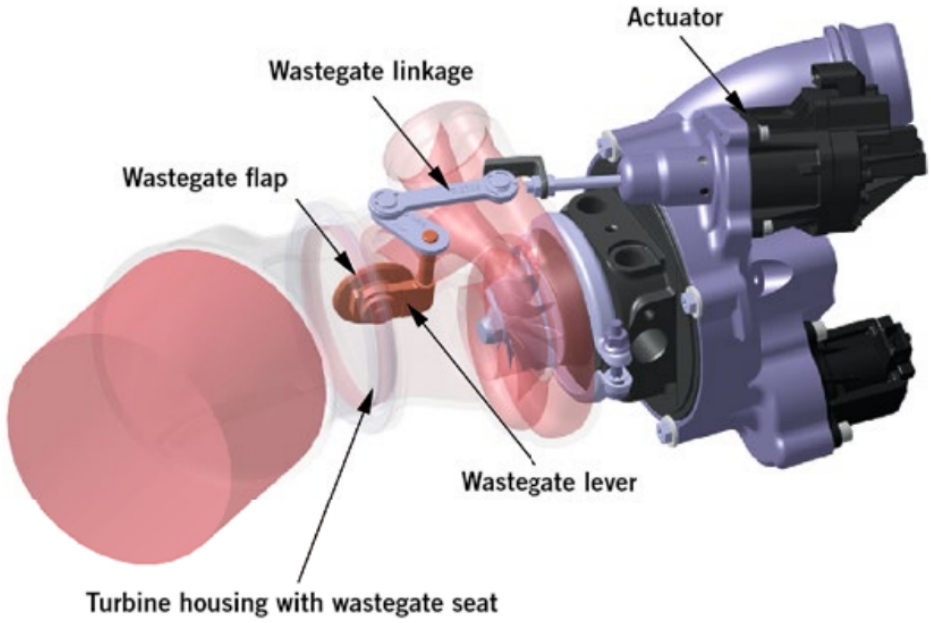

Figure 2-23: The wastegate system of a BMW four-cylinder gasoline engine with twin-scroll turbine technology (Wibmer et al., 2015)

Figure 2-23 shows a typical wastegate system on a gasoline engine. The wastegate system plays an important role in the turbocharger system as it is the main element to regulate the booster pressure (Wibmer et al., 2015). On the other hand, there is little research where this element is taken into consideration in the mapping method. Most models use a wastegate flow coefficient to calculate the mass flow passing through the

wastegate based on the research conducted by Heywood (Heywood, 1988):

$$\dot{m} = C_f A_{ref} \frac{P_{01}}{\sqrt{RT_{01}}} \left(\frac{P_4}{P_{01}}\right) \sqrt{\frac{2\gamma}{\gamma - 1} \left[1 - \left(\frac{P_4}{P_{01}}\right)^{(\gamma-1/\gamma)}\right]} \tag{2.27}$$

This equation is to calculate the mass flow that passes through a poppet valve, thus for the turbine choked flow, where the expansion ratio becomes:

$$\frac{P_4}{P_{01}} \leq \left(\frac{2}{\gamma + 1}\right)^{(\gamma/\gamma-1)} \tag{2.28}$$

the choked mass flow is then calculated by

$$\dot{m} = C_f A_{\text{ref}} \frac{P_{01}}{\sqrt{RT_{01}}} \sqrt{\gamma} \left(\frac{2}{\gamma + 1}\right)^{\gamma+1/2(\gamma-1)} \tag{2.29}$$

where P_{01} represents the inlet total pressure and P_4 represents the static exit pressure, R and γ represent the gas constant and the specific heat ratio of air respectively. A_{ref} is the reference area.

Samala (2020) did a comparison of different wastegate positions. The wastegate itself is a simplified flow coefficient of C_f, the differences between the discharge coefficient and flow coefficient were not analyzed clearly. In their research, the wastegate opening percentages are controlled from 0% as fully closed to 80% opening for two different turbos, and these experimental data are then fitted by a model fitting method as a function of turbine expansion ratio and wastegate opening position with the error of ±5% as shown in Figure 2-24.

Salim Bin Wan Salim (2015) used a similar model for a wastegate in twin entry turbos. An average flow coefficient C_f was used in this research and compared versus the value of $\frac{l}{d_{ref}}$ which is the ratio of the valve displacement or lift(l) to the reference diameter d_{ref}, the diameter of the valve inlet port for ten different wastegate lifts. This researcher concluded that the actual mass flow through the turbine in wastegate

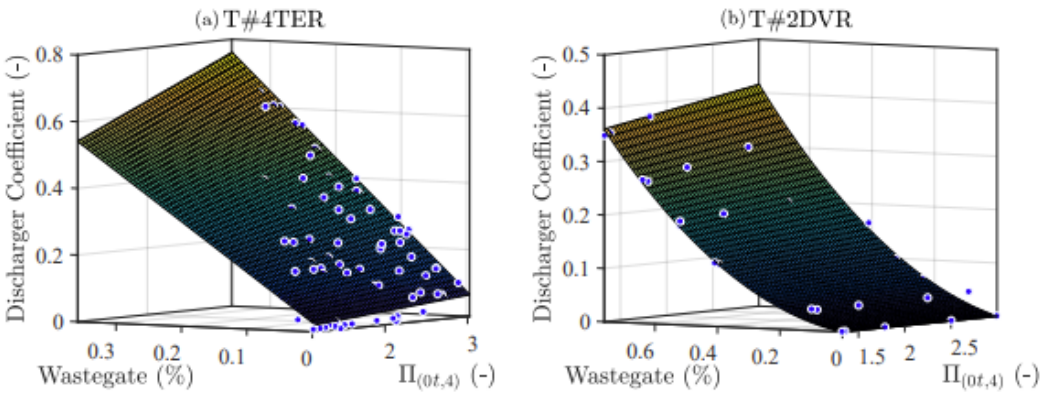

Figure 2-24: Fitting method for C_d (Samala, 2020)

opening conditions is different from that predicted by summing the mass flow through the individual flow components. This is because of the flow losses within the additional piping setup and the added geometrical complexity of the system, which was found by Capobianco and Marelli (2007), where they studied the waste-gated turbines internally. The close arrangements of components in such devices is expected to be more susceptible to further losses due to flow mixing at the turbine exit. Additionally, a higher mass flow rate predicted will bring lower calculated values of efficiency due to the mass flow rate being a component in the calculation of isentropic power. The deviation of the predicted efficiency could have been up to 7.4%

Wibmer et al. (2015) did a simulation on wastegate dynamics but only under unsteady conditions with the wastegate fully shut and did not focus on the flow passing through the wastegate. Bin Wan Salim (2015) analyzed both steady and unsteady conditions on an external wastegate turbine but there was no 3D model used and they used a set of external pipes to represent the wastegate. Serrano et al. (2017) design an experimental procedure to characterize the two-stage turbocharger wastegate discharge coefficient. The mass flow through the wastegate was calculated based on wastegate fully closed conditions.

In the CFD model of Khairuddin and Costall (2018) shown in Figure 2-25, the waste-

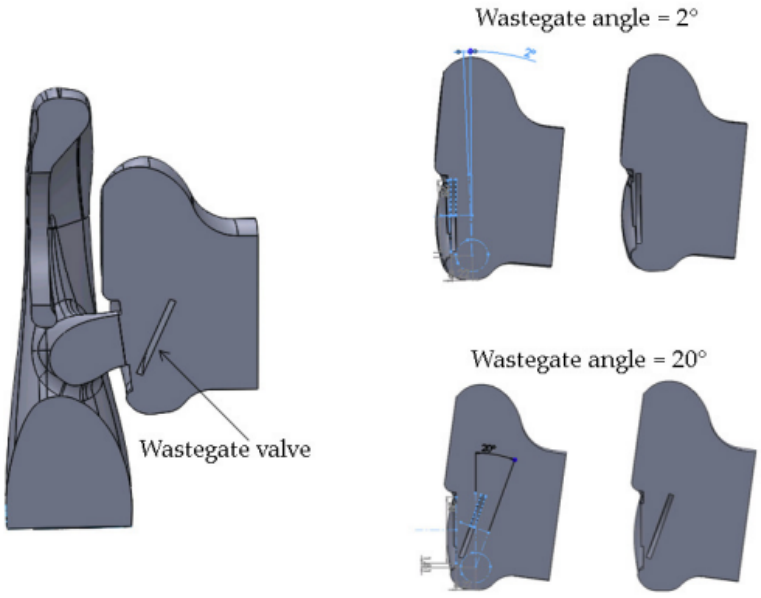

Figure 2-25: Wastegate CFD model (Khairuddin and Costall, 2018)

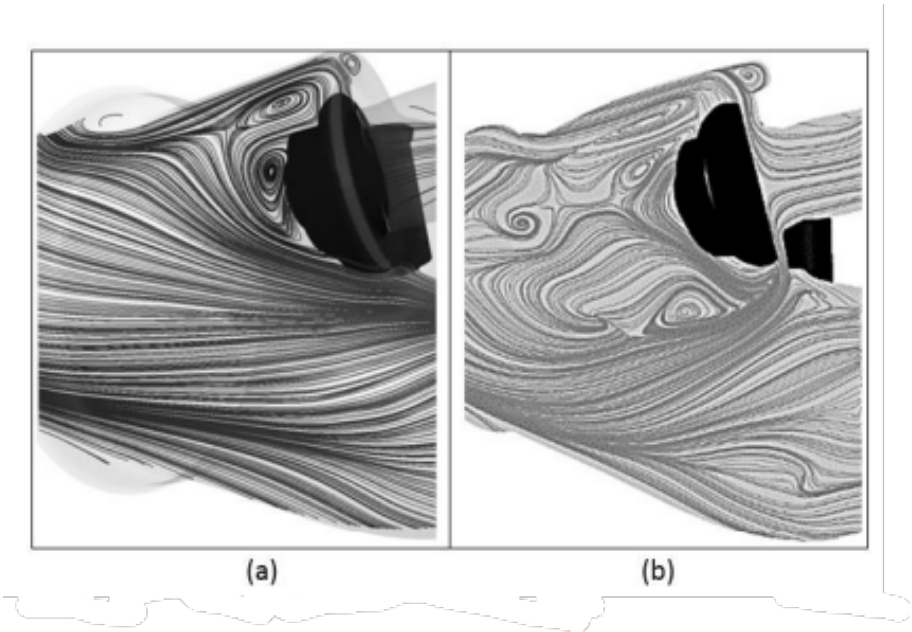

Figure 2-26: Wastegate CFD result of (Alaviyoun, Ziabasharhagh and Farajpoor, 2020)

gate is simplified as a single plane. Although the opening is able to vary in different angles, it is far from the case in a reality where the wastegate plane has a complex shape and it is essential to replicate the true geometry in CFD. In the study of Alaviyoun, Ziabasharhagh and Farajpoor (2020) as shown in Figure 2-26, they only used a small opening of less than 7°and there is no measurement of the mass flow rate as the validation of CFD results. As a summary of this section, there is a gap in the literature to model the wastegate in different opening conditions in a precise way, and there is a lack of an experimental method for mapping with wastegate opening too.

2.5 Conclusion of the Chapter

As the literature review states, three main areas are covered in this chapter. The first topic is turbine modeling. In this literature review, empirical models, one-dimensional models, and three-dimensional models were all discussed to show the state of the art in turbine modeling in these aspects. The second area is experimental work of turbine mapping. The thesis provides a literature review from early research of experimental work on the pulsating nature of turbines to the most recent instantaneous measurement methods. The third area is the wastegate study. The thesis has given a brief review of the wastegate study in both experimental mapping methods and modeling.

Based on this literature review, some research gaps are raised:

1. There is a lack of a precise and accurate experimental methodology where instantaneous pressure, temperature, rotational speed, and mass flow rate variations could be captured under engine-like hot conditions. This research gap will be a question answered in Chapter 3 where the experimental methodology used in this thesis will be discussed.

2. How will unsteady mapping differ from the steady experiment? Is it possible to use a model to assess the feasibility of the unsteady mapping method? This

research gap question will be discussed in Chapter 5 *Unsteady Mapping Method*.

3. Without the unsteady data, can a CFD model be built and used in mapping? This research gap question will be answered in Chapter 4 and in Chapter 5.

4. Is there a better way to map the turbine under different wastegate conditions and properly model the wastegate? This research gap question will be answered in Chapter 6 where the research question of 'How to map a wastegate turbine?' will be discussed.

Chapter 3

Experimental Methodology

3.1 Outline of the Chapter

The point of mapping is to measure some key performance metrics for the turbocharger which are mass flow (expressed as mass flow parameter), pressure ratio, speed (as speed parameter), and efficiency (total to static) (SAE, 1995b).

This chapter aims to answer the research question raised in Chapter 1 *Introduction*: 'How to collect mapping data and quantify the operating conditions for a single entry radial turbine precisely?', thus the experiment methodology used in this research will be illustrated in this chapter. This mainly includes three sections:

- Steady Mapping Apparatus

  Section 3.2 will discuss this topic and in this section, standard state mapping under hot gas stand inlet conditions has been discussed. The experimental data for turbine characteristics are then extended by using a closed loop mapping apparatus by adding a pressured or vacuum facility at the inlet of a compressor.

- Instantaneous Unsteady Mapping Apparatus

Section 3.3 will cover this topic. The apparatus which is able to measure turbine characteristics under unsteady conditions is described. The turbine inlet conditions are exposed under an unsteady environment equipped with a pulse rig to simulate the engine exhaust gas. The fast responses sensors for pressure, temperature, and mass flow rate are used to measure the instantaneous parameters.

- Steady Wastegate Opening Mapping Apparatus

  Section 3.4 will discuss this topic and in this section, the turbine is measured with different wastegate openings. The flow coefficient is calculated by measuring the mass flow that passes through the turbine inlet and wastegate pipe, and the wastegate openings angles are controlled by the pressure calibrator connected with the wastegate actuator and measured by the current of the signals.

3.2 Steady Measurement and Uncertainty Analysis

3.2.1 Introduction of the gas stand

Turbocharger gas stand description

The turbocharger gas stand at the The University of Bath, shown in Figure 3-1, is used for mapping turbocharger compressors and turbines in different configurations. The schematic diagrams in Figure 3-2 illustrate the configuration of the various items of equipment and instrumentation listed in Table 3.1

The air supply for the turbine side comes from two electric screw compressors outside the test cell (which enters the gas stand at item 1 in Figure 3-2), with a maximum mass flow rate of 0.7 kg/s and a maximum pressure of 7 bar (absolute). The mass flow rate of air is measured using two pairs of McCrometer V-Cone (labelled 4 and 5 in Figure 3-2, which cover different flow ranges), which is a differential pressure-type

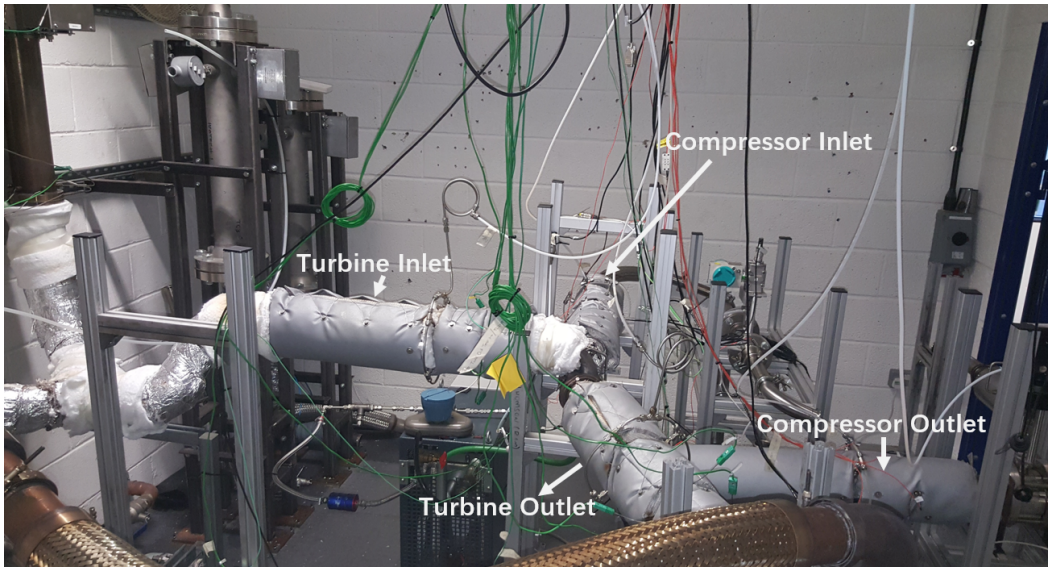

Figure 3-1: Photograph of turbocharger gas stand, shown with single entry turbine

Table 3.1: Turbocharger gas stand equipment list for a single entry turbine test (numbers refer to labels in Figure 3-2).

No.	Item description
1	SMC pneumatic pressure regulator
2	Ball type valve with Kinetrol electro-pneumatic positioner
3	Schubert & Salzer digital positioner-type gate valve
4	3" McCrometer V-Cone mass flow meter with Siemens DSIII differential pressure transmitter
5	2" McCrometer V-Cone mass flow meter Siemens DSIII differential pressure transmitter
6	Bowman gas-to-gas heat exchanger
7	Axes Design variable power electric heater (44 kW)
8	Turbocharger turbine
9	Turbocharger compressor
10	Lubrication and cooling conditioning unit (Reglopas)
11	Turbine inlet measuring section
12	Turbine outlet measuring section
13	Compressor inlet measuring section
14	Compressor outlet measuring section
15	Electrically controlled roof extraction fan
16	Axes Design variable power electric heater (48 kW)

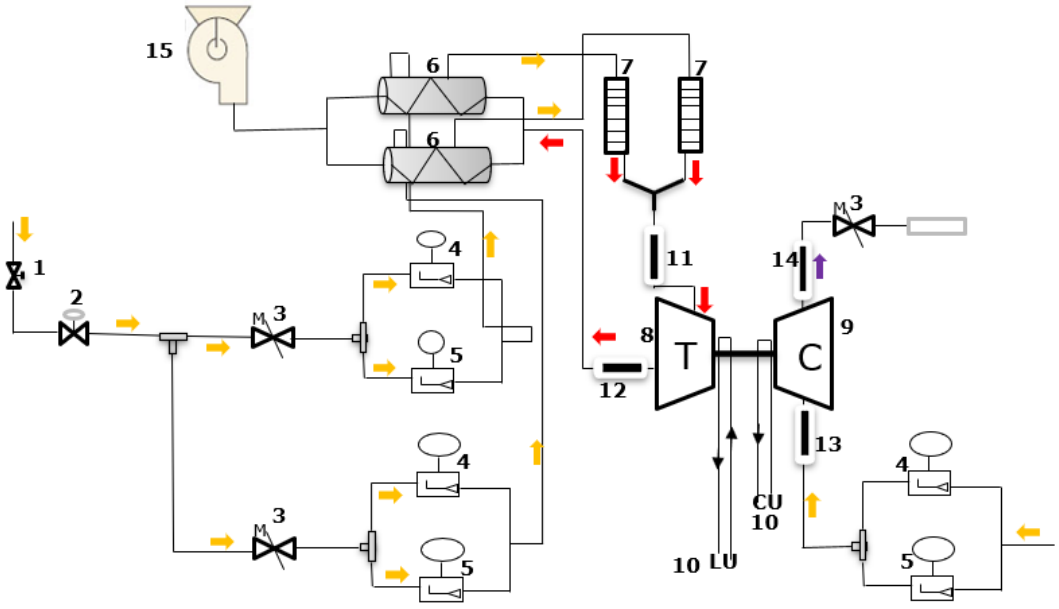

(a) Two heaters apparatus

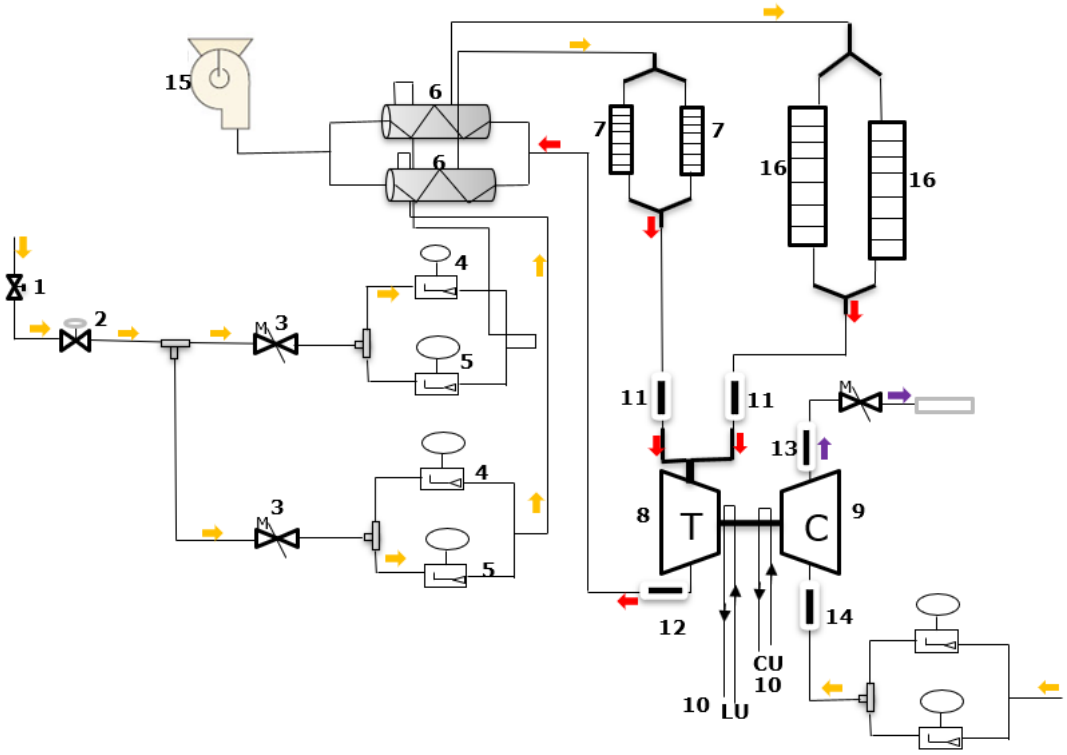

(b) Four heaters apparatus

Figure 3-2: Turbocharger gas stand schematic for (a) two heaters, (b) four heaters.

flow meter. The geometry of each V-Cone will be illustrated in the section on mass flow measurement. Downstream of the V-Cone measurements of mass flow rate, the air enters a pair of Bowman gas-to-gas heat exchangers where it is pre-heated by the exhaust flow from the turbine outlet as it leaves the gas stand. Then the air is fed into (up to four) electrical heaters (depending on the required turbine inlet configuration, e.g., single or two entries). The electrical heater temperature set-points (and hence power level) is controlled remotely by the operator, via the Sierra CP control and data acquisition system with a maximum sampling frequency of 40 Hz (Duda, 2017). This facility is suitable for testing turbochargers as it is equipped with four heaters and two independent air feeding lines. Thus it can be used for both single-entry and twin-entry turbines by changing the pipework. All remote control of the gas stand facility and acquisition for steady performance data was carried out by the Sierra CP system, in which the maximum sampling frequency is 60 Hz. Moisture is removed by using a refrigerated compressor air drier (Duda, 2017) so that the air arrives at the test facility in a cold and dry condition. Each air feeding path is able to connect to single or double heaters, where each heater can heat the air to about 700°C.

The compressor is used as the loading device and controlled by a gate valve at it's outlet downstream, thus compressor and turbine's performance data can be collected simultaneously. For the standard turbine mapping, the turbine inlet temperature is controlled by varying the power of electric heaters. One of the drawbacks of this mapping method is compressors are restricted by choking and surging conditions thus turbines are only able to be mapped at a limited range. In this project, turbine and compressor data are collected by using SAE format (SAE, 1995a). The SAE format for turbocharger turbine mapping (SAE, 1995a) requires the following measurement parameters:

- Speed parameter [unit of $\mathrm{min}^{-1}/\,\mathrm{K}^{0.5}$]

$$\text{Turbine speed parameter} = \frac{\text{Turbine rotor speed (rpm)}}{\sqrt{\text{Turbine inlet total absolute temperature (K)}}}$$

- Turbine gas flow parameter [units of $\text{kg/s} \cdot \text{K}^{0.5} \cdot \text{kPa}^{-1}$]

$$\text{Turbine gas flow} = \frac{\text{Turbine gas flow} \times \sqrt{\text{Turbine inlet total absolute temperature (K)}}}{\text{Turbine inlet total absolute pressure(kPa)}}$$

- Total-to-static expansion ratio [no units]

$$\text{Turbine expansion ratio} = \frac{\text{Inlet gas total absolute pressure(kPa)}}{\text{Outlet gas static absolute pressure(kPa)}}$$

- Total-to-static efficiency [no units]

$$\text{Combined turbine} \times \text{mechanical efficiency}(\%) = \frac{\text{Actual total enthalpy rise across compressor stage}}{\text{Isentropic total enthalpy drop across turbine stage through expansion ratio}}$$

- Speed parameter [unit of $\text{min}^{-1}/\ \text{K}^{0.5}$]

- Mass flow parameter [units of $\text{kg/s} \cdot \text{K}^{0.5} \cdot \text{kPa}^{-1}$]

- Total-to-static expansion ratio [no units]

- Total-to-static efficiency [no units]

Static pressure rather than total pressure is used at the turbine outlet because the kinetic energy available at the rotor exit of a single-stage turbine is usually hard to measure. The total to static basis of turbine efficiency is used to calculate efficiency.

According to Duda (2017) and based on the SAE format turbine mapping, in the turbine performance parameters, the mass flow and turbine speed are reduced to pseudo-non-dimensional parameters, i.e. mass flow parameter (MFP)

$$MFP = \dot{m}\frac{\sqrt{T_{03}}}{P_{03}} \tag{3.1}$$

and speed parameter (SP)

$$SP = \frac{N}{\sqrt{T_{03}}} \tag{3.2}$$

In an SAE format map, the turbine gas flow parameter is often plotted against the turbine expansion ratio at different speed parameters. The turbine expansion ratio is given by

$$ER_t = \frac{P_{03}}{P_4} \tag{3.3}$$

As mentioned before, static pressure is used at the turbine outlet because the kinetic energy available at the exit of the rotor is considered to be not recovered. The measured values from sensors estimate the static pressure and temperature values without a recovery factor. The recovery factor r is described as a function of the Mach number.

$$T_a = T + r(T_0 - T) \tag{3.4}$$

Where the acquired temperature T_a is related to the static and total temperature by a recovery factor r Newton (2014). By assuming recovery factor $r = 1$ in the experiment, the maximum uncertainty is $\pm 0.02K$.

The conversions between the static and total (stagnation) conditions are given by:

$$T_0 = T\left(1 + \frac{\gamma - 1}{2}\right) M^2 \tag{3.5}$$

$$P_0 = P\left(\frac{T_0}{T}\right)^{(\gamma/\gamma-1)} \tag{3.6}$$

where γ represents the ratio of specific capacity for gas, defined as a function of the universal gas constant R (Liu, 2020), and M represents the Mach number of the fluid.

The stage efficiency of the turbine is calculated by these equations:

$$\eta_t = \frac{\dot{W}_{t,act}}{\dot{W}_{t,isen}} \tag{3.7}$$

where the $\dot{W}_{t,act}$ is calculated from:

$$\dot{W}_{t,act} = \dot{W}_{c,act}/\eta_{\text{mech}} \tag{3.8}$$

and the isentropic power of the turbine is calculated from:

$$\dot{W}_{t,isen} = \dot{m}_t c_{p_{t,avg}} T_{3t} \left[1 - \left(\frac{1}{PR_t}\right)\left(\frac{\gamma_{t,avg}-1}{\gamma_{t,avg}}\right)\right] \tag{3.9}$$

Thus turbine efficiency could be calculated from:

$$\eta_t = \frac{P_c/\eta_{\text{mech}}}{\dot{m}_t c_{p_{t,avg}} T_{03}\left[1 - \left(\frac{1}{PR_t}\right)^{\left(\frac{\gamma_{t,avg}-1}{\gamma_{t,avg}}\right)}\right]} \tag{3.10}$$

Closed loop mapping

The range of results collected in the standard steady mapping method is limited because compressors are often used as the "brake" and it is limited by surge and choked flow. In order to tackle the drawback of the standard steady mapping method, which is the limited range of results, this test cell also includes closed-loop testing at the compressor side where the compressor discharge gas could be cooled and returned at the compressor inlet feeding (Duda, 2017). In this way, compressor inlet pressure will be regulated by vacuum or pressured valves as shown in Figure 3-3. This configuration enables the ability to adjust compressor inlet pressure thus changing the turbine load. When operating at a closed loop module, the Bowman air-to-water heat exchanger is used to cool down the compressor air at the outlet and then feed into the compressor inlet as

a return.

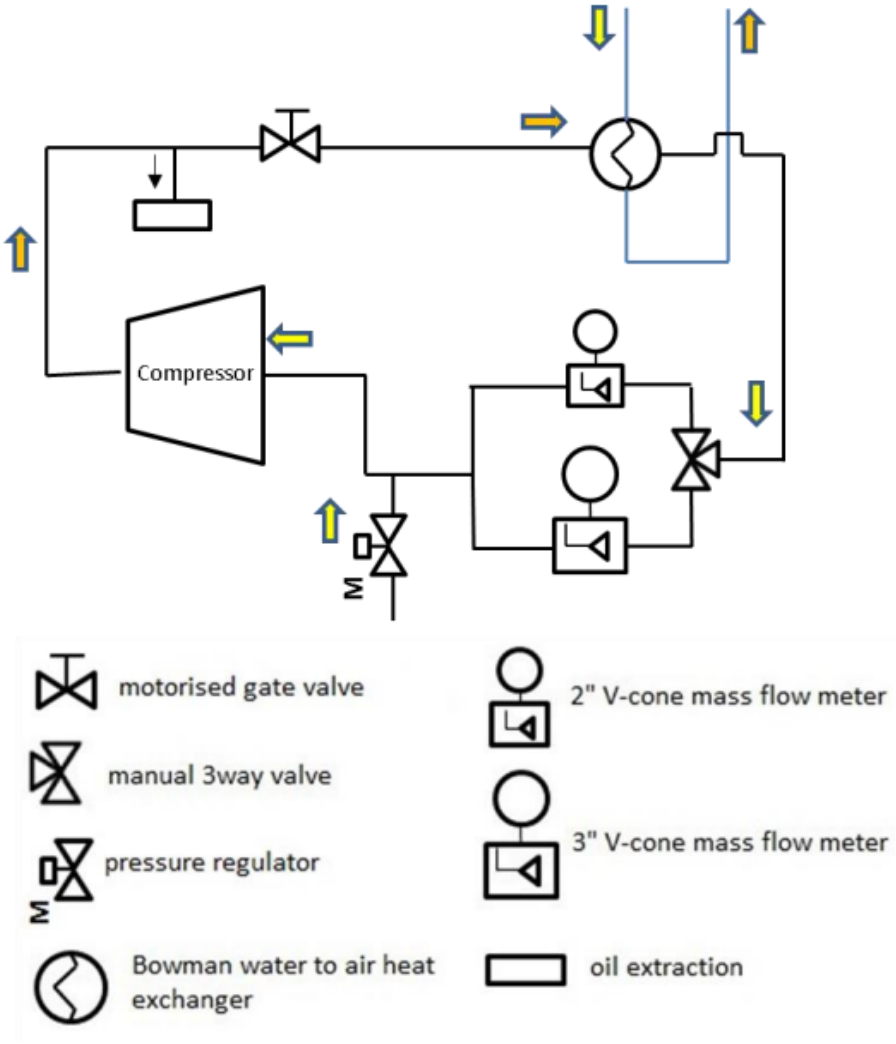

Figure 3-3: Closed loop module at compressor side (Duda, 2017)

3.2.2 Calculation of uncertainty

The uncertainty calculation approach used for each case is discussed first before taking the uncertainty of the individual variable into consideration.

Standard deviation

By doing the calibration process from different measurements, a desired physical property, y, (e.g. pressure), is linked to the measured signal x (usually in terms of current or voltage) directly, which is given by:

$$y = f(x) \tag{3.11}$$

The deviation of each of the calibration points can be used to determine the uncertainty in a measured variable (Newton, 2014). The standard deviation of the calibration points and the calculation are given by

$$s = \left[\frac{1}{n-2}\sum(y_i - mx_i - c)^2\right]^{1/2} \tag{3.12}$$

here s represents the standard deviation, and $n-2$ in the denominator of the equation is equal to the number of degrees of freedom. Two restrictions are placed on the possible values of y because most of the measurement in the gas stand is linearly calibrated, thus two quantities namely slope m and the intercept c are calculated (Kirkup, 2019) as shown:

$$y_i = mx_i + c \tag{3.13}$$

Combination of uncertainty

There are several parameters involved in the experiments within this thesis that are a function of several individual parameters, such as mass flow parameter, pressure ratio, etc. For those parameters, the overall uncertainty must be a function of each individual parameter uncertainty, which is given by:

$$Y = f(x_1, x_2, ...x_n) \tag{3.14}$$

According to Bentley (1983), the standard deviation of Y is given by:

$$\sigma_Y = \sqrt{\left[(\frac{\partial Y}{\partial x_1})^2 {\sigma_{x_1}}^2 + (\frac{\partial Y}{\partial x_2})^2 {\sigma_{x_2}}^2 + ... + (\frac{\partial Y}{\partial x_n})^2 {\sigma_{x_n}}^2\right]} \tag{3.15}$$

This equation is only vaild when the converiances are negligiglae and uncertainties are small, which is the case. The uncertainty σ_Y is associated with the parameter Y, which is therefore independent on each uncertainty of parameters σ_{X_1},σ_{X_2} and σ_{X_n}, which refers as the Root Sum Square (RSS) uncertainty (Bentley, 1983), (Newton, 2014), which gives an approximate value for the uncertainty in parameter Y, equal to the uncertainties in each of the constituent parameters.

3.2.3 Steady pressure measurement

There are four measurement sections at the compressor and turbine side, that is, compressor inlet and outlet, and turbine inlet and outlet. At each measurement section. There are four static pressure sensors used to measure the pneumatic pressure (Liu and Copeland, 2018). This is achieved by using a four-tapping-ring with pressure sensors installed on it, which is shown in Figure 3-4 and Figure 3-5, the tapping is all perpendicular to the pipe walls, and each tapping angle in between is fixed at 90 °(Liu, 2020).

The calibration uncertainty is given by Table 3.2.

Uncertainty of pressure sensor

The uncertainty value associated with the steady pressure sensor tapping geometry is estimated according to Newton (2014) as $\pm 5Pa$. Thus the uncertainty of static pressure is

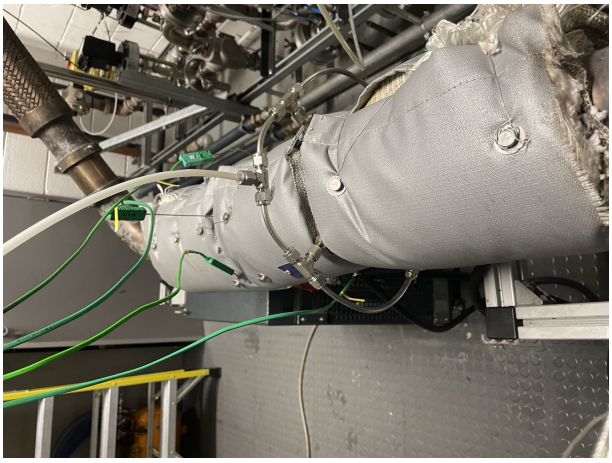

Figure 3-4: Steady pressure measurement in the University of Bath gas stand

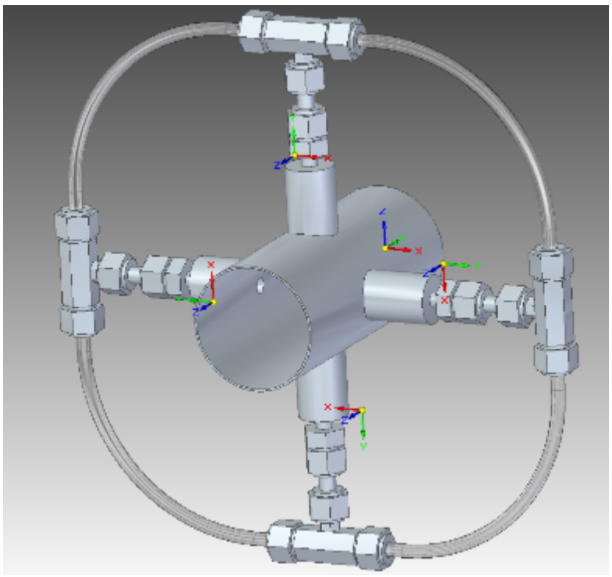

Figure 3-5: Steady pressure measurement (Liu, 2020)

Table 3.2: Pressure Sensor Actual Uncertainty (Liu, 2020)

Sensor Location	**Quantity**	**Order From**	**Sensor Type**	**Actual Accuracy**	**Sensor range**
Compressor Inlet	Static Pressure	Omega	PX312-100GV	$\pm 0.25\% FS$ $\pm 1.72 kPa$	$0 - 100 psi$ gauge
Compressor Outlet	Static Pressure	Omega	PXM419-007	$\pm 0.08\% FS$ $\pm 0.56 kPa$	$0 - 7 bar$ gauge
Turbine Inlet	Static Pressure	Omega	PXM419-007	$\pm 0.08\% FS$ $\pm 0.56 kPa$	$0 - 7 bar$ gauge
Turbine Outlet	Static Pressure	Omega	PXM419-002BGV	$\pm 0.08\% FS$ $\pm 0.16 kPa$	$0 - 2 bar$ gauge
Barometric Pressure	Static Pressure	Omega	PXM319-060AV	$\pm 0.25\% FS$ $\pm 0.86 kPa$	$0 - 50 psi$ ABS

$$\sigma_{P_{Static}} = \sqrt{\left[(\frac{\partial P_{Static}}{\partial P_{TAPPING}})^2 {\sigma_{P_{TAPPING}}}^2 + (\frac{\partial P_{Static}}{\partial P_{CALIB}})^2 {\sigma_{P_{CALIB}}}^2 + (\frac{\partial P_{Static}}{\partial P_{BARO}})^2 {\sigma_{P_{BARO}}}^2 \right]} \tag{3.16}$$

Since the actual absolute pressure is a linear combination of those components (Newton, 2014), each of the partial differentials in this equation is equal to unity.

The sensors used for each measurement section are listed in Table 3.2. Thus the absolute pressure uncertainty is calculated and the averaged uncertainty is shown in Table 3.3.

Table 3.3: Pressure Sensor Averaged Uncertainty

Pressure measurement	Average uncertainty
compressor inlet static pressure	±1.923kPa
compressor outlet static pressure	±1.026kPa
turbine inlet static pressure	±1.026kPa
turbine outlet static pressure	±0.874kPa

3.2.4 Steady temperature measurement

The measurement of static temperature takes four k-type thermocouples (turbine side) or PRTs arithmetical average values. The measured temperature is an approximation of the total temperature. The sensors are inserted 90 degrees between each other and

Table 3.4: Temperature Sensor Actual Uncertainty

Sensor Location	**Quantity**	**Order From**	**Sensor Type**	**Actual Accuracy**	**Sensor range**
Compressor Inlet	Static Temperature	TC Direct	PT100	$\pm 0.15K$	233K-523K
Compressor Outlet	Static Temperature	TC Direct	PT100	$\pm 0.15K$	233K-523K
Turbine Inlet	Static Temperature	TC Direct	1.5mm K-Type	$\pm 1.52K$	233K-1273K
Turbine Outlet	Static Temperature	TC Direct	1.5mm K-Type	$\pm 1.52K$	233K-1273K

installed perpendicular to the pipe. Similar to pressure, the sensor uncertainty is listed in Table 3.4:

The arrangement of those thermocouples is illustrated in Figure 3-6 and Figure 3-7 (Duda, 2017). At 0 °and 180 °of the section, the sensors are inserted at 1/2 of the radius of the tube, at 90 °the sensor is inserted at 3/4 radius, and at 270 °the sensor is inserted at 1/4 radius. Table 3.4 lists the specifications of temperature sensors used in this gas stand.

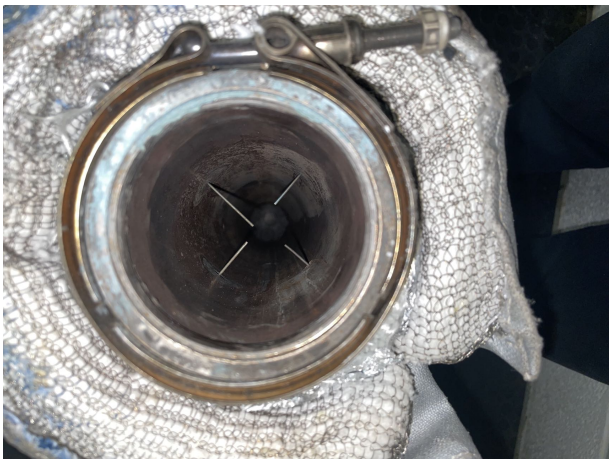

Figure 3-6: Thermocouple measurement

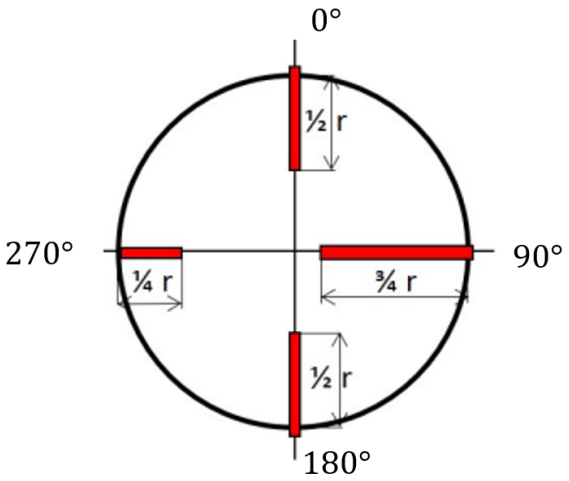

Figure 3-7: Thermocouple location (Duda, 2017)

Uncertainty of temperature sensor

The temperature measurements used in this thesis, the thermocouples were selected based on the working range according to Duda (2017). The overall thermocouple uncertainty of turbine inlet static measurement is ±2.38°C.

In a fluid flow, there are two different temperatures, that is the static and the total temperature (or stagnation temperatures) (Newton, 2014). The stagnation condition T_0 is calculated as by:

$$T_0 = T\left(1 + \frac{\gamma - 1}{2} M^2\right) \tag{3.17}$$

which indicates the stagnation temperature is the temperature that the fluid would reach if it were brought to zero speed by a steady, adiabatic process with no external work. M represents the Mach number and γ is a function of the universal gas constant R (Newton, 2014).

3.2.5 Steady mass flow rate measurement

The volume flow rate is measured by differential pressure type McCrometer V-Cone meters at both the turbine and compressor side. The University of Bath gas stand is

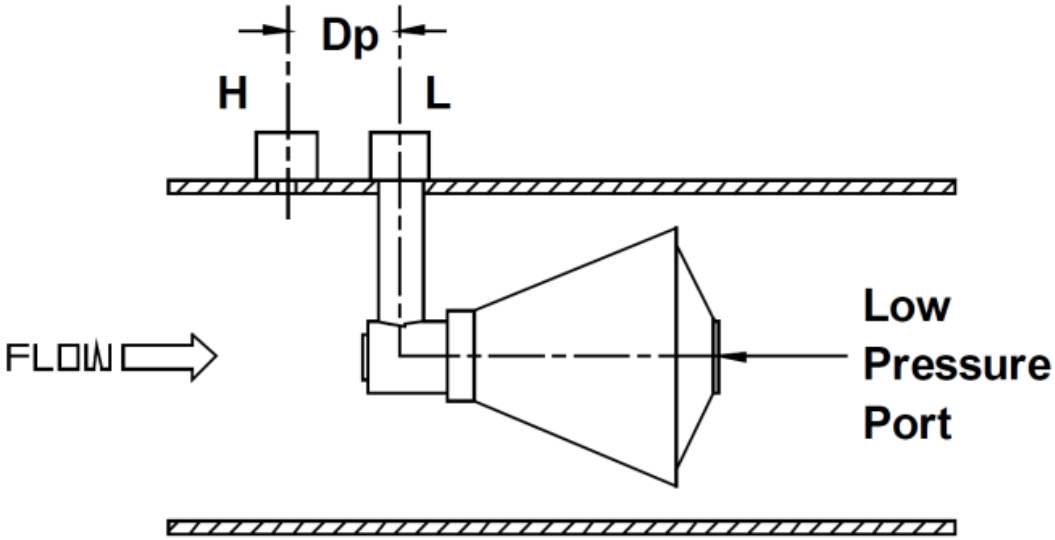

Figure 3-8: V-Cone geometry (SIEMENS, 2021)

equipped with four legs of V-Cone in order to give the capability of the different mass flow ranges and different types of turbine -double entry or single entry. According to Bernoulli's theorem, the energy is conserved in a closed pipe thus for a constant flow, the pressure is inversely proportional to the square of the flow velocity in the pipe. As shown in Figure 3-8, the pressure difference created by the V-Cone prime element is then measured by a previously calibrated Siemens Sitrans DS III transmitter. A PRT is installed prior to each V-Cone entry leg and a pressure transducer is installed at the high-pressure side of the V-Cone. These measurements give the information for the calculation of flow density thus calculating the mass flow rate. The specification of those sensors is listed in Table 3.5.

The mass flow of air from the V-Cone is calculated as the equation:

$$\dot{m} = \sqrt{\rho} F_a C_d Y k_1 \sqrt{\Delta P} \tag{3.18}$$

where ΔP is the differential pressure measured from the DP sensor, ρ represents the

Table 3.5: V-Cone sensor Actual uncertainty

Sensor Location	**Quantity**	**Order From**	**Sensor Type**	**Actual Accuracy**	**Sensor range**
Turbine Inlet Large 1	Differential Pressure	Siemens	Sitrans P DSIII	±0.065%	0-400 bar
Turbine Inlet Large 1	Static Temperature	TC Direct	PT100	$\pm 0.15K$	233K-523K
Turbine Inlet Large 1	Static Pressure	Omega	PX302	±0.15%	0-100 psi
Turbine Inlet Large 2	Differential Pressure	Siemens	Sitrans PDSIII	±0.065%	0-400 bar
Turbine Inlet Large 2	Static Temperature	TC Direct	PT100	$\pm 0.15K$	233K-523K
Turbine Inlet Large 2	Static Pressure	Omega	MMA100V10 P2C1T3A3P	±0.15%	0-100 psi
Turbine Inlet small 1	Differential Pressure	Siemens	Sitrans PDSIII	±0.065%	0-400 bar
Turbine Inlet small 1	Static Temperature	TC Direct	PT100	$\pm 0.15K$	233K-523K
Turbine Inlet small 1	Static Pressure	Omega	PX302	±0.15%	0-100psi
Turbine Inlet small 2	Differential Pressure	Siemens	Sitrans PDSIII	±0.065%	0-400 bar
Turbine Inlet small 2	Static Temperature	TC Direct	PT100	$\pm 0.15K$	233K-523K
Turbine Inlet small 2	Static Pressure	Omega	MMA100V10 P2C1T3A3P	±0.15%	0-100 psi
Compressor Inlet large	Differential Pressure	Siemens	Sitrans PDSIII	±0.065%	0-400 bar
Compressor Inlet large	Static Temperature	TC Direct	PT100	$\pm 0.15K$	233K-523K
Compressor Inlet large	Static Pressure	Omega	PX302	±0.15%	0-100 psi
Compressor Inlet small	Differential Pressure	Siemens	Sitrans PDSIII	±0.065%	0-400 bar
Compressor Inlet small	Static Temperature	TC Direct	PT100	$\pm 0.15K$	233K-523K
Compressor Inlet small	Static Pressure	Omega	PX302	±0.15%	0-100 psi

density of the air, and is calculated from the pressure and temperature as:

$$\rho = \frac{P_s}{RT_s} \tag{3.19}$$

where R represents the individual gas constant of air, F_a and k_1 represent the material thermal expansion factor and the flow coefficient respectively, Y is the gas expansion factor, and C_d is the discharge coefficient. The gas expansion factor Y is calculated by:

$$Y = 1 - (0.649 - 0.696\beta^4)\frac{U_1 \Delta P}{\gamma P} \tag{3.20}$$

where U_1 is a unit conversion constant given by McCrometer and β is the beta-ratio, which is a function of V-Cone geometry:

$$\beta = \sqrt{1 - \frac{d^2}{D^2}} \tag{3.21}$$

where d and D represent the inner and outside diameters of the V-Cone pipe.

Uncertainty of mass flow measurement

The RSS uncertainty calculated by using equation 3.10 is as follows, where the uncertainties of constant values given by the supplier (F_a,C_d, and k_1) is neglected:

$$\sigma_{\dot{m}_{RSS}} = \sqrt{\left[(\frac{\partial \dot{m}}{\partial \rho})^2 {\sigma_\rho}^2 + (\frac{\partial \dot{m}}{\partial T_s})^2 {\sigma_{T_s}}^2 + (\frac{\partial \dot{m}}{\partial \Delta P})^2 {\sigma_{\Delta P}}^2\right]} \tag{3.22}$$

For the mass flow case in the experiment conducted in this project, the maximum uncertainty by using the turbine inlet small V-Cone is $\pm 2.21\%$ and an average uncertainty of $\pm 1.75\%$ with a 95% confidence interval, and $\pm 2.04 g/s$ maximum and $\pm 1.41 g/s$ in absolute terms. As for the compressor side, the average uncertainty is $\pm 0.49\%$ and maximum uncertainty $\pm 1.61\%$ with the absolute terms of $\pm 0.81 g/s$ average and $\pm 1.02 g/s$ maximum.

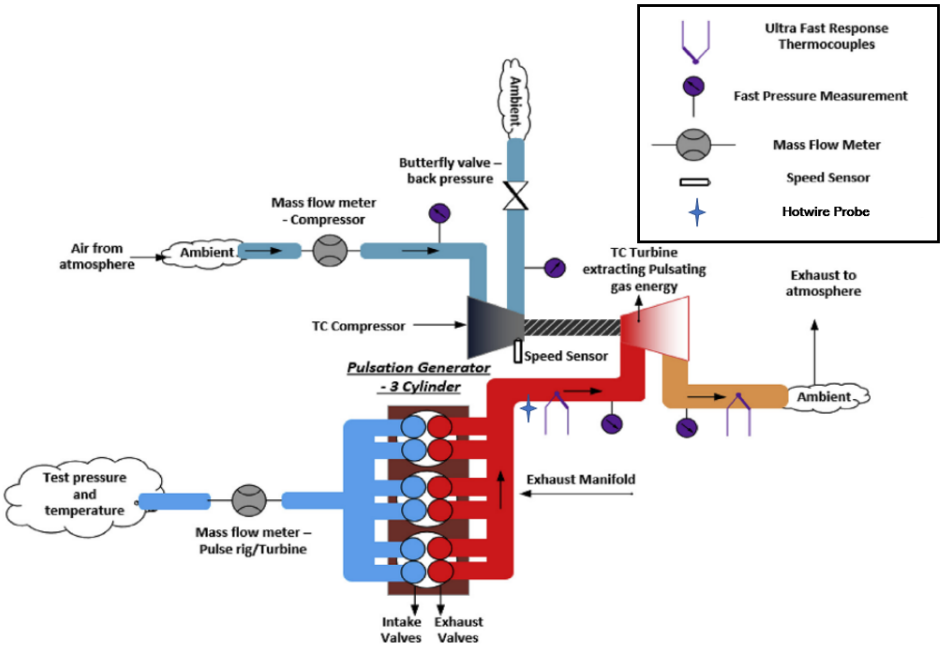

Figure 3-9: Unsteady mapping apparatus (Vijayakumar et al., 2019)

3.3 Unsteady Pulse Rig

In this thesis, a 3-cylinder pulsation generator was also connected with the turbine inlet section to test how the turbine reacts under pulsating conditions based on the research of (Vijayakumar et al., 2019) as shown in Figure 3-9. The fast measurement sensors for pressure, temperature, and mass flow rates are used as the figure shows.

The instantaneous mass flow measurement was collected by National Instrument data acquisition cards on the Dantec Streamware pro system, which is able to collect data of the maximum frequency 250 kHz(Dantec Dynamics, 2019). The instantaneous pressure, as well as temperature measurement, was collected via the Dewetron Sirius data acquisition cards with the capability of measurement up to 100 kHz. These two fast measurement units work together with the slow measurement unit of the Sierra data acquisition system used for steady time-averaged measurement at 40 Hz. By receiving a trigger simultaneously, these three systems record synchronized data.

3.3.1 Instantaneous pressure measurement

Turbine inlet and outlet pressure signals were measured through high-frequency response strain gauge sensors Kistler® type 4049B shown in Figure 3-10. This sensor includes a water cooling channel allowing the sensor to be exposed to gas temperatures in excess of 1100 °C. The sensor accuracy is less than ±0.3% of the full-scale output (FSO) of 0-10 bar. As mentioned by Lam et al. (2002) and Hellström et al. (2009) in their CFD study, the volute has the effect of damping the pressure wave. Additionally, in order to minimize the 'filling and emptying' effect resulting from the mass accumulation of the volute, and reduce the phase-shift between isentropic power and actual power due to the spatial difference of measuring plane, the inlet sensor is mounted close to the rotor. The outlet pressure sensor is mounted in the middle of V-Cone connected to the turbine outlet, which is capable of capturing the pressure fluctuations. It is worth mentioning that electronic low-pass filters connected to the pressure sensors were used to smooth measured signals, and this would reduce the high-frequency noise.

The fast pressure sensors were also calibrated by a pressure calibrator for the slow pressure transducers in previous sections. The overall uncertainty of the turbine inlet fast pressure sensor is ±1.76 kPa at average and ±2.23 kPa at maximum. The overall uncertainty of the turbine outlet fast pressure sensor is ±1.46 kPa at average and ±1.94 kPa maximum.

3.3.2 Instantaneous temperature measurement

This study has a particular motivation of experimentally measuring the temperature under pulsating flow conditions. As mentioned earlier, the commonly used method of evaluating the pulsating temperature is based on an isentropic expansion of ideal gases, starting from measured mean inlet pressure and temperature and instantaneously static pressure. According to Chapter 2, quite a few papers evaluated the instantaneous temperature experimentally due to the requirement of fast response thermocouples.

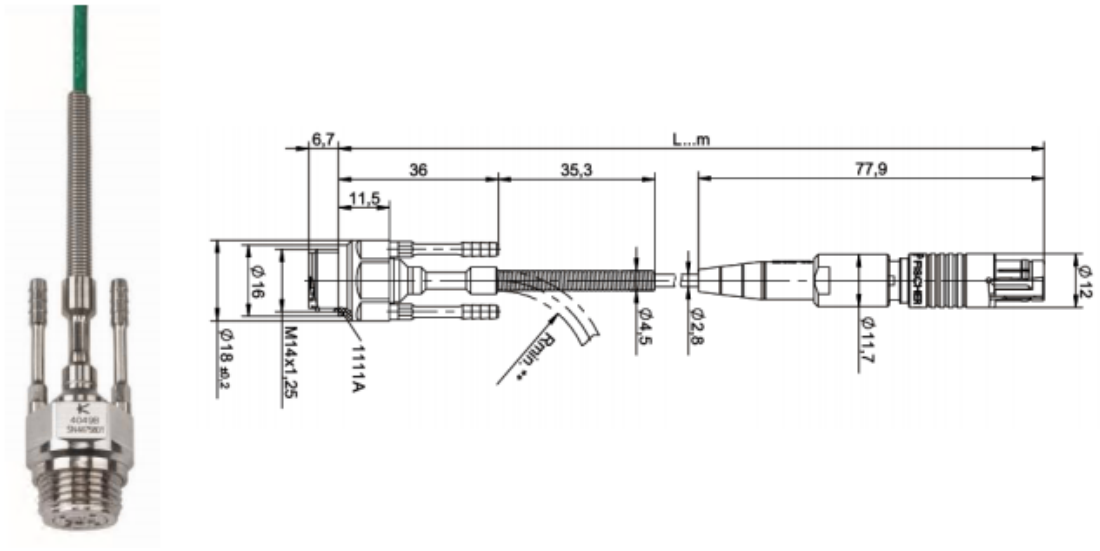

Figure 3-10: Kistler instantaneous pressure measurement(Duda, 2017)

Taking a 50 Hz pulse for example, which corresponds to an engine speed of 2000 rpm of a 3-cylinder engine. From the valley to the peak of the pulse, it requires less than 200 ms for the thermocouple to respond, as shown in Figure 3-11.

A fine-type thermocouple manufactured by Anbesmt co. is used in this study. This thermocouple has a small contact area of the thin tip (small heat capacity) thereby absorbing and transferring the heat quickly. In addition, a small tip wire section area minimizes heat loss. However, this thermocouple cannot take much strength at this tip wire diameter. Therefore, the tip wire and main wire are insulated together at an expense of sacrificing the dynamic response. ANBE SMT co. Japan (2010) compared the temperature response caused by adiabatic compression using different sizes of fine-type thermocouples, as shown in Figure 3-11.

The red, blue, and green curves are referring to the measurement by using 13 μm, 25 μm, and 50 μm thermocouples respectively, and the black curve stands for conventional thermocouples. The data shows that fine type thermocouples are very effective at measuring changing gas temperatures, and the 13 μm one has the fastest response

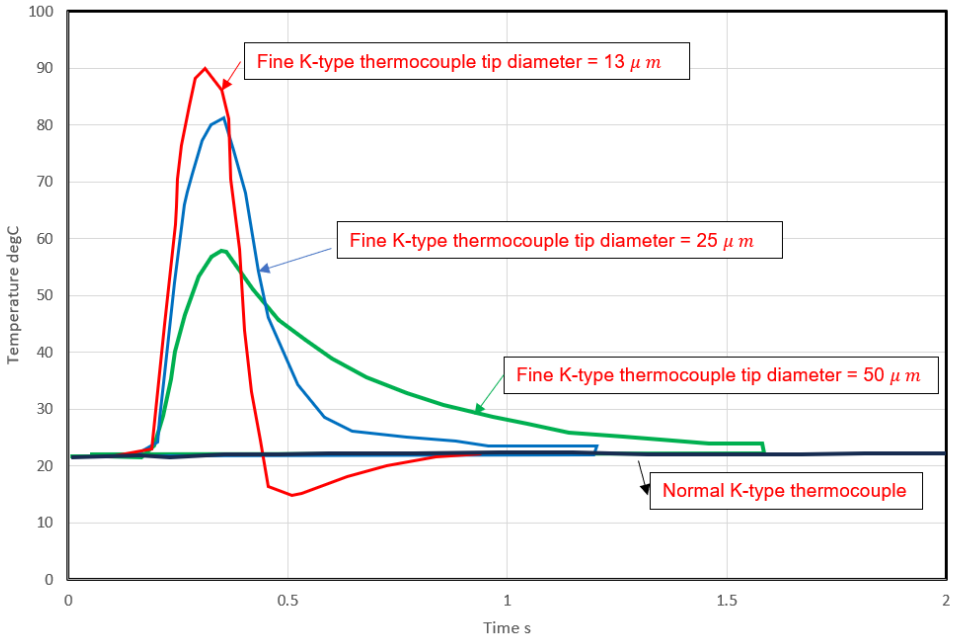

Figure 3-11: Instantaneous temperature measurement (ANBE SMT co. Japan, 2010)

and reaches the highest peak temperature. According to Anbesmt co., this thermocouple can capture a temperature variation in less than 200 ms of about 30 °C. The thermocouple performances with the tip wire size of 13 μm are used in this study based on the unsteady mapping conducted by Liu (2020) that the smallest tip diameter of the thermocouple will give a faster response on turbine inlet temperature when tested under pulsating flow conditions at an average temperature of 400 K. This particular dimension of the thermocouple will give better matching against the assumption of isentropic expansion and compression.

The instantaneous temperature measurement is connected to a fast acquisition system which includes noise that could not be ignored. The instantaneous static temperature could then be validated by the method of Rajoo (2007) by using Equation 3.23:

$$T_{S\_inst} \approx \bar{T} \left(\frac{P_{S\_inst}}{\bar{P}} \right)^{\gamma - 1} / \gamma \tag{3.23}$$

where the average temperature measurement uses the same apparatus as in the steady state. According to Rajoo (2007), the instantaneous static temperature of the pulsating flow is deduced by means of isentropic compression assumption between the pressure and temperature at the 'measurement plane'. In the research, these four K-type thermocouples at the 'measurement plane' provide the time-mean static temperature (T) as described in the previous part for steady measurement. Additionally, the time-mean pressure measured from a slot pressure transducer and instantaneous static pressure measurement at the location are measured with the static tapping and high-response transducer respectively, thus the instantaneous temperature could be calculated and compared with this fine type K-type thermocouple, which will be further discussed in Chapter 5.

What should also be mentioned is that it is quite difficult to get useful data from a thermocouple at a sampling rate of more than 100 Hz. And this is an issue due to the whole measurement chain, including the data acquisition system, which affects also very thin thermocouples.

3.3.3 Instantaneous speed measurement

An DS05 type eddy current probe (with $\pm 0.2\%$ FSO) manufactured by Micro-Epsilon mounted close to the compressor wheel was used to detect turbocharged rotational speed, as shown in Figure 3-12. The rotation of blade passages generates a periodic electromagnetic field from the coil, while every blade generates an inductive pulse. Therefore, the pulse frequency is strictly linked to the turbocharger speed. The time interval between two subsequent pulses was measured by a fast-speed transistor-transistor logic (TTL) counter thereby deriving the instantaneous rotational speed (Duda, 2017), (Liu, 2020).

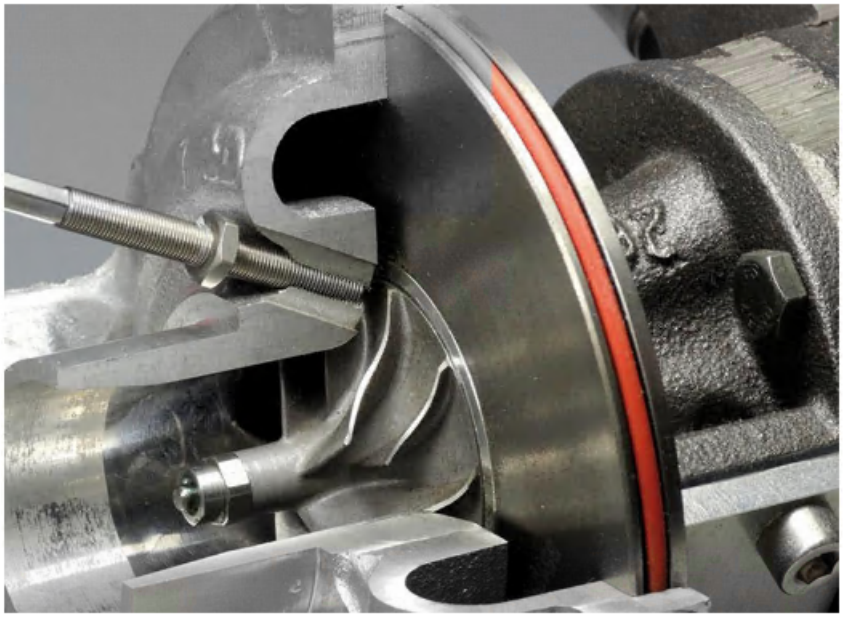

Figure 3-12: Instantaneous speed measurement (Liu, 2020)

3.3.4 Instantaneous mass flow measurement

Hot-wire anemometry

Hot-wire anemometry (HWA) is based on the heat transfer from a heated wire or film element into the fluid flow. It uses the heat transfer from a thin wire that is immersed in the gas stream to determine the condition of flow. Any change in the fluid flow will be detected by the heated element because of its heat transfer instantaneously by a constant temperature or constant current hot wire anemometry system, therefore, it is used to provide information for the change of velocity and temperature of the flow as aforementioned in Chapter 2.

Hotwire probes

The hotwire probes used in this research are type $55R11$ fiber film probes. They have cylindrical thin film sensors and are often used as a substitute for wire probes in liquid or gas applications due to the fact that they are more robust than compared with

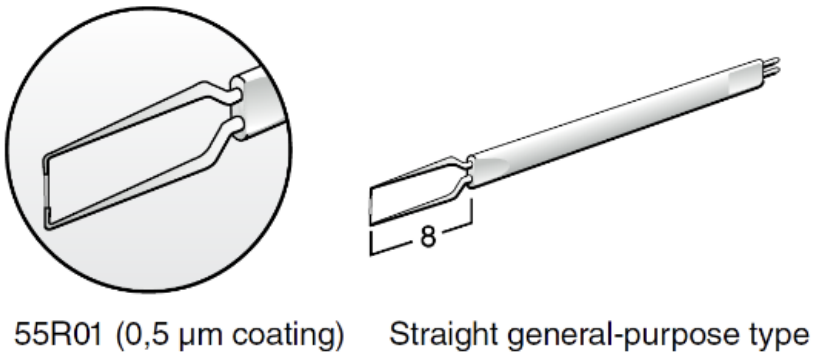

Figure 3-13: The layout of 55R01 straight fibre film probe (Dantec Dynamics, 2019)

miniature wire probes (Dantec Dynamics, 2019). As Figure 3-13 shows, these probes have straight prongs with the sensor perpendicularly installed in the direction of flow velocity at the position of the volute tongue and wastegate as shown in Figure 3-14. The probe holders are marked from the length to make sure their wires are put in the centroid of the plane which is perpendicular to the flow velocity which will be further discussed in Chapter 7 *How to Map a Wastegate Turbine*.

The probe is a sensing element that is associated with an electronic circuit, and it aims to give an instantaneous response because of the turbulence of the flow. There are two main modes of a hot wire probe when operating the measurement:

- the Constant-Current mode (CC), where the probe temperature varies and the current is kept constant.

- the Constant-Temperature mode (CT) mode, where the probe resistance, as well as its temperature, is kept virtually constant by changing the current (Bruun, 1996).

For fast response in fast fluctuations in pulsating flow experiments, a probe system by Dantec Dynamics which is used with Constant Temperature Anemometers (CT) or (CTA) is equipped. The CT anemometer is considered to be the most widely used

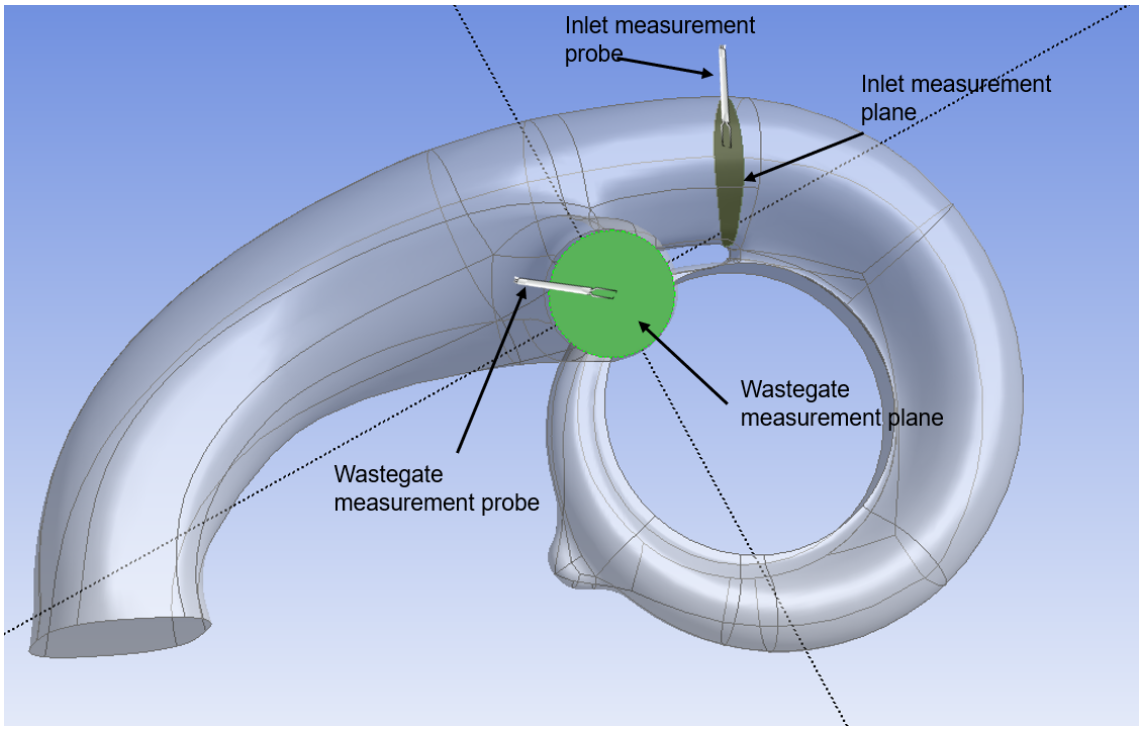

Figure 3-14: Probe measurement

instrument for measurement and analysis of the micro-structures in turbulent gas and liquid flows. It has advantages in maintaining the hot-wire or hot film at constant operational temperature conditions with constant hot resistance because in this mode, the thermal inertia of the sensor element will be adjusted automatically when the flow conditions change (Bruun, 1996). It is realized by utilizing a feedback differential amplifier into the HWA circuit to give rapid feedback to the instantaneous flow velocity variations.

Before conducting the experiment, the system calibrator - StreamLine Pro Automatic Calibrator was used to provide an automatic, fast, and accurate transfer function to the system from a velocity range of $5m/s - 300m/s$. What is more, a two-step calibration was also conducted under steady conditions, in which the measurement of probes of mass flow rate is compared with the V-Cone measurement as shown in Figure 3-15.

As shown in Figure 3-15, the dashed lines represent $\pm 5\%$ difference. By studying the

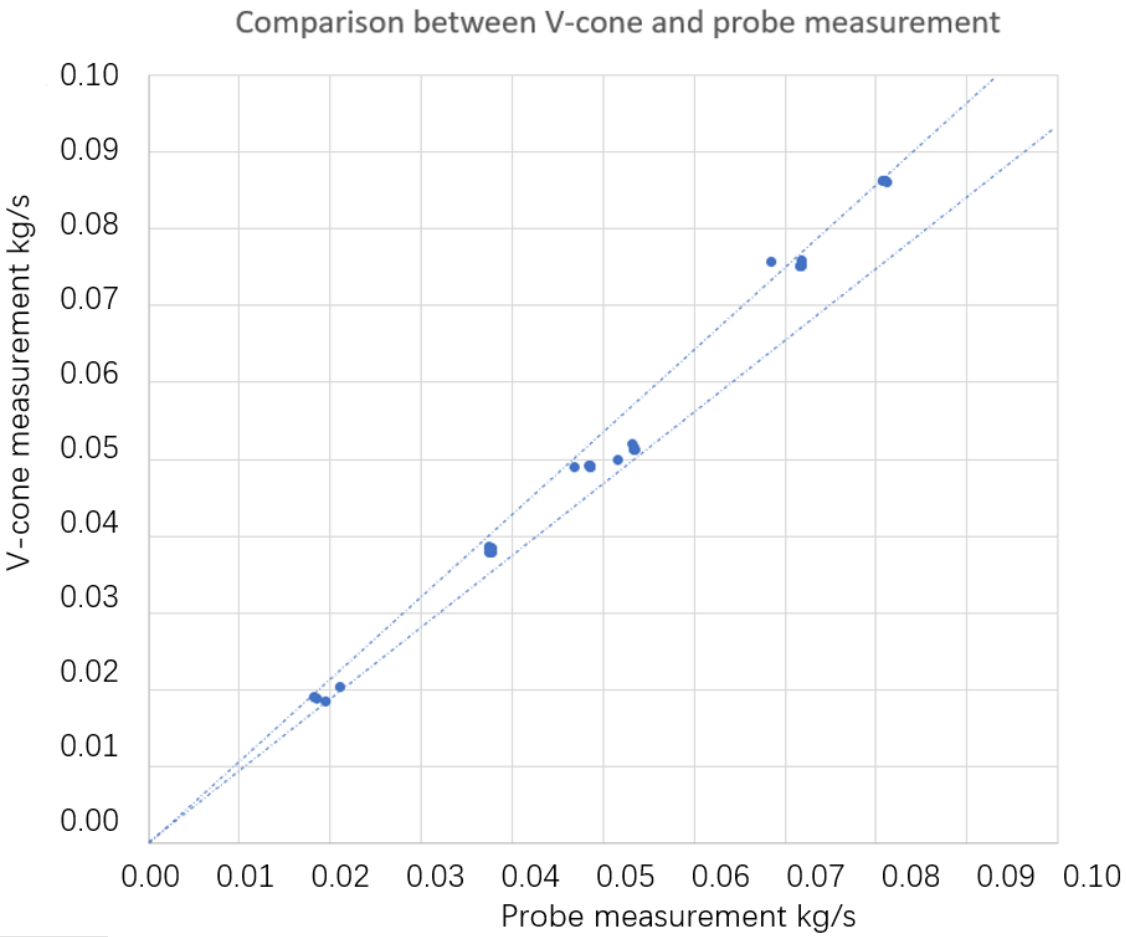

Figure 3-15: V-cone measurement VS hotwire measurement under steady conditions

standard deviation in the error between these two measurements, if the uncertainty associated with the V-Cone measurement is ignored as seen in the research of (Newton, 2014) as discussed in steady mass flow measurement, the average uncertainty of the hotwire used in this thesis becomes ±17.7 g/s with a maximum ±19.2 g/s , and with the consideration of V-Cone uncertainty, the overall uncertainty of the hotwire used in this thesis is ±21.78 g/s for the average value.

In this research, the hotwire system is used to measure the wastegate flow proportions in steady conditions. Several attempts were conducted under an unsteady environment, but it was not robust enough to survive under pulses, which will be discussed in Chapter

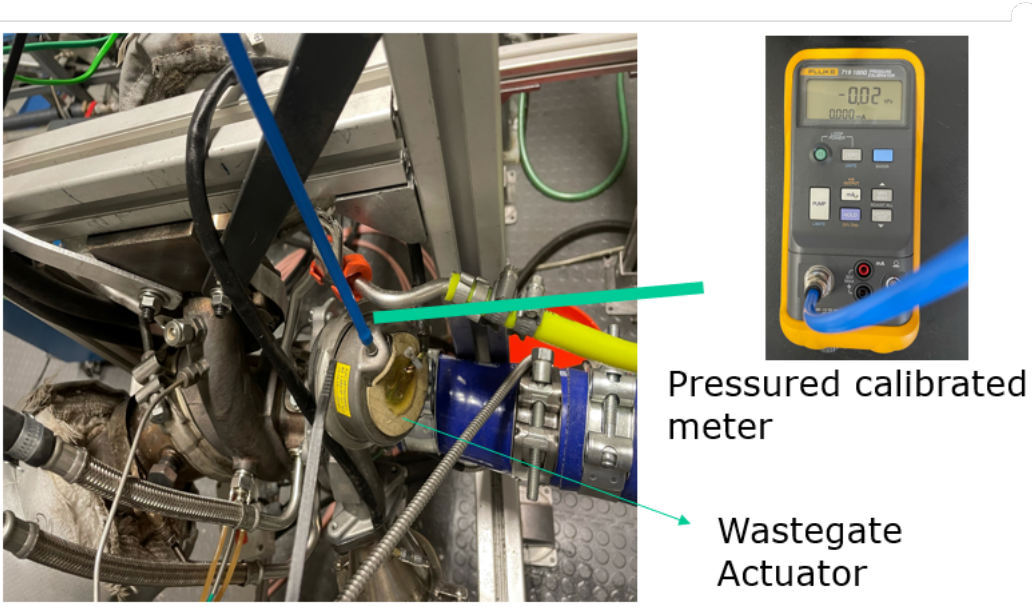

Figure 3-16: The layout of wastegate control unit

4.

3.4 Wastegate Study

In this thesis, different wastegate positions and their influence on turbine performance are also studied. The wastegate characterization experimental facility is shown in Figure 3-16. A pressure-calibrated sensor is connected to the wastegate actuator to control the wastegate opening before collecting the data. The opening is fixed by using two screws connected to the actuator rod shown in Figure 3-17. Instantaneously during the experiment. The wastegate opening is also measured via a displacement sensor connected to the data acquisition system, which will be further discussed in Chapter 7.

What is more, a hotwire probe is also installed inside of the wastegate in order to measure the portion of the mass flow that passes through the wastegate as shown in Figure 3-14 and Figure 3-18.

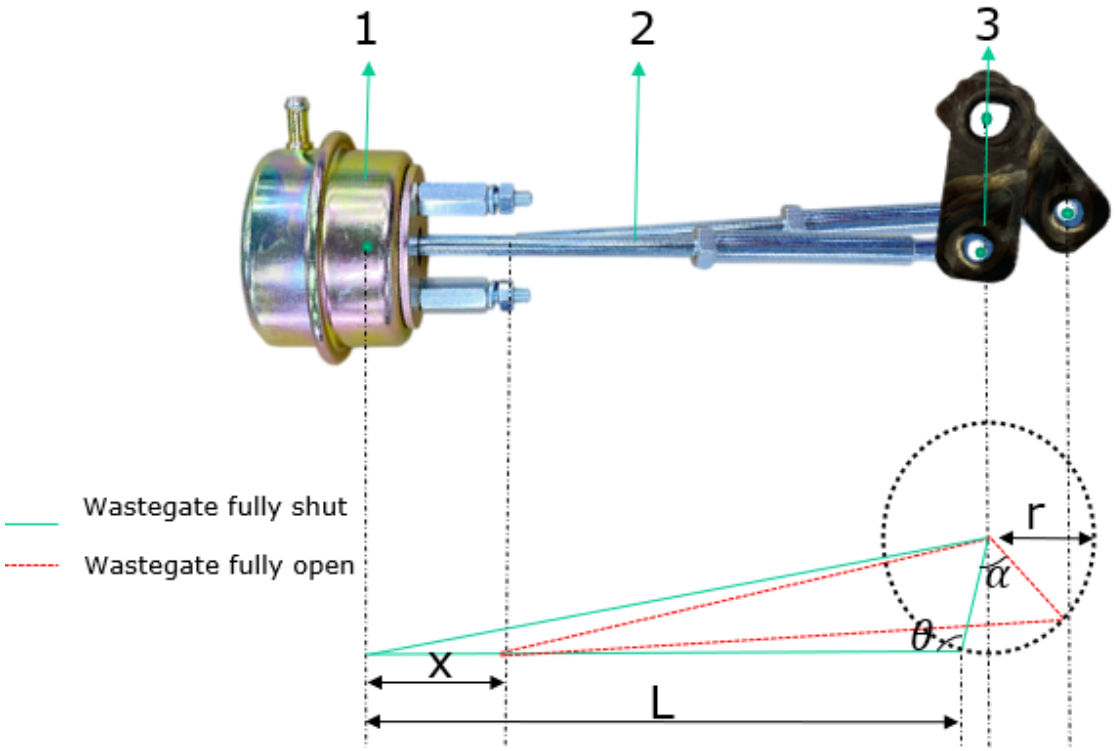

Figure 3-17: Wastegate actuator

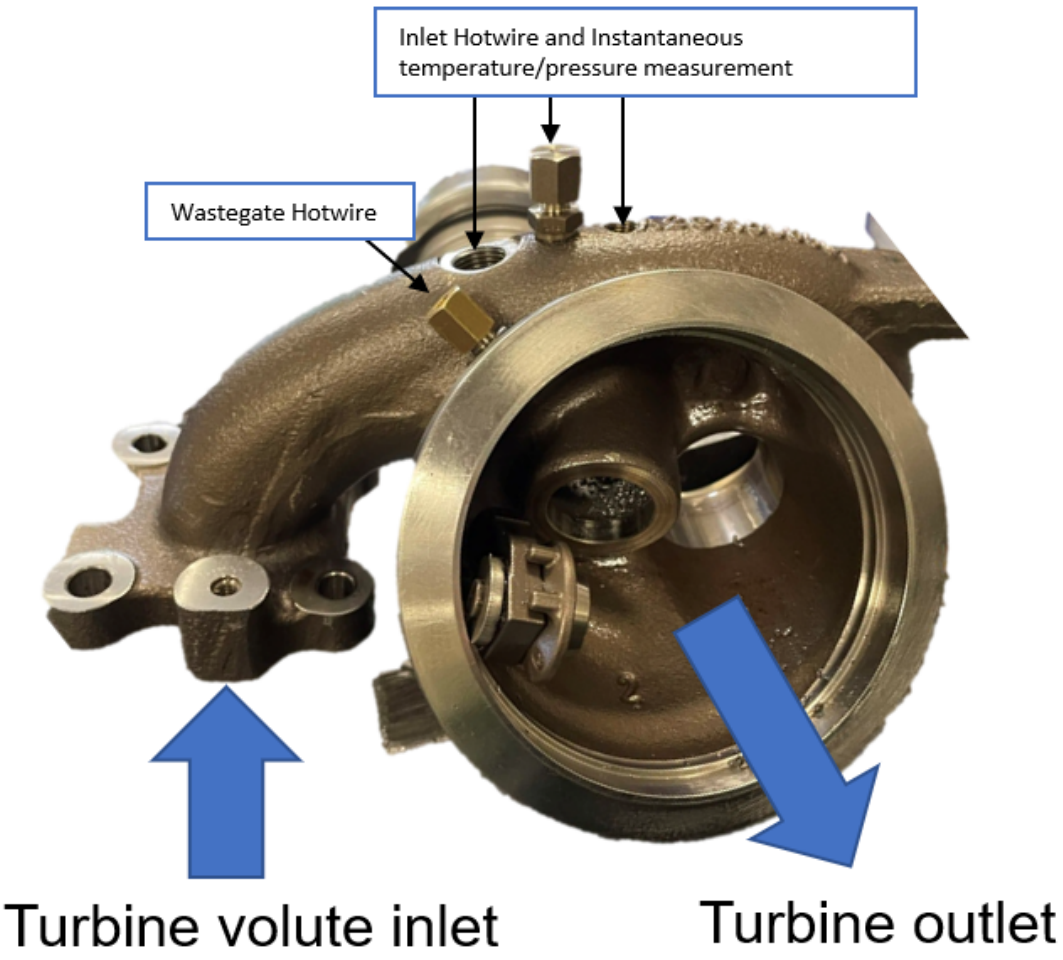

Figure 3-18: Wastegate mass flow instantaneous measurement

Figure 3-17 shows the layout of the wastegate actuator. The opening of the wastegate is controlled by the wastegate actuator, where a change in the displacement shown x will result in a change in the opening of α. Domain 1 is the actuator of the wastegate, and there is a spring unit inside of it. Domain 2 represents the actuator rod, and domain 3 is the wastegate arm that connects with the wastegate $r = 30.54$ mm representing the length of the wastegate arm, α is the change of the wastegate between fully closed and fully open, θ is the angle of actuator rod and wastegate arm when fully closed $L = 153.77$ mm, x represents the displacement of actuator rod, thus according to Hooke's law of elasticity, the displacement change in x will be linearly related to the change of α. In this research, x is measured with several points from the wastegate actuator boosted to be fully closed to fully shut conditions. The displacement x was measured from a pressure calibrator using the linear correlation between voltage and displacement. This measurement was initially calibrated before experimenting by taking out the wastegate part from the turbine. The maximum displacement measured equals 21.4 mm with $\alpha = 31.86^o$. With the uncertainty coming from the measurement of the full length of the rod of ± 0.01 mm, the average uncertainty of the angle is around $\pm 1^o$.

3.5 Conclusion of the Chapter

In this chapter, the experimental methodology used in this research has been illustrated, which includes:

- Standard steady mapping

  This method results along with the steady closed loop mapping will be discussed in Chapter 6, where the uncertainty of the turbine characteristics such as mass flow rate, pressure ratio, and efficiencies will be discussed based on the measurements illustrated in this chapter.

- Steady closed loop mapping

The results of this method will be combined with the standard steady mapping and discussed in Chapter 6. A comparison of these two combined experimental results against the CFD data will be analyzed.

- Steady mapping with different wastegate openings

  The results of this method will be discussed in Chapter 7, where a mathematical wastegate model will be built based on the experimental data collected using this method.

- Unsteady mapping pulse rig

  The results of this method will be discussed in Chapter 5, where a dual-nozzle model will also be used as the comparison of the unsteady mapping results.

What is more, all of the key sensors used for turbine characteristics including turbine inlet and outlet pressure sensors, turbine inlet and outlet thermocouples, and turbine inlet mass flow rate sensors were all analyzed in this chapter and studied the uncertainty. This should clearly respond to the research question raised in Chapter 1, 'How to collect mapping data and quantify operation conditions for a single entry radial turbine precisely?', as a methodology of measuring turbine characteristics in a precise way was built in this chapter.

Chapter 4

Numerical Methodology

4.1 Outline of the Chapter

This chapter aims to answer the research question raised in Chapter 1 *Introduction*: how to model a single-entry radial turbine precisely in 1D and 3D ways? a mix of 3D CFD modeling and 1D modeling will be used in order to simulate the turbine in both steady and unsteady conditions in this thesis, and in this chapter, the numerical methodology used in this research will be illustrated.

For 3D numerical methods, two CFD models will be described to predict turbine characteristics including:

- Simplified CFD model

  This simplified CFD model is used for the validation of experimental data collected in standard steady mapping. This CFD model simulated the turbine in wastegate fully shut conditions, thus the wastegate pipe on the turbine volute domain is taken away.

  This model is then coupled with a mathematical mechanical loss model which

gives a good agreement between the experiment and simulation results which will be discussed in Chapter 6.

- Wastegate CFD model

  This model used the CAD with the wastegate where the wastegate itself was meshed by the solid mesh method. The wastegate opening conditions were simulated by changing the angle between the turbine outlet part on the volute domain and the wastegate itself. This model gives validation of the mass flow rate measured on the wastegate by using the hotwire probes which will be discussed in Chapter 7.

Due to the fact that the 3D CFD model is time-consuming, especially for transient cases, the 1D modeling method is also used in this thesis. For the 1D modeling method, a dual-orifice model will be built in this research where the turbine is modeled as a dual-nozzle section. In this way, different turbine inlet conditions including steady and unsteady are tested on this 1D simulation code to give a prediction of the experiment in different conditions which will be discussed in Chapter 5.

In this chapter, section 4.2 will discuss the CFD methodology used in this thesis including the introduction, the CAD cavity model prepared, and the mesh sensitivity. The simplified CFD model and the wastegate CFD model are then discussed in separate sub-sections. Further results and discussions of these two CFD models will be illustrated in Chapter 6 and Chapter 7 respectively. Section 4.3 discussed the dual-orifice model which will be analyzed and discussed in Chapter 5. Section 4.4 will give a conclusion of this chapter on numerical methodology.

4.2 3D Numerical Methodology

4.2.1 Introduction

In this section, the 3D simulation method of this project will be illustrated. Computational fluid dynamic (CFD) is used to compare with instantaneous experimental measurements and give the correction in regard to the wastegate opening position.

The CFD method is commonly used in the study of turbine internal flow field analysis and the conservation laws of fluid flow and related transport phenomena are governed by the Navier-Stokes equations, and the partial differential equations of mass, momentum and energy conservation (PDEs) (Moukalled et al.,2016).

In their project, the CFD model uses SST (Shear-Stress Transport Model) according to Menter (1994). This turbulence model has been tested rigorously for a large number of flows (Moukalled et al.,2016).

The aim of the analysis is to compare the experimental results versus CFD predictions, and especially to compare the CFD prediction of mass flow rate at a specific plane with the point measurement by hotwire in an experiment. Additionally, by using the CFD model as a baseline, a mechanical loss model which will be discussed in Chapter 6 is also built to correct the CFD model.

Turbulence model

The definition of turbulence models in Computational Fluid Dynamics (CFD) is a method to include the effect of turbulence in the simulation of fluid flows.

- $k-\varepsilon$ models

  The $k-\varepsilon$ is the first major model that is widely used to simulate turbulence in CFD. The basis of this model is to relate the turbulent eddy viscosity to the turbulence kinetic energy. This approach uses the fluctuating components of the turbulent velocity in three coordinate axles to calculate the turbulent kinetic

energy from (Gorman et al., 2021).

$$k = \frac{1}{2}\left(\overline{u'^2} + \overline{v^2} + \overline{w'^2}\right) \tag{4.1}$$

where k is the additional turbulent energy calculated from the time-fluctuating turbulent motions. Apart from this, a turbulent dissipation ε is also used in this turbulence model to solve the governing equations. This model is built with the assumption of full turbulence, and the molecular viscosity effects are negligible. It predicts well for free-shear flows that are far from walls as suggested in (Newton, 2014), but it is likely to have issues when predicting near-wall flows with adverse pressure gradient in the boundary layer zones(Liu, 2020).

- $k - \omega$ models

  $k - \omega$ is considered to be a significant development in the CFD world for the reason that it replaced the transport equation ε with a specific rate of turbulence dissipation ω, which gives an improvement of the CFD method to predict boundary layer flows. The drawback of this model is it requires fine mesh near the wall (Menter, 1994).

- Shear Stress Transport model

  The Shear Stress Transport model is considered to be a mixing of $k-\omega$ and $k-\varepsilon$, it is able to switch these two models in free stream regions $(k - \varepsilon)$ and boundary layer zones $(k - \omega)$ thus gives a better result than other models (Bayón, 2022).

Wall function

CFD models must treat boundary layers properly in order to get an accurate result because of the fact that the turbulent boundary layer consists of multiple layers(Schetz and Fuhs, 1999) as shown in Figure 4-1. The layer that is nearest to the wall is the viscous sub-layer (or laminar layer) as illustrated in the figure, in this region, the shear strain is extremely high and the molecular viscosity effects dominate as aforementioned

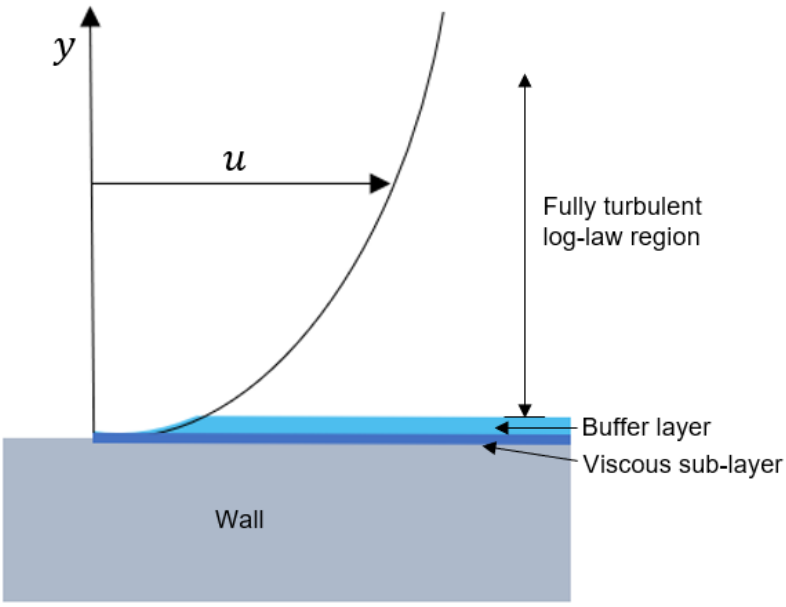

Figure 4-1: Regions in a turbulent boundary layer (Newton, 2014)

in the turbulence model section. The buffer layer shown in the figure is where the flow is affected by both molecular viscosity and turbulence effects. Outside of the buffer layer is the log-law region where turbulent effects dominate.

If each turbulent boundary layer is classified according to its non-dimensional wall distance(y^+),

the y^+ length is calculated by

$$y^+ = \frac{y}{\delta_\nu} = \frac{u_\tau y}{\nu} \tag{4.2}$$

where δ_ν represents the viscous length scale

$$\delta_\nu \equiv \nu \sqrt{\frac{\rho}{\tau_w}} = \frac{\nu}{u_\tau} \tag{4.3}$$

u_τ is the friction velocity tangent direction and ν is the kinematic viscosity. As Figure 4-2 shows

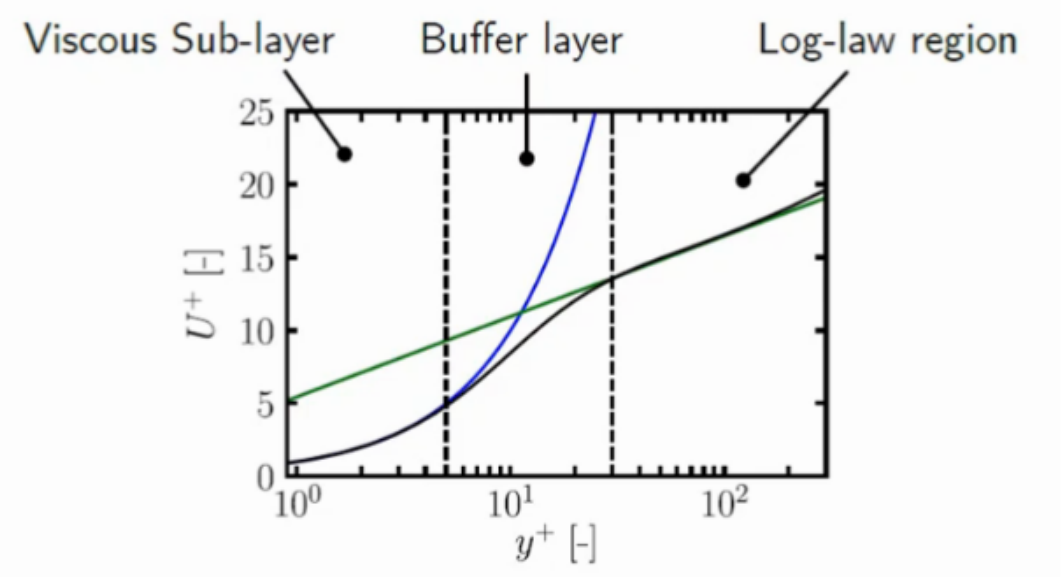

Figure 4-2: Law of wall plot for a turbulent boundary layer (Bayón, 2022)

- $0 < y^+ < 5$: Viscous sub-layer
- $5 < y^+ \leq 30$: buffer layer
- $30 < y^+ \leq 300$: fully turbulent log-law region

In conclusion, it often requires an extremely fine near-wall mesh with a y^+ value smaller than 1, as well as at least 10 inflation layers with the inner layer. Additionally, because in the buffer layer, both Reynolds stresses and wall shear stress impact the calculation. It is also necessary to avoid placing the first internal grid point in the buffer layer region (Bayón, 2022),(Liu, 2020). These were checked in both the simplified CFD model and the wastegate CFD model mesh settings.

4.2.2 Simplified CFD model

In order to validate the experimental data collected under steady conditions and learn about the trade-offs between the experimental data and CFD results, a simplified CFD model is built in this research with the wastegate fully shut.

CAD model prepared

The CAD model of this radial turbine used for the geometry in CFD analysis is conducted by cutting the turbine volute by a 0.2mm wire as shown in Figure 4-3 and scanning the parts.

The volute part has been taken out of the wastegate part and kinked geometry removed that may cause issues for CFD convergence.

The rotor was directly scanned to CAD and then generated the flow path in the Design Modeler of ANSYS as shown in Figure 4-4. Both single stage (Figure 4-5) and full rotor (Figure 4-6) are built and for this simplified CFD model without wastegate, a single passage model was used to save computational time. These results are then further compared with the CFD wastegate (WG) case with WG fully shut to show the single passage is reliable enough, which will be discussed in section 4.2.3.

A long pipe of length four times longer than the wheel diameter was also created separately based on the volute geometry in order to make sure the outlet condition is ambient.

Mesh sensitivity of the simplified CFD model

The mesh sensitivity is conducted in regards to three domains inside the turbine: volute, wheel, and pipe. Three different settings from coarse to fine.

The mesh for this simplified CFD was conducted in ANSYS Meshing and TurboGrid for different domains as shown in Figure 4-5. This general-purpose meshing tool in ANSYS Workbench is able to generate hexahedral, prism, and pyramid mesh elements for different complex geometry with the user's inputs for mesh controls. Body sizing, face sizing for interfaces, and inflation methods are used in those domains to keep the mesh quality acceptable.

As Figure 4-4 shows, in this research, a scanned turbine wheel was put into the Design-

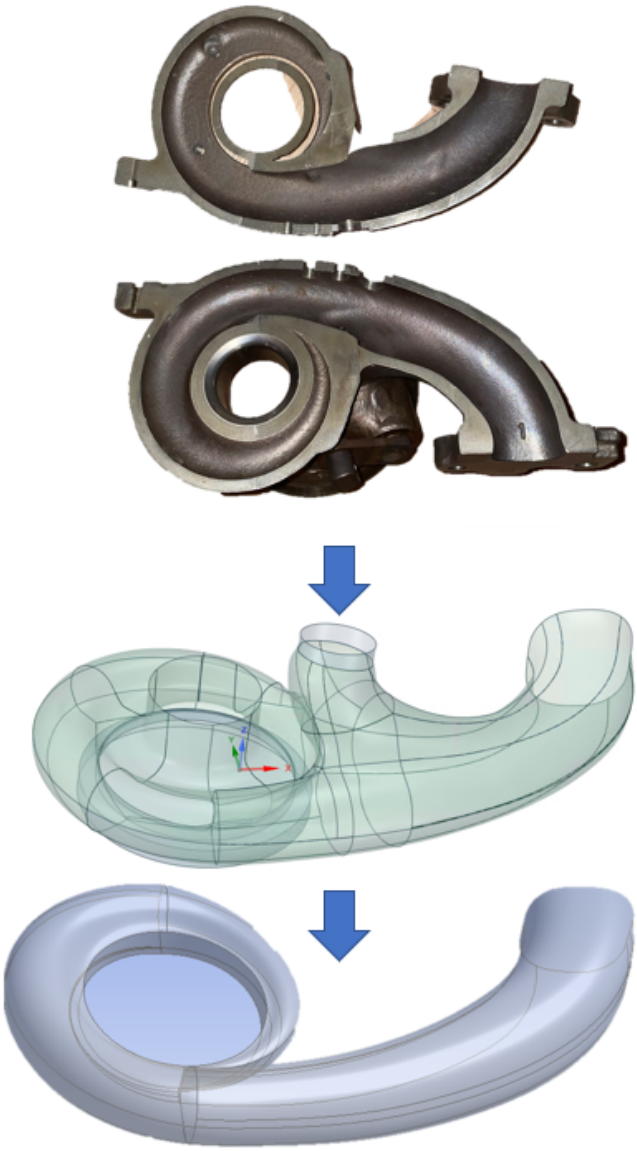

Figure 4-3: Volute CAD

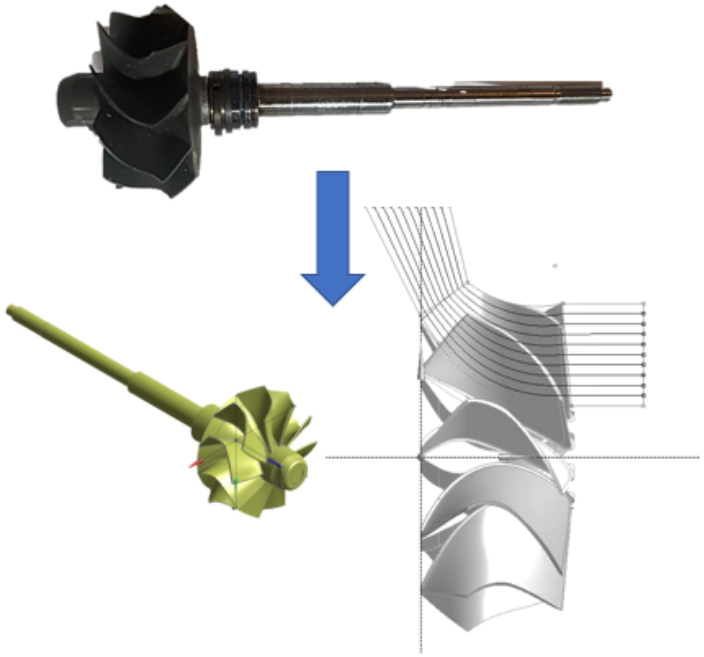

Figure 4-4: Rotor CAD

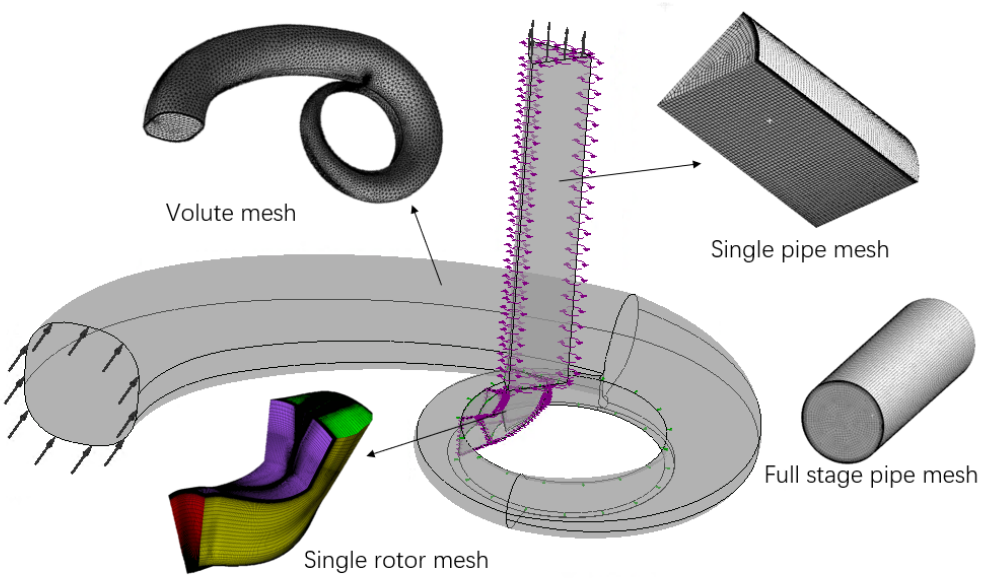

Figure 4-5: Single passage model of CFD domains

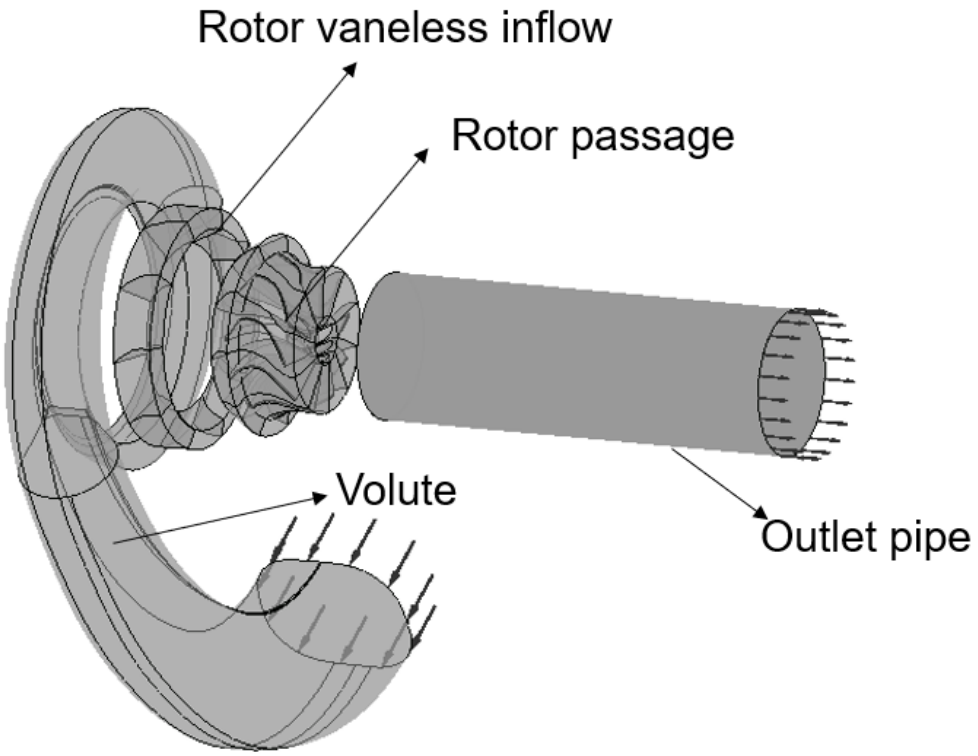

Figure 4-6: Full rotor model of CFD domains

Table 4.1: Mesh Sensitivity for simplified CFD model

Regine	**Baseline**	**Fine Mesh**
Volute	951,362	1,225,755
Wheel	3,673,312	10,005,488
Diffuser	436,058	1,002,250
total	5,060,732	11,143,744

Modeler where the wheel's hub, shroud, inlet, and outlet surface are manually selected to generate the flow path and then fed into TurboGrid. Turbine wheel domain was meshed in ANSYS TurboGrid. This function inside of ANSYS workbench could generate mesh automatically for different shapes of blades with high quality. The user could also manually change some mesh settings including the global size factor and the mesh size at a selected topology edge based on preferences.

The mass flow parameter and the isentropic efficiency are chosen to be the target parameters in the mesh sensitivity study. This study used for each subdomain varied from coarse to fine mesh to estimate the discretization error. The convergence criteria use the coefficient of variation < 0.0005 for mass flow rate as well as efficiency. Table 4.1 shows the mesh elements number from coarse to fine.

The mesh sensitivity results figures are shown as follows in Figure 4-7, Figure 4-8, and Figure 4-9.

This is used to estimate the discretization error. As expected, the largest influence on solution accuracy comes from the turbine domain, where momentum change occurs. Taking results accuracy and computational time into consideration, the baseline is chosen as a total domain of $5,060,732$ elements (wheel $3,673,312$ elements, outlet $436,058$ elements, and volute $951,362$ elements) as there is 1% uncertainty for mass flow rate and efficiency with respect to the finest mesh solution.

All the meshed domains were then used in ANSYS CFX-Pre, where 3D CFD simulations are set up. For all of the stationary domains, the 'general interface' was set

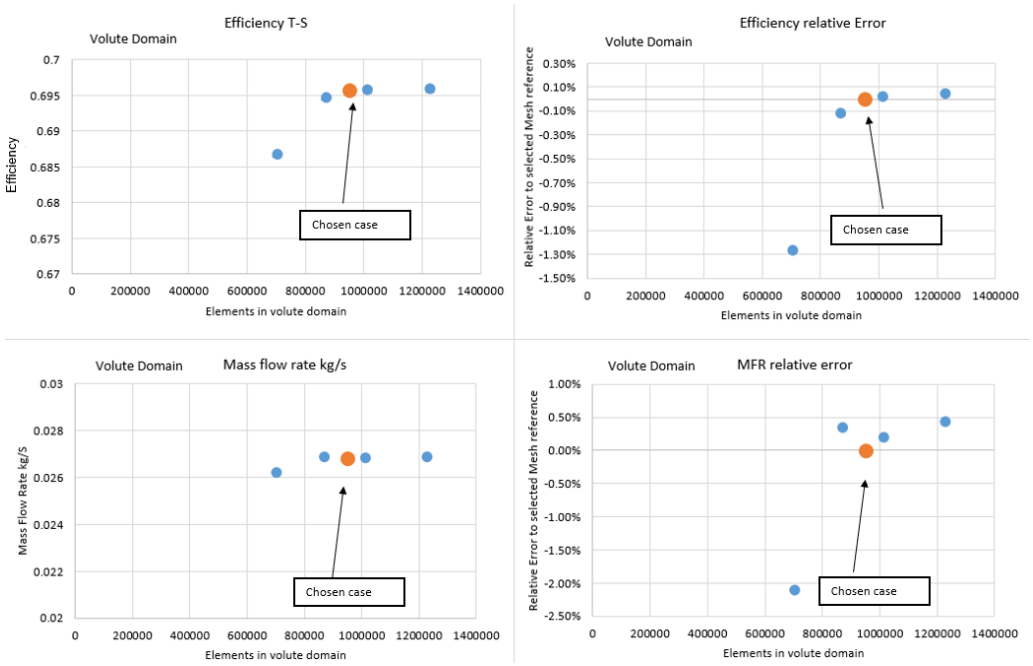

Figure 4-7: Mesh sensitivity study of volute domain (Simplified CFD)

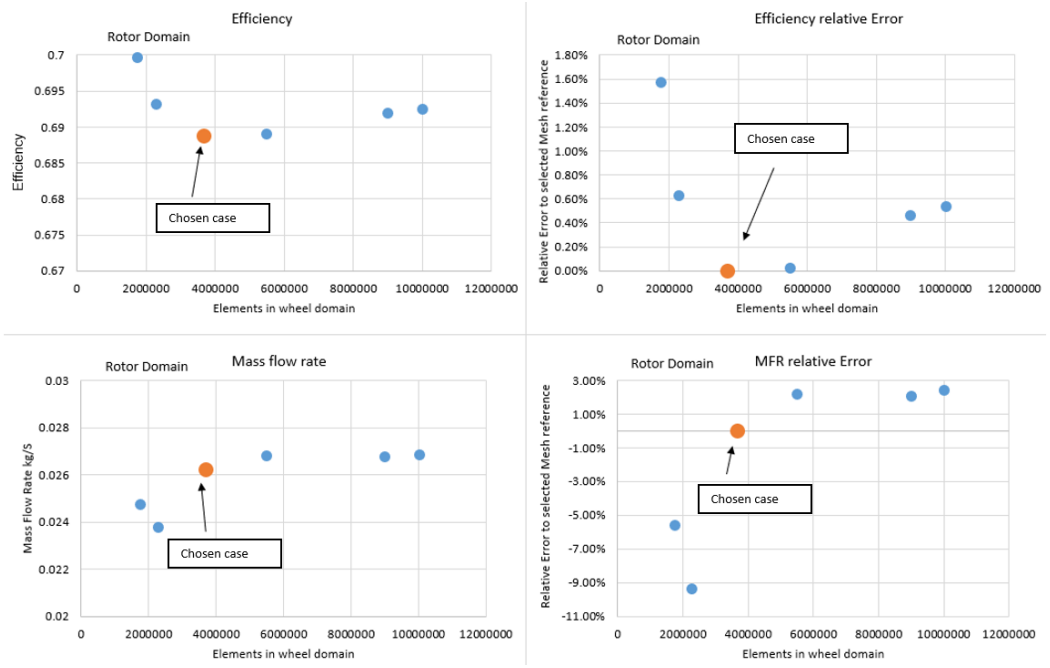

Figure 4-8: Mesh sensitivity study of single-rotor domain (Simplified CFD)

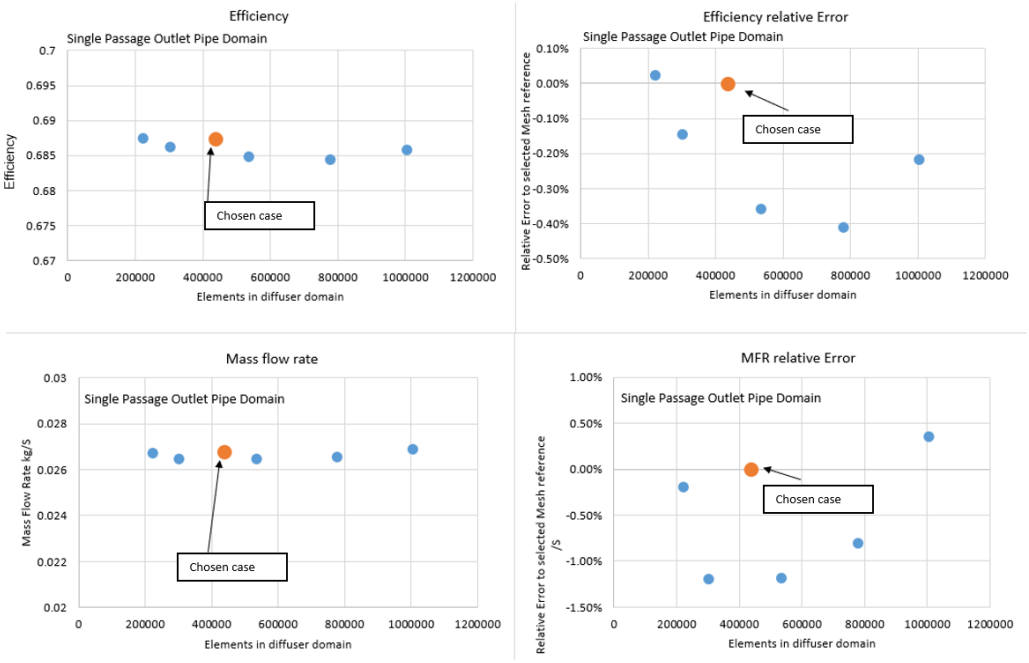

Figure 4-9: Mesh sensitivity study of diffuser domain (Simplified CFD)

and for the interface that connects rotational and stationary domains like wheel and pipe, the 'frozen rotor' option was chosen, as the differences are listed aforementioned in Chapter 2, the definitions of these two options are:

- Frozen Rotor (Multiple reference frame)

  The frozen rotor interface uses the assumption that the rotor and stator kept the same relative position during the simulation

- Sliding Mesh (Mixing Plane)

  The sliding mesh method is when the rotor mesh is moving during the simulation, and the stator and rotor mesh are coupled together at each time-step

The main reason why this research used the frozen rotor method is that the CFD model for validation and comparison with experimental data, rather than the analysis of detailed flow field, and the frozen rotor method is more computationally economic. A single passage rotor is used in the simplified CFD model for the same reason. The inter-

Model Type	Simplified CFD model	Wastegate CFD model
Rotor Passage	Single passage	Full rotor
Max. Iterations	200	500
Wastegate	No	Yes
Analysis Type	Steady	
Inlet Type	Inlet Total Pressure	
Outlet Type	Static Pressure	
Medium	Air Ideal Gas	
Walls	Adiabatic and Non-slip	
Converge Criteria	$RMS = 1 \times 10^{-6}$	
Turbulence Model	SST	
Wall Function	Automatic	
Heat Transfer	Total Energy	
Advection Scheme	High Resolution	

Table 4.2: CFD setup

face between each wheel passage used periodic boundary conditions as shown in Figure 4-5. (Figure 4-6 shows full rotor model for the simplified CFD). The enthalpy transport is considered because it is needed to compute properly for the turbine efficiency.

On the other hand, for the wastegate CFD model where the outlet pipe interface is more complex than the simplified one, the full passage is used. The differences between this simplified single-passage model and the wastegate CFD mode with fully shut WG are shown in Chapter 7.

Due to the high-speed flow inside of the rotor passage, the compressibility effects are considered by modeling the transport of enthalpy using the total-energy scheme. All the walls were assumed to be non-slip and adiabatic. Further mechanical loss models are discussed in Chapter 6.

For the wastegate CFD case, a higher value of maximum iterations of 500 is used due to the complexity of the model. The detailed information of settings, and the differences between the simplified CFD and the wastegate CFD model are listed in Table 4.2.

4.2.3 Wastegate CFD

Apart from a simplified CFD model, the researcher also studied the CFD results on different wastegate openings, thus a wastegate CFD model as shown in Figure 4-10 is also built, which will be further discussed in Chapter 7.

CAD model prepared

Similarly, in order to study the effects of different wastegate openings, the outlet part was also scanned and generated a 3D CAD model.

Solid mesh

The main difference between the simplified CFD model aforementioned and this wastegate CFD model is the involvement of the wastegate which was meshed as a solid. The material was defined as the steel of a continuous solid.

Mesh sensitivity

The aim of using this CFD model with the function of different wastegate variations is to validate the flow coefficient model that has been discussed.

Before the comparison of experimental data measured from probes and the CFD results from the wastegate CFD model, the mesh sensitivity in this CFD with wastegate model is conducted as the results show in Figure 4-11, Figure 4-12, Figure 4-13 and Figure 4-14. Unlike the simplified CFD model used in Chapter 5, full rotor analysis is used in this section due to the complexity of flow characteristics when the wastegate is open. The mesh setting used in this research is chosen to be within 1% difference with the finest mesh case. Table 4.3 shows the mesh elements number from coarse to fine.

The comparison between the WG fully shut model and the simplified CFD model is conducted by plotting the operating points of a single speed line. The result shows that there is less than 3% difference in these two CFD results for those operating points in

Table 4.3: Mesh Sensitivity for Wastegate CFD model

Regine	**Baseline**	**Fine Mesh**
Volute	508,280	716,540
Wheel(per stage)	3,692,994	7,123,223
Diffuser	486,990	696,890
Wastegate	37,793	58,046
Total	37,963,003	72,703,706

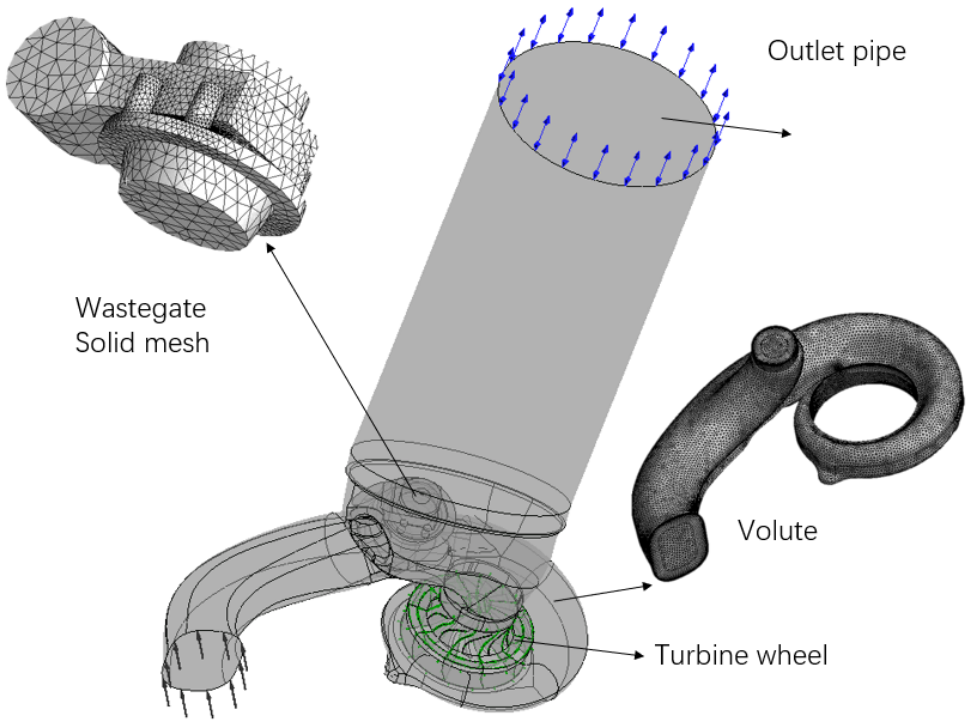

Figure 4-10: Setting up the wastegate CFD

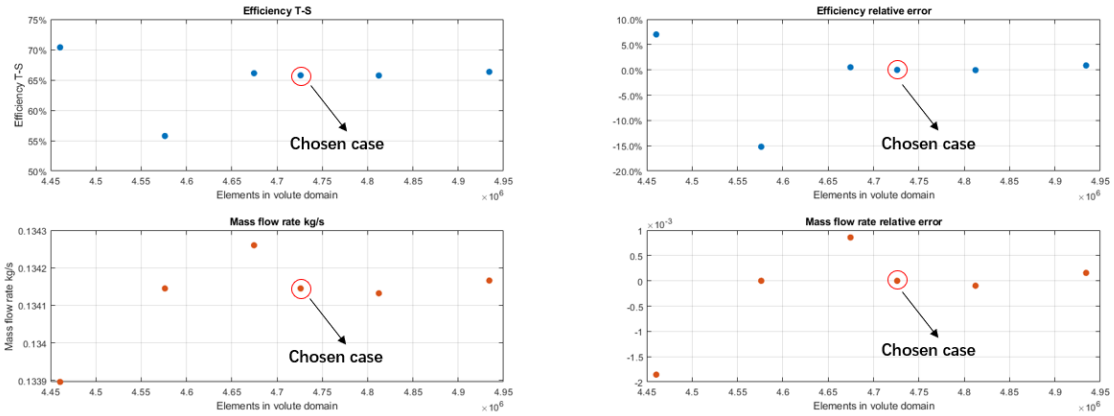

Figure 4-11: Mesh sensitivity study volute (wastegate CFD)

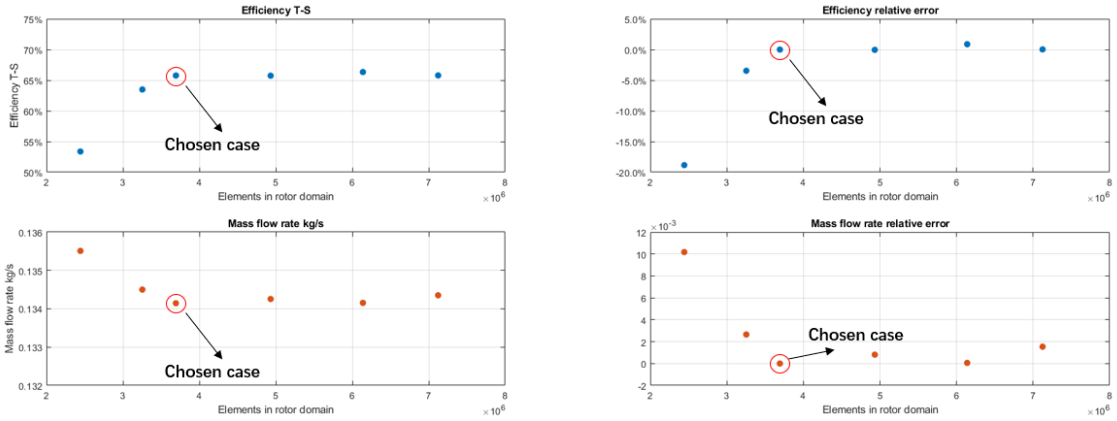

Figure 4-12: Mesh sensitivity study full-rotor (wastegate CFD)

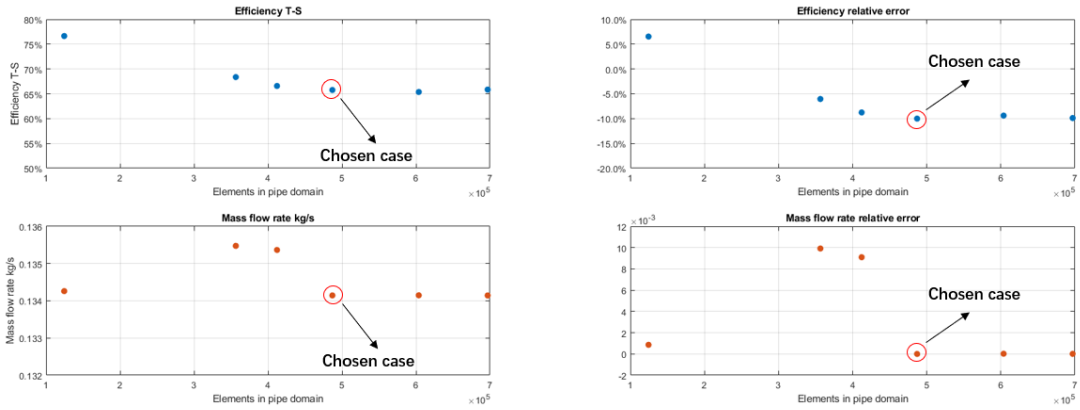

Figure 4-13: Mesh sensitivity study diffuser (wastegate CFD)

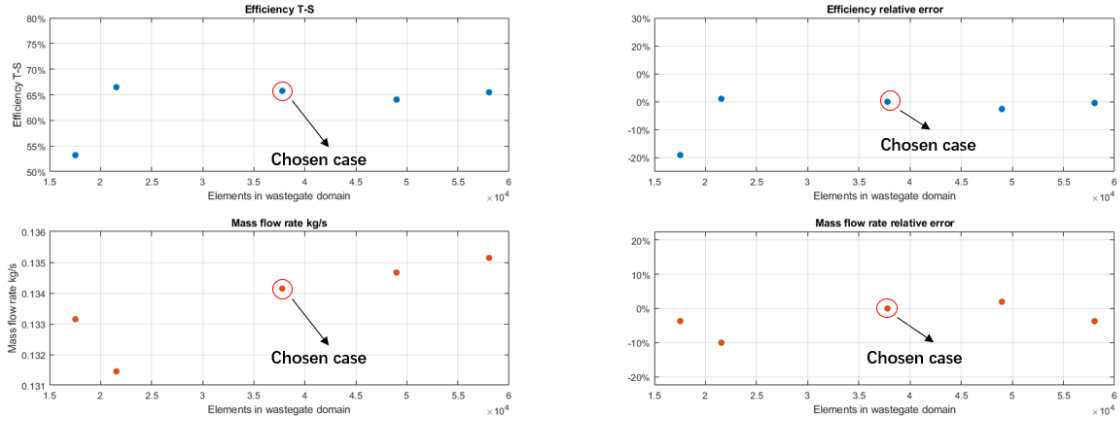

Figure 4-14: Mesh sensitivity study wastegate (wastegate CFD)

both efficiency and the mass flow rate simulated at the turbine volute inlet which will be further discussed in Chapter 7.

4.3 1D Dual-nozzle Code for Predicting Unsteady Data

Due to the difficulty of collecting unsteady data, the thesis also seeks a way to model the radial turbine under unsteady conditions. The CFD model illustrated in the previous sections will take more than a month for a CFD model to run the whole pulse under transient conditions, while a 1D model will only take several minutes to run several pulses under unsteady conditions. Thus a dual-nozzle code that has been validated from an engine test of a similar radial turbine is utilized to predict the unsteady data and test the ability of the extrapolation method under unsteady conditions, which will be discussed in Chapter 5.

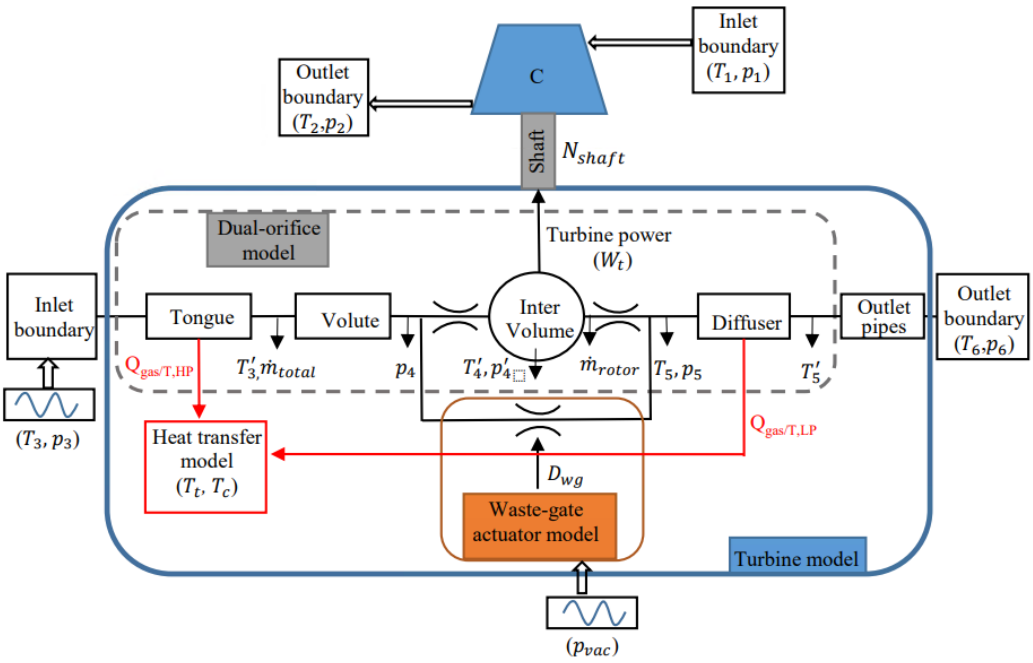

Figure 4-15: The overview of 1D dual-orifice n turbine model(Deng, 2017)

The 1D model shown in Figure 4-15 was built in GT-Power according to the physi-

cal arrangement of the test facility based on the research conducted by Deng (2017). Rather than using a GT-Power standard turbine model, the heat transfer model and the wastegate model were removed for the specific usage in this thesis. The dimensions of pipes, cylinders, pipe junctions, etc. were strictly modeled based on real measurements. Similar to the physical pulse rig, the piston was fixed during the simulation, and the revolution of the inlet and outlet valves produce pressure pulsation.

Since the turbine rotor is regarded as a quasi-steady device in GT-Power, the volume of the volute has to be modeled to take into account the mass accumulation under pulsating flow conditions. The location of the pressure sensor was set close to the volute tongue. Because the mass accumulation effects could only be captured within the region between the measuring section and the rotor inlet, the volume from the volute inlet to the measuring section was not taken into account. The arc length from the volute tongue to the nominal rotor inlet is 85 mm. Although this region could be modeled as a curved pipe, it should note that the flow could only be solved in one dimension. The curvature would only have the effect of increasing the fraction coefficient thus larger pressure drop across the pipe. However, the flow losses in the volute are already considered in the steady mapping data, therefore the pressure loss coefficient and the fraction multiplier are set to zero. Hence, one tapered pipe with an inlet diameter of 28 mm and an outlet diameter of 20 mm are used to model the fluid domain between the volute tongue and the nominal rotor inlet.

The aim of using the 1D simulation is to compare the turbine performance regarding response rate, expansion ratio, and stage efficiency, with different pulse frequencies at the turbine inlet as a prediction of engine-stand mapping results and compare the difference with steady mapping results.

The detailed case studies of this dual-nozzle model with a wide range of turbine inlet pressure pluses of different frequencies will be discussed in depth in Chapter 5. Additionally, two sets of sensors described in Chapter 2 will also be modeled by using the

dual-orifice model to see how will these sensors react in different pulse conditions.

4.4 Conclusion of the Chapter

In this chapter, two different CFD models were illustrated as the validation for experimental data collected under steady conditions with both wastegate fully shut and different openings.

A dual-orifice 1D simulation code which was validated with experimental data was used in this research to predict how the turbine reacts under pulsating flows and the results from sensors with different response times under a variation of turbine inlet conditions.

This chapter illustrated the modelling methodology. The research question raised in Chapter 1, 'How to model a single-entry radial turbine precisely?' refers to the following Chapter 4, Chapter 5 and Chapter 6.

Chapter 5

Unsteady Mapping Method for a Radial Turbine

5.1 Outline of the Chapter

The chapter aims to use simulation to evaluate the feasibility of unsteady mapping and answer the research question raised in Chapter 1:'How to measure and model a turbine under unsteady conditions?' This model used is a dual-orifice model of a turbine that initially comes from a 1.0 L engine and has been validated against engine data from Deng (2017).

The chapter will first describe how the dual-orifice model was built and why this is used to predict unsteady mapping in this research. Then the capability of the model is analyzed to see if it could be an evaluation for the feasibility of unsteady mapping.

Additionally, the different definitions and sensitivity of sensors are then modeled to predict how these sensors will react in reality. In other words, how will unsteady performance appear when data is collected in reading sensors.

To summarize, the aim of this chapter is to use a model to assess the feasibility of

the unsteady mapping method described in Chapter 3. To do this, the following three research questions arise:"

- What types of models are able to predict unsteady behavior and of these models which one(s) are best for assessing the feasibility of unsteady mapping? The ability of this model to represent unsteady behavior is essential to meet the aim of this chapter.

- How is unsteady behavior different from steady flow behavior in a mapping context? This is a critical assumption if unsteady data is to be used to predict steady flow maps.

- What will we see in reality by using the sensors in an unsteady pulse rig by studying the simulation results?

In section 5.2, the unsteady results collected so far by using the pulse rig and the instantaneous measurement sensors will be shown. Different types of models that could be used as the assessment of the pulse rig will be compared.

In section 5.3, the turbine performance predictions under different frequencies of inlet pressure conditions will be analyzed by using the dual-orifice model described in section 5.2 to show how unsteady behaviors differ from the steady performance of a specific turbine.

In section 5.4, the sensors that are used in the unsteady mapping described in Chapter 3 will be modeled by adding a first-order filter with the reaction time provided by manufacturers to show how the unsteady mapping looks if the same sensors are used.

Section 5.5 will give the conclusion of this chapter.

5.2 The Unsteady Results Collected and 1D Dual-orifice Model

Using the unsteady experimental method described in Chapter 3, several unsteady cases using different pulse rig frequencies have been conducted and data collected.

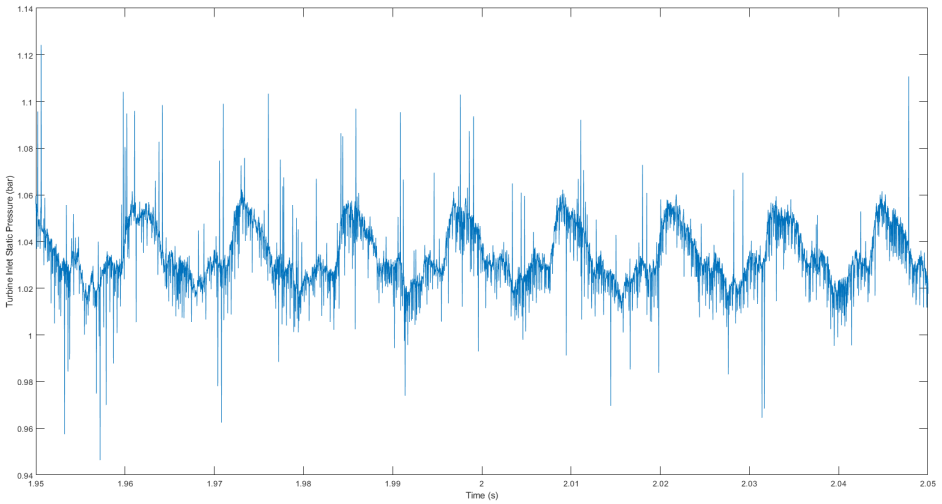

(a) Unsteady experimental results of inlet pressure

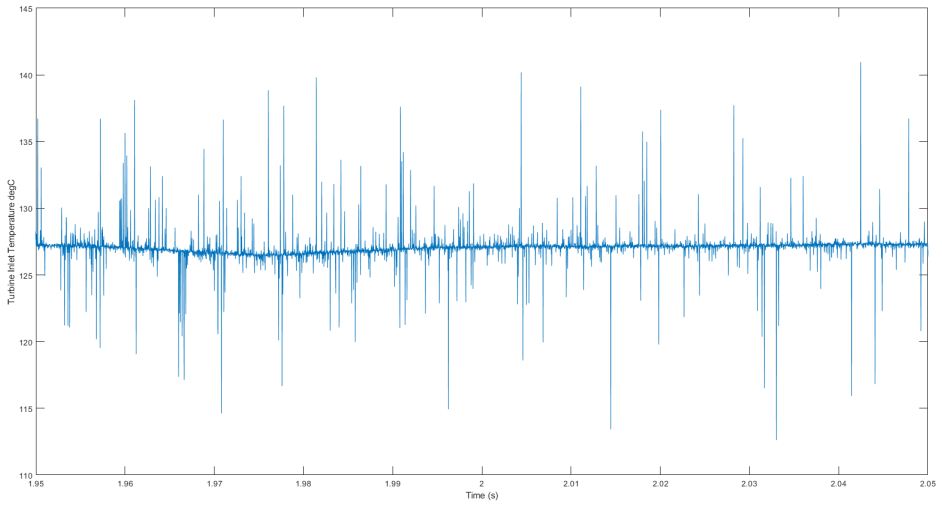

(b) Unsteady experimental results of inlet temperature

Figure 5-1: Unsteady results

What has been found as shown in Figure 5-1 is that although the fluctuations of pressure were able to be seen according to the results (Figure 5-1a shows that the data are able to reflect the pressure pulse), the temperature measured from the fast response thermocouple is far from satisfactory (figure 5-1b shows that there is noise seen in the data collected). Moreover, the hotwire probe described in the previous section could only work under the environmental temperature of 150 °C, which is much lower than the actual engine exhaust gas temperature. Even some cases of unsteady experiments were conducted under a cold environment of turbine inlet temperature below 150 °C, the particles which may come out from the pulse generator brought many failures of the probe deflects. Thus, a research question is raised: Is simulation possible to evaluate the feasibility of unsteady mapping? What models could be used?

There are many ways to use simulation as an evaluation method of the feasibility of unsteady mapping, which is aforementioned in Chapter 2.

A simple extrapolation method used for most 1D simulation software like GT and Ricardo Wave is used as a map, which assumes the turbine behaves under steady conditions, thus it would not cover the usage for the purpose of unsteady mapping because it is empirical extrapolation-based data collected under steady conditions.

A 3D computational fluid dynamic model is capable of predicting turbine performance under unsteady conditions, but it is time-consuming: a typical cycle may take several days to get the results, thus it is not a good idea for the purpose of this study, which is an evaluation at the initial stage. A model with a faster running time will be beneficial.

There are a lot of 1D models that are widely used to show the unsteady nature of turbines, as discussed in Chapter 2. Mean-line models have to validate against experimental data at the design point, and are not able to capture the spatial and temporal variations, thus are not suitable for the main purpose of this study. Another widely-used approach is the nozzle model, where the turbine is simulated as a series of nozzles

or pressure drop boundary and predicts the mass flow rate by estimating the effective area of this orifices(Winterbone, Nikpour and Alexander, 1990),(Payri, Benajes and Reyes, 1996). It is simple and effective, but may bring some limitations when solving radial turbine chocked flows. In the research of Deng (2017), the researchers improved this shortage by using a series of 1D pipes to consider the acoustic effects, which will be discussed in the following section.

For the reasons listed, this 1D dual-orifice model is selected as it is fast to run and has been validated with engine data.

5.2.1 The theory of the 1D dual-orifice model

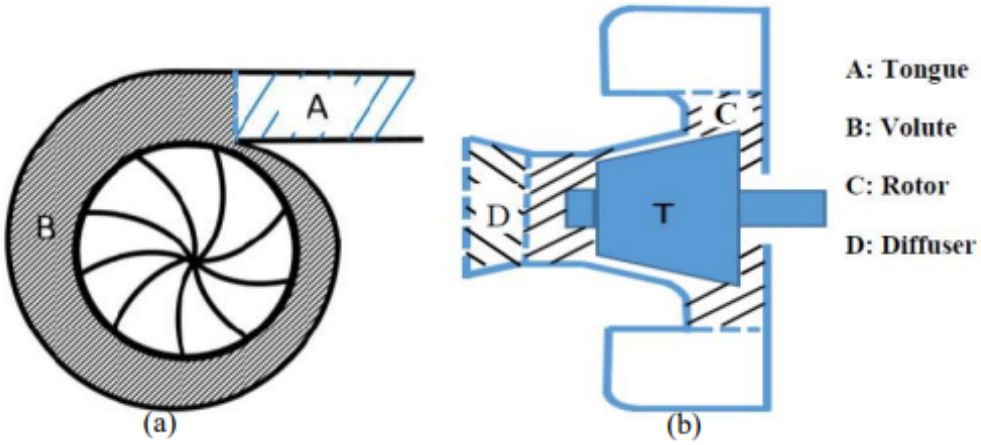

Figure 5-2: Schematic volumetric diagram of dual-orifice(Deng, 2017)

As shown in the schematic diagram in Figure 5-2, the dual-orifice model can be divided into four parts named: tongue (A), volute (B), rotor (C), and diffuser (D). The turbine tongue (A), volute (B), and diffuser (D) were described by one-dimensional pipes taking into consideration of their acoustic influences with the same volume as their respective 3D shapes (Deng, 2017).

In this model as shown in Figure 5-3, the turbine inlet tongue and diffuser were modeled by tapered pipes based on the real geometry of the pipes in the turbine. The turbine

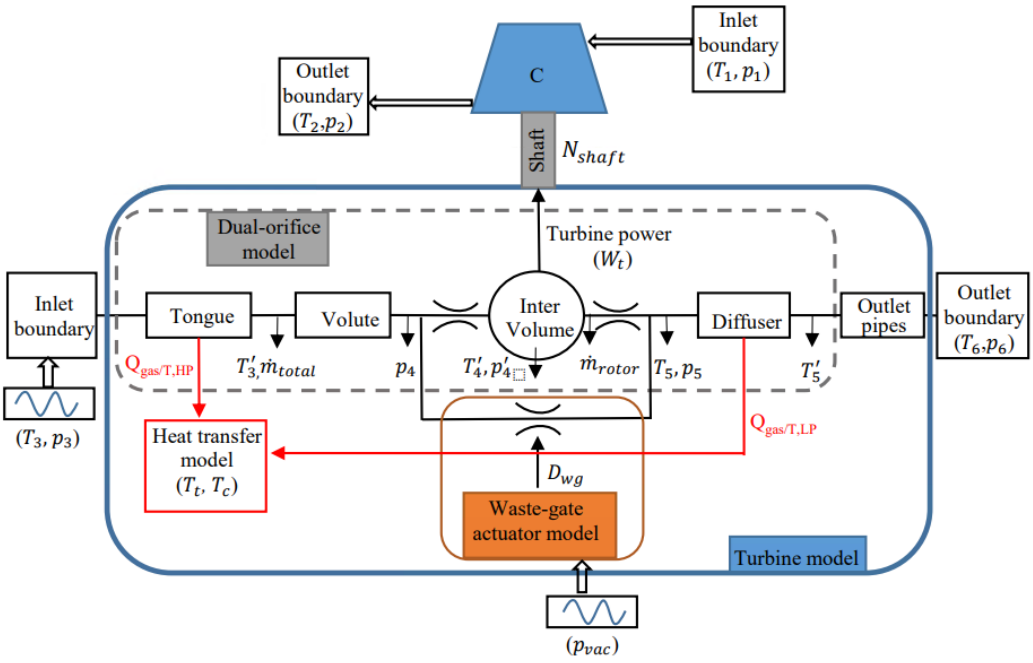

Figure 5-3: Overview of 1D dual-orifice turbine model(Deng, 2017)

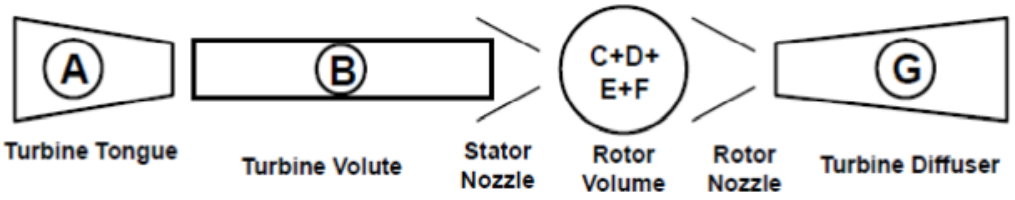

Figure 5-4: Turbine geometry to account for acoustics influences(Deng, 2017)

volute (section B) was simplified to be a straight pipe, with the same diameter of the outlet of the tongue and length with consideration of the volume criterion. The intermediate volume was modeled to be the same total volume as volume C shown in Figure 5-4. The effective area of stator and rotor orifices are built as a function of turbine speed and expansion ratio, which were derived and interpolated from the turbocharger characteristic maps. The extrapolation of the turbine map and the effective area maps of the stator and rotor were derived with the basis of the previous methods of (Payri, Benajes and Reyes, 1996), (Serrano et al., 2008) and (Deng, 2017).

The pressure variations were modeled to occur in the places of the turbine stator and the rotor due to the changing of effective area and the expansion work done by impellers respectively. Thus the stator and the rotor were modeled by two separate orifices: the effective areas were changed due to pressure variations, and the inter-volume between these two orifices is used to reproduce the filling and emptying behavior of the mass flow. Additionally, the pipes connecting the nozzles stand for the flow paths and produce the wave transmission through the turbine flow passage (Deng, 2017).

This model was validated by 44 operating points collected in the wastegate fully closed condition with steady inlet conditions of pressure from 1.3 bar to 3.5 bar and temperature from 600 K to 1000 K within the typical area of the turbine map, with the maximum error of mass flow of 4% and pressure ratio of 0.6% (Deng, 2017).

5.2.2 The advantage of 1D dual-orifice model

Using a nozzle to replace a turbine is widely used for modelling because it is simple and effective to reproduce the pressure variations and transmissions from turbine inlet to outlet, especially for medium-duty axial turbines (Deng, 2017). On the other hand, the single nozzle modelling method is faced with limitations when used for radial turbine choking conditions with higher expansion ratios (Payri, Benajes and Reyes, 1996). As aforementioned in Chapter 2, a two-nozzle model is built by (Payri, Benajes and Reyes, 1996) to predict choking conditions and reproduce the mass flow accumulation in turbine volute.

The dual-orifice turbine model used in this section is based on the model of Payri, Benajes and Reyes (1996) and Deng (2017):

- The turbine gas-dynamic model is based on the research of Payri, Benajes and Reyes (1996)
- The acoustic effects were accounted for by adding a series of 1D pipes (see Figure

5-5)

- This model was based on the real geometry of turbine volute and diffuser and has been validated by experimental data

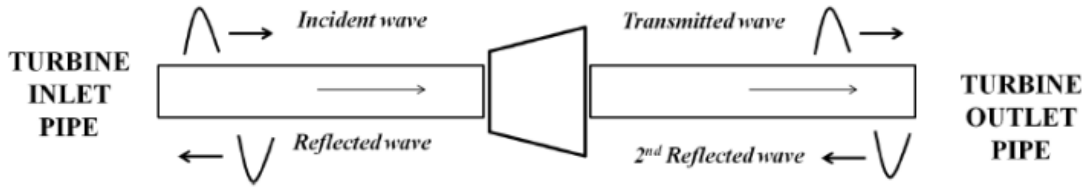

Figure 5-5: Turbine pressure component nomenclature(Deng, 2017)

Figure 5-5 shows how the pressure waves were decomposed at the turbine inlet and outlet, the incident wave and transmitted wave were defined as the forward transmit wave. The reflected wave and the second reflected wave were defined as the reflected waves. In this way, the forward and backward pressure waves are decomposed, and the turbine model would be excited by the incident pressure wave as well as the second reflected pressure wave.

This 1D model is used as the predicted apparatus for unsteady measurement in hot conditions, due to the cost and challenges of unsteady measurements on the hot gas stand. Before it could be used for predictions of sensors, the capability of this model is analyzed.

5.3 Turbine Performance Predication in Different Frequencies

In this section, steady conditions of one turbine operating point in the experiment was analyzed and compared with different unsteady pressure inlet data from 0 Hz to 90 Hz. This is the most common working conditions in reality for a turbine working with on-highway engines and also within the common range for pulse generator designed in

the University of Bath (Vijayakumar et al., 2019). For unsteady conditions, pressure is defined as a sinusoidal curve with the same average pressure as the steady condition.

The boundary conditions used in this section are listed in the table:

Case No.	No.1	No.2	No.3	No.4	No.5	No.6	No.7	No.8	No.9	No.10
Frequency Hz	0	2	12	25	35	50	65	75	85	90
Total Pressure	$P = 2.25 + 0.75sin(2\pi ft)$[bar], where f represents pulse frequency									
Ambient Pressure	1 bar									
Ambient Temperature	300 K									
Total Temperature	750 K									
Turbo Speed	160000 rpm									

In all of the cases shown in the table, the 2Hz case is considered to be quasi-steady condition. A sinusoidal wave of the pressure pulse is defined as the inlet condition for all of the cases with the same amplitude and main value as shown in Figure 5-6:

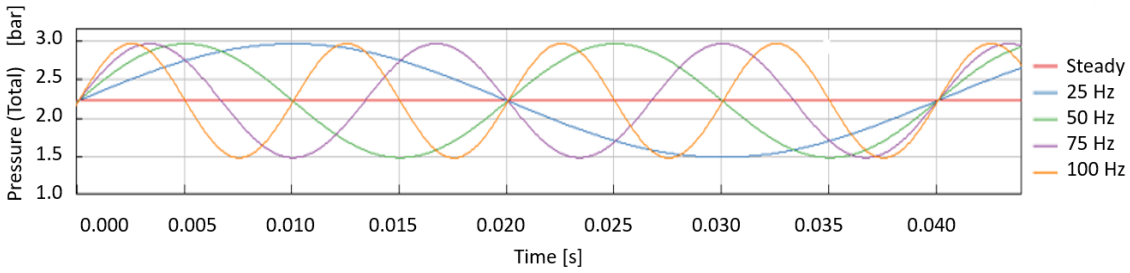

Figure 5-6: Inlet pressure defined in the dual-orifice model

Firstly, the turbine performances in different pulse frequency conditions are studied.

5.3.1 Turbine swallowing capacity analysis and the unsteadiness in different frequency cases

In a typical internal combustion engine with the turbine exposed to the exhaust gas from the engine, the inlet pulse of the turbine could be considered as the first five terms of a Fourier series. As a result, in general cases, the pulsating flow effect can be studied under harmonic inlet pulses as mentioned by Da Lio, Manente and Lazzaretto (2017). The expansion ratio versus mass flow rate for different frequency cases is shown in Figure 5-7.

Da Lio, Manente and Lazzaretto (2017) did a sensitivity study of the pulse frequency up to 50 Hz on the effect of unsteadiness of turbine performance, or in other words, the deviation between unsteady and steady performance as a hysteresis loop. Although similar results are seen in the results of the dual-orifice model used in this research as shown in Figure 5-7a, compared with higher frequency cases, low-frequency cases have a flatter hysteresis loop, indicating a lower unsteadiness. Steady data only shows a single running point while the quasi-steady of 2 Hz case shows a range of operating points in a mapping line.

On the other hand, for the cases with a higher frequency than 50 Hz, the variation of the characteristic loop tends to be flatter with a higher frequency up to 90 Hz, but with a higher range of expansion ratio variation. While in the research of Da Lio, Manente and Lazzaretto, the expansion ratio variation remains the same in all conditions. The reason for this may be because the turbine behaves very locally in time, or in other words, for the sharp wave front case and its instantaneous behaviors highly rely on the local temporal gradient of pressure waves, which was found in many researchers (Da Lio, Manente and Lazzaretto, 2017),(Cao et al., 2014). Thus the next step is to study the pressure effects in regard to the frequency in different parts of the model.

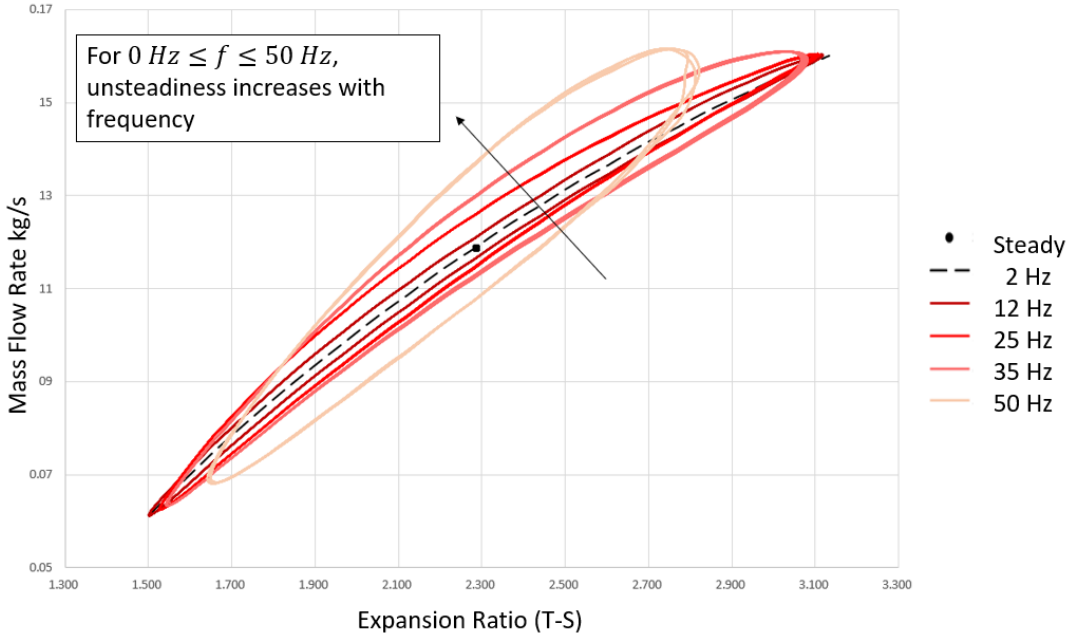

(a) Cases of frequency no more than 50 Hz

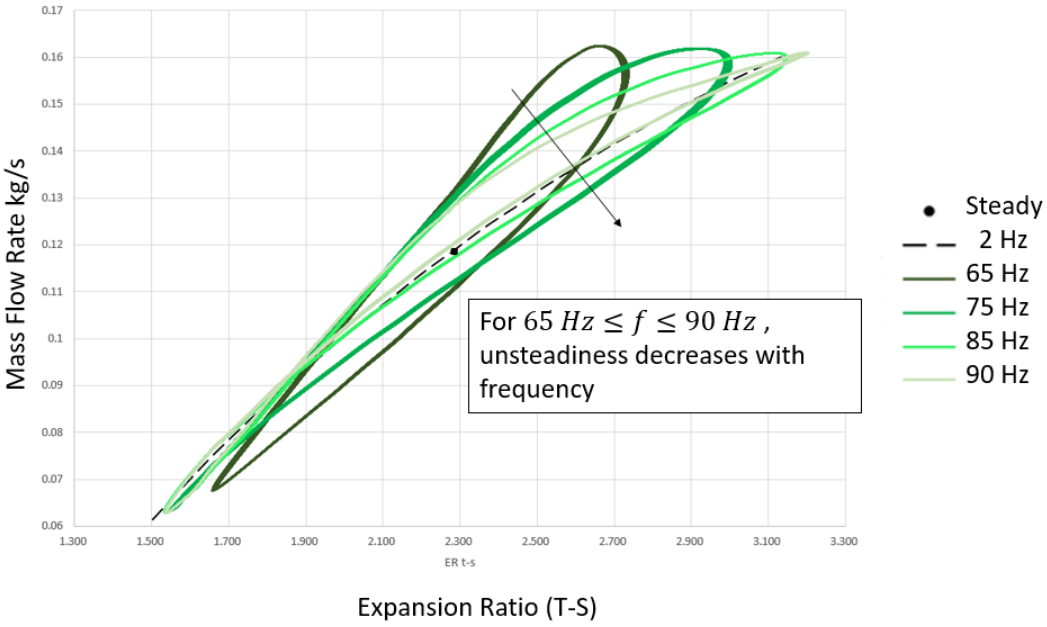

(b) Cases of frequency more than 50 Hz

Figure 5-7: Turbine swallowing capacity characteristics in different pulse frequency

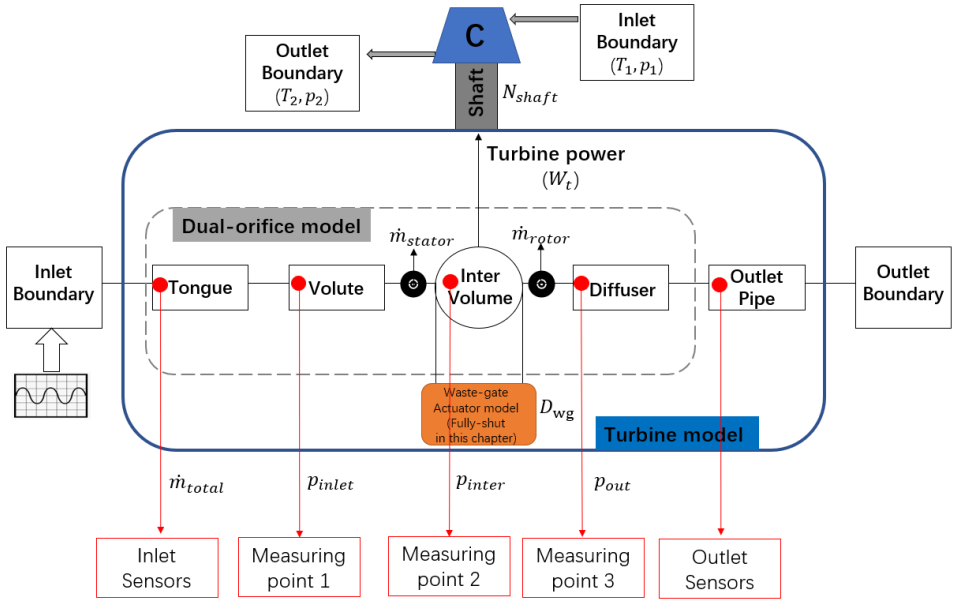

Figure 5-8: The layout and measurement points for the dual-orifice model

5.3.2 Results of turbine performance prediction-pressure and the degree of reaction

There is less than 1 % difference in the pressure variations modeled at inlet tongue volume, which refers to the position of the tongue in Figure 5-8.

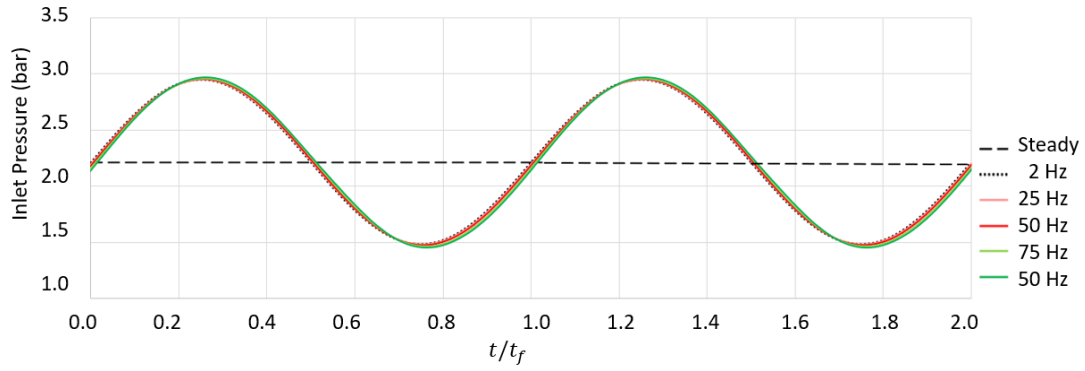

Figure 5-9: Static pressure variation at volute (Measuring point 1 in Figure 5-8)

in Figure 5-9, the y-axis shows how the static pressure changes at the measurement point 1 referring in Figure 5-8, the inlet volute pipe, while the x-axis uses t/t_{total} to

make it easier to visualize the amplitude in each frequency case. As pressure variation is measured in the position of the volute pipe, the case of 2 Hz is considered to be quasi-steady. With an increase of frequency, the fluctuation at the beginning of the first pulse increases, which is excluded in the plot for a clear comparison. In other words, the first five pulses of each case are ignored to get rid of the convergence time needed for the GT power calculation. According to the plots, the average value for a steady pulse of pressure is very similar in all frequency cases, indicating the model shows a good transition of pressure pulses from the boundary condition of the turbine to the volute pipe.

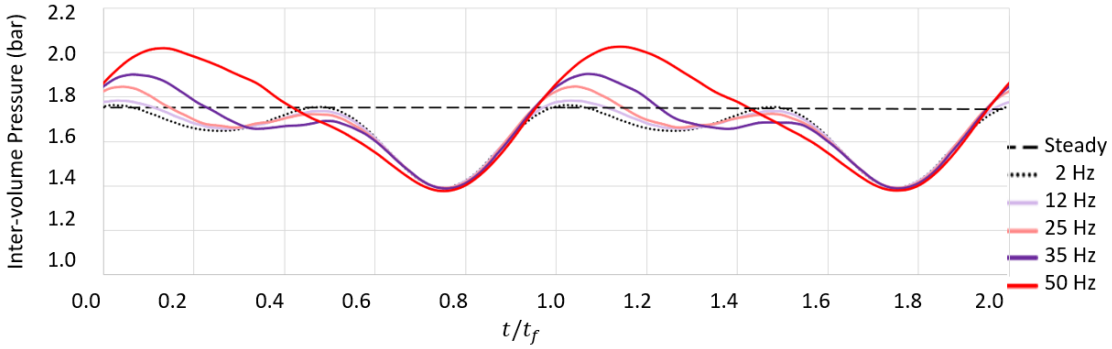

(a) Cases of frequency no more than 50 Hz

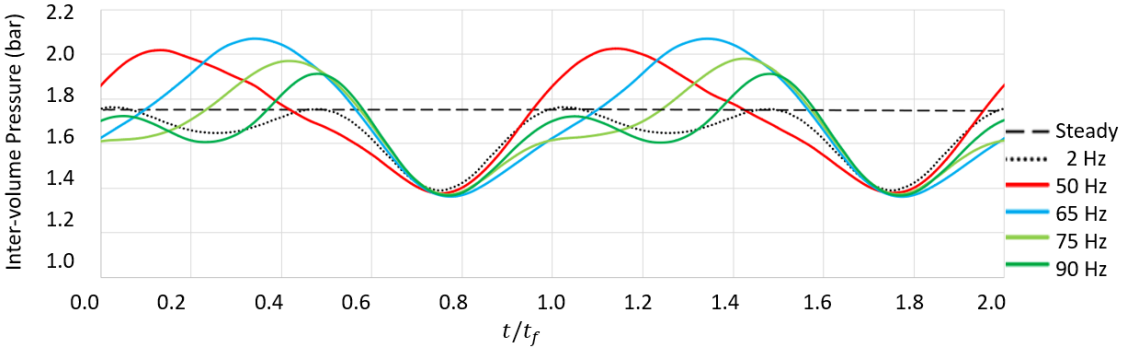

(b) Cases of frequency more than 50 Hz

Figure 5-10: Static pressure variation in the inter-volume between stator and rotor (Measuring point 2 in Figure 5-8)

As the measurement point changes from the volute to the rotor, the part that many

researchers believe produces most of the unsteadiness of the turbine, the pressure variation differs for different frequency cases. Figure 5-10 shows how static pressure varies in the inter-volume between the stator and rotor, referring to measurement point 2 in Figure 5-8. Similarly with inlet volute volume, in all cases from quasi-steady to 100 Hz, with the increase of frequency, it will take a longer time period for the flow to be steady thus the first four pulses are discounted from the plots.

When the static pressure value stabilized in the inter-volume, for the cases of frequency from quasi-steady (2 Hz) to 50 Hz, with the increase of frequency, the peak value of static pressure increased as a result. For the cases of 2 Hz, 12 Hz, 25 Hz and 35 Hz, there are two crests in one cycle of each case, indicating resonance of the flow occurs, while for the case of 50 Hz and 65 Hz, the pressure pulses have a sinusoidal shape.

On the other hand, for the cases of frequency higher than 65 Hz, as shown in b of Figure 5-10, with the increase of frequency in the cases of 75 Hz, 85 Hz, and 90 Hz, they also have two crests in a cycle, and the peak pressure value decreases with the increase of frequency in these cases. This trend could not be fully explained from the researcher's perspective, which indicates that further study of the natural frequency of the turbocharger is required, which will be discussed in the following sections.

As for the outlet pipe of measuring point 3 (referring to Figure 5-8) shown in Figure 5-11, a longer period of time will be taken in all cases to stabilize compared with the time taken in the inter-medium pipe. The trend of pressure pulse differs at different frequency ranges when frequency increases. For lower frequency cases of quasi-steady to 65 Hz, the peak static pressure of a stabilized period increases with the increase of frequency, while decreases for cases of frequency for 65 Hz to 90 Hz. This trend explains why the PR range in Figure 5-7 is different from different frequency cases.

The degree of reaction in all frequency cases is also studied as shown in Figure 5-12. The definition used for the degree of reaction is the proportion of the pressure expanded

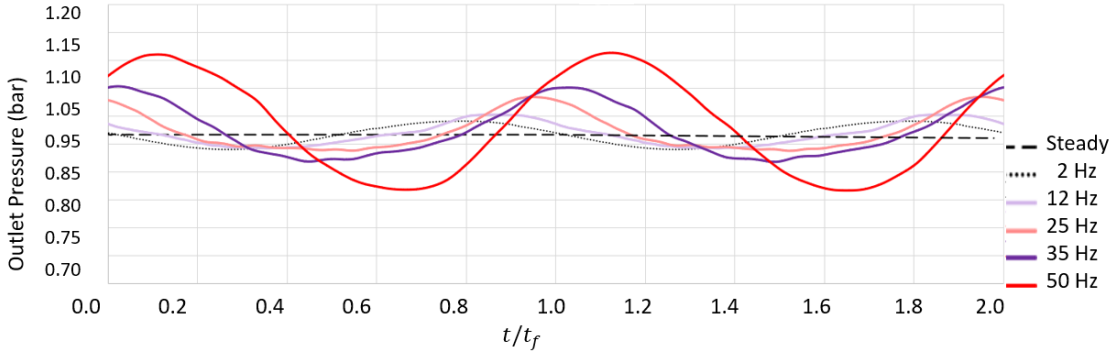

(a) Cases of frequency no more than 50 Hz

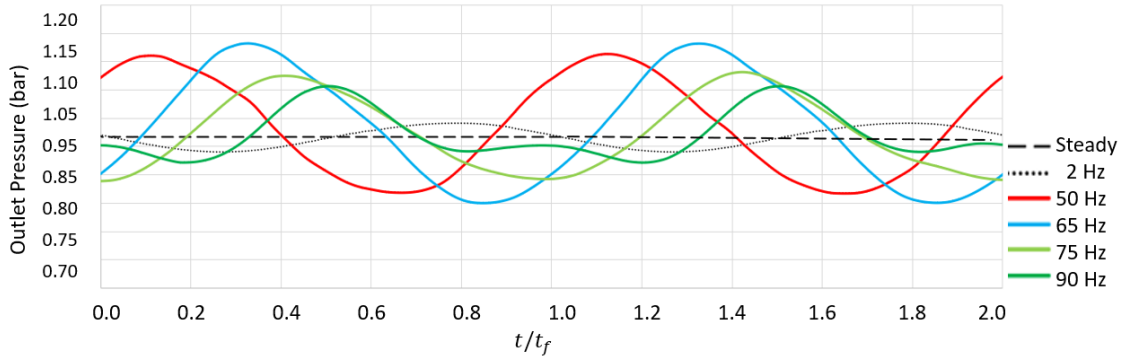

(b) Cases of frequency more than 50 Hz

Figure 5-11: Static pressure variation in outlet (Measuring point 3 in Figure 5-8)

in the stator to the pressure expanded across the whole turbine.

In all cases, a higher frequency will lead to a higher fluctuation time period for the degree of reaction to stabilize with a higher peak value. The first five pulses are excluded for a clear comparison. For cases of frequency less than 50 Hz, the higher the frequency is, the lower value of the degree of reaction is in the stabilized period of pulses, while for the cases of frequency from 65 Hz to 90 Hz, a higher frequency will lead to a higher peak of the degree of the reaction shown in the stabilized period of pulses. The turning point where the threshold frequency occurs for the changing in trend direction is about 65 Hz.

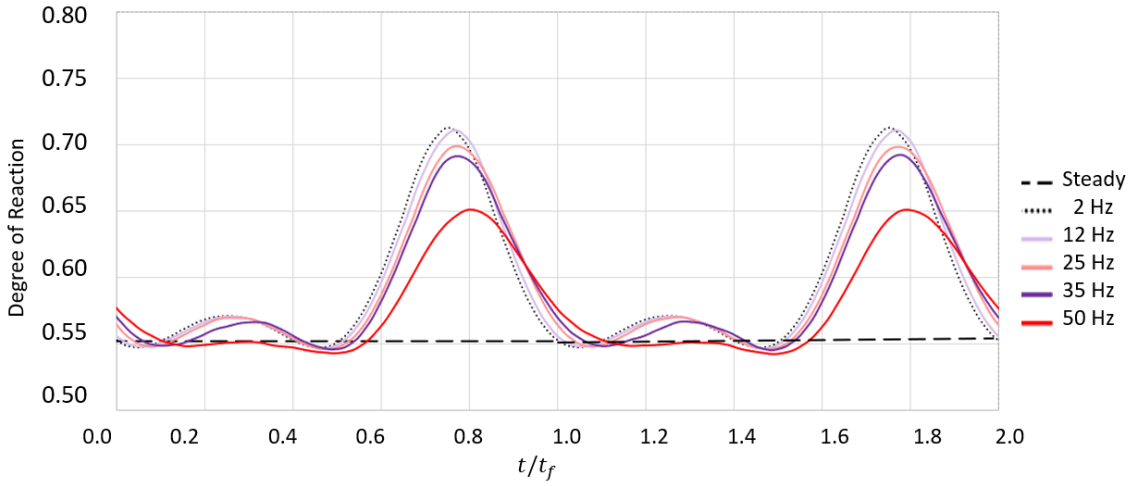

(a) Cases of frequency ¡ 50 Hz

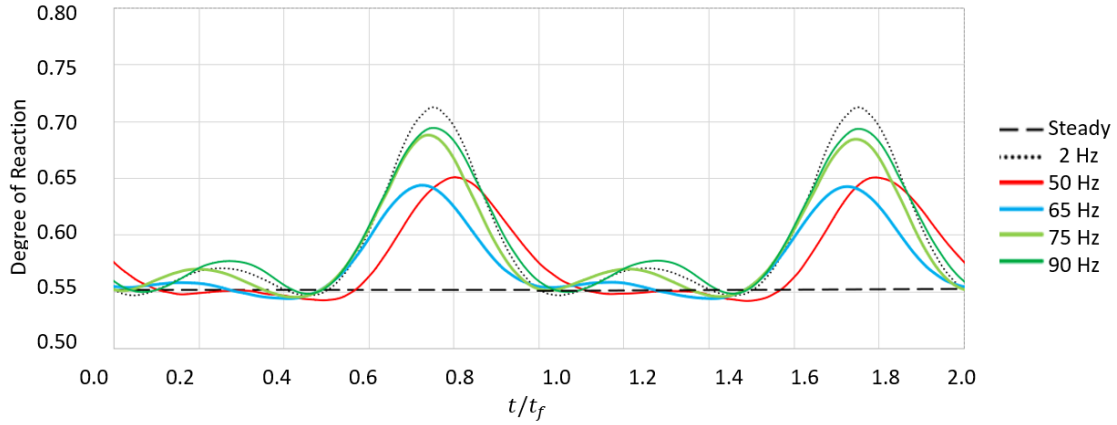

(b) Cases of frequency $\geq 50Hz$

Figure 5-12: Degree of reaction in all cases

5.3.3 Results of turbine performance prediction-pressure drop and mass flow rate

As for pressure drop variations in a different part of the model, Figure 5-13 shows how pressure drops when flow passes through the stator, similar to the trend shown in the pressure variation and the degree of reaction in the previous section. All of the cases show the same trend that a higher frequency will lead to a longer period of time for pressure drop value to stabilize. To be specific, the 50 Hz case takes about three pulses

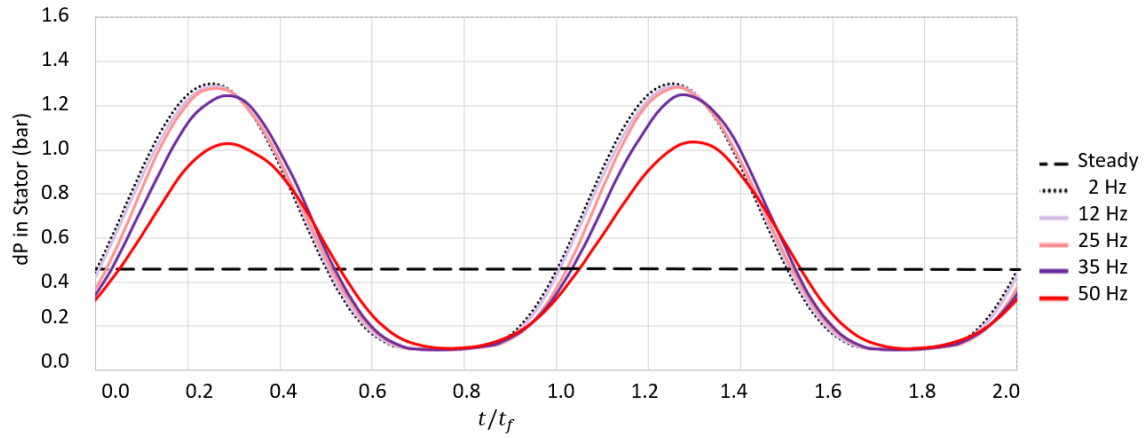

(a) Cases of frequency no more than 50 Hz

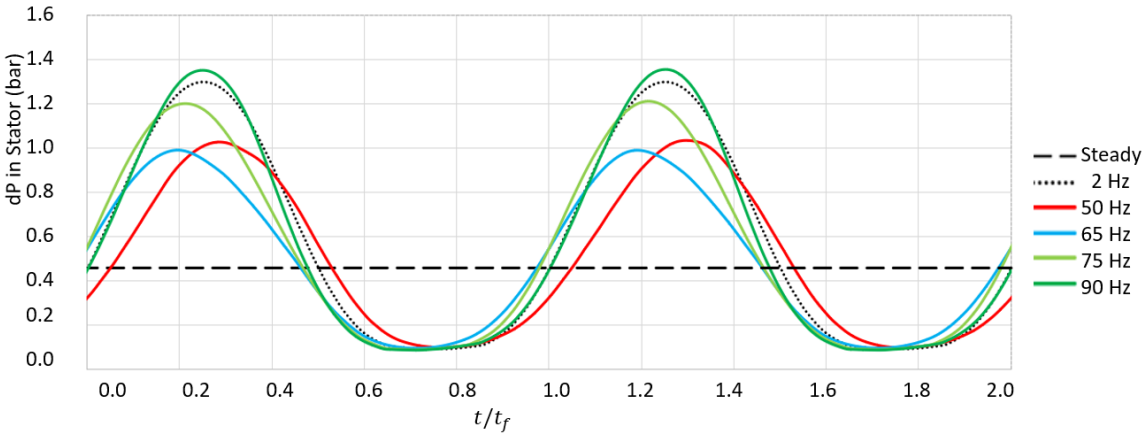

(b) Cases of frequency more than 50 Hz

Figure 5-13: Pressure drop in stator

to stabilize while for 90 Hz case, it takes more than five cycles of pulses until the peak value of pressure drop stabilized to about 1.4 bar, thus in Figure 5-13b, more period of time is shown compared with lower frequency cases. The turning of the trend direction happens at a frequency of about 65Hz as has been shown in the pressure variations and the degree of reaction.

For cases from steady (frequency = 0 Hz) to the case of frequency = 50 Hz, the pressure drop through the stator decreases with the increase of frequency, and for cases

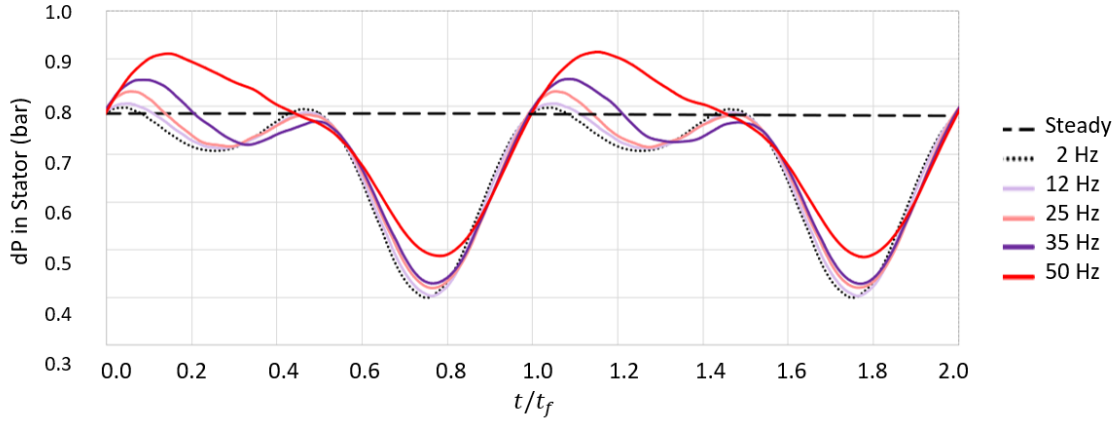

(a) Cases of frequency no more than 50 Hz

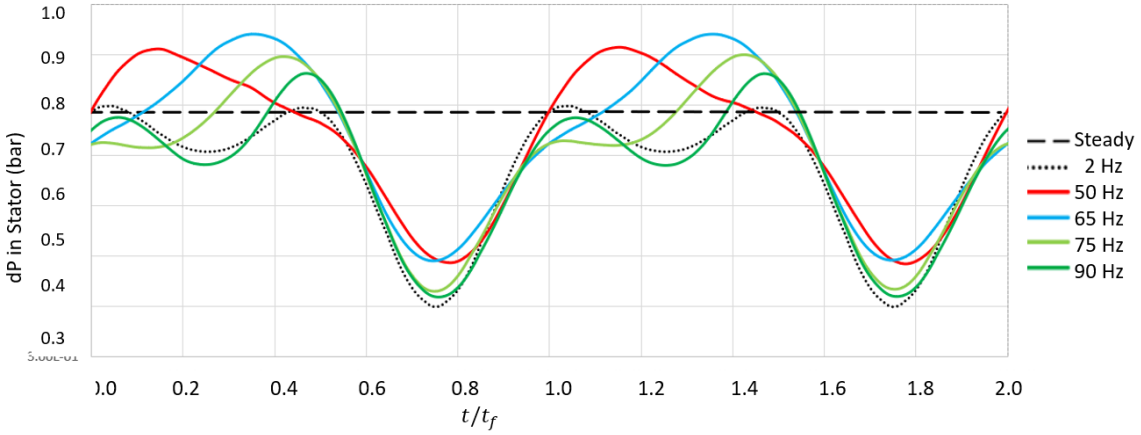

(b) Cases of frequency more than 50 Hz

Figure 5-14: Pressure drop in rotor

of frequency from 65 Hz to 90 Hz, the peak value in a stabilized pulse increase with the increase of frequency, which is expected according to the variations in inter-volume and the inlet pipe discussed in the previous section.

On the other hand, for the pressure drop through the rotor, as shown in Figure 5-14, a longer time period is taken for higher frequency cases. For cases of frequency from 0 Hz to 50 Hz, pressure drop increases as frequency increases, while for cases of 65 Hz to 90 Hz, it follows the opposite trend. For the cases of 2 Hz, 12 Hz, 25 Hz, 75 Hz, and 90 Hz, the variation of pressure drop shows a similar trend as in the pressure

variation in the inter-volume, that is, they all have two crests in a single pulse while for the case of 50 Hz and 65 Hz, where the highest stabilized peak value occurs, for a single variation pulse, it only has one crest. Similarly, in regards to the mass flow rate (MFR) variations as shown in Figure 5-15 and Figure 5-16, they follow the same trend as seen in the pressure difference (dP) in the stator in Figure 5-13.

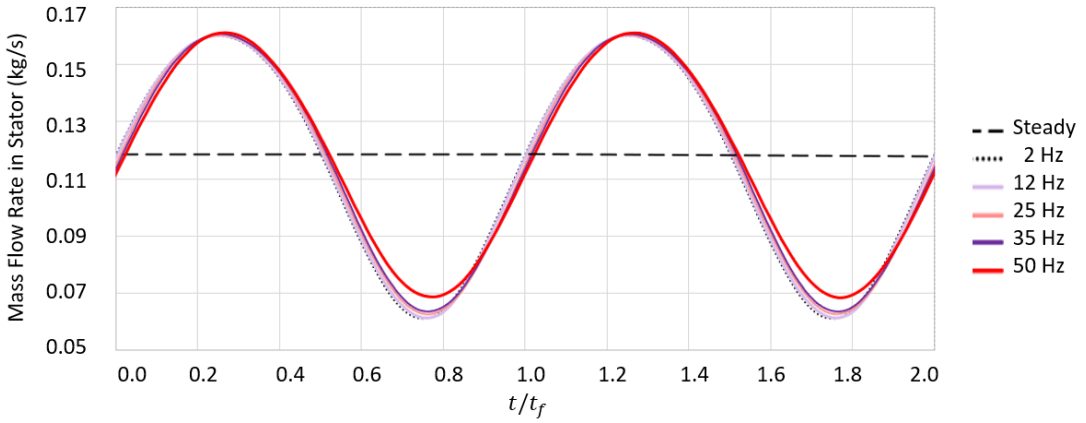

(a) Cases of frequency no more than 50 Hz

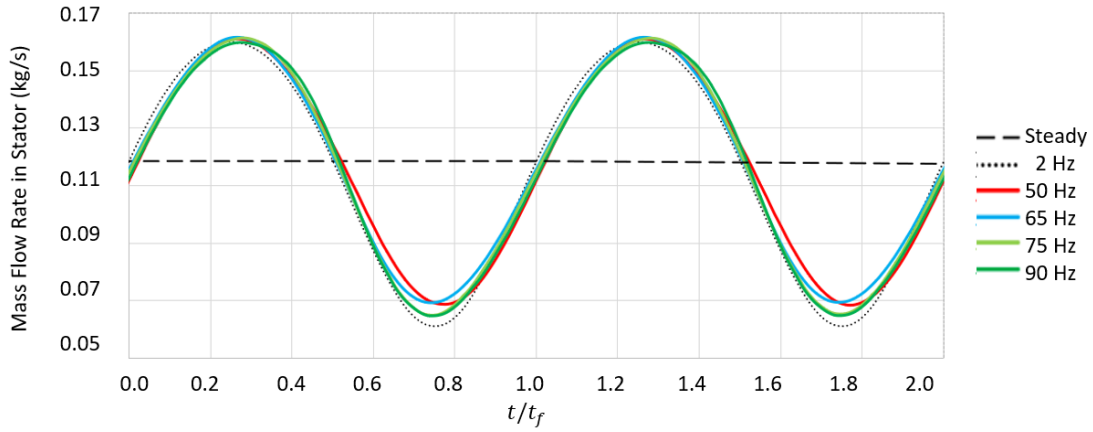

(b) Cases of frequency more than 50 Hz

Figure 5-15: Mass flow rate variation in stator

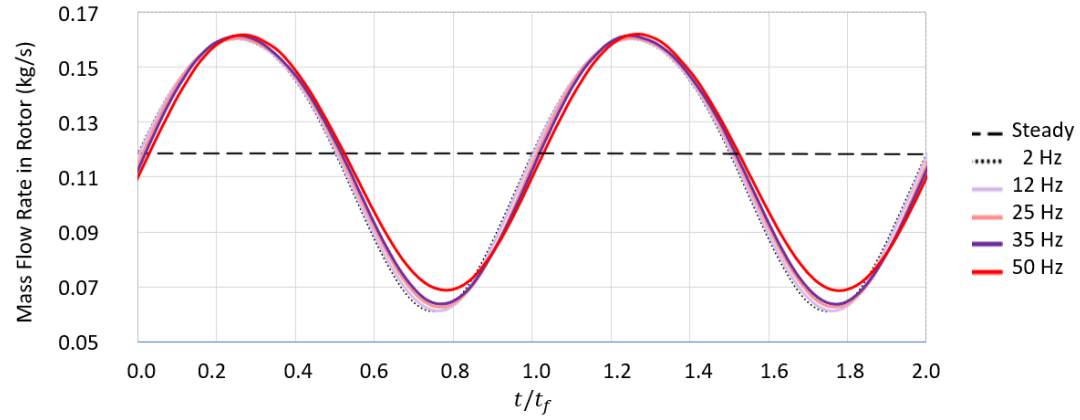

(a) Cases of frequency no more than 50 Hz

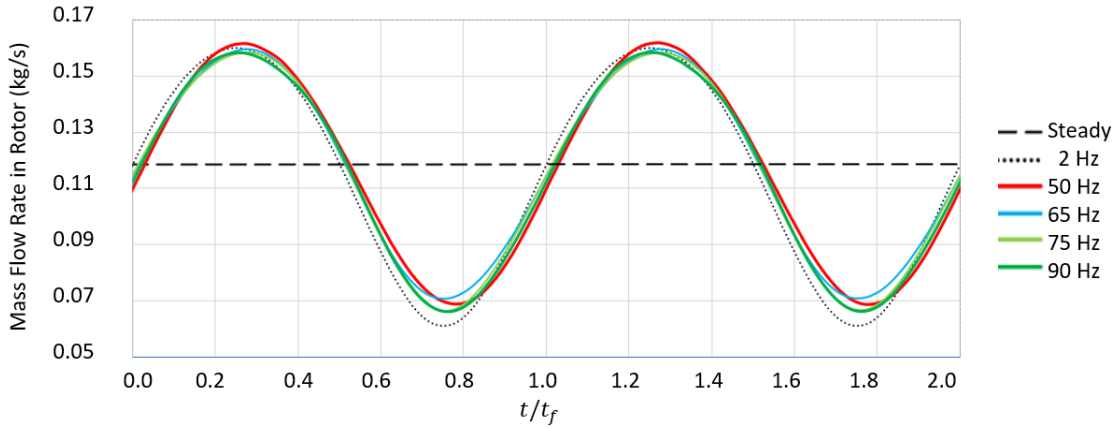

(b) Cases of frequency more than 50 Hz

Figure 5-16: Mass flow rate variation in rotor

5.3.4 Pipe diameter analysis in the inter-volume

Due to the trends that have been discussed in the previous section, another research question has been raised: is the frequency where the peak pressure in the inter-volume and the lowest frequency of reaction occuring because of the natural frequency of the turbine itself? Thus a sensitivity study of the diameter of the inter-volume of the pipe has been conducted in this section. In other words, different turbine geometrical parameters are used in this model to see the relation of the turning point in pressure and mass flow variations.

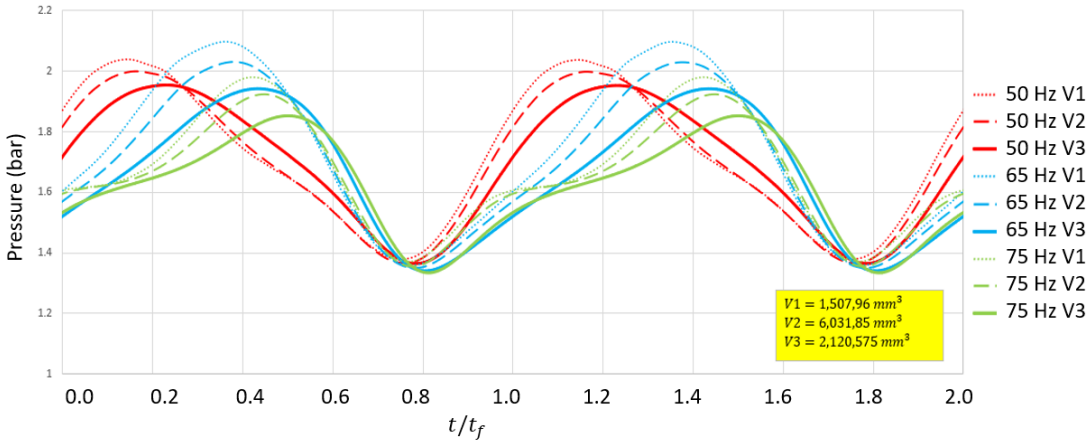

Figure 5-17: Inter-volume diameter versus static pressure variations

Figure 5-17 shows the variations of static pressure in the inter-volume pipe in Figure 5-10. The three lines (dot lines, dashed lines and solid lines) represents three different inter-volume pipe diameter from small to large respectively. The volume here is set to be extremely big to shown the turbine geometry affects the results.

By varying the diameter of the inter-volume pipe, these three sets of diameter cases represent three different turbines. Three pressure pulses frequencies set at the boundary conditions of 50 Hz, 65 Hz, and 75 Hz are compared. What can be seen is that for a diameter of smallest case of dashed lines, which is 80 mm (V1), the stabilized peak value of pressure occurs in the case of a frequency of 65 Hz while the peak case occurs in the frequency of 50 Hz in the group of the largest diameter equals 300 mm (solid lines). This leads to the conclusion that the turning points that have been discussed in the previous section are related to different turbines' natural frequencies, and will result in a different value of unsteadiness. This result agrees with much of the literature on the unsteadiness criterion used in pulsating flows. The pulse frequency is not the only factor to determine the unsteadiness, the natural frequency of the turbine also needs to be taken into consideration.

Additionally, another finding from Figure 5-17 is that with a higher value of inter-

volume diameter, which results in a bigger turbine, the pressure pulse at the inlet with the same frequency will lead to a lower peak value of variation. In other words, a bigger turbine will show less pressure variation with the same pressure pulse at the inlet.

Therefore, the conclusions of this section are listed as follows:

- This test data-validated dual-orifice model is able to show the behavior of the turbine under unsteady conditions.
- According to the simulation results, there is a difference between the turbine's unsteady and quasi-steady behavior in regard to pressure and mass flow rate variations of a frequency of more than 12 Hz, while for cases of frequency under 12 Hz, the performance of the turbine is quite similar with quasi-steady (2 Hz).
- According to the simulation, the unsteadiness is related to the natural frequency of a specific turbine. For the inter-volume of 150796 mm^3 case, the threshold frequency where the direction for the trend of pressure, mass flow rate and other parameters variations changes is about 65 Hz while for the inter-volume of 2120575 mm^3. The turning point of the frequency is about 50 Hz, which means it varies from the inter-volume. This is an important factor that needs to pay attention to consider the unsteadiness.

The model has demonstrated that there is a difference between steady performance and unsteady performance in high-frequency cases as the hysteresis loops shown in unsteady cases. The next question is can this be observed when real sensors are used.

5.4 Sensors Study

In this section, the sensors that have been described in Chapter 3 are also modeled in this dual-orifice model to show what results will be seen when data collected from a pulse rig by using those sensors and why the data collected before were not good enough to show the unsteady behavior of the turbine.

In this section, the pressure sensors, thermocouples, as well as flow sensors used in the experiment are compared in their capability of measuring unsteady data up to 100 Hz.

5.4.1 Pressure sensors

The pressure sensors that are used in the gas stand are Omega pressure sensors which have 0.1s of response time and Kistler pressure sensors of 0.000001s of response time. All of the response time data is from the manufacturer's websites.

Figure 5-18 shows according to the simulation, how these two sets of pressure sensors react. The black dashed line represents the slow measurements used in the gas stand for a steady mapping experiment, which is the Omega pressure sensors, and the green line represents the fast Kistler pressures reaction of 100 Hz sinusoidal inlet pressure as the boundary condition. The reaction of the fast sensors is within a 5% difference from the real reaction from the simulation results, thus, in conclusion, the fast set of pressure sensors is good enough for unsteady measurement up to 100 Hz of the pulse. While the slow pressure sensors are not able to measure the fluctuations of the pulse and it will take about 0.4 s to reach the steady value, which is the same as the mean value of the pressure pulse according to the simulation.

5.4.2 Thermocouples

The thermocouples that are used in the gas stand are standard K-type thermocouples of 1.1 s reaction time, and ultra-fine K-type thermocouples of 0.25s reaction time. As the Figure 5-19 shows, neither slow nor fast sensors are able to reflect the real variation of the inlet total temperature due to the fact that the reaction time for both of these sensors is not fast enough. It takes about 0.4 s for the fast response thermocouple to reach the mean value of the temperature in reality in a pulse and for the slow sensors, it takes more than 2 s.

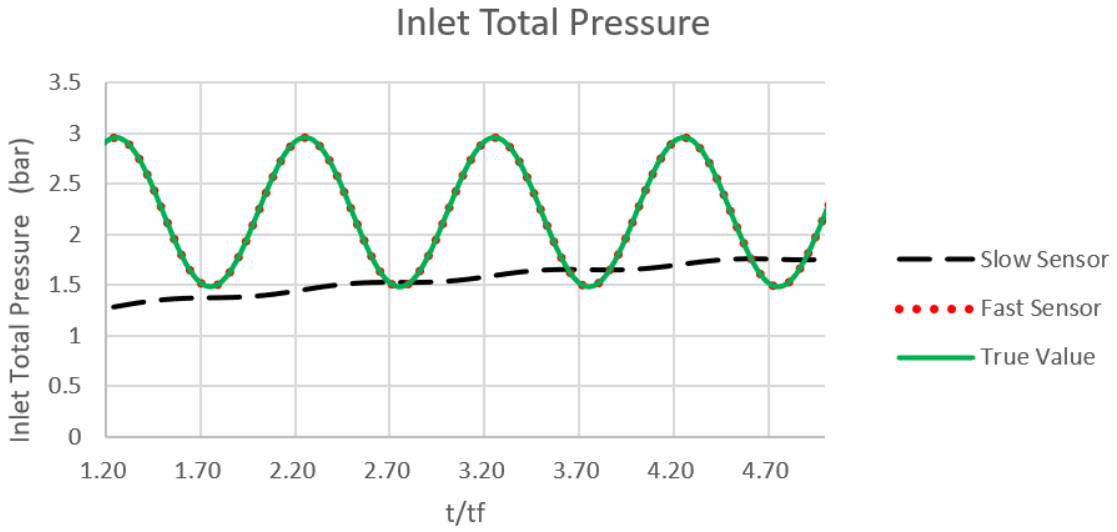

(a) Inlet pressure measurements in different sensors

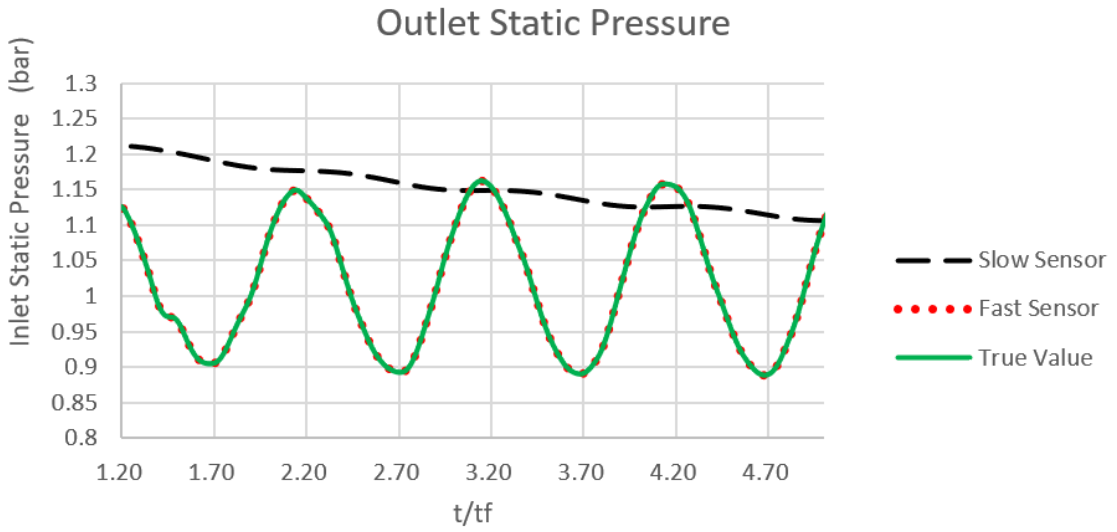

(b) Outlet pressure measurements in different sensors

Figure 5-18: Inlet and outlet pressure measurement by different sensors

5.4.3 Flow sensors

The flow sensor used in the gas stand is an ABB flow sensor which has a reaction time of 0.025s and hotwire probe of 0.000007s reaction time. According to the simulation results shown in Figure 5-20, there is no obvious difference between the real results

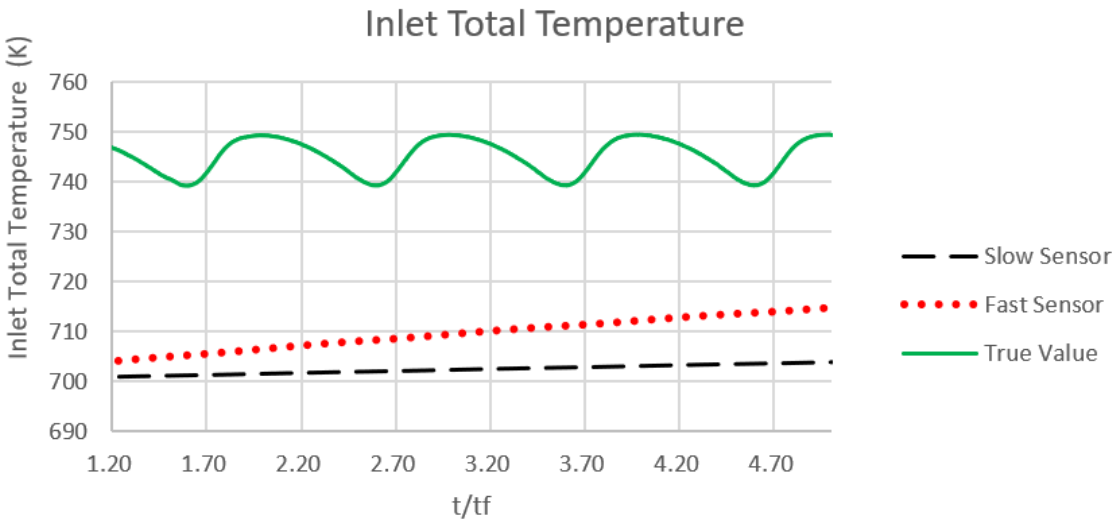

(a) Inlet temperature measurements in different sensors

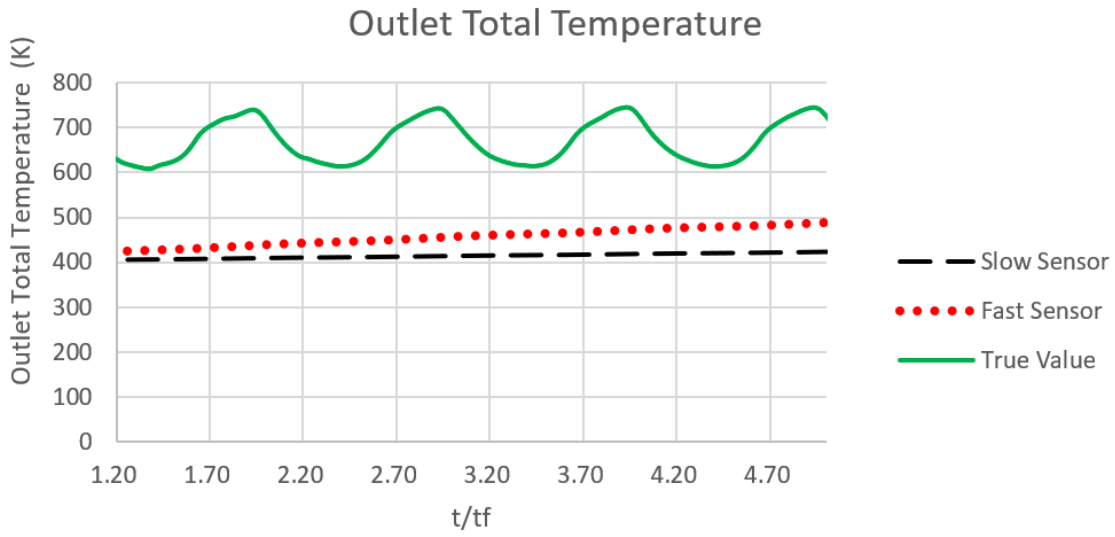

(b) Outlet temperature measurements in different sensors

Figure 5-19: Inlet and outlet temperature measurement by different sensors

and the measurement from the fast response hotwire sensors. What should be noted is that the capability of hotwire probe measurement temperature is below 150 °C, which is much lower than the real temperature of a hot engine exhaust. As for the slow ABB flow sensor, it will take about 0.15 s to reach the mean value of the mass flow rate of a pulse.

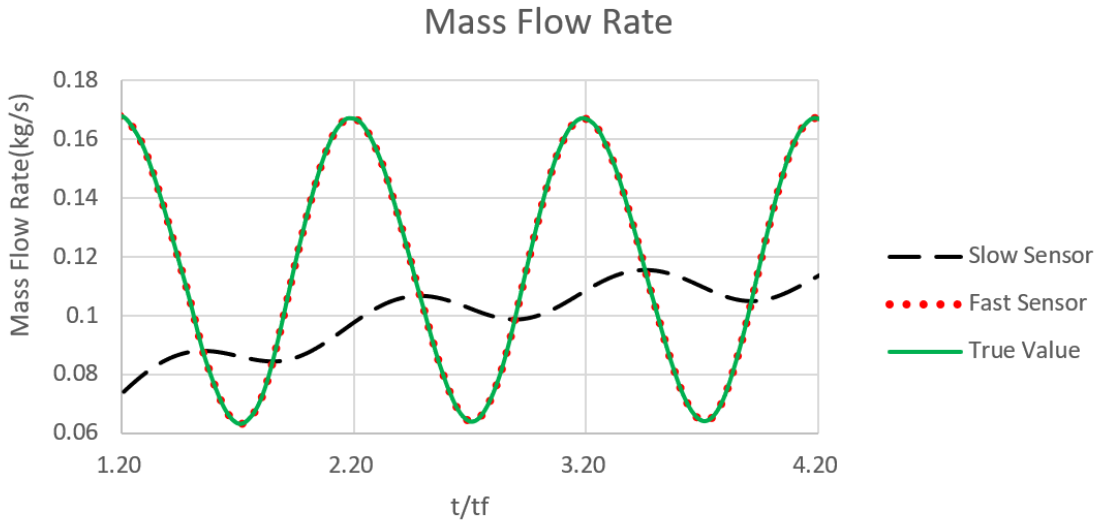

Figure 5-20: Mass flow rate measurements

5.4.4 Turbine characteristics used - ER and MFP comparison

As a consequence of the simulation results of the pressure sensors aforementioned, the expansion ratio value calculated by the inlet and outlet pressure shows little difference from the real results by using the fast pressure sensors as shown in Figure 5-21. Additionally, the slow set of pressure measurements will need more than 0.3 seconds to reach the mean value.

As for the mass flow parameter, because there is no accurate measurement for the temperature, Figure 5-22 shows that the measurement value from a fast set of sensors will be slightly lower than the real value.

Additionally, the stage efficiencies are also plotted in Figure 5-23 in the condition of using fast sensors and the real simulation results. There is an overestimate of cycle-average efficiency of 15% and the peak efficiency of 11.3%.

In conclusion, none of the slow sets of sensors could measure turbine characteristics under pulsating flow conditions according to the simulation results. Fast pressure sensors are able to reflect the real variation of pulse flow at 100 Hz. As for the flow

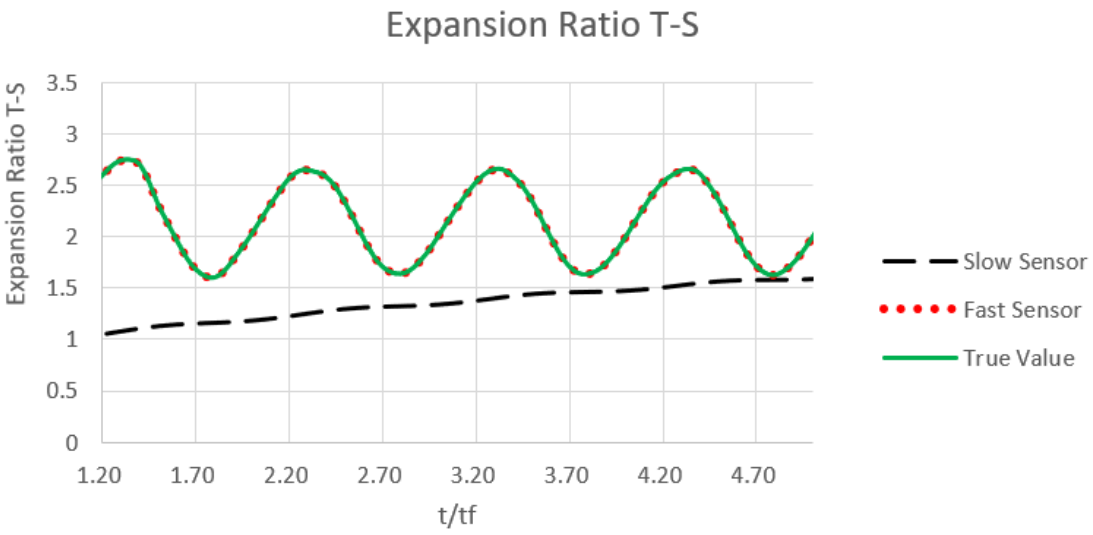

Figure 5-21: Expansion ratio based on the measurement in different sensors

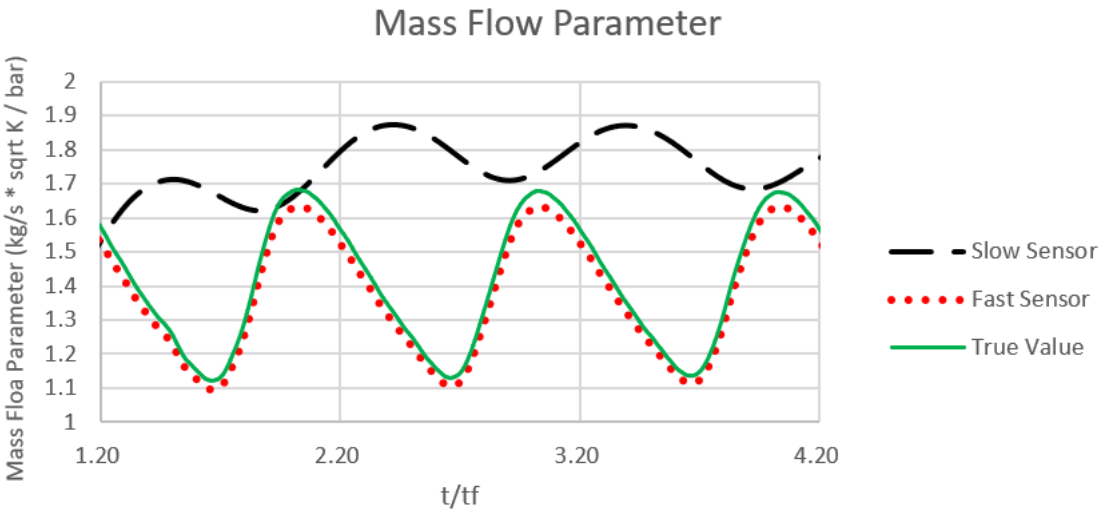

Figure 5-22: Mass flow parameter based on the measurements in different sensors

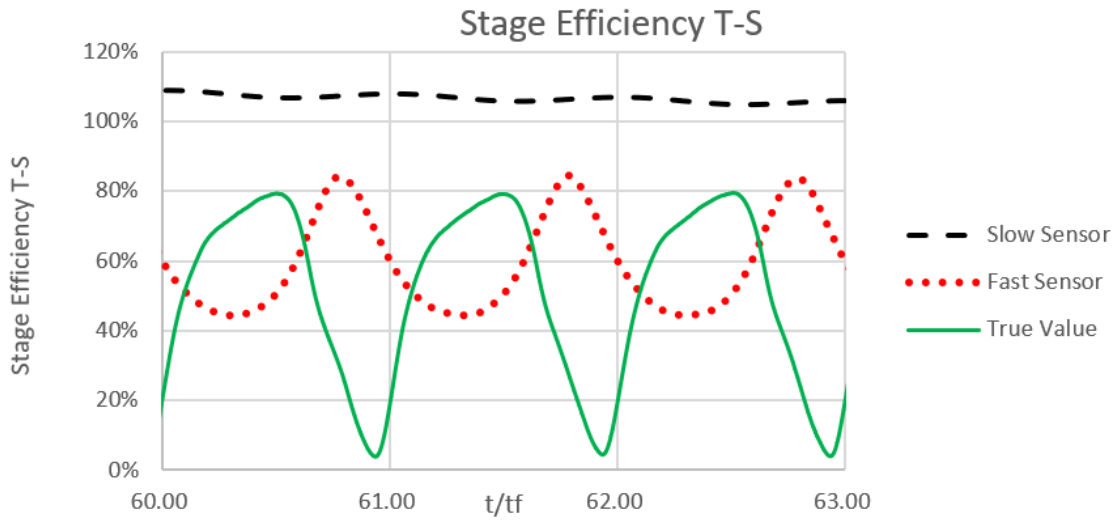

Figure 5-23: Stage efficiency

sensor, although according to the results, the hotwire can reflect the real variation, the temperature limitation of the hotwire is a key factor that needs to be taken into consideration for future tests.

As a result, the expansion ratio variation under pulsating flows could be accurately measured and calculated by the fast pressure sensors, and the mass flow parameter might be slightly lower if using the sensor results compared with the real values according to the simulation.

5.5 Conclusion of the Chapter

In this chapter, a dual-orifice model is used as a prediction of the unsteady performance of a turbine. There are mainly three questions that have been answered in this chapter as aforementioned in the first section:

- What types of models are able to predict unsteady behavior and of these models which one(s) are best for assessing the feasibility of unsteady mapping?

  This question is related to the literature review in Chapter 2 where different types

of turbine models are compared and discussed. A dual-orifice mode was used in the analysis of this chapter due to the fact that it is fast and easy to run, and it has been validated by an experimental test of 44 points with reference to the literature. A feasibility check was also discussed in the second section of this chapter.

- How is unsteady behavior different from steady flow behavior in a mapping context?

  This question was analyzed in the third section of this chapter by setting a range of inlet pressure frequency from 0 Hz to 90 Hz as the boundary condition of the dual-orifice model. By studying the performance of the model, it was shown that the dual-orifice model can show the unsteady nature of a specific turbine under pulsating conditions. The variations of pressure, mass flow rate, degree of reaction are not only influenced by pulse frequency but also a factor of turbine's specific geometrical parameters.

- What will be seen in reality by using the sensors under an unsteady pulse rig by studying the simulation results?

  This question was analyzed by using the first-order filter as a time response node, by feeding into the reaction time provided from the manufacturer's data. Two sets (slow and fast) of sensors including pressure sensors, thermocouples, and flow sensors are compared. Then a conclusion was given that the fast response pressure sensor is good enough to predict how the unsteady behaviors of the turbine even though fast flow sensors. The hotwire probes can show how unsteady turbine mass flow rate variation looks like under pulse conditions. The temperature limit according to the manufacturers should also be taken into consideration. On the other hand, none of the thermocouples can reflect the unsteady nature of inlet temperature variations leading to a 3% difference in the mass flow param-

eter prediction and an overestimate of cycle-average efficiency of 15% and peak efficiency of 11.3%.

Chapter 6

CFD Mapping for a Radial Turbine

6.1 Outline of the Chapter

In this chapter, the research question 'Can CFD models be used to map a turbine?' is discussed. The background for the reason why turbines need to be mapped correctly and accurately is discussed in section 1 and also as aforementioned in Section 5.4 for the difficulties of measuring turbine inlet and outlet temperature by using current sensors. Then steady data in both standard operation and close-loop operation collected by using the methodology illustrated in Chapter 3 are discussed. The CFD model is built and compared with the steady mapping data.

The differences between the CFD results and experimental data are discussed and a mechanical loss model is built based on the experimental data. As a result, a coupled model is built which is able to give a better prediction for turbine characteristics.

In order to answer the research question of this Chapter, the following three steps arise:

- How accurate are the data collected by using conventional experimental methods

described in Chapter 2 for a specific radial turbine? This question is essential as the experimental data will give boundary conditions for the CFD model that will be discussed in the following sections. Then arises the second step.

- What are the differences between the CFD model results and the experimental data and what are the reasons for the differences? This question is essential to understand where the differences come from then the next step will be how to reduce them.

- How to minimize the difference between CFD results and experimental data? The approaches to decrease the differences between CFD and experimental results are discussed so that CFD can be used as a better tool to predict the turbine map.

Section 6.2 will introduce the background for the usage of turbine mapping and why it is important to get precise and reliable results.

In section 6.3, the steady mapping results collected by using the experimental methodology described in Chapter 3 will be discussed. In this section, both the results of standard steady mapping and the closed-loop mapping results will be stated and analyzed.

Section 6.4 will compare the simulation results based on the numerical methodology described in Chapter 4 for a simplified CFD model with the experimental data collected, and also attributes the reasons for the differences between them.

In section 6.5, a mechanical loss model with the aim to improve the matching between experimental data and CFD results will be built and discussed. This section was published as a conference paper in Wang, Burke and Copeland (2020).

Section 6.6 will give the conclusion of this chapter.

6.2 Background for the Usage of Turbine Mapping

The purpose of utilizing a 1D engine model as aforementioned in Chapter 2 is to predict engine performance in a wide range of working conditions. However, 1D engine simulation models commonly use a look-up table of turbochargers where a limited range of data is often collected under steady conditions and extrapolated by empirical relations.

Turbine maps are widely used in a turbine model to predict engine performance. A typical way to generate a turbine map is to use the compressor as the loading device and connect it to a turbine. By varying the compressor load, the turbine's operating points will be collected at the same time. On the other hand, compressors' operating points will be limited by the surge and the choked conditions, thus only a small range of turbine performance data will be collected by experiments. This limited range of data, once input into 1D simulation software, will then be extrapolated by empirical relations. This extrapolation method may bring some errors in the results, especially for the off-design points, thus the main aim of this chapter is to estabilish the feasibility of using CFD as a method to predict mapping data.

To answer this question, the experimental data and the simulation results are compared with the uncertainties.

6.3 Steady Mapping Results

6.3.1 Steady results and analysis

As aforementioned in Chapter 3, in this research, a turbocharger comes from a 1.5 L engine and is used to conduct steady mapping in the hot gas stand at the University of

Bath. This mixed flow single entry vane-less turbine is coupled with a compressor as a loading unit, and by changing the feeding turbine inlet mass flow rate and compressor back pressure, different operating points for the compressor from choked to surge are captured thus turbine is mapped at the same time. By using the methodology illustrated in Chapter 3, the results collected in the gas stand at the University of Bath of the steady mapping are shown in Figure 6-1. The figure is based on rothalpy thus lines do not overlap. The measurement starts from the compressor's high mass flow condition where the increase of the air feeding leads to a similar compressor inlet mass flow rate. The mild surge condition is determined by the fluctuation of compressor back pressure and noise shown by using a fast response pressure sensor. The turbine is connected to a compressor. For a specific speed line, the compressor mass flow rate is controlled to be maximum by fully opening the back-pressure valve. In other words, the compressor side is controlled to be at the choked point. By adjusting the back-pressure valve position, 10 operating points are measured from the choked to the surge positions. For the turbine side, the data are taken instantaneously. The results are collected and then compared with the manufacturer's data within a 1% difference at the turbine side (not shown due to manufacturer confidentiality). The data collected are shown in Figure 6-1.

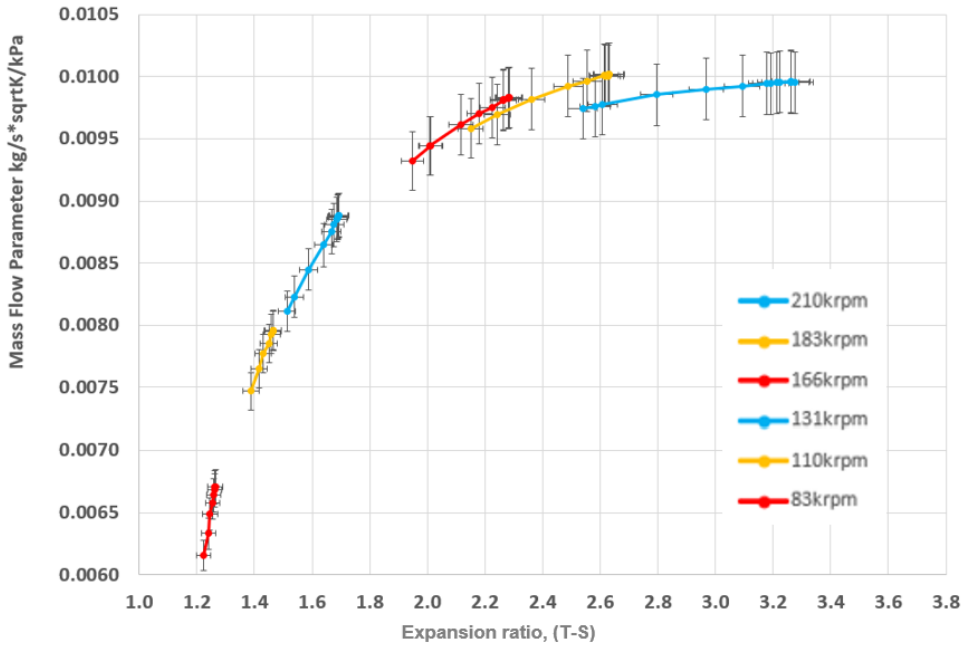

(a) Steady turbine mapping flow characteristics

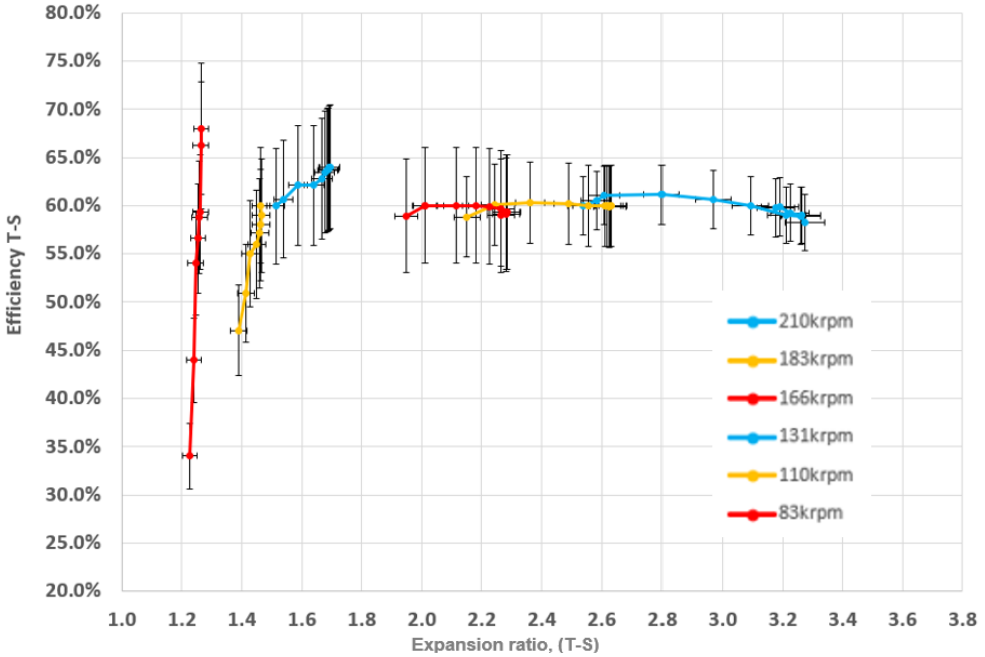

(b) Steady turbine mapping efficiency

Figure 6-1: Turbocharger turbine mapping results

6.3.2 Closed loop mapping

The compressor works as a loading facility in the turbine mapping process and because of its choked and surge conditions, only a small range of turbine data can be mapped. Closed loop mapping is considered to be an effective way to extend the range of turbine data, in which the compressor inlet and outlet are connected together by an intercooler system. The compressor inlet pipe is coupled with a pressured or vacuum pipe to obtain a higher or a lower inlet pressure so that for turbine side, the data are extended as a consequence. In order to extend the range of the mapping and have a wider range of data, a so-called closed-loop mapping method is used.

Figure 6-2b shows the results of a closed loop mapping. This experiment is conducted to give an extended set of data compared with the steady method as a baseline for the new mapping method. As aforementioned in Chapter 3, by adding an extra pressured value or a vacuum value at the compressor inlet, the extended range of the turbine map is able to be measured. This complexity of the device is not needed if a CFD model is used as a mapping method because it can be easily done by changing the boundary conditions. An uncertainty analysis was also conducted in the closed loop experiment, and for clarity, it is not included in Figure 6-2b where the extended operating points of the turbine are shown in dashed lines.

6.3.3 Uncertainty of performance parameters

Having presented in the plots the experimental results of standard steady mapping and its extended results in closed-loop maps, it is important to state the uncertainty of the performance parameters used in this thesis, as shown in the error bars in Figure 6-1.

The calculation of these uncertainties has used the combination of the uncertainty method of (Kirkup, 2019) as was used by (Szymko, 2006) and (Newton, 2014). For a

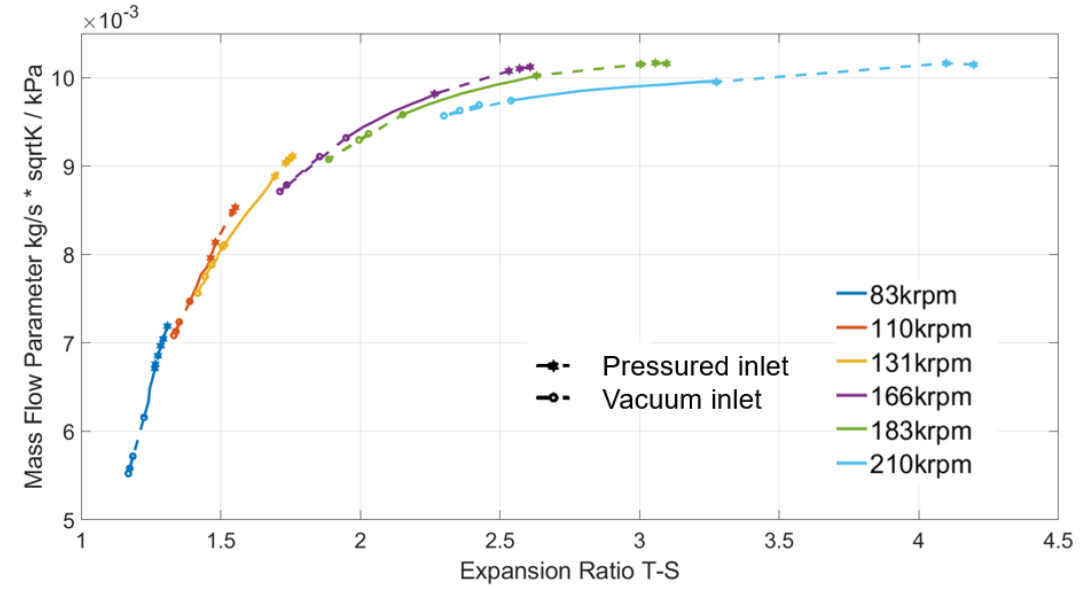

(a) Closed loop turbine mapping flow characteristics

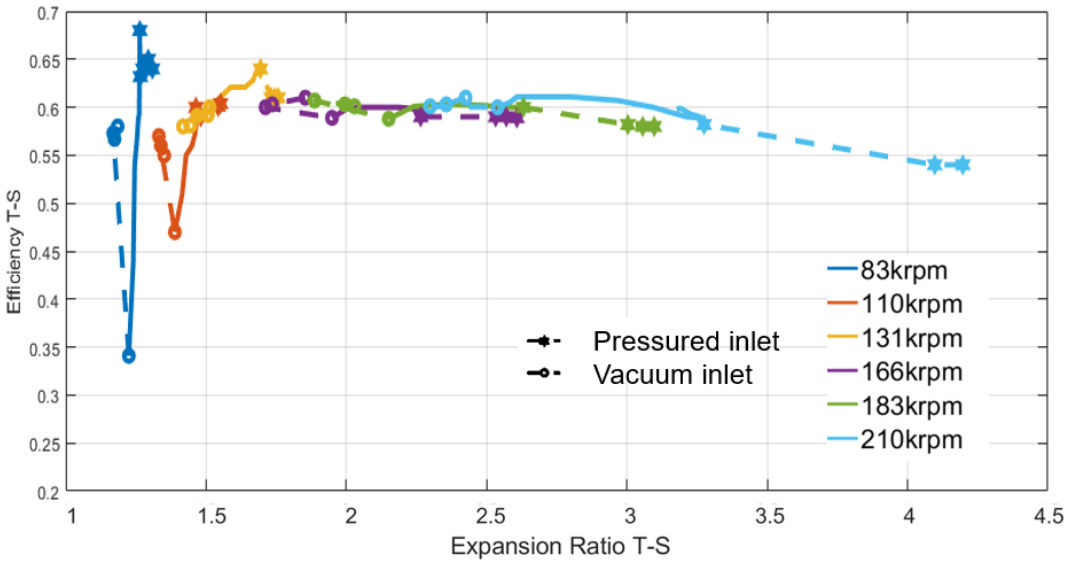

(b) Closed loop turbine mapping efficiency

Figure 6-2: Turbocharger closed loop turbine mapping results

parameter Y as a function of n different properties x_1,x_2,...x_n as:

$$Y = f\left(x_1, x_2 \ldots x_n\right) \tag{6.1}$$

The uncertaintyΔY of the parameter Y is calculated from:

$$\Delta Y_{RSS} = \sqrt{\left[\left(\Delta x_1 \times \frac{\partial Y}{\partial x_1}\right)^2 + \left(\Delta x_2 \times \frac{\partial Y}{\partial x_2}\right)^2 + \cdots + \left(\Delta x_n \times \frac{\partial Y}{\partial x_n}\right)^2\right]} \tag{6.2}$$

as aforementioned in Chapter 3, where Δx represents the uncertainty of the parameter x. This method is referred to as the Root Sum Square (RSS) uncertainty. Thus taking the mass flow parameter (MFP) of the turbine as an example, the equation of MFP is

$$MFP = \frac{\dot{m}\sqrt{T_3}}{p_3} \tag{6.3}$$

where T_3 is the turbine inlet temperature, p_3 is the turbine inlet pressure and $\dot{m}$ is the mass flow rate of air,

$$\sigma_{MFP_{RSS}} = \sqrt{\left[\left(\frac{\partial MFP}{\partial \dot{m}}\right)^2 \sigma_{\dot{m}}^2 + \left(\frac{\partial MFP}{\partial T_3}\right)^2 {\sigma_{T_3}}^2 + \left(\frac{\partial MFP}{\partial p_3}\right)^2 \sigma_{p_3^2}\right]} \tag{6.4}$$

For smaller compressor speed running points, smaller values of uncertainties are shown, which is counter-intuitive to many manufacturers' results. There are two main reasons for this:

- Heat loss was ignored in this thesis

  This uncertainty analysis conducted in this research is a raw analysis without taking heat loss into consideration for total pressure calculation and there is no heat transfer considered in the calculation of efficiency.

- Lower cut-off mass flow of V-Cone was used in this thesis

  Compared with the experimental apparatus used in commercial manufacturers, the gas stand of the University of Bath has a much lower cut-off value of the V-Cone (about 40 times less). This is the measurement of steady mass flow rate,

which decreases the uncertainty of the operating points of lower speeds.

A maximum uncertainty value of ±10.5% is shown in the plots of turbine efficiency while ±5.2% and ±3.7% maximum uncertainty values are shown in the mass flow parameter using small or large V-Cone measurement for mass flow rate respectively.

6.3.4 Summary of steady mapping results

In this section, the experimental results collected by using the methodology described in Chapter 3 were analyzed. This includes standard steady mapping results and closed-loop mapping results. As the results show, only a limited range of turbine operating points could be collected due to the surge and choked limits on the compressor side. By using a pressured or a vacuum device on the compressor inlet section, a wider range of turbine operating points could be obtained.

If CFD could be used as the method to map a turbine accurately, this complex apparatus will not be needed because by changing boundary conditions, CFD could easily examine a wider range of operating points for turbines.

6.4 The Steady CFD Model Results

A simplified CFD model of the internal flow characteristics for this radial turbine is built in this project to show the possibility of using a CFD model to predict turbine mapping data.

Figure 6-3 shows how this 3D model is built as aforementioned in Chapter 4, in which the mesh sensitivity study and interface setting were discussed.

To achieve a better computational time, this project utilized a frozen-rotor method and uses a single passage rather than the full rotor, which was illustrated in Chapter 4. The solution of the turbulence function uses the SST turbulence model.

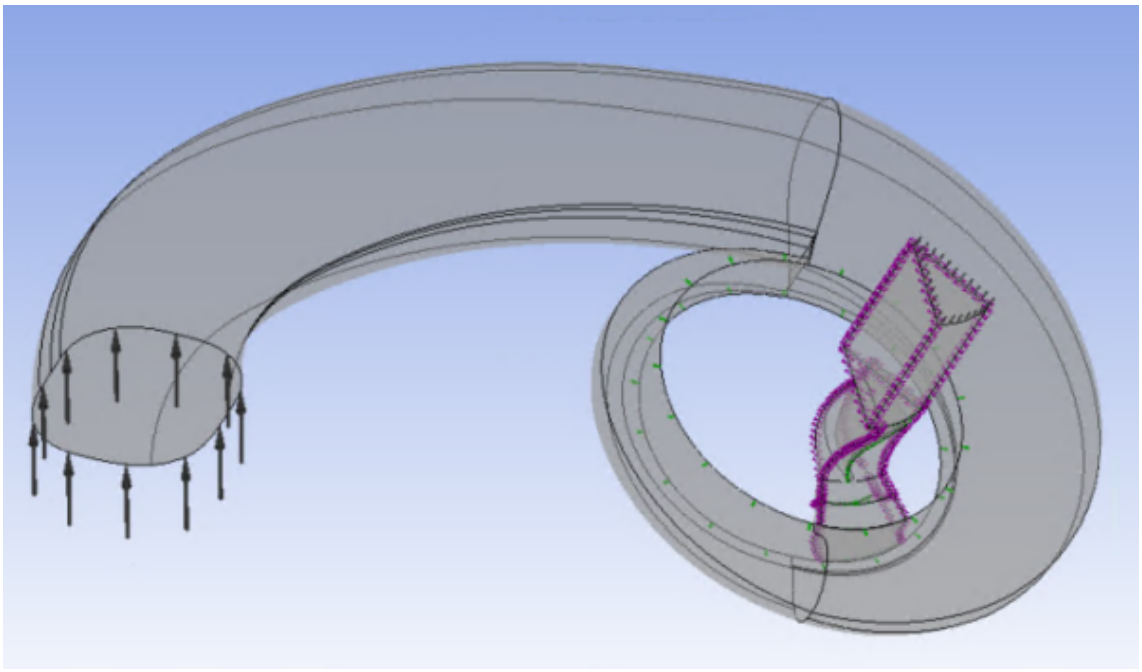

Figure 6-3: The layout of wastegate control unit

6.4.1 Comparison between CFD results and mechanical loss model description

CFD results

Based on the CFD model that has been described, the boundary condition based on steady mapping experiments is used to show the comparison between this simplified CFD model and the experimental data in Figure 6-4:

The results as seen in Figure 6-4a show good agreement in regard to turbine PR as well as turbine mass flow rate between the experimental data and CFD results. There is a consistent less than 5% difference in the mass flow parameters at all operating points. Noted that the CAD model used in the 3D CFD model comes from cutting the volute by a 0.2 mm wire so a smaller value of mass flow is expected when using the internal volume generated by scanning, and this correction has been added to the CAD model.

On the other hand, in Figure of 6-4b, a mismatch between CFD results and experi-

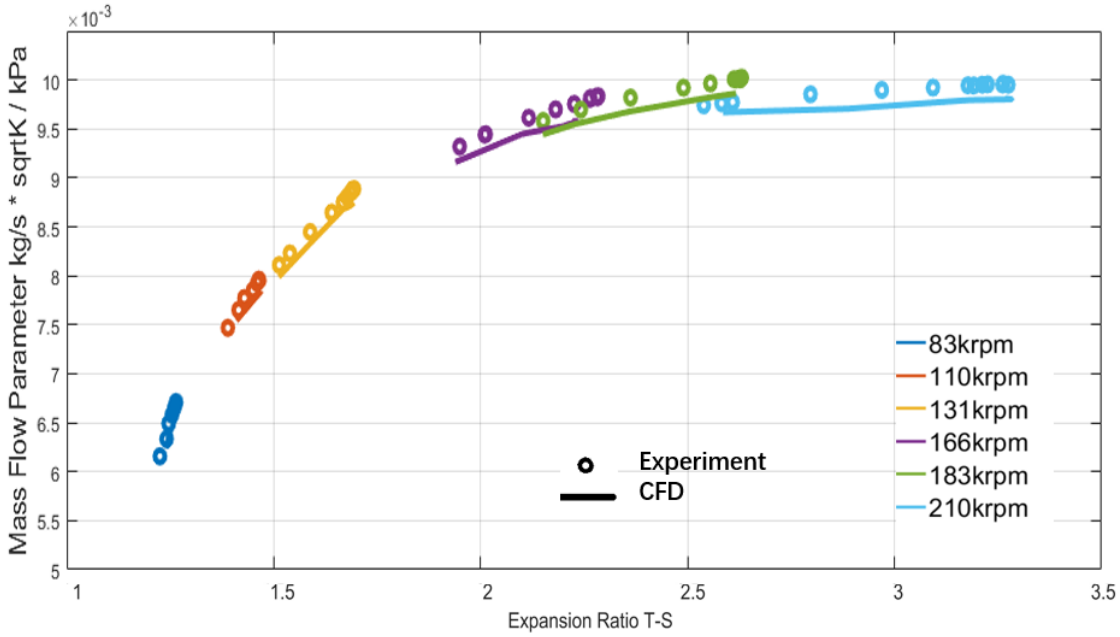

(a) MFP versus ER in experiment and CFD

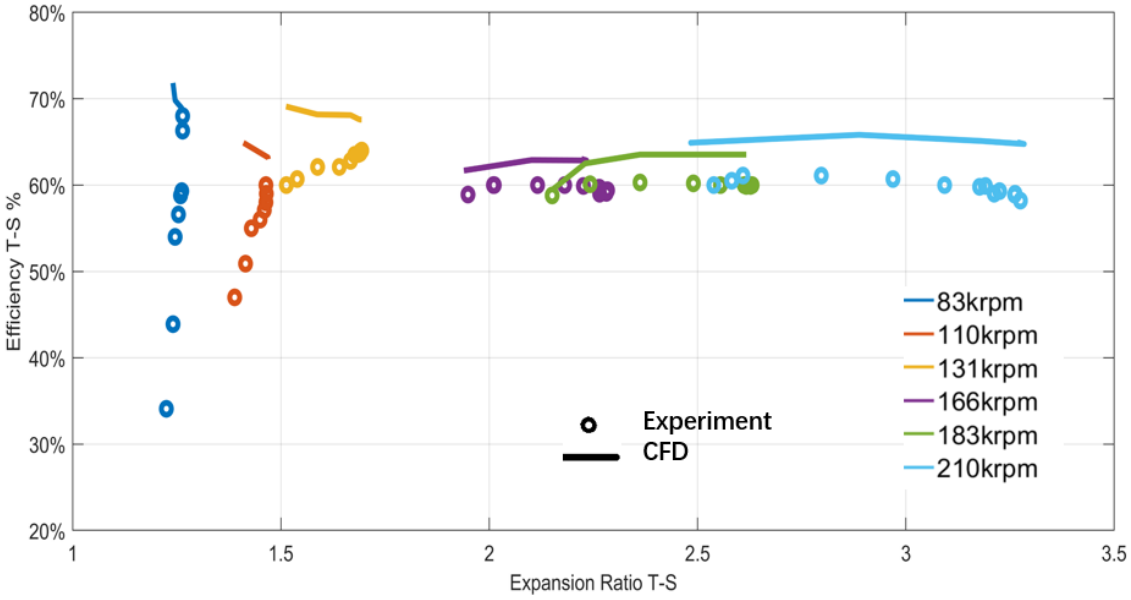

(b) Efficiency versus ER in experiment and CFD

Figure 6-4: CFD results versus Steady experimental results

mental results is shown. The reasons for this include:

- CFD is simulated for adiabatic condition

  The experiment was not conducted under adiabatic conditions, but insulating material was used for each pipe from the turbine inlet to the outlet to reduce the heat transfer effect as much as possible.

- CFD model neglects the mechanical loss

  In the CFD model, the mechanical loss because of the shaft between the turbine and the compressor could not be captured. On the other hand, it could not be neglected in the experiment due to the bearing housing system power loss, thus it is important to estimate the mechanical loss in a turbocharger system.

In order to show the influences of different factors on the error between CFD results and the steady experimental data, the differences in stage efficiency between these two sets of data are compared against turbine rotational speed, expansion ratio, turbine mass flow parameter, and turbine shaft power as seen in Figure 6-5.

According to Figure 6-5, in lower rotational speed operating points, where the heat transfer effects will dominate, there is a large mismatch in the CFD and experimental results. For higher rotational speed operating points, the difference between CFD and experiment is also obvious, which is because the mechanical loss effects are neglected in the CFD model. Similar trends are also shown in expansion ratio, mass flow parameter, and turbine shaft power.

In order to prove the effect of heat transfer loss at low-speed conditions, an adiabatic mapping of this specific turbine was also conducted by using a methodology similar to Serrano et al. (2021a). As shown in Figure 6-6, where the compressor outlet temperature, turbine inlet temperature, oil inlet temperature, and water inlet temperature were kept within a difference of 5 °C.

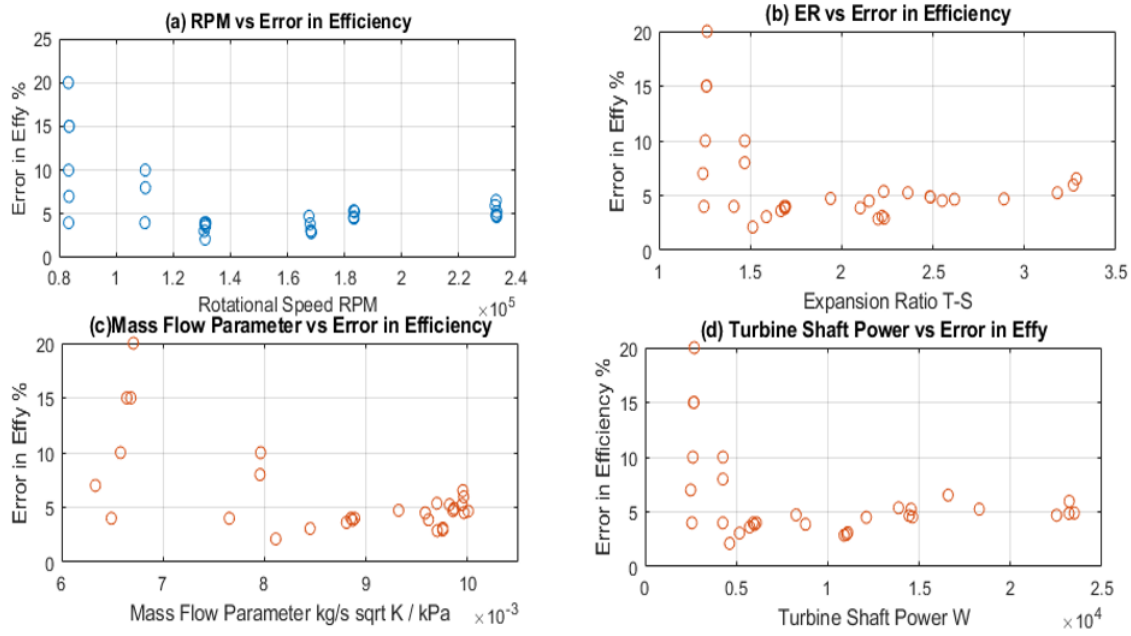

Figure 6-5: The error of efficiency (T-S) between CFD results and experimental data

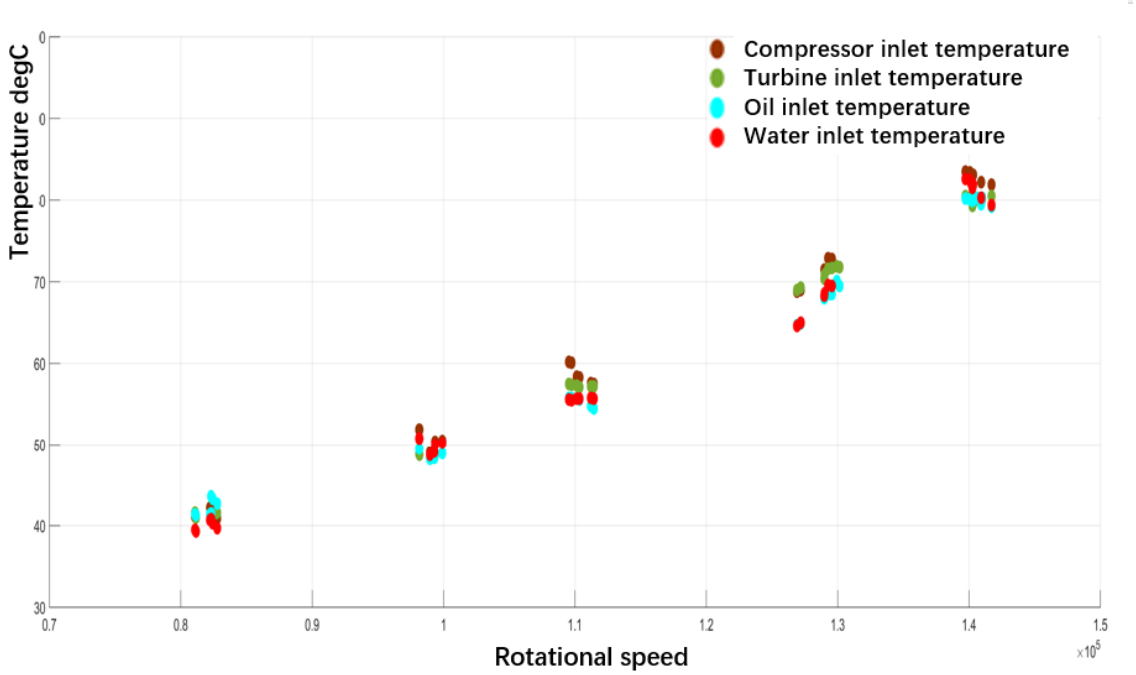

Figure 6-6: Recorded data of temperature under adiabatic experiments

As Figure 6-6 shows, in order to get the almost adiabatic condition, the maximum temperature differences between the lubrication and cooling unit (oil inlet temperature and water inlet temperature), and the compressor and turbine housing (turbine inlet and compressor outlet temperature) are kept within 5 °C. As aforementioned, the heat transfer effect will be decreased if the adiabatic mapping method is conducted, thus these operating points are then used as the boundary condition of the simplified CFD model described in the previous section to show the difference in regards to the stage efficiency as shown in Figure 6-7.

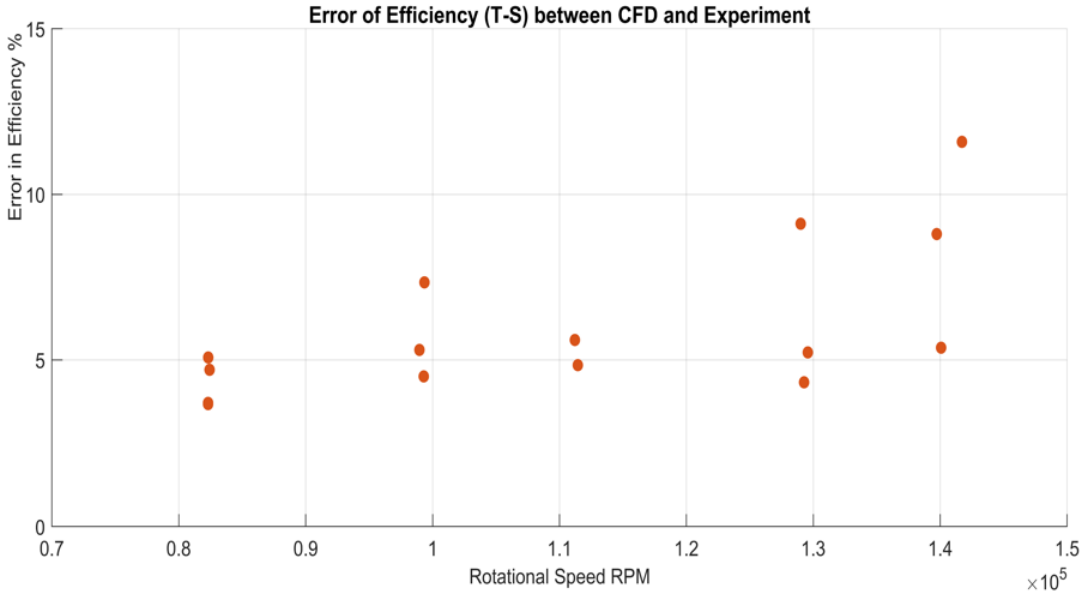

Figure 6-7: Efficiency difference between adiabatic mapping results and CFD

Figure 6-7 shows that with the increase of rotational speed, the difference in regards to the stage efficiency between the CFD model and the almost-adiabatic experimental data increases, which shows a bigger effect of mechanical loss at higher rotational speed conditions. This shows the necessity to address the effect of mechanical loss, as what can be seen in Figure 6-5 and Figure 6-7, the mismatching between CFD results and experimental results in high rotational speed operating points is not negligible. This lead to the next section of this chapter, where a mechanical loss model will be discussed.

6.5 CFD Model with Mechanical Loss Model

As has been illustrated in the comparison of the CFD results and experimental data, a mechanical loss model is built and described in this section.

6.5.1 The theory of mechanical loss model

The definition of turbine efficiency in the gas stand is

$$\eta_t = \frac{P_c/\eta_{mech}}{\dot{m}_t c_{p_{t,avg}} T_{3t}[1-(\frac{1}{PR_t})^{\frac{\gamma_{t,avg}-1}{\gamma_{t,avg}}}]} \tag{6.5}$$

$$\eta_t = \frac{1-\frac{T_{04}}{T_{03}}}{1-(\frac{P_4}{P_{03}})^{\frac{\gamma_{ex}-1}{\gamma_{ex}}}} \tag{6.6}$$

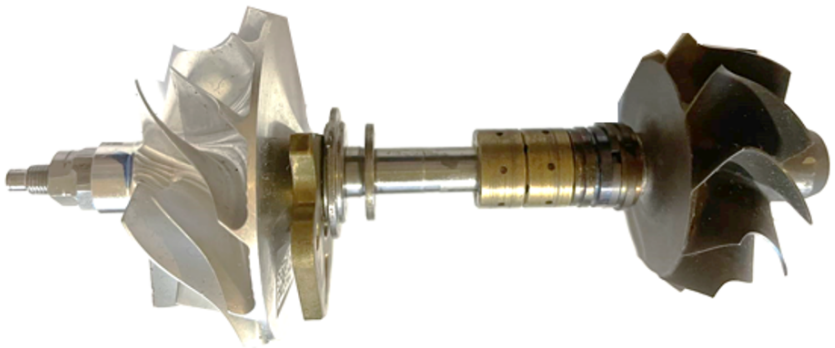

Figure 6-8: Turbine and compressor shaft and bearings (Wang, Burke and Copeland, 2020)

Figure 6-8 shows the shaft and bearing system for the turbine that was analyzed in this research.

Figure 6-9 illustrates how the energy flows in a turbocharger system (Wang, Burke and Copeland, 2020) (Watson and Janota, 1982). In a turbocharger system, the turbine is always driven by exhaust gas, and the work is then transferred to the compressor with heat loss and mechanical loss via a shaft. The mechanical loss consists of the energy loss

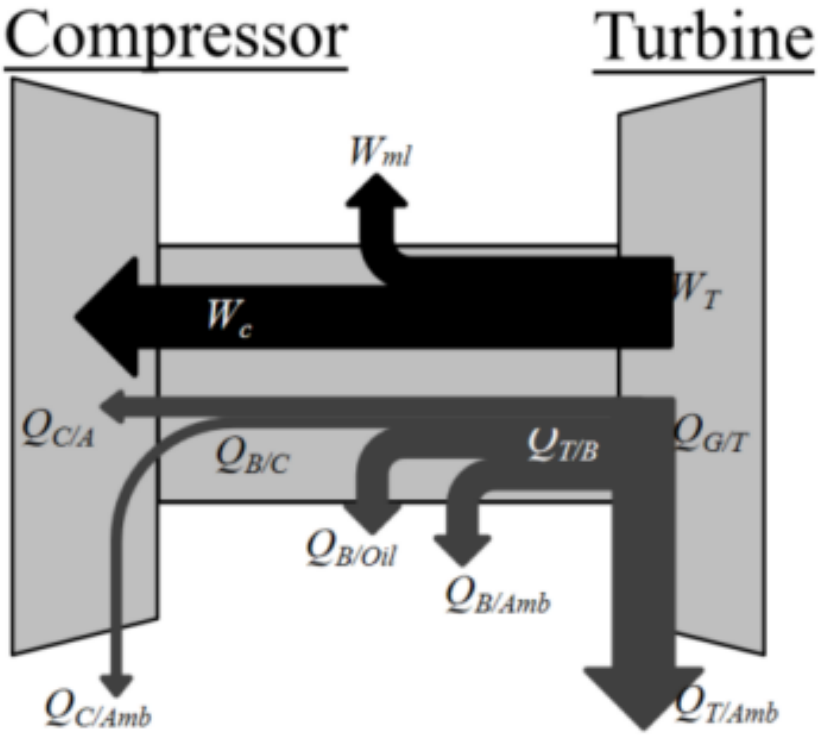

Figure 6-9: The energy flows in a turbocharger (Wang, Burke and Copeland, 2020) ,(Watson and Janota, 1982)

in the shaft, lubrication unit, bearing, and other mechanisms coupled with the shaft in the turbocharger system (Watson and Janota, 1982)(Serrano et al., 2013)(Wang, Burke and Copeland, 2020). The definition of turbine efficiency is based on the amount of power transfer from engine exhaust gases to turbine and compressor work in succession (Watson and Janota, 1982)(Serrano et al., 2013)(Wang, Burke and Copeland, 2020).

CFD uses the adiabatic condition where the heat transfer and mechanical loss are not taken into consideration. This is the case for turbochargers that mainly work on medium to high load conditions, in which the effect of heat transfer and mechanical losses are negligible. However, for light-duty radial turbines used for automobiles, the heat and friction losses can form an important part as their value might be similar to the mechanical power of the compressor. As a consequence, the mechanical loss identification becomes a vital part when addressing turbine performance (Serrano et al.,

2021b).

Hu et al. (2010) emphasized that axial thrust due to the end of compressor impeller and turbine backplate pressure difference forms an important part of the mechanical loss. Serrano et al. (2013) came up with a physical model which could solve the Navier-Stokes equations and was adjusted with experimental data in a cold test campaign. The root-mean-square mismatching between their model and experiment data is around 15%. Payri et al. (2010) built an empirical model by connecting some dimensionless factors including Reynolds number, Prandtl number, and pressure difference based on the work of Hu et al. (2010).

The similarity of their model is they all used two main parts to build up the mechanical model, that is to say, journal bearing and thrust bearing, as these two types of bearings consists of the bearing system (Hu et al., 2010), (Payri et al., 2010), (Serrano et al., 2013), which is

$$W_{ml} = W_{jb} + W_{tb} \tag{6.7}$$

Figure 6-10 shows the journal bearing, the thrust bearing as well as washer utilized in the turbine and compressor system analyzed in this project. Where the journal bearing term in Equation 6.7 is attributed to the power losses that occurred in radial bearings and the thrust bearing term is for thrust bearing.

In both bearing systems, viscous stresses are heating the oil due to a tangential speed gradient in the oil film. As a consequence, this causes a loss in the power transferred from the turbine to the compressor. In this research, a similar model was built based on the work of Payri et al. (2010),Serrano et al. (2013) and then fitted with experimental data, taking into consideration the effect of a variety of parameters.

The important factors of those parameters are analyzed, and as a consequence, pressure difference and rotor speed are set to be sensitive to operating points. A more accurate

Figure 6-10: Journal bearing, thrust bearing, and washer (Wang, Burke and Copeland, 2020)

mechanical loss model is built where a less than 7% mismatching of turbine efficiency is achieved in high-speed conditions.

Journal bearing model description

The schematic layout of a journal bearing is shown in Figure 6-11, where the work dissipated can be calculated from:

$$\dot{W}_{jb} = \boldsymbol{k}_{jb} 2\pi {R_{jb}}^3 \frac{L_{jb}}{\boldsymbol{h}_{jb}} \cdot \mu\left(\bar{T}_{oil}\right) n^2 \tag{6.8}$$

where k_{jb} is the fitting parameter that is used as a correction for the oil tangential speed gradient in the center, which is ideally near zero at the edges in the journal bearing. R_{jb} L_{jb} are the geometric parameters shown in Figure 6-11 and h_{jb} is the oil film thickness at the interface between the journal bearing and the shaft. $\mu(\bar{T}_{oil})$ represents the oil viscosity at the specific mean oil temperature measured during the system which is a look-up chart from the manufacturer's website.

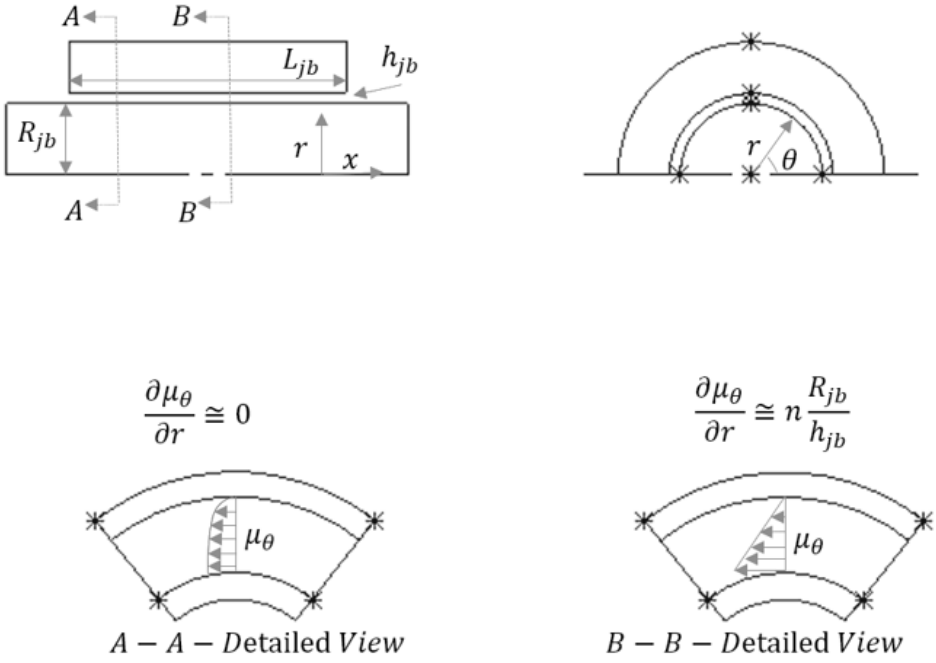

Figure 6-11: Schematic layout of a journal bearing (Wang, Burke and Copeland, 2020)

Thrust bearing model description

The schematic layout of a thrust bearing is shown in Figure 6-12, where the work dissipated can be calculated from:

$$\dot{W}_{tb} = \boldsymbol{k}_{tb}\pi \left({R_{tb,max}}^2 - R_{tb,min}^2 \right) \cdot \bar{R}_{tb}^2 \sqrt[3]{\frac{F_{at}\rho}{6k_m \dot{m}\varphi\mu}} \left(\bar{T}_{oil} \right) n^2 \tag{6.9}$$

where φ is a dimensionless parameter defined by geometry as:

$$\varphi = \frac{{\boldsymbol{R}_{tb,\max}}^2}{2} \cdot \log\left(\frac{\boldsymbol{R}_{tb,\max}}{\boldsymbol{R}_{tb,\min}} \right) + \left(\frac{{\boldsymbol{R}_{tb,\min}}^2 - {\boldsymbol{R}_{tb,\max}}^2}{4} \right) \tag{6.10}$$

F_{at} represents the resultant force in the thrust bearing system, which consists of two parts as shown in Figure 6-13:

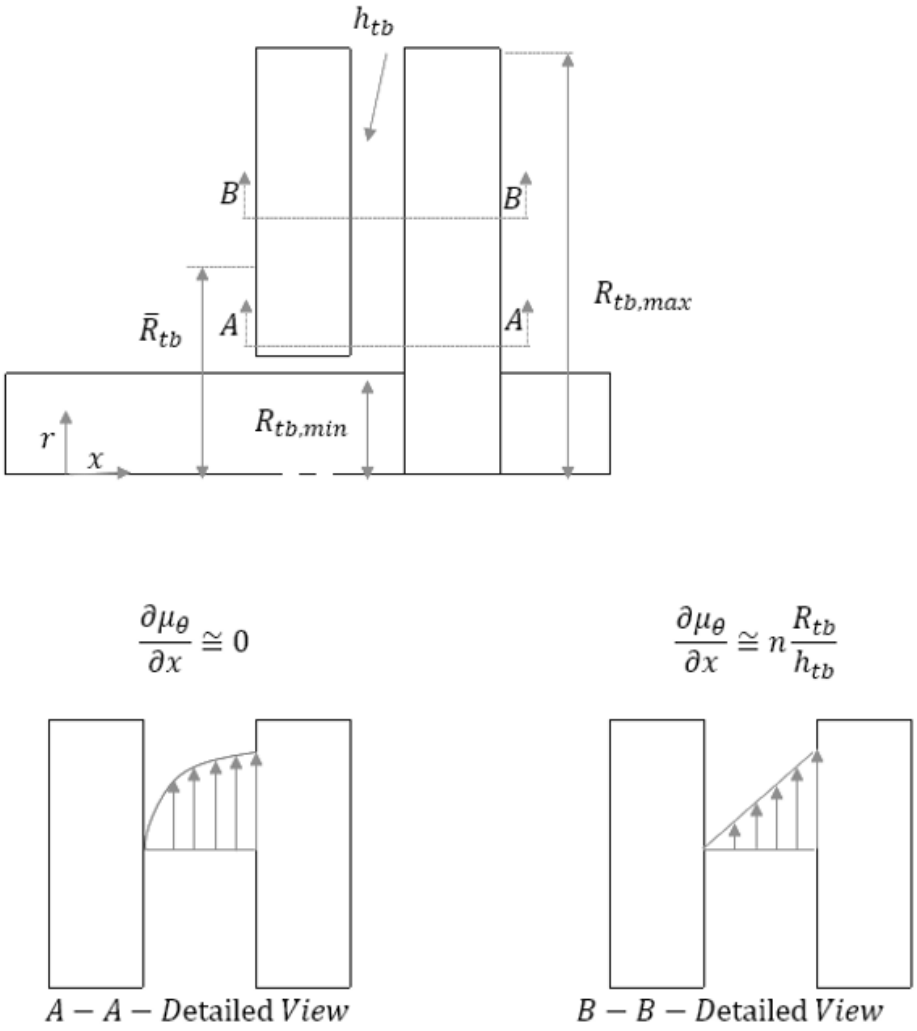

Figure 6-12: Schematic layout of a thrust bearing (Wang, Burke and Copeland, 2020)

$$F_{\text{at}} = |F_{\text{comp}} + F_{\text{turb}}| = \left| A'_{\text{comp}} \frac{p_1 - p_2}{4} + A'_{\text{turb}} \frac{p'_3 - p_4}{2} \right| \tag{6.11}$$

where the A'_{turb} and A'_{comp} are the effective area projected on the axial shaft and multiplied by a factor for the compressor and turbine respectively to correct the pressure distribution in the wheel. $p_{2'}$ stands for pressure at the outlet of the compressor wheel and is assumed to be the mean between the pressure at the inlet (p_1) and the pressure

at the outlet p_2. The weighted mean temperature of the oil is calculated from the equation:

$$\bar{T}_{\text{oil}} \simeq T_{\text{oil, in}} + k_T \left(T_{\text{oil , out}} - T_{\text{oil,in}}\right) \tag{6.12}$$

and the viscosity of the oil is calculated:

$$\mu\left(\bar{T}_{oil}\right) = K_1 \cdot e^{\frac{K_2}{\bar{T}_{oil} - K_3}} \tag{6.13}$$

This is based on the theory from Deligant, Podevin and Descombes (2011) that the power loss calculation in thrust bearing assumes a constant temperature that is equal to the inlet oil temperature. This will lead to an overestimation of temperature thus a correction for viscosity is used. The correlation factors used K_1, K_2 and K_3 are obtained based on the engine oil manufacturer. This calculation uses the factors that are fitted from experimental data.

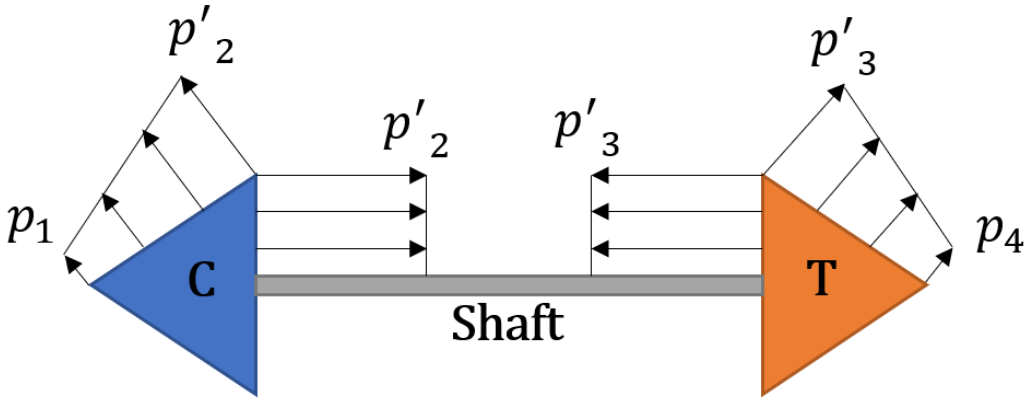

Figure 6-13: Schematic pressure layout of a turbocharger shaft(Wang, Burke and Copeland, 2020)

The model of the mechanical loss becomes :

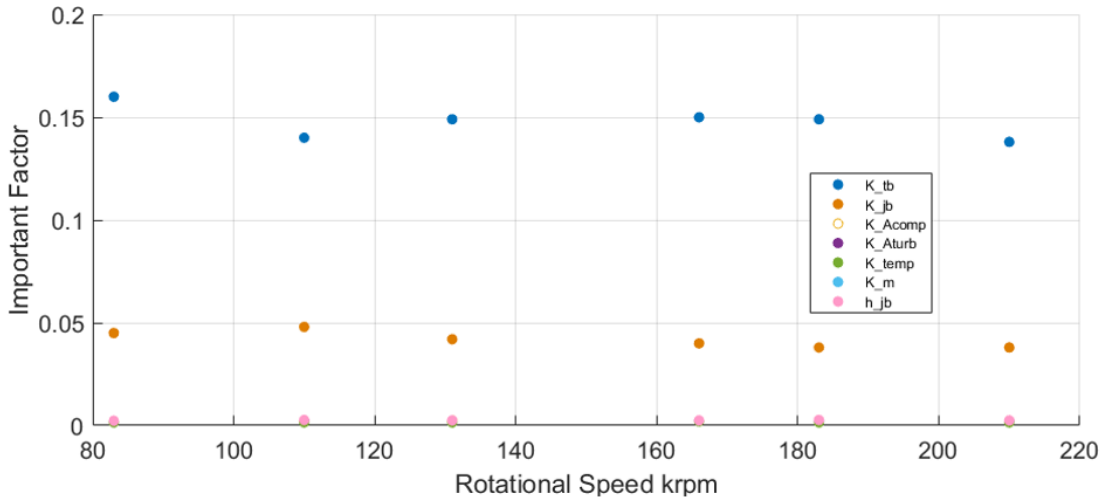

Figure 6-14: Important factor analysis(Wang, Burke and Copeland, 2020)

$$\begin{aligned}\dot{W}_{\mathrm{ml}} &\simeq \dot{m}c\left(T_{\mathrm{oil,out}} - T_{\mathrm{oil,\ in}}\right) = \dot{W}_{\mathrm{jb}} + \dot{W}_{\mathrm{tb}} \\ &= k_{\mathrm{jb}} 2\pi R_{\mathrm{jb}}^3 \frac{L_{\mathrm{jb}}}{h_{\mathrm{jb}}} \mu\left(\bar{T}_{\mathrm{oil}}\right) n^2 + k_{\mathrm{tb}} \pi \left(R_{\mathrm{tb,max}}^2 - R_{\mathrm{tb,min}}^2\right) \cdot \\ &\bar{R}_{\mathrm{tb}}^2 \sqrt[3]{\left|\frac{F_{\mathrm{at}}\rho}{12k_m\dot{m}\varphi\mu\left(\bar{T}_{\mathrm{oil}}\right)}\right| \cdot \mu\left(\bar{T}_{\mathrm{oil}}\right) n^2}\end{aligned} \tag{6.14}$$

With parameters used for fitting listed in Table 6.1.

The factors are fitted with experimental data collected in steady mapping. Rather than using constant factors, an important factor analysis is conducted as shown in Figure 6-14 and the parameters with the most weighted important factors k_{tb} as well as k_{jb} are set to be sensitive to turbine inlet and compressor outlet pressure difference, oil temperature, rotor speed, as shown in the equation:

$$k_{tb}, k_{jb} = f(n, p, T_{oil}) \tag{6.15}$$

Table 6.1: Fitting parameters of mechanical loss model (Wang, Burke and Copeland, 2020)

Name	Nomenclature	Definition
Thrust bearing factor	k_{tb}	A correction for tangential speed gradient and grooves or gaps in the bearing
Journal bearing factor	k_{jb}	A correction for uneven oil tangential speed gradient
Effective area of compressor factor	$k_{A_{comp}}$	A correction for non-linearities of pressure distribution in compressor wheels
Effective area of turbine factor	$k_{A_{turb}}$	A correction for non-linearities of pressure distribution in turbine wheels
Oil temperature factor	k_T	A correction for non-isothermal approximation
Oil mass flow factor	k_m	A correction for a constant fraction of total oil mass flow to the ideal thrust bearing
Oil film thickness	h_{jb}	An estimation for oil film thickness

Sensitivity study of 0D model

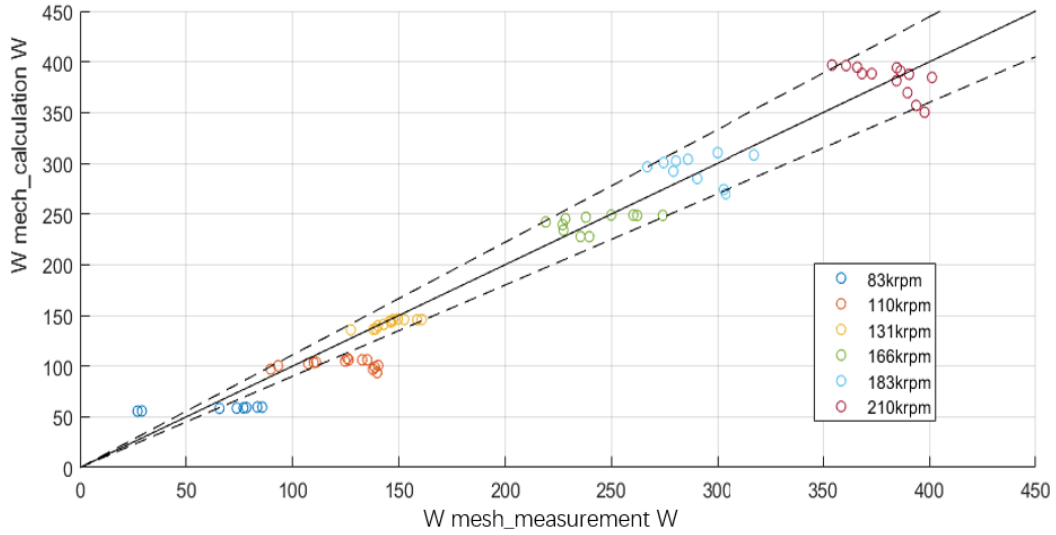

Figure 6-15: Difference between mechanical work measurement and calculation (Wang, Burke and Copeland, 2020)

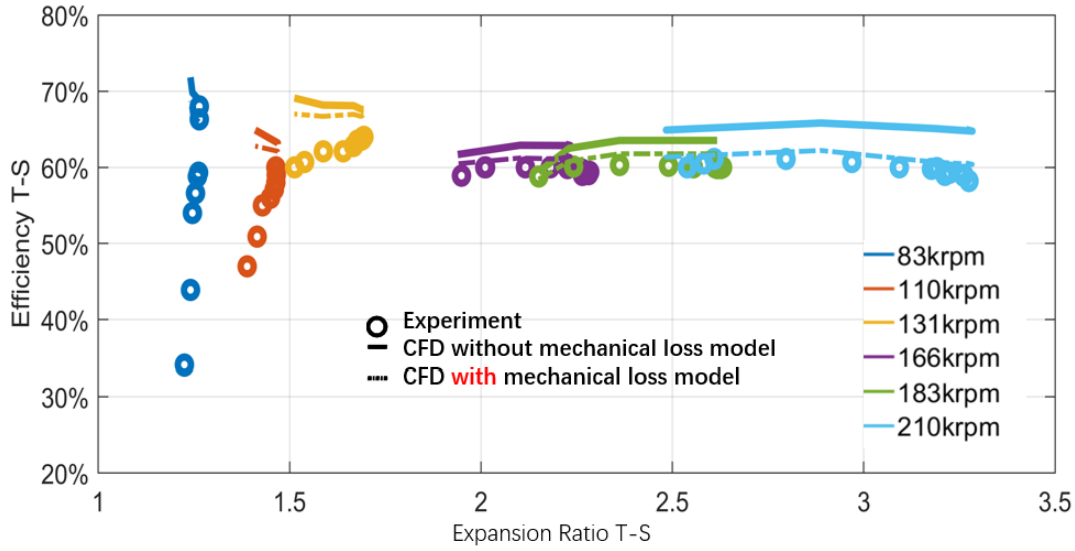

Figure 6-16: Efficiency versus Expansion Ratio with/without mechanical loss model

In order to improve the accuracy of matching the model against different working conditions (rotor speed/pressure drop/oil temperature/system temperature), a global

sensitivity analysis was conducted. Note that because of the difficulty of getting an accurate oil film thickness, it is fitted as an input parameter to the total root mean square of error.

The global sensitivity analysis is done by using the Matlab GSAT toolbox, which could be used for dealing with scalar models :

$$y = f(x) \tag{6.16}$$

Where

$$y \in R, x \in R^n \tag{6.17}$$

This is an effective method to quantify the contribution of each input parameter x_i. In this case, the seven constant parameters, to the total variance of the output y. The total variance of the output is defined by the root mean square error compared with experiment data.

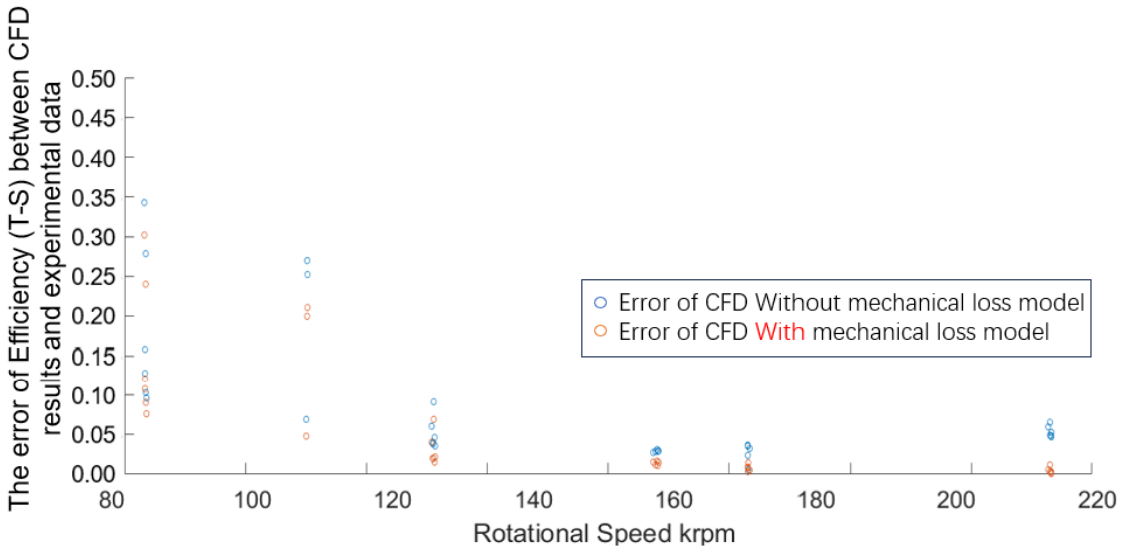

Figure 6-17: The error of efficiency (T-S) between CFD results with(orange)/without(blue) mechanical loss model and experimental data

The important factor is defined as the percentage change in predicted value per percentage change in the input parameter. For this case, it is defined as the percentage change in the mechanical loss in the input of these seven parameters in a range of different speed parameters. These are shown as follows: K_{tb} and K_{jb} are the two most important factors, and they both vary from different speeds and pressure drops. This is because the oil tangential speed distribution will change with rotor speed, pressure drop, and temperature.

To get an improved mechanical loss model to predict a closer performance, these most important parameters are selected from Table 6.1 to be sensitive to rotor speed, the pressure drop between turbine inlet and outlet, the pressure difference between compressor inlet and outlet, lubrication oil temperature, turbine and compressor temperature difference between inlet and outlet, as shown in:

$$k_{tb}, k_{jb} = f(n, p, T_{oil}) \tag{6.18}$$

Figure 6-5 shows that although CFD gives a good alignment of the mass flow parameter in all operating points, without the use of the mechanical loss model, there will be a mismatch of up to 30% in regard to efficiency. By using the pressure/rotor speed/temperature sensitive mechanical loss model, a better match between mechanical loss calculation and mechanical loss from the experiment is achieved as shown in Figure 6-15 with the RMS=0.0135 (compared with the best candidate the dimensionless mechanical loss model could achieve an RMS error of 0.03) (Wang, Burke and Copeland, 2020).

Better match in experimental data and modelled results shown in Figure 6-16 is achieved by setting the two most important factors to speed, pressure, and temperature sensitivity. Additionally, the error in efficiency between CFD results and experimental data is also shown in Figure 6-17, indicating the usage of this mechanical loss will decrease the error of CFD, especially at high-speed conditions.

6.6 Conclusion of the Chapter

Based on the illustration in previous sections, research question 3 raised in Chapter 1 has been answered in this chapter. The conclusions of this chapter are listed:

- Standard steady and close loop mapping could only provide limited conditions of turbine data and relies on extrapolation. Thus a CFD model is proposed to be an effective way of mapping.
- State-of-art current standard CFD results do not match the experiment – especially at low load conditions because CFD could only calculate under adiabatic conditions. In this research, a mismatch of 10% is shown in high-speed conditions, and more than 30% is seen in low-speed conditions. The mismatch was due to the heat transfer effects which dominate in low-speed conditions and van be removed from the experiments using adiabatic mapping while mechanical losses are more challenging.
- Once the mechanical loss is used, less than 7% mismatch of efficiency between CFD and experiment is achieved in high-speed conditions.

Chapter 7

How to Map a Wastegate Turbine

7.1 Outline of the Chapter

In Chapter 4, the methodology of using CFD to map a turbine has been discussed. This method was used to model the experimental measurements conducted with the wastegate fully closed.The turbine was modeled as a simplified internal volume without the wastegate. However, when the mapping results are used with a 1-D engine simulation code, the turbine usually operates with the wastegate open. Several researchers have discussed how to model a wastegate in different ways as aforementioned in Chapter 2. Most of them used a wastegate flow coefficient to calculate the mass flow passing through the wastegate as a poppet valve, but there is a research gap where the wastegate is precisely modeled in different opening conditions. There is no a reliable experimental method to measure the wastegate opening and the mass flow passing through it. This chapter aims to answer the research question 6 as aforementioned in the introduction 'How to measure and model different wastegate openings in mapping?', and targets objective 6: 'To map the turbine in different wastegate conditions

correctly and precisely, and model different wastegate conditions with comparison of the experimental data'.

In reality, the wastegate will open frequently on highway conditions when the inlet pressure of the wastegate is more than the threshold value of the wastegate actuator. The wastegate will change the opening to target specific boost pressure. This chapter will illustrate a way to model turbine wastegate in a more accurate way for different wastegate openings.

In this chapter, detailed wastegate measurement apparatus will be described so that the mass flow rate passing through the turbine inlet as well as the wastegate pipe at three different wastegate opening conditions is measured. Thus the flow coefficient of these different wastegate openings will be modelled by fitting an empirical model with the root mean square error of less than 3%. The experimental results will then be cross-checked by a 3D CFD model and shown to be within a mass flow rate difference of 5%.

In section 7.2, the experiment apparatus of the wastegate measurement will be discussed.

In section 7.3, the wastegate flow will be analyzed by comparing the discharge coefficient and the flow coefficient values. The coefficients calculation will be conducted by using CFD results and experiment data.

Section 7.4 will summarize the results collected in this chapter and give the conclusion.

7.2 Wastegate Experiment Apparatus and the Use of Hotwire

7.2.1 Wastegate experiment apparatus layout

As aforementioned in Chapter 3, the same apparatus of figure 3-2a is used and two hotwire probes are inserted at the cross-section of the turbine inlet and wastegate inlet

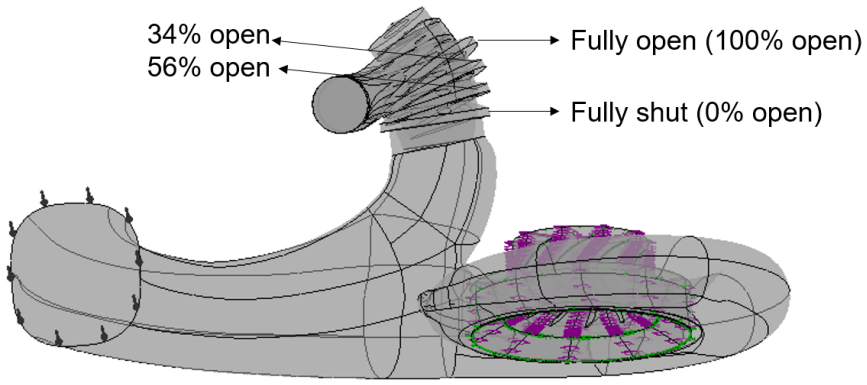

Figure 7-1: Wastegate openings

plane to measure the velocity of the flow at these two sections as shown in Figure 3-18.

For convenience, the data collected for wastegate openings is defined as the angle of the wastegate opening divided by the fully open wastegate angle as shown in Figure 7-1. These four wastegate positions are shown in the figure, and the test cases are listed in Table 7.1:

$$WG_{Position} = \frac{\alpha}{\alpha_{max}} \tag{7.1}$$

Here α is the change of wastegate angle from its fully closed position and $\alpha_{max} = 31.86^o$

The wastegate is set based on the Table 7.1.

7.2.2 Actuator motor calibration

The turbocharger comes with an electro-mechanical device connected with the wastegate, and the wastegate opening is measured from the apparatus shown in Figure 7-1. The displacement x is controlled by the pressure calibrator which is connected to the wastegate actuator as shown in Chapter 3 Figure 3-16.

Table 7.1: Wastegate test cases

case number	Wastegate Position	Turbine Speed Parameter	Turbine inlet Temperature
1	0%	2800	373 K
2	0%	3740	373 K
3	0%	4700	373 K
4	0%	5100	373 K
5	34%	2800	373 K
6	34%	3740	373 K
7	34%	4700	373 K
8	34%	3740	373 K
9	56%	2800	373 K
10	56%	3740	373 K
11	56%	4700	373 K
12	56%	5100	373 K
13	100%	2800	373 K
14	100%	3740	373 K
15	100%	4700	373 K
16	100%	5100	373 K

When the turbocharger is equipped on the engine, this actuator will directly communicate with the electronic control unit (ECU) and adjust the opening of the wastegate valve by engine speed, throttle position, and other sensor detection signals described in the research by Serrano et al. (2017). In this study, the signal that comes from the actuator is connected to a computer via CP data acquisition system, and records the voltage of the wastegate actuator. The hypothesis of this measurement is based on the research of Serrano et al. (2017) in which the correlation of voltage and wastegate opening is linearly related. As shown in Figure 7-2, three different calibration processes were conducted before collecting the data. The wastegate fully shut condition was controlled by a fixed position screw nut which fixed the displacement of the wastegate as fully shut. The fully open 100% wastegate opening condition was achieved when the signal of wastegate actuator pressure is the maximum value on the actuator, as it means the wastegate achieved the maximum displacement of opening.

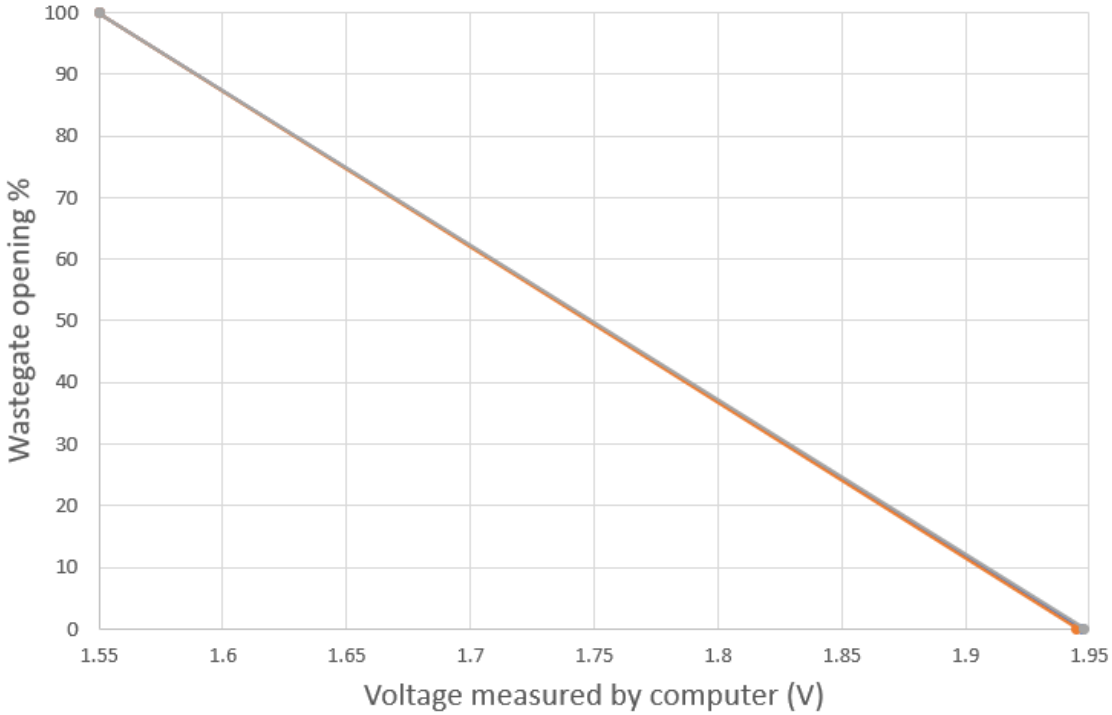

Figure 7-2: Wastegate calibration of the motor

These three calibrations were conducted at the same inlet temperature conditions of the experiment and the maximum deviation of voltage measured at a specific wastegate opening is within 3%, which cross-checked the measurement of wastegate openings. The uncertainty of the measurement was discussed in Section 4 of Chapter 3, where by recording the fully closed and fully open positions measured by a caliper and then reading from the pressured calibrator. A linear relationship between the Δx which represents the change of displacement of the actuator rod and the reading of voltage on the calibrator is established and used to calculate the exact wastegate position in the experiment.

7.2.3 Hotwire and V-cone measurement two-way calibrations

The mass flow rate that enters the turbine inlet is measured in two different ways as described in Chapter 3. The first one is the V-Cone which gives a time-averaged value

of mass flow rate based on the pressure differences inside of the orifice in V-Cone. The second measurement is the hotwire sensor that was installed in the turbine housing tongue. These two measurements are calibrated separately and compared in different inlet conditions.

Figure 3-15 shows the comparison between V-cone and probe measurement at the turbine inlet pipe when the wastegate is fully shut. V-Cone measured the inlet mass flow by measuring the pressure difference of a nozzle inside. The hotwire uses Constant Temperature Anemometers where the probe is kept at a constant temperature and constant resistance. By measuring the changing of the current, the flow variation is measured. The difference between these two measurements is within $\pm 5\%$.

The calibration is to give the validation of hot wire measurement under steady conditions because of the installation of the hotwire. Before the installation of in the measurement plane, two holes on the volute inlet and wastegate inlet were drilled separately. The probes were marked so that they are installed perpendicular to the flow direction and at the middle of the plane.

The hotwire measurement gives the velocity of the air and calculates the mass flow rate,

$$\dot{m} = u \cdot \rho \cdot A \tag{7.2}$$

where u represents the flow velocity, the cross section area is calculated based on Figure 7-3. The probe that measures the inlet turbine mass flow (probe 1) is installed perpendicularly to the volute wall (which is volute wall side 2 as shown in Figure 7-3), and the plane 1 represents where the probe takes the measurement of the velocity u. However, this velocity is not the same as the mass flow averaged velocity of the plane that goes through the mass flow measurement point, shown as u^*. In order to derive u^*, several planes are shown:

- plane 1: perpendicular with volute wall side 2 and pass through the measurement

point of the probe

- plane 2: the cross-section plane which is used to get u^*
- plane 3: the cross-section plane passes through the perpendicular planes in both volute wall sides.

The equation to calculate the average mass flow rate passes through the cross-section of the probe measurement becomes:

$$\dot{m} = u^* \cdot \rho \cdot A^* \tag{7.3}$$

where A^* is the cross-section area of plane 2 shown in Figure 7-3. The cross-section area of the inlet part is

$$A^*_{inlet} = 467.4379mm^2 \tag{7.4}$$

and the cross-section area of the wastegate is

$$A^*_{WG} = 415.47mm^2 \tag{7.5}$$

The density of flow that passes through the inlet and wastegate is calculated by

$$\rho = \frac{P_s}{RT_s} \tag{7.6}$$

where P_s and T_s here use the static pressure and static temperature that measures from turbine inlet and turbine outlet, and R is the gas constant of air (287 $Jkg^{-1}K^{-1}$). Before conducting the analysis, cases 1-4 are selected with different expansion ratio conditions to have a comparison between the mass flow rate measured from V-Cone and hotwire. As the figure 3-15 shows, the difference is within 5% as shown in the dashed lines, as aforementioned, the overall uncertainty of the hotwire calculated is about ±21.78g/s for the average value. Similarly, the plane 2 for wastegate measurement

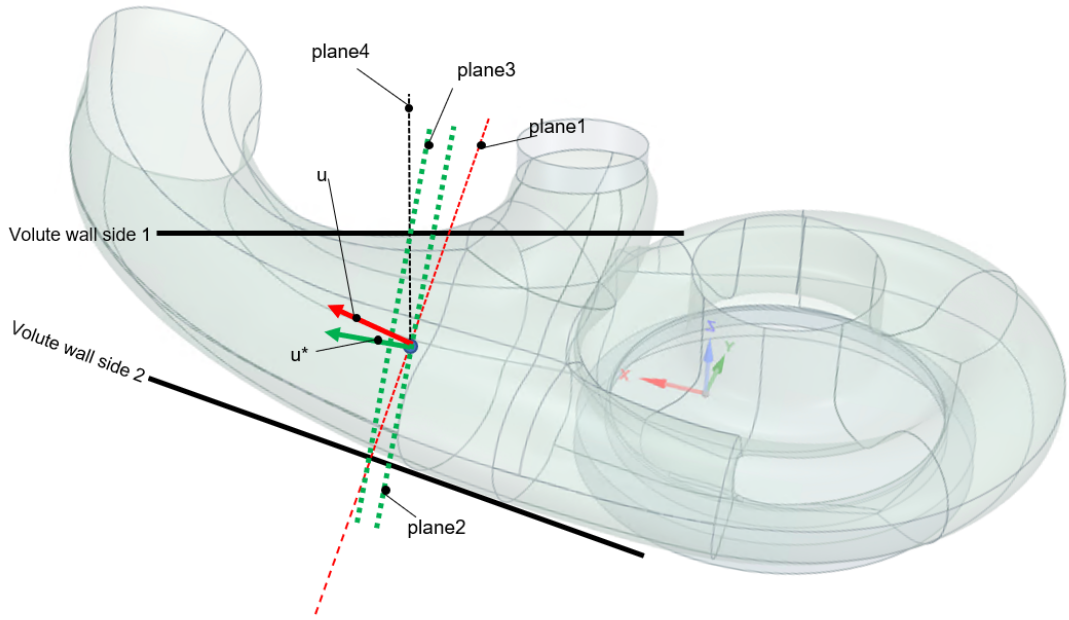

Figure 7-3: Hotwire measurement planes: inlet

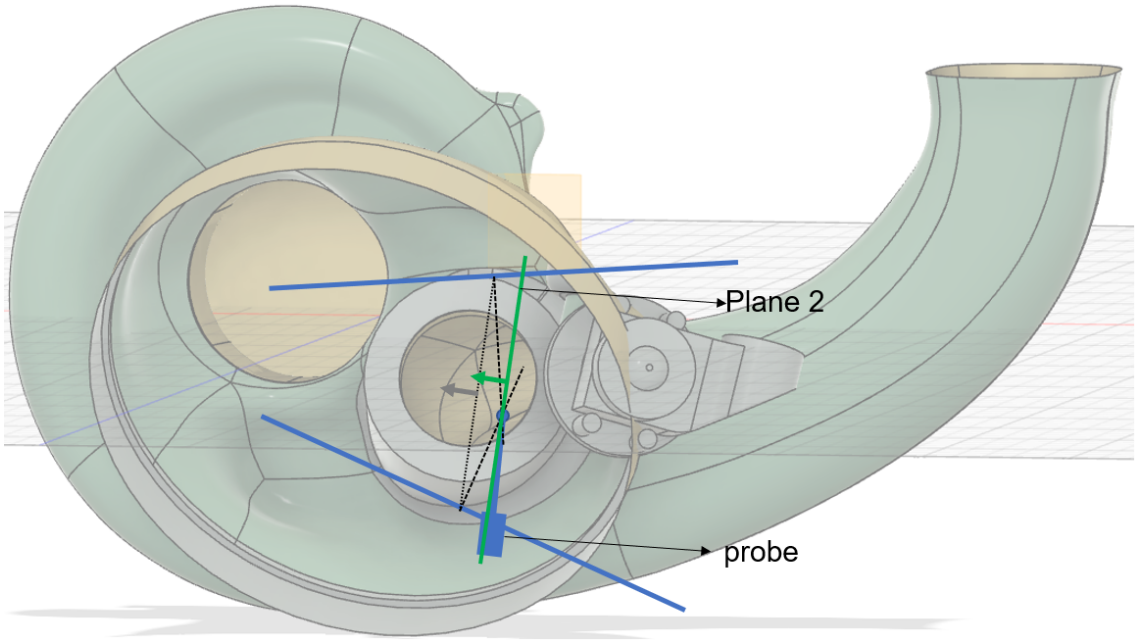

Figure 7-4: Hotwire measurement planes: wastegate

A^*_{WG} is shown in Figure 7-4.

7.3 Wastegate Flow Analysis

The wastegate is often considered a simple orifice in an engine model where the boost pressure is calculated at each side so that the corresponding wastegate area is used for different engine operating points.

Very few studies have considered the wastegate. In the real working condition for turbocharged engines, the wastegate position varies. In order to study this, the wastegate valve opening is measured by the displacement sensor. Different wastegate conditions are studied in both experiments and simulations.

In order to build a reliable model of this radial turbine, a mapping experiment is conducted. Then the turbine was cut by using a 0.2 mm wire and scanned to get the inner CAD. The wastegate geometry is shown as figure **??**. The measurements for the volute inlet and wastegate inlet are illustrated and shown in Figure **??**. Two probes are installed with the wire perpendicular to the direction of flow. The length where the probes needed to be installed was measured and marked on the probe holders for the accuracy of measurement. This measured velocity was recorded and by measuring the cross-section area of these planes from CAD as well as the air density, the mass flow rate values that pass through these two planes are calculated.

7.3.1 The discharge coefficient and flow coefficient analysis of wastegate

Flow choking definition at an orifice is based on the Mach number where

$$M = \frac{U}{a} \tag{7.7}$$

U is the local fluid speed and a is the local speed of sound.

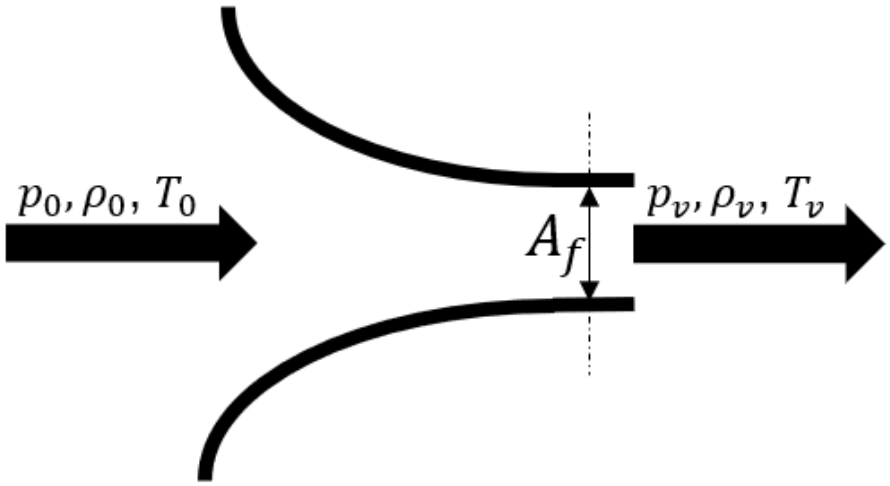

Figure 7-5: The chocking nozzle (Taylor and Costall, 2019-2020)

As the Figure 7-5 shows, the flow passed through the wastegate is modeled as a nozzle flow as shown in the figure, for a given inlet flow condition pressure p_0, density ρ_0 and temperature T_0. The mass flow rate will increase through the nozzle with a reduced pressure p_v until a critical value p_c reached at the condition where the Mach number equals 1, where

$$p_v = p_c \tag{7.8}$$

At this point, the influence of downstream pressure will no longer propagate upstream and the mass flow rate will remain constant no matter how much reduction is achieved from p_0 to p_v. This choking pressure ratio can be calculated from:

$$\frac{p_v}{p_c} = (\frac{\gamma + 1}{2})^{\frac{\gamma}{\gamma - 1}} \tag{7.9}$$

$$\dot{m}_{\mathrm{c}} = \rho_0 A_{\mathrm{f}} a_0 \left(\frac{2}{\gamma+1}\right)^{\frac{(\gamma+1)}{2(\gamma-1)}} \tag{7.10}$$

where

$$a_0 = \sqrt{\gamma R T_0} \tag{7.11}$$

$$\dot{m}_{\mathrm{c}} = K(\gamma) A_{\mathrm{f}} \frac{p_0}{\sqrt{R T_0}} \tag{7.12}$$

where

$$K(\gamma) = \gamma^{\frac{1}{2}} \left(\frac{2}{\gamma+1}\right)^{\frac{(\gamma+1)}{2(\gamma-1)}} \tag{7.13}$$

The expression of mass flow at the choking condition in Equation 7.12 enables an estimated calculation of the maximum mass flow rate that passes through a valve based on the upstream conditions and a minimum flow area A_f.

As Figure 7-6 illustrates, there are two different versions of the geometric valve area definitions:

- Valve curtain area $A_1 = \pi dl$ which is a surface of revolution, with a diameter equal to that of the valve and a length equal to the valve lift
- Valve seat area $A_2 = \frac{\pi}{4} d^2$

Additionally, a correction factor or a coefficient is also needed to make the geometric area equal to the effective area.

The summary of different versions of flow correction is listed in the Table 7.2 (Taylor and Costall, 2019-2020):

Table 7.2: Flow coefficient (Taylor and Costall, 2019-2020)

Version	**Curtain**	**Seat**
Geometric valve area A_v	$A_v = A_1 = \pi dl$	$A_v = A_2 = \frac{\pi}{4}d^2$
Type of correction coefficient	Discharge coefficient	Flow coefficient
Effective valve area A_f	$A_f = C_d A_v$	$A_f = C_f A_v$
Comments	1. Reference curtain area varies with valve lift 2.Curtain area is the limiting factor at low lift	1.Reference seat area does not vary with valve lift 2.Seat or port area is the limiting factor at high lift

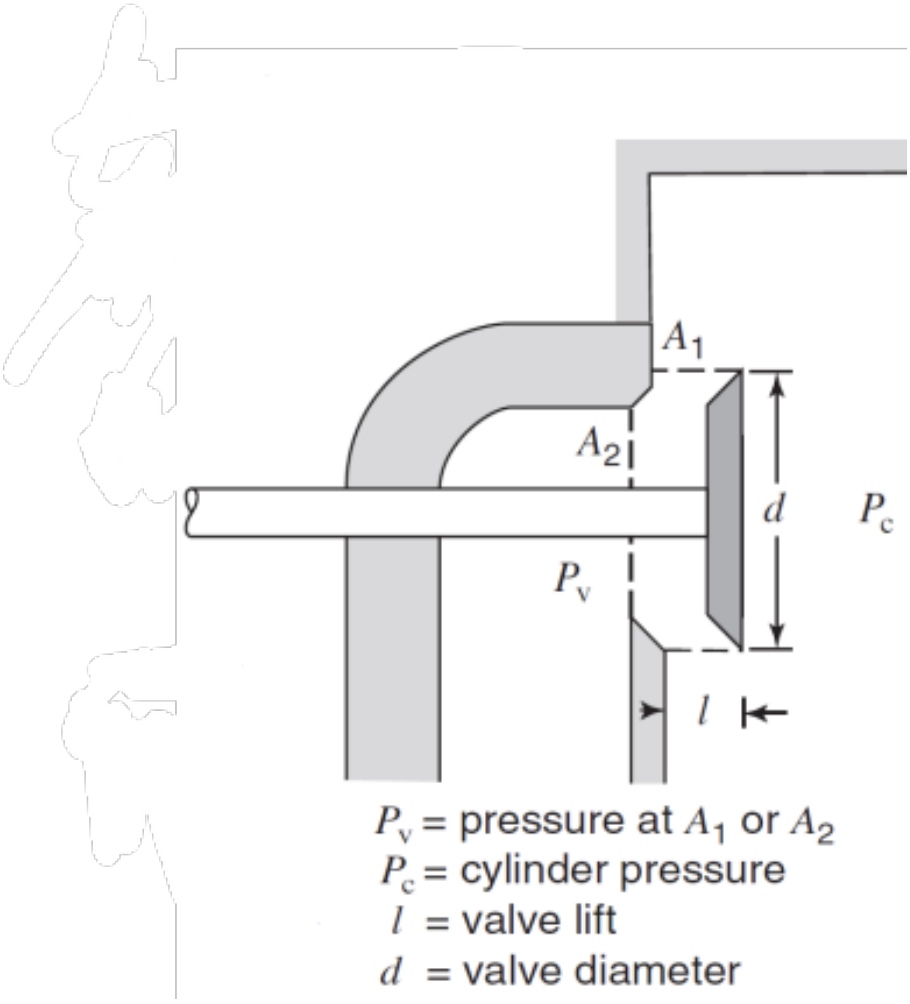

Figure 7-6: Curtain and seat area definition (Taylor and Costall, 2019-2020)

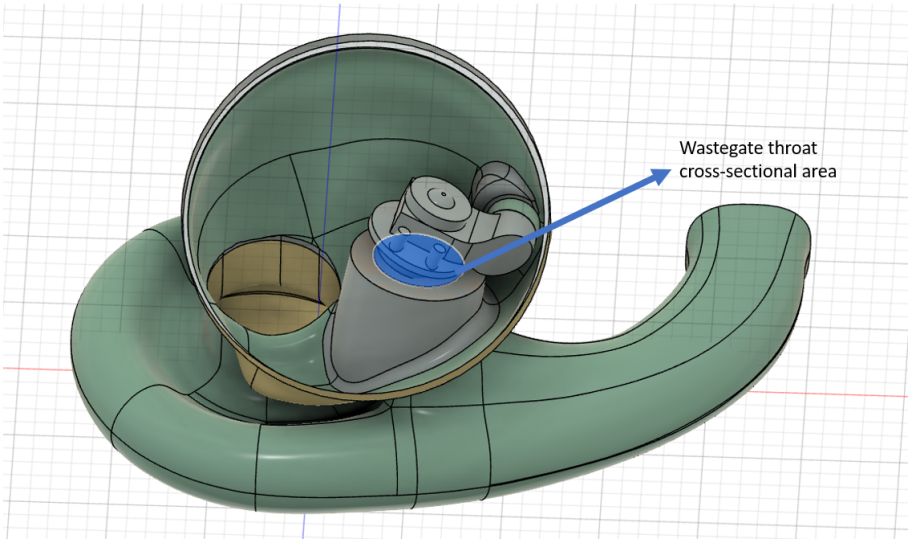

Figure 7-7: Wastegate throat area

Definition of discharge coefficient and flow coefficient

Depending on the choice of curtain or valve area, the convention of flow coefficient is defined:

- Discharge coefficient C_d for curtain area
- Flow coefficient C_f for seat area

The definitions are listed as:

$$C_f = \frac{A_f}{A_{ref}} \tag{7.14}$$

Where A_f is the effective flow area through the wastegate valve as it increases with the rotation of the wastegate lever from zero, while the reference area is defined as

$$A_{ref} = \frac{\pi D_{WG}^2}{4} \tag{7.15}$$

which represents the wastegate throat cross-sectional area, and it is estimated from the CAD file and using the diameter of the wastegate section as shown in Figure 7-7.

Unlike C_f, the discharge coefficient C_d is defined using a varying reference area. The

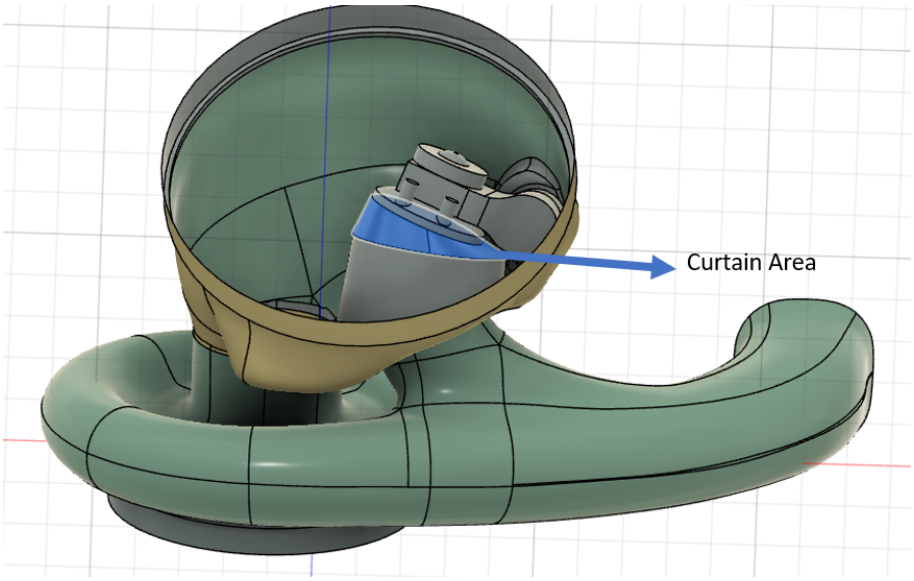

Figure 7-8: Wastegate curtain area

equation goes the same as:

$$C_d = \frac{A_f}{A_{ref}} = \frac{A_f}{A_{curtain}} \tag{7.16}$$

because the reference area becomes the 'curtain area' of the wastegate as shown in Figure 7-8. In order to explain the variation of flow patterns in different wastegate positions, three different wastegate positions are chosen and compared against the experimental data collected. According to the previous analysis, the mass flow that passes through the wastegate could be rewritten as :

$$\dot{m} = C_f A_{\text{ref}} \frac{P_{0,\text{ in}}}{\sqrt{RT_{0,\text{ in}}}} \left(\frac{P_{S,\text{ exit}}}{P_{0,\text{ in}}}\right) \sqrt{\frac{2\gamma}{\gamma-1}\left[1-\left(\frac{P_{S,\text{ exit}}}{P_{0,\text{ in}}}\right)^{(\gamma-1/\gamma)}\right]} \tag{7.17}$$

and as for the choked conditions where

$$\frac{P_{\text{exit}}}{P_{0,in}} \leq \left(\frac{2}{\gamma+1}\right)^{(\gamma/\gamma-1)} \tag{7.18}$$

the mass flow rate becomes

$$\dot{m} = C_f A_{ref} \frac{P_{0,in}}{\sqrt{RT_{0,in}}} \sqrt{\gamma} \left(\frac{2}{\gamma + 1} \right)^{\gamma + 1/2(\gamma - 1)} \tag{7.19}$$

Where $P_{S,\text{ exit}}$ and $P_{0,in}$ are the exit static pressure and inlet total pressure of the turbine respectively.

Steady wastegate C_f

Experimental data was collected at three different wastegate positions in a range of operating points, based on the calculation of Equation 7.19. This measurement data are then used to build up an empirical model for the wastegate flow coefficient.

What should also be noted according to the data collected is that the velocity measurements from probes fluctuate around $\pm 5 m/s$ as shown in Figure 7-9. An FTT was conducted by no distinct frequency was present. The time average value of velocity for each operating point is used by dividing the result of the area calculation by the duration of the sample.

What has also been seen is the noise of the measured velocity is relative to turbine speed, this is because an increasing turbo speed will result in more vibrations from the wastegate closing, thus leading to increased noise.

With the measurement of wastegate flow velocity and inlet flow velocity, the flow coefficient variations versus different wastegate positions are shown in Figure **??**. Unlike Salehi, Vossoughi and Alasty (2014), who suggested the flow coefficient is linearly related to the wastegate positions, the flow coefficient is found to be a function of both wastegate positions and expansion ratio.

This fitting method to determine an expression that could be used for predicting the mass flow rate variations of both wastegate and turbine inlet at different operating points is shown in Figure 7-10. The main benefit of this method is to predict how

Coefficient	Value
a	-0.2658
b	0.2048
c	0.00518
SSE	0.003071
R^2	0.9728
Adjusted R^2	0.9713
RMSE	0.00911

SSE: sum of the square due to error
RMSE:root mean square error

much the mass flow passes through the wastegate using an empirical model with a polynomial equation.

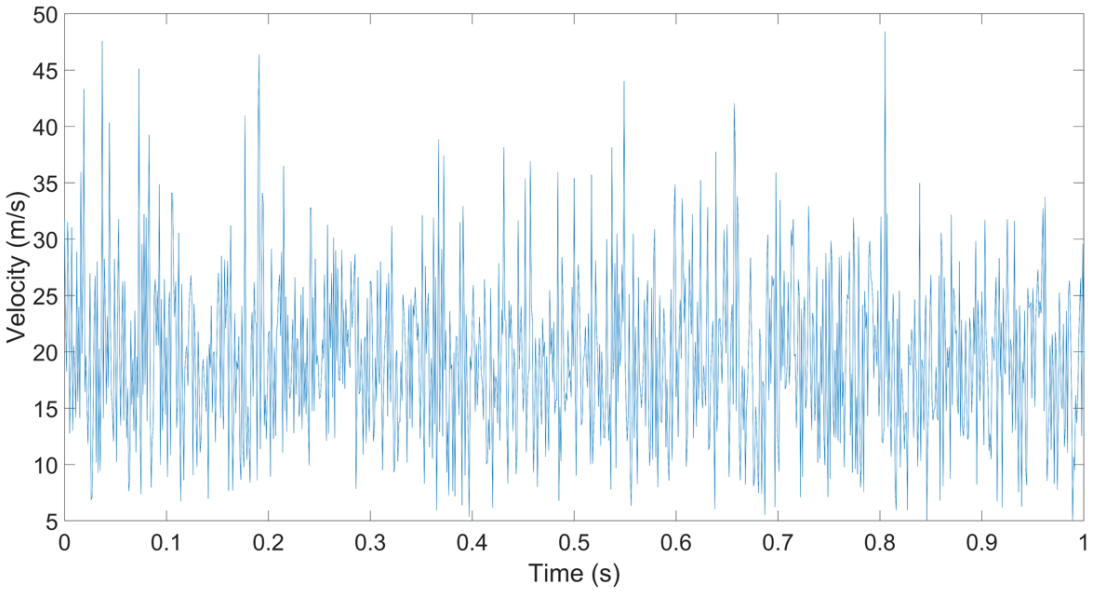

Figure 7-9: Probe measurement noises

As a result, by using this C_f fitted wastegate model, the comparison between the model results and experimental data collected by using the hotwire in the wastegate is shown in Figure 7-11 and Figure 7-12. This model gives a prediction of the mass flow parameter of the wastegate plane within the root mean square error of 0.018% and the flow coefficient root mean square error of 3.3%.

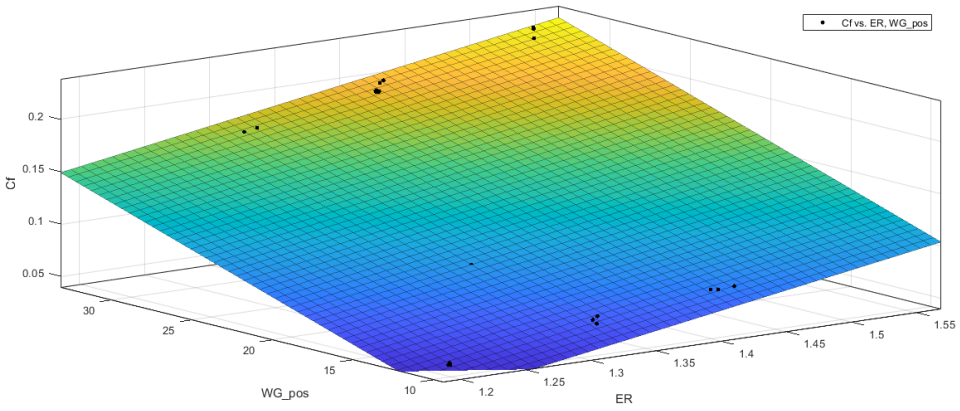

Figure 7-10: Flow coefficient C_f fitting model

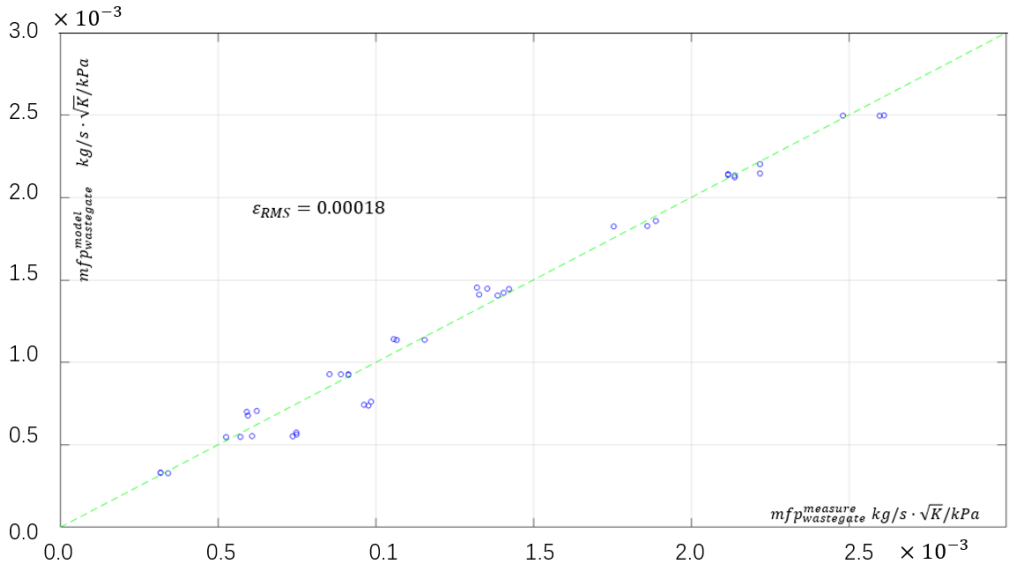

Figure 7-11: Mass flow parameters comparison of measurement and model

The empirical model results will then be compared with the simulation data from a wastegate CFD model that will be discussed in the following sections.

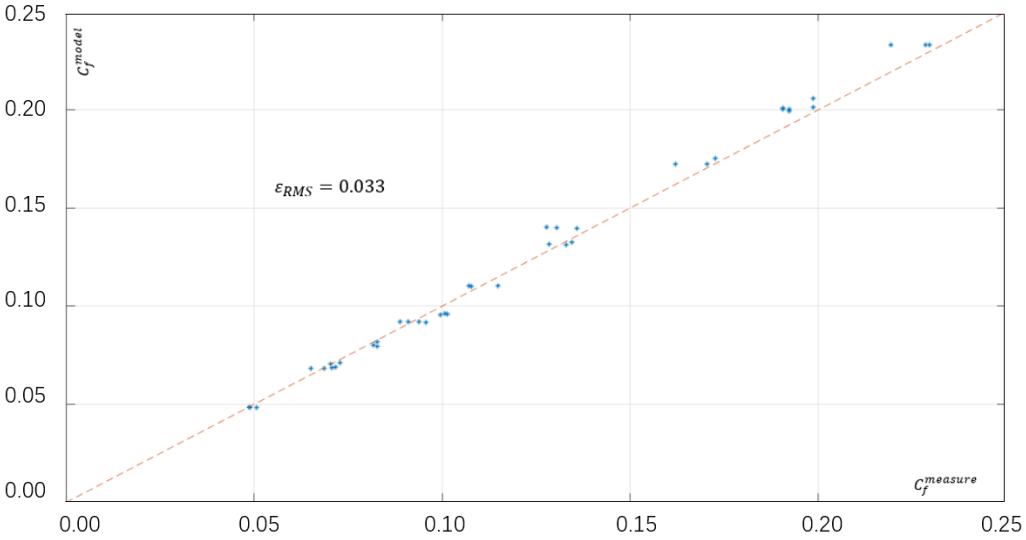

Figure 7-12: Flow coefficient C_f comparison of measurement and model

7.3.2 Wastegate used in 3D model and cross-checking for the wastegate flow coefficient

As Figure 7-1 shows four different wastegate positions that were used for the experiment in this research, in CFD analysis, these positions are set based on experimental data. The wastegate is set to be steel, and due to the complexity of the model, the full stage is used and a long outlet pipe is modeled for the outlet condition similar to the experiment as shown in the domain layout in Figure 7-13.

The area average values of velocity simulated in the CFD model at the cross-sectional area of the volute inlet and the wastegate in each case were compared with the data measured by hotwire. The CFD model here is used as a cross-checking of this experimental method. Total to static (T-S) efficiency is used here as SAE format efficiency aforementioned in Chapter 3.

A single speed line's turbine characteristics were compared in both the simplified CFD model and the wastegate CFD model with the wastegate fully shut. Figure 7-14 and Figure 7-15 show that there are less than 3% differences in these two CFD results

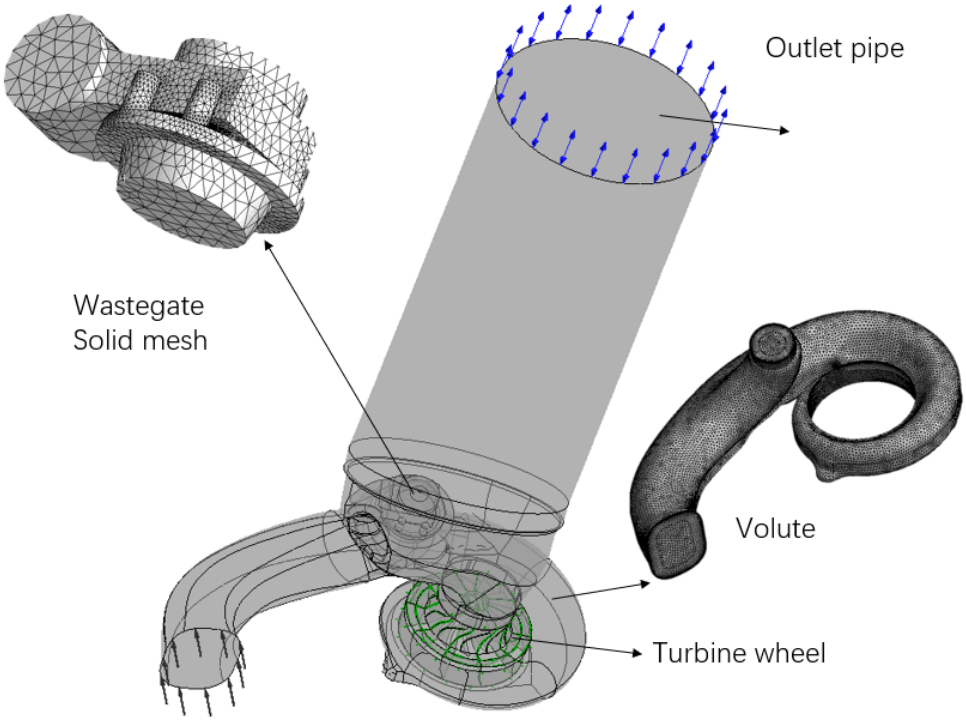

Figure 7-13: Domains setup in Wastegate CFD model

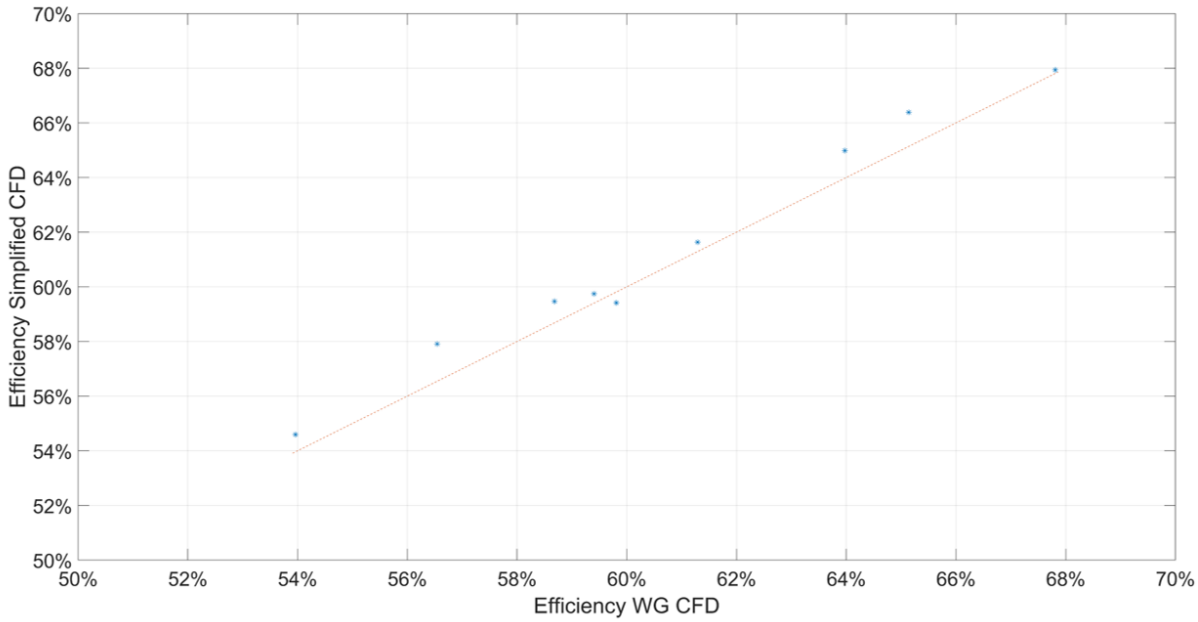

Figure 7-14: Two CFD models results in comparisons in efficiency

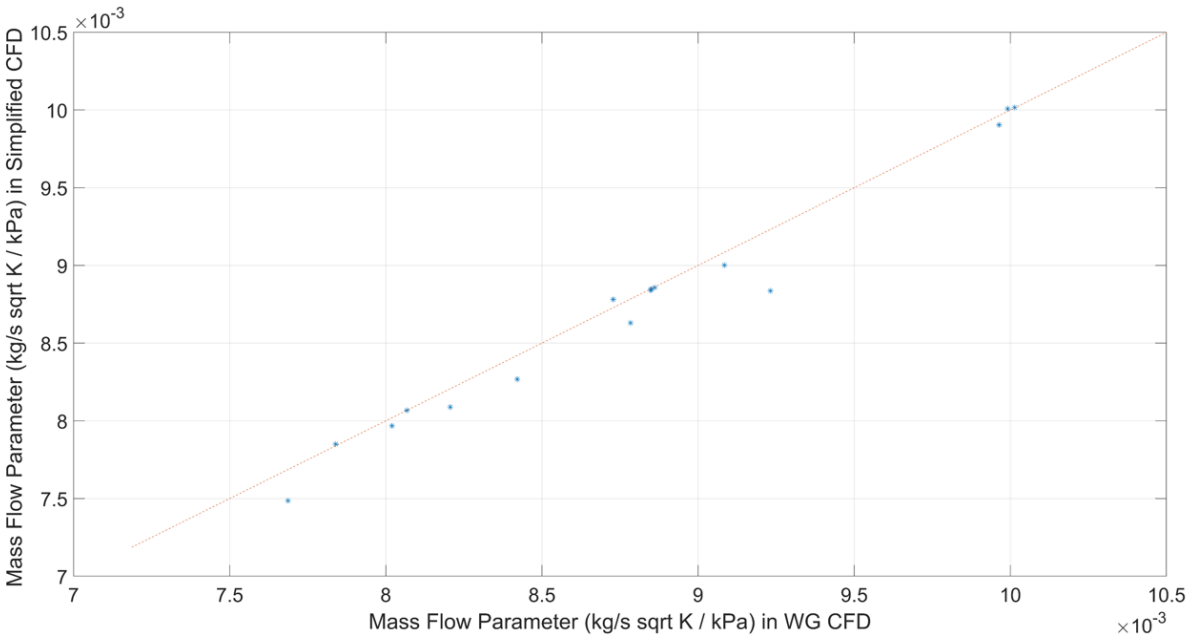

Figure 7-15: Two CFD models results in comparisons in MFP

for those operating points in both efficiency and the mass flow rate simulated at the turbine volute inlet. This is acceptable as the convergence of these two CFD models

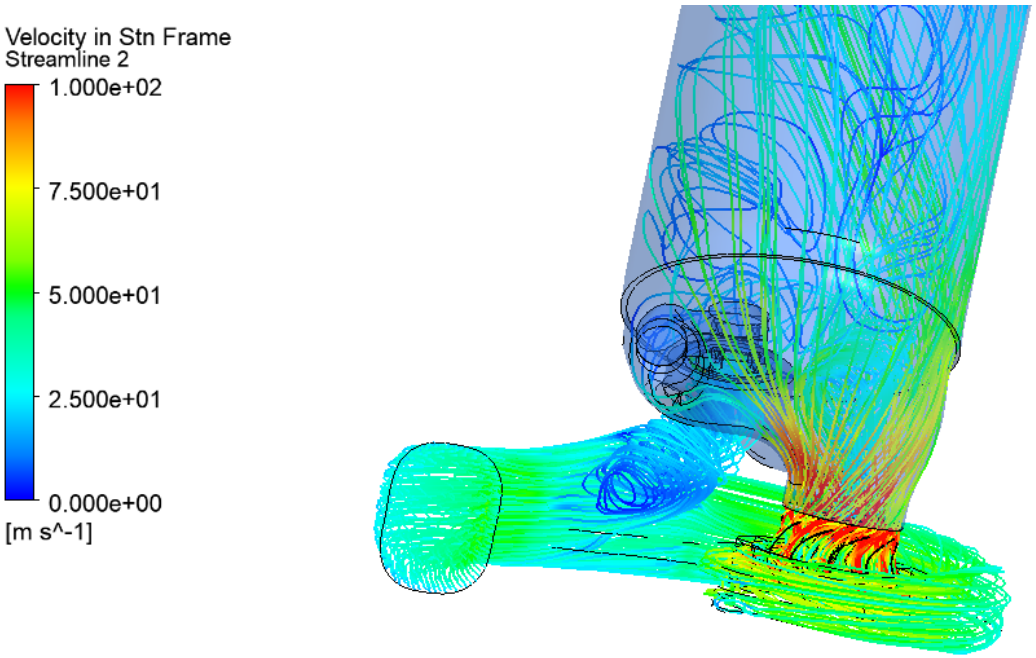

Figure 7-16: Wastegate CFD results of 0% wastegate opening

might be slightly different.

7.3.3 Comparison between CFD results and wastegate model results

As Figure 7-16 and Figure 7-17 show, the velocity of flow streamlines in both conditions of wastegate fully shut and wastegate fully open are compared. With the same turbine operating points at the same rotational speed, there is an increasing velocity shown when the wastegate is fully open, while for the wastegate fully closed condition, the closed section of volute works as a 'flow pocket'.

Several operating points with different wastegate openings are compared with the experimental data as shown in Figure 7-18, the percentage of opening is defined as the wastegate angle divided by a fully open angle: The dashed lines represent the ±5% deviation, which indicated the cross-checking from CFD results of the experimental data.

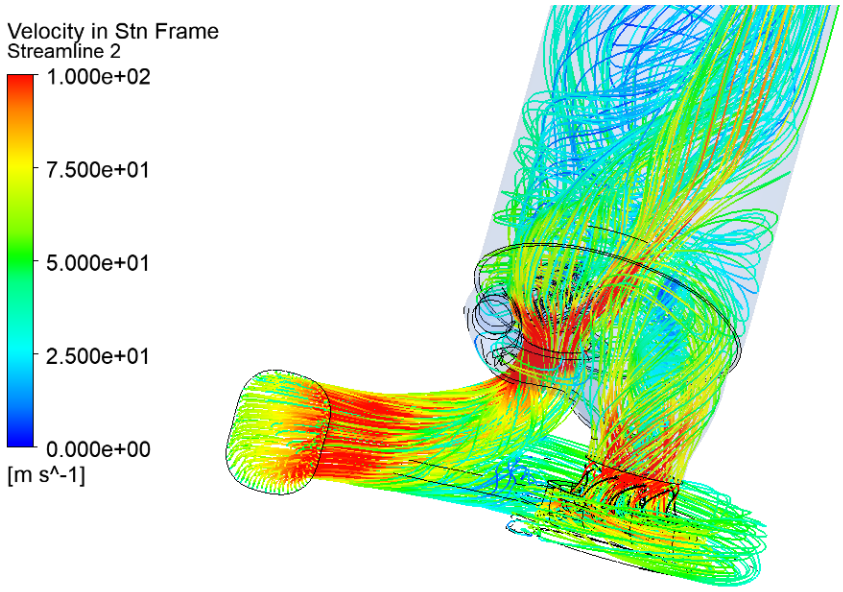

Figure 7-17: Wastegate CFD results of 100% wastegate opening

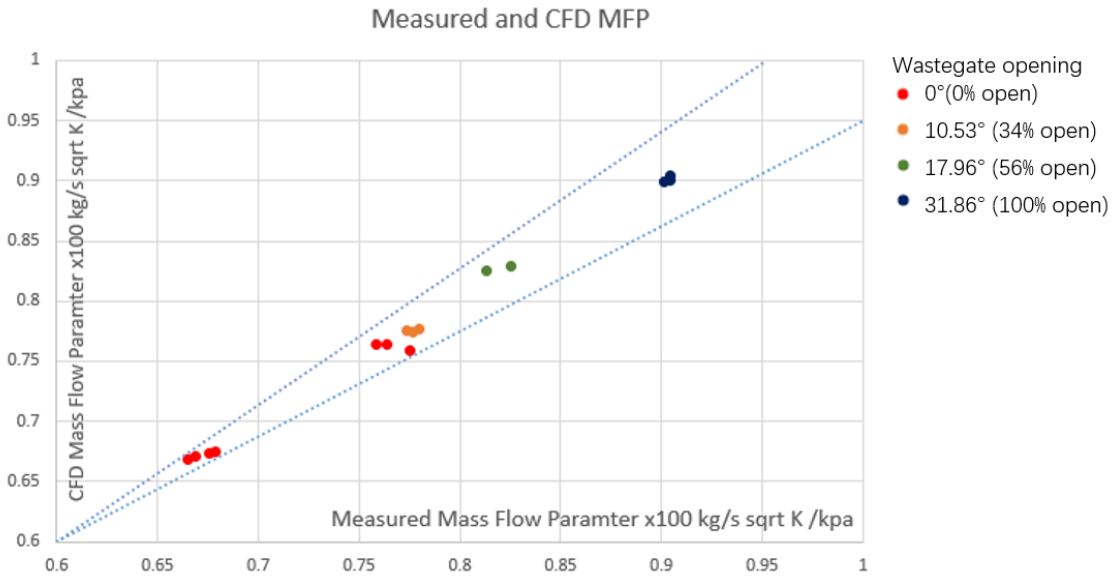

Figure 7-18: Measured MFP vs. wastegate CFD MFP results

7.4 Conclusions of the Chapter

In this chapter, a detailed experimental methodology of mapping a turbine with different wastegate opening conditions was illustrated. It uses two hotwire probes to measure the wastegate inlet and volute inlet mass flow rate separately.

A wastegate CFD model with the capability to simulate different wastegate openings were built, and the results cross-checked the experimental method to measure the flow percentage at different wastegate openings, which is a new approach according to the literature review. The wastegate CFD model showed a good alignment when compared with the simplified CFD model described in Chapter 6 at wastegate fully shut conditions.

The cross-checked experimental data were then used to build a wastegate flow coefficient model which is able to use as a factor of turbine map data for 1D engine code. The comparison between mass flow passes through the wastegate by using the flow coefficient model and using experimental data collected by hotwire showed a good agreement with the root mean square error of 3.3%.

The research question that raised in Chapter 1 'How to measure and model different wastegate openings in mapping' has been answered.

Chapter 8

Conclusions

8.1 Conclusions of the Research Questions

Based on the previous chapters, the conclusions of this research have been summarized based on the research questions raised in Chapter 1 Introduction.

1. What is the up-to-date mapping method for single-entry radial turbines?

   This question was answered in Chapter 2 *Literature Review*, where the state-of-art literature about turbine mapping work in experimental and numerical methods has been reviewed.

   Although several experimental methodologies have been discussed by researchers, the unsteady nature of the turbine under pulsating flow conditions is difficult to measure accurately. Moreover, the experimental method to measure the wastegate openings accurately is still a challenge. Additionally, CFD models are under adiabatic conditions with no mechanical loss considered. There are also very few researchers who discussed the usage of wastegate in mapping. These gaps were highlighted and several research questions were raised based on these gaps.

2. How to collect mapping data for a single entry radial turbine precisely?

   This question was answered in Chapter 3 *Methodology Experimental*, where the mapping data were collected both by standard steady state and an extended closed loop apparatus.

   Apart from that, the unsteady data was conducted by using a pulse rig, and the instantaneous measurements for pressure were successfully conducted while the instantaneous mass flow rate measurement of probes could not be used under hot conditions. On the other hand, the instantaneous measurement of a pair of fast response thermocouples often suffers high noises, thus a new question is raised to build up a model of the gas stand to simulate how fast the measurement apparatus should be.

3. How to model a single-entry radial turbine precisely?

   With the aim of this thesis to improve the way to map a fixed geometry radial turbine, this research question was answered in Chapter 4 *Methodology Numerical*, where the usage of both a dual-orifice 1D model and two 3D CFD models (the simplified CFD model and the wastegate CFD model) are explored as effective ways.

   These numerical methods were illustrated in Chapter 4 and the simulation results by using these models and the comparison against experimental data were further discussed in Chapter 5 *Unsteady Mapping* (1D dual-orifice model), Chapter 6 *Can CFD Be Used to Map a Turbine Accurately?* (3D simplified CFD) and Chapter 7 *How to Map a Wastegate Turbine* (3D wastegate CFD).

   The dual-orifice model discussed in Chapter 5 showed its capability of reflecting the unsteady nature under different frequencies of pulses, which will be further concluded in question 4. The level of accuracy of the simplified CFD model shows an error of less than 5% of MFR but more than 10% of error in efficiency due to

the neglected mechanical loss and heat transfer effects. The improvement of this will be further concluded in question 5. Additionally, the wastegate CFD model shows a good agreement within ±5% deviation when compared with a wastegate flow coefficient model fitted by experimental data collected using hotwire probes, which will be further answered in question 6.

4. How to measure and model a turbine under unsteady conditions?

   This question was answered in Chapter 5 *Unsteady Mapping Method*, where as stated in Chapter 2, the instantaneous temperature measurement suffered from noise. The instantaneous measurement of mass flow rate by using hotwire could only survive in a low temperature of around 150 °C. Thus a dual-orifice model was illustrated in this chapter, and the measurements were analyzed and compared. For the characteristics of pressure, mass flow rate, and temperature, none of the slow sensors described in Chapter 2 could capture the fluctuations under pulse conditions. While using fast pressure sensors and mass flow sensors, the fluctuations of pressure and mass flow rate could be captured with the operating range under 150 °C. As for the temperature measurements, the fast thermocouples used are not able to capture the fluctuations of temperature according to the simulation results.

5. Can CFD models be used to map a turbine?

   This question was answered in Chapter 6 *Can CFD be used to map a turbine accurately?*, where the CFD methodology discussed in the previous chapter was used to build the CFD model and the comparison between steady mapping results and numerical results was analyzed. The average difference between experiments and CFD is about 10% in efficiency. A mechanical loss model was built in this chapter to improve the accuracy of the CFD prediction for mapping results within 3% in efficiency and mass flow rate at high-speed conditions.

6. How to measure and model different wastegate openings in mapping?

   This question was answered in Chapter 7 *How to Map a Wastegate Turbine*, where three different wastegate openings angles were measured. The mass flow rate passed through both wastegate and turbine inlet pipe were measured by using fast response hotwire probes thus a mathematical model of flow coefficient are built and compared with a CFD model which was validated with experimental results of wastegate fully shut.

Based on those research questions, three main research gaps are discussed in detail in Chapter 5 *Unsteady Mapping Method*, Chapter 6 *Can CFD Be Used to Map a Turbine* and Chapter 7 *How to Map a Wastegate Turbine*, and the detailed conclusions are listed in the following sections:

8.1.1 Conclusion of unsteady mapping

In Chapter 5, a dual-nozzle model is used as a prediction of the unsteady performance of a turbine. There are three questions that have been answered:

- What types of models are able to predict unsteady behavior and of these models which one(s) are best for assessing the feasibility of unsteady mapping?

  This question is related to the literature review in Chapter 2 where different types of turbine models are compared and discussed. A dual-orifice mode was used in the analysis, and it has been validated by an experimental test of 44 points. A feasibility check was also discussed with the conclusion that within the typical area of the turbine map, the maximum error from the model results in the mass flow of 4% and pressure ratio of 0.6%.

- How is unsteady behavior different from steady flow behavior in a mapping context?

  This question was analyzed in the third section of Chapter 5 by setting a range

of inlet pressure frequency from 0 Hz to 90 Hz as the boundary condition of the dual-orifice model. By studying the performance of the model, it was shown that the dual-orifice model can predict the unsteady nature of a specific turbine under pulsating conditions, and the variations of pressure, mass flow rate, degree of reaction is not only influenced by pulse frequency but also is a factor of the turbine's specific geometrical parameters.

Pulse frequency acts as the most important factor that influences turbine performance. According to the simulation, the unsteadiness is also related to the natural frequency of a specific turbine, and for the inter-volume values changed by 10 times, the threshold frequency where the direction for the trend of pressure, mass flow rate and other parameters variations changes will change from 65 Hz to about 50 Hz, which means the unsteady behavior will be influenced by the natural frequency of the turbine.

- What will we see in reality by using the sensors under an unsteady pulse rig by studying the simulation results?

  This question was analyzed by using the first-order filter modeled based on the time constant of available sensors discussed in Chapter 3 *Experimental Methodology* in the gas stand experiment as a time response node, by feeding into the reaction time provided by the manufacturer's data. Two sets (slow and fast) of sensors including pressure sensors (Omega pressure sensor with the time constant of 0.1 s and high-frequency response strain gauge sensors with the time constant of 0.000001s), thermocouples(1.5 mm tip diameter K-type thermocouples with the time constant of around 1.1 s and 13 μm tip diameter K-type thermocouple with the time constant of around 0.25 s), and flow sensors (V-Cone measurements 0.025 s time constant and hotwire fiber-film probes with the time constant of around 0.000007 s) were compared.

The conclusion is made that the fast response pressure sensor is good enough to predict how the unsteady behavior of the turbine even though fast flow sensors. The hotwire probes can show how unsteady turbine mass flow rate variation looks like under pulse conditions. The temperature limit according to the manufacturers will also need to be considered. On the other hand, none of the thermocouples used in the thesis can reflect the unsteady nature of inlet temperature variations leading to a 3% difference in the mass flow parameter prediction and an overestimate of cycle-average efficiency of 15% and peak efficiency of 11.3%.

8.1.2 Conclusion for CFD used in mapping

Based on the illustration in previous sections, research question 3 raised in Chapter 1 *Introduction* has been answered. The conclusions of this chapter are listed:

- Physical experiments including standard steady and close loop mapping could only provide limited conditions of turbine data and rely on extrapolation. Thus the CFD model is proposed to be an effective way of mapping.
- State-of-art current standard CFD results do not match the experiment – especially at low load conditions because CFD could only calculate under adiabatic conditions. In this research, a mismatch of 10% is shown in high-speed conditions, and more than 30% is seen in low-speed conditions. The heat transfer effects dominate in low-speed conditions, while mechanical losses are more challenging under adiabatic conditions.
- Once the mechanical loss is used, less than 5% mismatching with experiment data of efficiency is achieved in high-speed conditions.

8.1.3 Conclusion for mapping a wastegate turbine

In this thesis, a CFD model with the capability to simulate different wastegate openings was built. The results gave a validation of the experimental method to measure the

flow percentage at different wastegate openings, which is a new approach according to the literature review.

This detailed experimental methodology of mapping a turbine with different wastegate opening conditions uses two hotwire probes to measure the wastegate inlet and volute inlet mass flow rate separately.

These validated experimental data were then used to build a wastegate flow coefficient model.

Several operating points outside the experimental catalog are used as boundary conditions for the 3D waste-gated model, and the results from the 3D model show a good agreement with the flow coefficient curve.

- Steady mapping method could only provide a limited range of data for the wastegate
- Hotwire measurement did not have a good agreement with 3D modeling wastegate prediction and is improved significantly by adding a mechanical loss model

8.2 Recommendation for Future Work

Based on the research outcomes, the recommendations for future work are divided into two parts:

8.2.1 Experimental work

- Mechanical loss measurement with wastegate opening

  The mechanical loss model built in this thesis has been tested by comparing the mechanical loss work calculated from the model and from experimental data. Further work is needed to validate the model if the mechanical loss work is collected under different wastegate openings.

- Hotwire measurement of different positions

  In this thesis, the hotwire probes were used to measure the flow velocity that passes through the turbine inlet as well as the wastegate. However, the measurement could be more precise if the position of the hotwire probe on the measurement plane could be measured, so that the uncertainty of the cross-section area will be decreased. Additionally, a more robust layout of measurements could be determined in the future so that the unsteady mass flow could also be measured and compared against the simulation data collected in the dual-orifice model.

8.2.2 Numerical work

- Improved CFD combined mechanical loss model under transient conditions

  Further transient CFD simulations could be conducted to improve the working conditions of the mechanical loss model.

- Wastegate CFD model under transient conditions

  Further transient CFD simulations could be conducted to improve the working conditions of the wastegate model.

- Heat transfer model

  Further study could be done on building a heat transfer model of this radial turbine so that a CFD combined with a mechanical loss model as described in previous chapters could be coupled with a heat transfer model to decrease the error between the simulation results and experimental data.

Bibliography

Abidat, M., Hachemi, M., Hamidou, M. and Baines, N., 1998. Prediction of the steady and non-steady flow performance of a highly loaded mixed flow turbine. *Proceedings of the institution of mechanical engineers, part a: Journal of power and energy*, 212(3), pp.173–184.

Alaviyoun, S., Ziabasharhagh, M. and Farajpoor, M., 2020. Experimental investigation and numerical simulation of gas flow through wastegated turbine of gasoline turbocharger. *Journal of applied fluid mechanics*, 13(6), pp.1835–1845.

ANBE SMT co. Japan, 2010. *Reason why ultra-fine and ultra-thin thermocouples have superiority* [Online]. Available from: `https:http://anbesmt.co.jp/en/library/fineTCthory.html`.

Avola, C., 2017. *Advanced characterisation of turbochargers with the focus of modelling two-stage turbocharging systems*. Ph.D. thesis. University of Bath.

Avola, C., Dimitriou, P., Burke, R. and Copeland, C., 2016. Preliminary doe analysis and control of mapping procedure for a turbocharger on an engine gas-stand. *Turbo expo: Power for land, sea, and air*. American Society of Mechanical Engineers, vol. 49866, p.V008T23A008.

Bayón, A., 2022. Online course notes in fulid mechanics-introduction to computational fluid dynamics.

Benson, R. and Scrimshaw, K., 1965. Paper 23: An experimental investigation of non-steady flow in a radial gas turbine. *Proceedings of the institution of mechanical engineers, conference proceedings*. SAGE Publications Sage UK: London, England, vol. 180, pp.74–85.

Benson, R.S., 1974. *Nonsteady flow in a turbocharger nozzleless radial gas turbine*. SAE Technical Paper.

Bentley, J.P., 1983. *Principles of measurement systems*. London: Longman.

Bin Wan Salim, W., 2015. *Study of externally waste-gated turbine performance under steady and pulsating inlet conditions for improved turbocharger matching*. Ph.D. thesis.

Bruun, H.H., 1996. Hot-wire anemometry: principles and signal analysis.

Cao, T., Xu, L., Yang, M. and Martinez-Botas, R.F., 2014. Radial turbine rotor response to pulsating inlet flows. *Journal of turbomachinery*, 136(7), p.071003.

Capobianco, M. and Marelli, S., 2007. *Waste-gate turbocharging control in automotive si engines: effect on steady and unsteady turbine performance*. SAE Technical Paper.

Chen, H., Hakeem, I. and Martinez-Botas, R., 1996. Modelling of a turbocharger turbine under pulsating inlet conditions. *Proceedings of the institution of mechanical engineers, part a: Journal of power and energy*, 210(5), pp.397–408.

Chen, H. and Winterbone, D., 1990. A method to predict performance of vaneless radial turbines under steady and unsteady flow conditions. *Imeche turbocharging and turbochargers, paper (c405/008)*, pp.13–22.

Chiong, M., Rajoo, S., Romagnoli, A., Costall, A. and Martinez-Botas, R., 2014. Integration of meanline and one-dimensional methods for prediction of pulsating performance of a turbocharger turbine. *Energy conversion and management*, 81, pp.270–281.

Chiong, M., Rajoo, S., Romagnoli, A., Costall, A. and Martinez-Botas, R., 2015. Non-adiabatic pressure loss boundary condition for modelling turbocharger turbine pulsating flow. *Energy conversion and management*, 93, pp.267–281.

Chiong, M.S., Rajoo, S., Costall, A.W., Bin Wan Salim, W.S.I., Romagnoli, A. and Martinez-Botas, R.F., 2013. Assessment of cycle averaged turbocharger maps through one dimensional and mean-line coupled codes. *Turbo expo: Power for land, sea, and air*. American Society of Mechanical Engineers, vol. 55249, p.V06CT40A026.

Chiong, M.S., Rajoo, S., Romagnoli, A. and Martinez-Botas, R., 2012. Unsteady performance prediction of a single entry mixed flow turbine using 1-d gas dynamic code extended with meanline model. *Turbo expo: Power for land, sea, and air*. American Society of Mechanical Engineers, vol. 44717, pp.781–795.

Copeland, C., Newton, P., Martinez-Botas, R. and Seiler, M., 2012. A comparison of pulsed flow timescales within a turbine stage. *10th imeche international conference on turbochargers and turbocharging*.

Costall, A., 2015. Lecturer notes of introduction to turbocharger matching.

Costall, A. and Martinez-Botas, R.F., 2007. Fundamental characterization of turbocharger turbine unsteady flow behavior. *Turbo expo: Power for land, sea, and air*. vol. 47950, pp.1827–1839.

Costall, A.W., McDavid, R.M., Martinez-Botas, R.F. and Baines, N.C., 2011. Pulse performance modeling of a twin entry turbocharger turbine under full and unequal admission. *Journal of turbomachinery*.

Da Lio, L., Manente, G. and Lazzaretto, A., 2017. A mean-line model to predict the design efficiency of radial inflow turbines in organic rankine cycle (orc) systems. *Applied energy*, 205, pp.187–209.

Dantec Dynamics, 2019. *Dantec Dynamics StreamWare Pro installation and user guide*.

Deligant, M., Podevin, P. and Descombes, G., 2011. Cfd model for turbocharger journal bearing performances. *Applied thermal engineering*, 31(5), pp.811–819.

Deng, Q., 2017. *Dynamic characterisation and 1-d modelling of turbochargers for ic engines*. Ph.D. thesis. University of Bath.

Deng, Q., Pennycott, A., Zhang, Q., Avola, C., Pohorelsky, L. and Burke, R., 2021. Dimensionless quantification of small radial turbine transient performance. *Proceedings of the institution of mechanical engineers, part d: Journal of automobile engineering*, 235(1), pp.188–198.

Department for Business, Energy Industrial Strategy, 2020. Updated energy and emissions projections 2021 to 2040.

Duda, T., 2017. *Turbocharger performance and surge definition on a steady flow turbocharger test stand*. Ph.D. thesis. University of Bath.

Fang, X. and Dai, Q., 2010. Modeling of turbine mass flow rate performances using the taylor expansion. *Applied thermal engineering*, 30(13), pp.1824–1831.

Fang, X., Dai, Q., Yin, Y. and Xu, Y., 2010. A compact and accurate empirical model for turbine mass flow characteristics. *Energy*, 35(12), pp.4819–4823.

Futral, S.M. and Wasserbauer, C.A., 1965. *Off-design performance prediction with experimental verification for a radial-inflow turbine*. National Aeronautics and Space Administration.

Galindo, J., Fajardo, P., Navarro, R. and García-Cuevas, L., 2013. Characterization of a radial turbocharger turbine in pulsating flow by means of cfd and its application to engine modeling. *Applied energy*, 103, pp.116–127.

Gamma Technologies Inc., 2017. *GT-Suite flow dynamics-manual*.

Gorman, J., Bhattacharyya, S., Cheng, L. and Abraham, J., 2021. Turbulence models commonly used in cfd. *Computational fluid dynamics*. IntechOpen.

Greitzer, E.M., Tan, C.S. and Graf, M.B., 2007. Internal flow: concepts and applications.

Hellström, F., 2010. *Numerical computations of the unsteady flow in turbochargers*. Ph.D. thesis. KTH.

Heywood, J.B., 1988. Combustion engine fundamentals. *1ª edição. estados unidos*, 25, pp.1117–1128.

Holt, N., 2012. Engine downsizing. *Automotive manufacturing solutions*.

Hu, L., Yang, C., Sun, H., Krivizky, E., Larosiliere, L., Zhang, J. and Lai, M.C., 2010. *Experimental and computational analysis of impact of self recirculation casing treatment on turbocharger compressor*. SAE Technical Paper.

Jensen, J.P., Kristensen, A., Sorenson, S.C., Houbak, N. and Hendricks, E., 1991. *Mean value modeling of a small turbocharged diesel engine*. SAE Technical Paper.

Kacker, S. and Okapuu, U., 1982. A mean line prediction method for axial flow turbine efficiency.

Kastner, L. and Bhinder, F., 1975. A method for predicting the performance of a centripetal gas turbine fitted with a nozzle-less volute casing. *Turbo expo: Power for land, sea, and air*. American Society of Mechanical Engineers, vol. 79771, p.V01BT02A003.

Khairuddin, U.B. and Costall, A.W., 2018. Aerodynamic optimization of the high pressure turbine and interstage duct in a two-stage air system for a heavy-duty diesel engine. *Journal of engineering for gas turbines and power*, 140(5).

Kirkup, L., 2019. *Experimental methods for science and engineering students : an*

introduction to the analysis and presentation of data. Second edition. ed. Cambridge: Cambridge University Press.

Lam, J., Roberts, Q. and McDonnell, G., 2002. Flow modelling of a turbocharger turbine under pulsating flow. *Imeche. conference transactions from 7th international conference on turbochargers and turbocharging*. pp.14–15.

Lee, D., Jiang, L., Yilmaz, H. and Stefanopoulou, A.G., 2010. Air charge control for turbocharged spark ignition engines with internal exhaust gas recirculation. *Proceedings of the 2010 american control conference*. IEEE, pp.1471–1476.

Leufven, O. and Eriksson, L., 2010. Engine test bench turbo mapping. *Sae 2010 world congress, april 13-15, detroit, michigan, usa*. SAE International.

Liu, Z., 2020. *Mapping and optimising a mixed flow turbocharger turbine under unsteady flow conditions*. Ph.D. thesis. University of Bath.

Liu, Z. and Copeland, C., 2018. New method for mapping radial turbines exposed to pulsating flows. *Energy*, 162, pp.1205–1222.

Liu, Z. and Hill, D.L., 2000. Issues surrounding multiple frames of reference models for turbo compressor applications.

Meitner, P.L. and Glassman, A.J., 1980. *Off-design performance loss model for radial turbines with pivoting, variable-area stators.* National Aeronautics and Space Administration Cleveland Oh Lewis Research Center.

Meitner, P.L. and Glassman, A.J., 1983. *Computer code for off-design performance analysis of radial-inflow turbines with rotor blade sweep*. National Aeronautics and Space Administration Cleveland OH Lewis Research Center.

Menter, F.R., 1994. Two-equation eddy-viscosity turbulence models for engineering applications. *Aiaa journal*, 32(8), pp.1598–1605.

Mottram, R., 1992. Introduction: An overview of pulsating flow measurement. *Flow measurement and instrumentation*, 3(3), pp.114–117.

Moukalled, F., Mangani, L., Darwish, M. et al., 2016. *The finite volume method in computational fluid dynamics*, vol. 113. Springer.

Newton, P., 2014. An experimental and computational study of pulsating flow within a double entry turbine with different nozzle settings.

Padzillah, M., Yang, M., Zhuge, W. and Martinez-Botas, R., 2014. Numerical and experimental investigation of pulsating flow effect on a nozzled and nozzleless mixed flow turbine for an automotive turbocharger. *Turbo expo: Power for land, sea, and air*. American Society of Mechanical Engineers, vol. 45639, p.V02DT42A027.

Palfreyman, D. and Martinez-Botas, R., 2005. The pulsating flow field in a mixed flow turbocharger turbine: an experimental and computational study. *J. turbomach.*, 127(1), pp.144–155.

Payri, F., Benajes, J. and Reyes, M., 1996. Modelling of supercharger turbines in internal-combustion engines. *International journal of mechanical sciences*, 38(8-9), pp.853–869.

Payri, F., Serrano, J., Fajardo, P., Reyes-Belmonte, M. and Gozalbo-Belles, R., 2012. A physically based methodology to extrapolate performance maps of radial turbines. *Energy conversion and management*, 55, pp.149–163.

Payri, F., Serrano, J.R., Olmeda, P., Paez, A. and Vidal, F., 2010. Experimental methodology to characterize mechanical losses in small turbochargers. *Turbo expo: Power for land, sea, and air*. vol. 44007, pp.413–423.

Qiu, X., Anderson, M.R. and Baines, N.C., 2009. Meanline modeling of radial inflow turbine with variable area nozzle. *Turbo expo: Power for land, sea, and air*. vol. 48883, pp.1185–1191.

Rahbar, K., Mahmoud, S. and Al-Dadah, R.K., 2016. Mean-line modeling and cfd analysis of a miniature radial turbine for distributed power generation systems. *International journal of low-carbon technologies*, 11(2), pp.157–168.

Rajoo, S., 2007. *Steady and pulsating performance of a variable geometry mixed flow turbocharger turbine*. Ph.D. thesis. Department of Mechanical Engineering, Imperial College London.

Rajoo, S., Romagnoli, A. and RF, M.B., 2012. Single entry mixed flow turbine performance prediction with 1-d gas dynamic code coupled with mean line model. *International journal of gas turbine, propulsion and power systems*, 4(2), pp.8–16.

Ricardo-Wave, 2019. *Ricardo WAVE-RT flow theory manual*.

SAE, 1995a. SAE J1826 REAF, MAR95 Turbocharger gas stand test code. *Society of automotive engineers, inc.*

SAE, 1995b. SAE J922_199506 Turbocharger nomenclature and terminology. *Society of automotive engineers, inc.*

Salehi, R., Vossoughi, G. and Alasty, A., 2014. Modeling and estimation of unmeasured variables in a wastegate operated turbocharger. *Journal of engineering for gas turbines and power*, 136(5).

Samala, V., 2020. *Experimental characterization and mean line modelling of twin-entry and dual-volute turbines working under different admission conditions with steady flow*. Ph.D. thesis. Universitat Politècnica de València.

Schetz, J.A. and Fuhs, A.E., 1999. *Fundamentals of fluid mechanics*. John Wiley & Sons.

Serrano, J., Arnau, F., Dolz, V., Tiseira, A. and Cervelló, C., 2008. A model of turbocharger radial turbines appropriate to be used in zero-and one-dimensional gas

dynamics codes for internal combustion engines modelling. *Energy conversion and management*, 49(12), pp.3729–3745.

Serrano, J.R., Arnau, F.J., Andres, T. and Samala, V., 2017. Experimental procedure for the characterization of turbocharger's waste-gate discharge coefficient. *Advances in mechanical engineering*, 9(10), p.1687814017728242.

Serrano, J.R., Arnau, F.J., García-Cuevas, L.M., Gómez-Vilanova, A., Guilain, S. and Batard, S., 2021a. A methodology for measuring turbocharger adiabatic maps in a gas-stand and its usage for calibrating control oriented and one-dimensional models at early ice design stages. *Journal of energy resources technology*, 143(4).

Serrano, J.R., Arnau, F.J., García-Cuevas, L.M., Gómez-Vilanova, A., Guilain, S. and Batard, S., 2021b. A methodology for measuring turbocharger adiabatic maps in a gas-stand and its usage for calibrating control oriented and one-dimensional models at early ice design stages. *Journal of energy resources technology*, 143(4).

Serrano, J.R., Olmeda, P., Tiseira, A., García-Cuevas, L.M. and Lefebvre, A., 2013. Theoretical and experimental study of mechanical losses in automotive turbochargers. *Energy*, 55, pp.888–898.

SIEMENS, 2021. SITRANS F Coriolis Flowmeters SITRANS FC330. `https://industry.siemens.com/dl/files/408/109764408/att_975270/v1/A5E44030648-ABen_FC330_OI_en-US.pdf`.

Sieros, G., Stamatis, A. and Mathioudakis, K., 1997. Jet engine component maps for performance modeling and diagnosis. *Journal of propulsion and power*, 13(5), pp.665–674.

Szymko, S., 2006. *The development of an eddy current dynamometer for evaluation of steady and pulsating turbocharger turbine performance*. Ph.D. thesis. Imperial College London.

Taylor, A. and Costall, A., 2019-2020. Lecture notes in thermal propulsion systems-future clean transport technology.

Vijayakumar, R., Akehurst, S., Liu, Z., Reyes-Belmonte, M., Brace, C., Liu, D. and Copeland, C., 2019. engDesign and testing a bespoke cylinder head pulsating flow generator for a turbocharger gas stand. *Energy*, 189, p.116291.

Wallace, F. and Blair, G., 1965. *The pulsating-flow performance of inward radial-flow turbines*, vol. 79900. American Society of Mechanical Engineers.

Wallace, F. and Miles, J., 1970. Performance of inward radial flow turbines under unsteady flow conditions with full and partial admission. *Proceedings of the institution of mechanical engineers*, 185(1), pp.1091–1105.

Wang, H., Burke, R. and Copeland, C., 2020. The sensitivity study of a mechanical loss model in turbocharger system. *Internal combustion engine division fall technical conference*. American Society of Mechanical Engineers, vol. 84034, p.V001T04A004.

Watson, N. and Janota, M., 1982. *Turbocharging the internal combustion engine*. Macmillan International Higher Education.

Whitfield, A. and Wallace, F., 1973. Study of incidence loss models in radial and mixed-flow turbomachinery. *Conference on heat and fluid flow in steam and gas turbine plant, coventry, england*. pp.122–128.

Wibmer, M., Schmidt, T., Grabherr, O. and Durst, B., 2015. Simulation of turbocharger wastegate dynamics. *Mtz worldwide*, 76(2), pp.28–31.

Winterbone, D., Nikpour, B. and Alexander, G., 1990. Measurement of the performance of a radial inflow turbine in conditional steady and unsteady flow. *Proceedings of the 4th international conference on turbocharging and turbochargers*. pp.22–24.

Zhu, S., Deng, K. and Liu, S., 2015. Modeling and extrapolating mass flow characteristics of a radial turbocharger turbine. *Energy*, 87, pp.628–637.